

Nano Materials for Electrochemiluminescent Biosensors

Anita Venkatanarayanan B.Sc. (Hons.)

A Thesis presented at Dublin City University
for the Degree of Doctor of Philosophy

Supervisors
Prof. Robert J. Forster
and
Prof. Tia E. Keyes
School of Chemical Science
Dublin City University

June 2010

DECLARATION

I certify that this thesis, which is submitted for the requirement of the award of doctor of philosophy, is entirely of my own research work carried out at Dublin City University and has not been taken from the work of other, save and to the extent that such work has been cited and acknowledged within the text of my work.

ABSTRACT

A biosensor is a compact analytical device incorporating a biologically active sensing element associated with a physicochemical transducer. The biological or biochemical event recognised by the sensing element is converted, selectively, into a detectable signal, electrical/optical, by the transducer, without prior separation of multi-component samples. An appropriate union between the electrochemical sensor and biological component is often essential to eliminate major limitations including high reagent consumption, large signal loss due to diffusion of the reagents out of the detection zone, low signal to noise ratio, non specific binding, electrode fouling etc. Effective immobilization of redox molecules can solve most of these issues to a significant extent.

The oxidative electropolymerization of two ruthenium complexes, $[\text{Ru}(\text{aphen})_2\text{bpy}]^{2+}$ and $[\text{Ru}(\text{aphen})_3]^{2+}$ where, aphen = 5-amino-1,10-phenanthroline, bpy = 2,2'-bipyridine), in aqueous and organic media is reported along with their electrochemical, photophysical and ECL properties. The results highlight the potential of these polymeric luminophores, as biological immobilization matrix in the development of biosensors.

Also in order to increase the sensitivity of the ECL biosensors, potential modulation technique coupled with synchronous lock-in detection was used to study surface confined $[\text{Ru}(\text{bpy})_2(\text{PVP})_{10}]^{2+}$ where, PVP = poly(vinyl pyridine) films. This novel approach provides the capability of phase sensitive detection, which allows differentiation of analytical signal from stray light. Thus, eliminating one of the key limitation of an ECL biosensor.

And finally a novel high brightness luminophore $[\text{Ru}(\text{bpy})_2(\text{pic})]^{2+}$ where, pic = 2-(4-carboxyphenyl)imidazo[4,5-f][1,10] phenanthroline, has been used as an electrochemiluminescent antibody (IgG) label to perform novel immunoassay . The performance of this assay has been optimized to detect very low concentrations of anti-IgG

CHAPTER I
LITERATURE SURVEY

1.1 INTRODUCTION

The world of medical diagnostics has advanced at a tremendous rate during the past decade or so, as a number of life threatening diseases like cancer, coronary artery disease, diabetes *etc.* are becoming more and more common.¹⁻⁴ The best method to diagnose and treat these life threatening diseases is by early detection and real time monitoring of early stage 'biomarkers'. Biomarkers have gained immense scientific and clinical interest in recent years.^{1,3,5-7} They are substances whose presence in the body indicates a particular disease state. For instance, elevated levels of troponin T or I (> 350 nM)⁸ indicate the occurrence of acute myocardial infarction (heart attack) and the longer the Troponin level is elevated, the more extensive is the infarct.⁹ A biomarker indicates a change in expression or state of a protein that correlates with the risk or progression of a disease, or with the susceptibility of the disease to a given treatment. Thus, they are very useful in the contexts of primary, secondary and tertiary prevention.⁴ Pico to femto level detection of biomarkers can be achieved by integrating the revolutionary advances made in biotechnology and genetics for the recognition of specific biomarkers with the advances in electrochemistry, photonics and nanotechnology for analytical capability. This integration has lead to the development of a new breed of sophisticated and reliable biosensors.

A biosensor is a compact analytical device incorporating a biologically active sensing element associated with a physicochemical transducer. The biologically active sensing element recognizes specific analyte. This recognition is selectively converted into a detectable signal, without separation of interfering components.^{10,11} Figure 1.1 depicts the basic components of a biosensor.

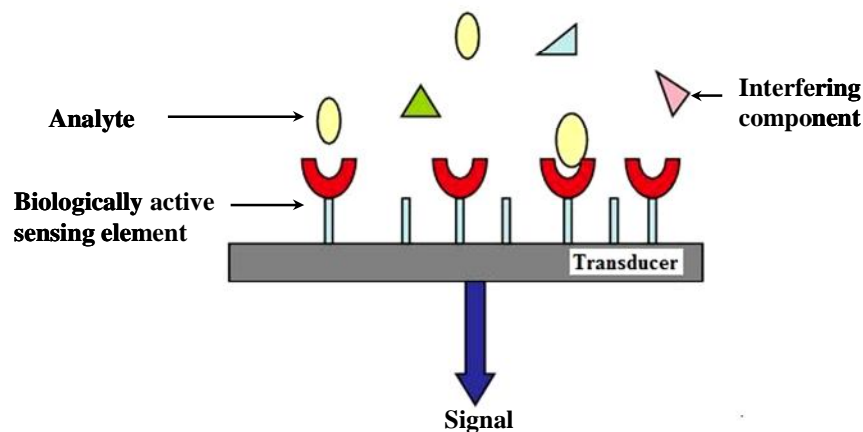


Figure 1.1: Basic components of a biosensor.

Sensors are built on surfaces and the nature of the support, the coating on its surface and the biomolecule immobilization strategies, all play pivotal role in determining its function. This thesis focuses on the utilization of novel ruthenium polypyridyl materials for the development of sensitive and selective electrochemiluminescent biosensor platforms.

This thesis is organized into several sections. Chapter 1 reviews relevant literature. The concepts relating to the solid state electrodes are introduced. Relevant literature related to transducer surface modification with metallopolymers and carbon nanotubes is briefly summarized. Finally, the general principles, mechanisms and analytical applications of electrochemiluminescence (ECL) are presented.

Chapter 2 outlines the experimental methods and procedures used to synthesise and characterize the various ruthenium polypyridyl complexes employed.

Chapter 3 describes the modification and characterization of glassy carbon electrodes with $[\text{Ru}(\text{bpy})_2\text{PVP}_{10}]^{2+}$ polymer layer, where bpy = 2,2'-bipyridine and PVP= poly 4 vinylpyridine. The polymer layer has been characterized using profilometry, cyclic voltammetry and AC impedance. The fabrication of vertically aligned single walled carbon nanotube (SWCNT) ITO electrodes

along with the functionalization of SWCNT and formation of IgG-G1-(Ru(bpy)₂PICH₂) where, PICH₂ is 2-(4-carboxyphenyl)imidazo[4,5-f][1,10]phenanthroline], bio-conjugates are described in detail in this chapter.

The electropolymerization of [Ru(aphen)₂bpy]²⁺ and [Ru(aphen)₃]²⁺ complexes where, aphen = 5-amino-1,10-phenanthroline, and the properties of the electropolymerised films formed by oxidative electropolymerization in two different media namely, anhydrous acetonitrile and sulphuric acid, are reported in Chapter 4. The photophysical and spectroscopic properties of the films including electrochemiluminescence properties are discussed. The advantage of these polymeric luminophores as an immobilization matrix and ECL emitters is highlighted.

Chapter 5 describes the use of an AC and DC potential modulation technique for sensitive detection of ECL from [Ru(bpy)₂PVP₁₀]²⁺ polymer modified electrode. The analytical performances of both DC and AC modulation techniques for the solution phase and surface confined ruthenium species is reported. For the purpose of interpretation, the impedance characteristics of the polymer film at different potentials have been modelled using a modified Randle-Ershler circuit.

Finally, Chapter 6 describes the patterned assembly of nanotube forests on transparent ITO substrates. Also two different methodology, drop coating and inkjet printing has been reported along with ultrasensitive detection of proteins by a novel approach using G1.5 acid terminated PAMAM dendrimers as size selective protein linkers. This chapter also provides an overview of the SWCNT-ITO immunosensors' analytical performance.

1.2 BIOSENSORS

The name biosensor itself signifies that the device has two elements, namely a bio-element and sensor element. The bio-element can be proteins, antibody, antigen, enzymes, DNA, living cells, tissues etc. The sensor elements can include a variety of transduction devices which work on various mechanisms like electric current, potential, light, impedance, intensity and phase of electromagnetic radiation, viscosity and mass.¹⁰⁻¹²

Based on the transduction method used, biosensors are classified¹¹ as thermal, optical, ion-sensitive or electrochemical.¹³ However, many biological molecules are not intrinsically electroactive and hence they cannot be detected directly. Indirect methods like using enzymes, which catalyze bio-specific redox reactions, are then employed. These enzymes facilitate the production of electroactive species, which can then be detected by electrochemical methods.¹¹

However, an appropriate union between the electrochemical sensor and biological component is often essential to eliminate major limitations including large signal loss due to diffusion of the reagents out of the detection zone or high reagent consumption, low signal to noise ratio, interferences due to non specific binding or electrode fouling *etc.* Effective immobilization techniques can solve most of these issues to a significant extent. The fundamental prerequisites of biomolecule deposition procedures are:³⁰

1. Efficient and stable immobilization of the biological macromolecule on the transducer surface
2. Complete retention of its biological properties
3. Biocompatibility and chemical inertness of the host structure and
4. Accessibility of the immobilized biomolecules so that they can bind their guests, e.g., antigen, nucleic acid etc.

1.3 ELECTROCHEMILUMINESCENCE

1.3.1 Introduction and general principles

Electrochemiluminescence or electrogenerated chemiluminescence (ECL) is a means of converting electrical energy to radiative energy.¹⁴ Although luminescence during electrolysis was observed in 1920, the first detailed report on ECL by Hercules¹⁵ was published in 1964. From then on, it has been extensively investigated to elucidate the mechanism and develop applications.

ECL mainly involves the production of reactive intermediates from stable precursors at the surface of the electrode. These intermediates then undergo electron transfer reactions under a variety of conditions to form excited states that emit light. ECL is very similar to chemiluminescence (CL), in the sense that in both processes light is produced by species that undergo highly energetic electron transfer reactions. However, luminescence in CL is initiated by mixing reagents and careful manipulation of fluid flow. In contrast, in ECL, luminescence is initiated and controlled by changes in the electrode potential.¹⁴ ECL has many advantages over the other luminescence techniques. Firstly, in ECL the electrochemical reaction allows for precise control over the time and position of the light emitting reaction. Control over time allows one to synchronise the luminescence and the biochemical reaction under study. Control over position not only improves sensitivity of the instrument by increasing the signal to noise ratio, but also allows multiple analytical reactions in the same sample to be analysed using an electrode array. ECL is also a more selective and non-destructive technique as varying the electrode potential can precisely control the generation of excited states and most of the ECL emitters are regenerated after emission. Many analytical methods such as high performance liquid chromatography (HPLC), liquid chromatography (LC), capillary electrophoresis (CE) and flow injection analysis (FIA) require the addition of reagents in separate streams to produce CL. This often results in expensive instrumentation, sample dilution and peak broadening. In ECL however, the reactants are generated *in situ*. Also there is no light source involved and hence problems related to scattering of light, auto fluorescence and presence of luminescent impurity are avoided.¹⁶ These make the

instrumentation for ECL simple and inexpensive. Most researchers in the field construct their own apparatus, either by modifying electrochemical apparatus to include a light detector, or by replacing the excitation light source in a spectrometer with an electrochemical cell, or more typically by building a dedicated ECL flow cell.¹⁷

The rapid development in the field of electrochemiluminescence detection indicates the importance of this technique in terms of ultra sensitive detection and quantification of biomolecules. ECL has great promise in the field of biosensors, which require miniaturization, multi-analyte sensing, high sensitivity, low detection limit and good selectivity. However, one of the biggest disadvantage of this technique is it greatly depends on the rate of charge transfer. High charge transfer rates significantly increase signal intensity and hence sensitivity. A better understanding of the ECL mechanisms, biomolecular interactions with ECL reactants, kinetics and thermodynamics of the analyte can provide valuable insights into the phenomena of charge transport through thin electrochemiluminescent layers.

The basic equipment needed for ECL generation is very simple and consists of an electrochemical cell and a light detector. ECL is typically detected with a photodetector such as a photomultiplier tube (PMT), a photodiode, or a charge-coupled device (CCD) that is positioned to collect light from the working electrode. In flow-based systems, part of the electrochemical cell is transparent so that the light generated at the electrode can reach the detector. The electrodes and the detector are contained within a light tight housing to reduce background light.¹⁸

Although several designs are present in the literature, many stem from the same basic design^{16,19} shown in Figure 1.2. However, a trend towards miniaturization is observed recently.²⁰⁻²³

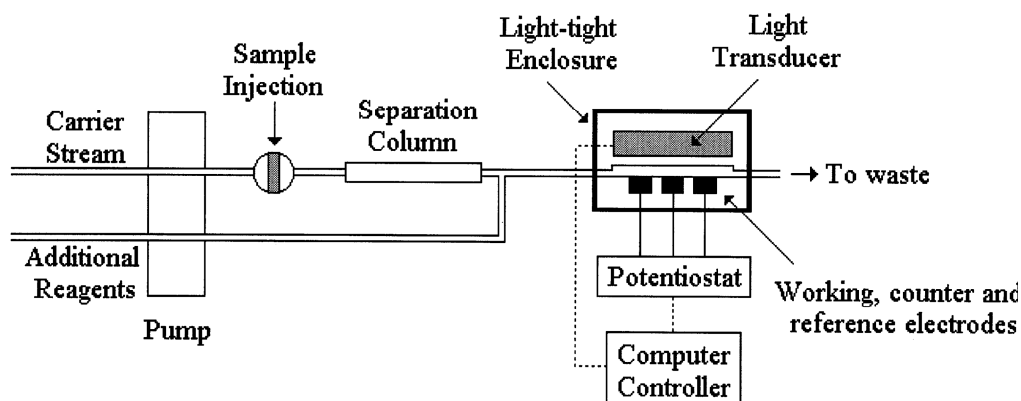


Figure 1.2: Schematic diagram of a typical basic experimental apparatus used for the generation and measure of ECL. Reprinted from Knight, A.; *A review of recent trends in analytical applications of electrogenerated chemiluminescence*, trends in analytical chemistry, 1999, 18, 1.

A major disadvantage with the current ECL setup is the light tight housing. Fluorescence and ECL detection both need “black box” conditions and this is a major road block in the field of chip based sensors. However, Preston and co-workers²⁴ have developed a novel ECL probe that does not require conventional dark box conditions and can exclude ambient light. This probe contains a shielded transducer and it was tested with $[\text{Ru}(\text{bpy})_3\text{Cl}_2]$ system and luminol ECL coupled with an immobilized oxidase enzyme. However, there still exists a need to develop ECL instrumentation such that chip based ECL sensors could be used outside the lab.

1.3.2 Mechanisms of ECL generation

ECL can arise from organic as well as inorganic substances.^{14,25,26} It can also be produced by annihilation reactions between reduced and oxidized forms of the same species. ECL can also be observed when a co-reactant is employed that forms an energetic oxidant or reductant on bond cleavage.¹⁸ Alternative pulsing of the electrode potential as well as direct current (D.C.) electrolysis may be used and the precursors may be generated sequentially at the electrode by CV or

potential step techniques or simultaneously at a rotating ring disk or double band electrode.

Traditionally, ECL was generated via annihilation, which involved electron transfer reactions between an oxidized and a reduced species, both of which were generated at an electrode by alternate pulsing of the electrode potential.¹⁴ This approach is typically called “annihilation”, and a general mechanism is outlined below:

Scheme 1



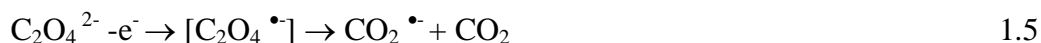
Where, Equation 1.1 is reduction at the electrode, Equation 1.2 is oxidation at the electrode, Equation 1.3 excited state formation and Equation 1.4 light emission. For example, when the potential of the working electrode is quickly changed between two values in order to generate the reduced, $A^{\bullet-}$ and oxidized, $A^{\bullet+}$ species (Equations 1.1 and 1.2, respectively) that will react near the electrode surface to form the emissive state, A^* (Equation 1.3). These types of reactions generally involve the use of rigorously purified and deoxygenated nonaqueous solvents (*e.g.* dimethylformamide and acetonitrile), since the available potential range in water is too narrow to generate the required energetic precursors.¹⁸ Many ECL reactions of this type have been investigated and their mechanisms are well understood.^{14,27,28}

However, as these reactions need organic solvents they are of limited applicability especially in the field of biosensors, as all bio-related samples or analytes require aqueous medium.

1.3.3 Co-reactant ECL

Of more interest to practical applications, is ECL that can be generated utilizing a co-reactant, in a single step.¹⁴ A co-reactant is a species' capable of forming strong oxidants or reductants upon bond cleavage such as oxalate ($\text{C}_2\text{O}_4^{2-}$) or peroxodisulphate ($\text{S}_2\text{O}_8^{2-}$).²⁶ However, it should be noted that while being a strong oxidizing/reducing agent is very important, it is not the only condition required for a co-reactant to produce ECL. Other conditions, like the solubility of the co-reactant in the reaction media, stability of the intermediate species generated electrochemically and chemical,²⁶ ability of the co-reactant to form intermediates is equally important. The intermediates should have sufficient reducing or oxidizing energy to react with the oxidized or reduced luminophore to form excited state.¹⁴ The co-reactant should also be able to produce intermediates that can undergo rapid reaction with the redox luminophore and should not be good quenchers of ECL²⁵. Finally the co-reactant itself should not emit any ECL signal over the potential range scanned.²⁶

Oxalate ion ($\text{C}_2\text{O}_4^{2-}$) was first reported by Bard's group²⁹ in 1977. It is believed to produce the strong reductant $\text{CO}_2^{\bullet-}$ upon oxidation in aqueous solution:



The oxidizing potential can also oxidize an ECL luminophore such as $[\text{Ru}(\text{bpy})_3]^{2+}$.



$[\text{Ru}(\text{bpy})_3]^{\bullet+}$ and $\text{CO}_2^{\bullet-}$ then react to produce an excited state which is capable of emitting light. In co-reactant ECL, the electrode typically only oxidizes or reduces the reagents in a single potential step, unlike the annihilation schemes where a double-potential step (*e.g.* oxidation followed by reduction) is required to generate the highly energetic precursors.¹⁴ Another system which has very important practical applications is the $[\text{Ru}(\text{bpy})_3]^{2+}$ / Tri-*n*-propylamine (TPA) system. The TPA system has become highly central, as it not only allows efficient ECL in aqueous media but also at physiological pH 7.4. ECL in this system is produced upon concomitant oxidation of $[\text{Ru}(\text{bpy})_3]^{2+}$ and TPA as

shown in Figure 1.3, in which tripropylamine in solution is either oxidized or reduced at the same potential step as the $[\text{Ru}(\text{bpy})_3]^{2+}$. The co-reactant then forms a new species, which reacts with the $[\text{Ru}(\text{bpy})_3]^{2+}$ to generate light. However, recent work utilizing cyclic voltammetric simulations, SECM and ECL experiments on the $[\text{Ru}(\text{bpy})_3]^{2+}/\text{TPA}$ system indicates that other reaction mechanisms for the production of the excited state are also possible. Four different schemes have been proposed^{14,25,30,31} and are as shown in Figure 1.4.

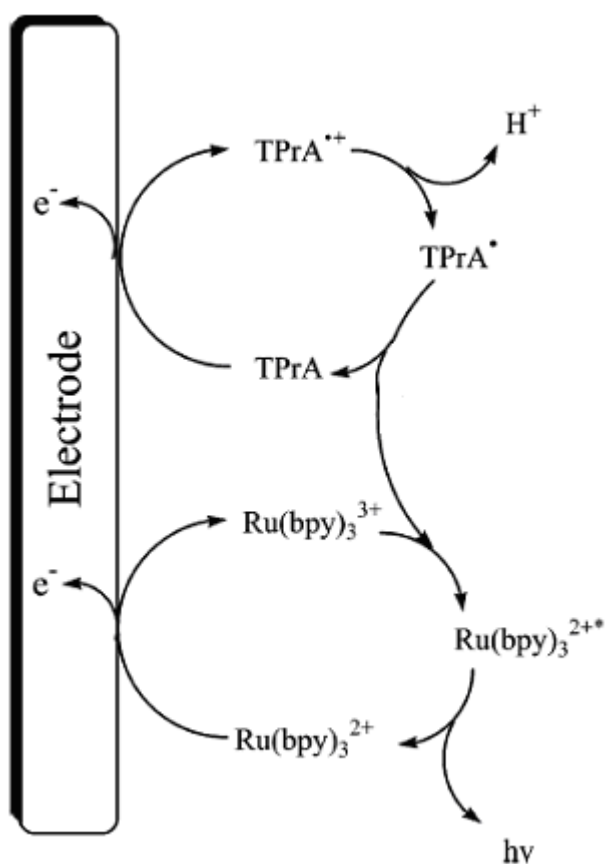
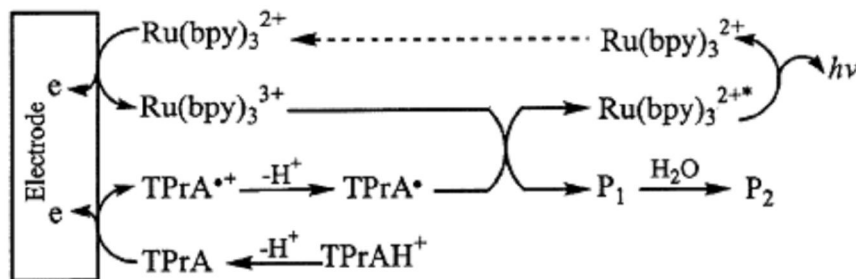
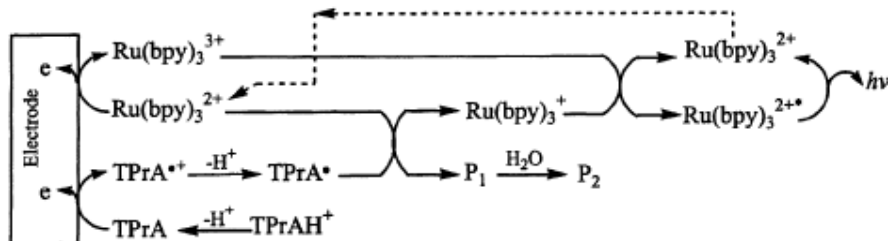


Figure 1.3: Proposed mechanism for $\text{TPA}/[\text{Ru}(\text{bpy})_3]^{2+}$ ECL system. Reprinted from *Electrochemiluminescence (ECL)*, Richter, M. M, Chem. Rev., 2004, 104, 3003-3036.

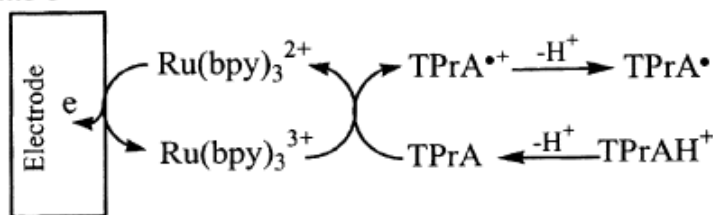
Scheme 1



Scheme 2



Scheme 3



Scheme 4

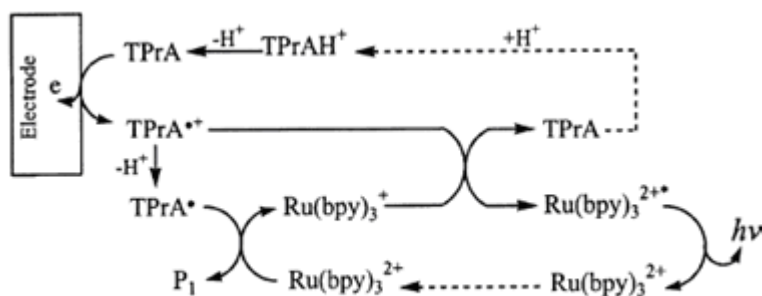


Figure 1.4: Schemes for tripropylamine and $[\text{Ru}(\text{bpy})_3]^{2+}$ reaction mechanism. Reprinted from *Electrogenerated Chemiluminescence* 69: The Tris(2,2'-bipyridine)ruthenium(II), $(\text{Ru}(\text{bpy})_3^{2+})$ /Tri-n-propylamine (TPrA) System Revisited-A New Route Involving $\text{TPrA}^{\bullet+}$ Cation Radicals, where, $\text{TPrA}^{\bullet+} = (\text{CH}_3\text{CH}_2\text{CH}_2)_3\text{N}^{\bullet+}$, $\text{TPrAH}^+ = \text{Pr}_3\text{NH}^+$, $\text{TPrA}^\bullet = \text{Pr}_2\text{NC}^\bullet\text{HCH}_2\text{-CH}_3$, $\text{P}_1 = \text{Pr}_2\text{N}^+\text{C}=\text{HCH}_2\text{CH}_3$ and $\text{P}_2 = \text{Pr}_2\text{NH} + \text{CH}_3\text{CH}_2\text{-CHO}$, *J. Am. Chem. Soc.*, 2002, 124, 48, 14478-14485.

From the above reactions mechanisms, it is evident that the key feature of ECL is that the reaction is highly exergonic and although production of ground state species is highly exergonic, faster kinetic pathways also exists.³² Significantly, these aspects should be taken into consideration when designing new ECL systems. Researchers are devoting significant efforts towards developing novel transition metal complexes to be used as ECL probes.^{33,34} Since all the work reported here has been done with ruthenium polypyridyl complexes their photophysical, spectroscopic and electrochemiluminescent properties are outlined below.

1.3.4 Ruthenium polypyridyl complexes as luminescent ECL probes

All the transition-metal complexes discussed here have six *d* electrons. The presence of ligands splits the *d*-orbital energy level into three lower (*t*) and two higher (*e*) orbitals³⁵ as shown in Figure 1.5. The extent of splitting is determined by the crystal-field strength Δ . The three lower-energy *d* orbitals are filled by the six *d* electrons. Transitions between the orbitals *t*→*e* are formally forbidden. Hence, even if *d-d* absorption occurs, the radiative rate is low and emission is not observed. Additionally, electrons in the *e* orbitals are antibonding with respect to the metal-ligand, so excited *d-d* states are usually unstable. The appropriate combination of metal and ligand results in a new transition involving charge transfer between the metal and the ligand. For the purpose of this study, metal-to-ligand charge transfer states are particularly important. They are the lowest-energy excited states for the metal complexes studied here and are responsible for their electrochemiluminescence processes.

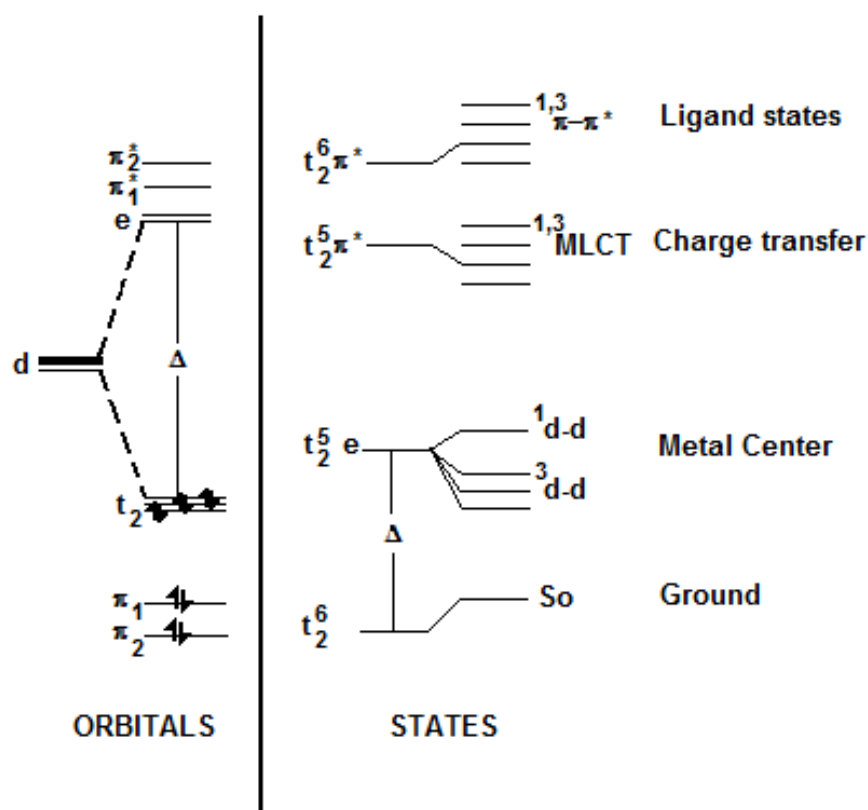


Figure 1.5: Orbital and electronic states of metal-ligand complexes. The d orbitals are associated with the metal and the π orbitals are associated with the ligands. Reprinted from Lakowicz, J. R.; *Principles of fluorescence spectroscopy*, second edition, 1999, 573-594.

The complexes that are dealt in this thesis are octahedral d^6 metal complexes. MLCT transitions in these complexes occur from occupied π_M (t_{2g}) metal based orbitals to empty π^* ligand based molecular orbital (MO) and formally corresponds to the oxidation of the metal and reduction of the ligand in the excited state.^{36,37}

Their energies are therefore related to the redox properties of the metal complex. Indeed, for complexes with easily reducible ligands such as α -diimines, MLCT levels are significantly stabilized. MLCT absorption bands are usually intense and emission from these states is formally phosphorescence. However, these states are somewhat shorter lived (hundreds of nanoseconds) than normal phosphorescence states. The luminescence of these MLCTs is thought to be

short lived due to spin-orbit coupling with the heavy metal atom, which allows the normally forbidden transition to the ground state.^{36,37}

A schematic diagram of the electronic property for typical ruthenium polypyridyl complexes is as shown in Figure 1.9.³⁸

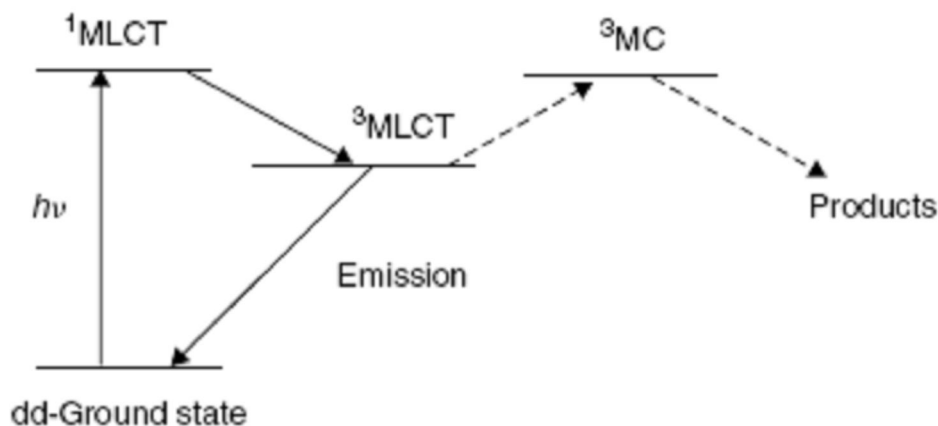


Figure 1.6: Schematic diagram of the electronic properties of typical ruthenium polypyridyl complexes. Reprinted from Forster, R. J.; Keyes, T. E.; Vos, J. G.; *Interfacial Supramolecular Assemblies*, John Wiley & Sons, Ltd, England, 2003.

Upon excitation of the molecule, an electron is promoted from a metal-based ground state, d–d in character, to a π^* -orbital of the 2,2-bipyridyl ligand. This is a singlet state $^1\text{MLCT}$ transition. Fast and efficient intersystem crossing occurs, in less than 300 fs, from this singlet state to a triplet $^3\text{MLCT}$ state.³⁸ From this state, deactivation can occur either via radiative or non-radiative pathways. The radiative decay will lead to emission, whereas in non-radiative pathway, the excess energy is dissipated by deactivation with solvent or via population of the metal-centered triplet (^3MC) state. Generally, the nonradiative decay rates (k_{nr}) are faster than radiative decay rates (γ), and the decay times are determined mostly by non-radiative decay rates.³⁵ Also, population of the ^3MC state has important implications. If this occurs, the electron occupies an anti-bonding metal-based orbital, resulting in distortion of the metal ligand axes and weakening the Ru–N bonds. This may cause photochemical decomposition of

the complex, which manifests itself as ligand loss followed by co-ordination of a substitute ligand, often solvent or electrolyte.³⁸

Because MLCT transitions generally involve a change in the dipole moment of the complex, on going from the ground to the excited states, their corresponding absorption and emission bands are usually solvatochromic, *i.e.* they shift on changing solvent polarity.^{36,37}

In general, the emission of luminescent transition metal complexes always arises from the lowest excited state, which is either a metal to ligand charge transfer (MLCT) or localized π - π^* transition.^{39,40,40}

The lifetime, τ , of the excited state and the emission quantum yield (ϕ_{em}) are important experimental parameters for the investigation of the spectroscopic properties of these molecules, and can be expressed as per Equation 1.7 and Equation 1.8, respectively.

$$\frac{1}{\tau} = k_r + k_{nr} \quad 1.7$$

$$\phi_{EM} = k_r \tau \quad 1.8$$

where, k_r and k_{nr} are radiative and non-radiative decay rate constants.

Ruthenium polypyridyl complexes continue to play a vital role in ECL based assay systems. Their dominance is mainly due to their nearly ideal reversible voltammetry and their attractive photophysical properties mentioned above, as well as synthetic versatility of the polypyridine ligand.³² Continuous research towards developing novel high brightness luminophores which not only possess excellent photophysical and electrochemical properties but also possess biomolecule binding capabilities. The best example for elucidating the binding capability is the commercially available ruthenium (III) tris-bipyridine N-hydroxysuccinimide,⁴¹ as shown in Figure 1.10.

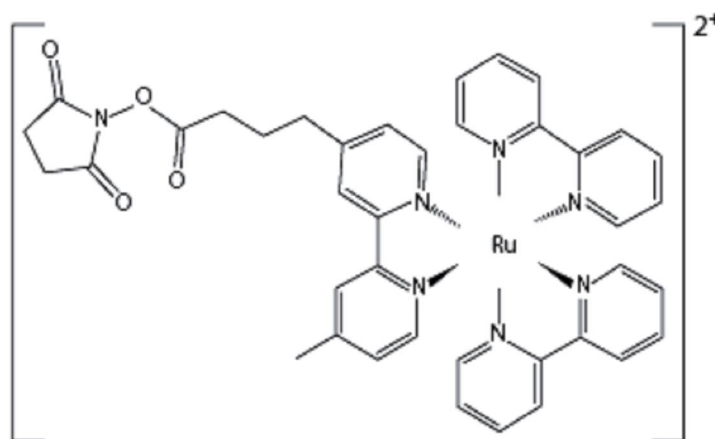


Figure 1.7: Ruthenium (III) tris-bipyridine N-hydroxysuccinimide label for biological molecules.

Another example developed by Pellegrin and co-workers⁴² is $[\text{Ru}(\text{bpy})_2\text{PICH}_2]^{2+}$ where, $\text{PICH}_2 = 2\text{-(4-carboxyphenyl)imidazo[4,5-f][1,10]phenanthroline}$. This complex contains a carboxyl group which can be covalently coupled to the amine bonds of biomolecules and it is reported that it has a 30% higher quantum yield than $[\text{Ru}(\text{bpy})_3]^{2+}$.⁴² However, its ECL properties have not been studied.

1.3.5 Analytical applications

Solution phase $[\text{Ru}(\text{bpy})_3]^{2+}$ ECL has been used in flow injection analysis to quantify aliphatic amines, which act as reducing agents in a manner analogous to oxalate. It was found that ECL emission from the reaction with amines increases in the order $1^\circ < 2^\circ < 3^\circ$ amines.²⁰ Because tertiary amines can produce a sensitive ECL response, studies were carried out to introduce such groups to initially less or non-ECL sensitive analytes, such as amino acids^{43,44} and fatty acids.^{44,45} Previously two reagents, dansyl chloride and divinyl sulfone were reported for ECL system with limits of detection being 2 pmol for amino acids and 1-30 pmol for primary amines.¹⁶

ECL technology has recently been commercially developed for the clinical diagnostic market.^{46,47} Assays have been developed for a wide variety of applications like infectious diseases,⁴⁸ cardiac diseases, tumors,¹⁶ drug, surface

water,⁴⁹ studying bone metabolism,¹⁶ hypothalamic, pituitary and adrenal disorders.⁵⁰

ECL assays are usually either solution phase or solid phase. Solid phase systems are used for biomolecules which have very poor or no co-reactant ability. Such biomolecules are linked with the ECL labels (*i.e.* $[\text{Ru}(\text{bpy})_3]^{2+}$ and are immobilized onto a solid substrate (like screen printed electrode or micro sized polystyrene bead or magnetic bead *etc.*). The ECL signal is proportional to the concentration of the analyte in the presence of added ECL co-reactant like tripropylamine. Conventional antigen-antibody reactions have also been combined with ECL generation with the help of streptavidin coated magnetic particles.^{19,23,25} The sample is combined with a reagent containing the biotinylated capture antibody and a ruthenium labelled secondary antibody. During incubation the antibodies capture the target molecules, the microparticles are then added and during a second incubation period the biotinylated antibody attaches to the streptavidin coated particles. The samples are then drawn into the ECL measuring cell along with a buffer containing TPA. A magnet located under the electrode captures the microparticles at the electrode surface and all unbound reagent is washed from the cell. The magnet is then removed and a potential is applied to the electrode, initiating ECL.²³

Some examples of solid state ECL system currently used, are illustrated in Figure 1.10, Figure 1.11¹⁶ and Figure 1.12. The panels a-c, d-f and g-h are DNA, antibody-antigen and peptide related assays respectively. Figure 1.11 is a schematic representation of DNA hybridisation (a) and sandwich type immunoassay using polystyrene bead as ECL label carrier and magnetic bead for separation of target analytes.¹⁶ Also multi-labelling of a biomolecule at a single site with dendritic label bearing multiple signal-generating units have been explored to increase the signal⁵¹ as shown in Figure 1.12. New techniques of generating ECL from CdSe quantum dots on gold nanoparticles for the detection of human pre-albumin⁵² have also been recently reported.

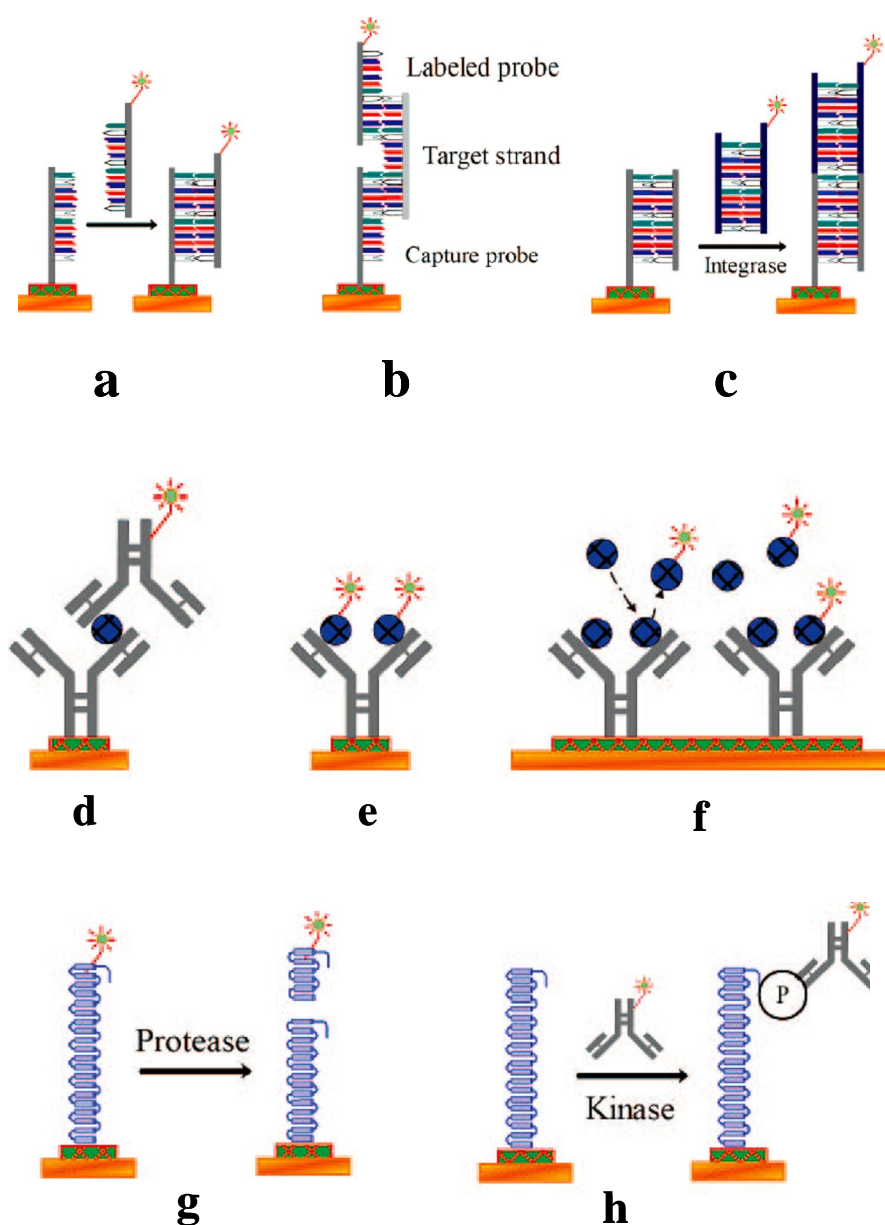









Figure 1.8: Schematic drawing of solid state ECL assay with DNA (a-c), antibody-antigen (d-f), and peptide (g-h) system, where  is solid substrate,  is immobilisation layer,  is single stranded DNA,  is antibody,  is antigen,  is ECL label and  is peptide. Reprinted from Miao, W.; Chem. Rev. 2008, 108, 2506-2553.

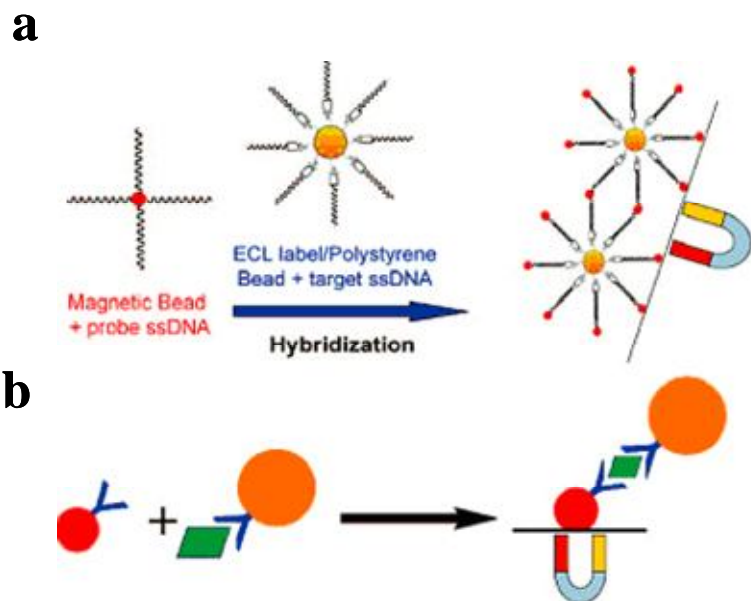


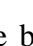

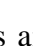
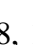


Figure 1.9: Representation of DNA hybridization (a) and sandwich type immunoassay where polystyrene beads are used as ECL label carrier and magnetic bead as target analyte separator. The symbol  is ssDNA,  is magnetic bead,  is ECL label loaded polystyrene bead,  is antibody,  is antigen and  is a magnet. Reprinted from Miao, W.; Chem. Rev., 2008, 108, 2506-2553.

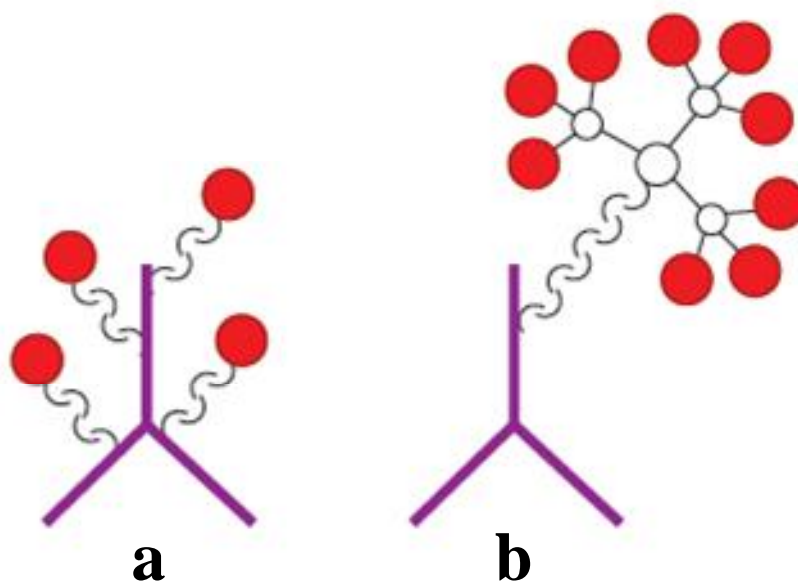


Figure 1.10: Multi-labelling scheme at (a) multiple and (b) single site using dendrimers. Reprinted from Zhou, M. R., *Multilabelling biomolecules at a single site, 1. Synthesis and characterization of a dendritic label for electrochemiluminescence assay*, Anal. Chem., 2003, 75:6708-6717

The use of co-reactant ECL in a wide range of analytical applications including chromatography,^{44,45,53} clinical diagnosis,⁵⁴ environmental projects²⁵ and biodefence⁵⁵⁻⁵⁷ is a clear proof of how important and powerful this technique is in terms of sensitive detection and quantification of biomolecules. Further progress in this field mainly depends on discovery of new advanced materials, interfacial films and nanoparticle coatings, advances in microfluidics leading to total analytical or lab-on-a-chip systems and new theoretical insights into the differences between plasmonic and quenching effects observed through optical and electrochemical excitation.³²

1.4 MODIFIED ELECTRODES

There are several disadvantages associated with solution phase ECL systems like loss of signal due to diffusion of the ECL reagent out of the detection zone, limited ability to repeatedly cycle an individual luminophore and high reagent consumption.⁵⁸ Great efforts have been made towards immobilization of ECL luminophore as a means to overcome these issues and simplify the experimental design.⁵⁹ Immobilization is also necessary in the context of biological sensors which rely on the use of functional molecules that are labile, rare and expensive, low in concentration and/or must be oriented in a particular way.⁶⁰ As $[\text{Ru}(\text{bpy})_3]^{2+}$ is a popular ECL luminophore,^{19,26,30} huge efforts have been undertaken to immobilize it to the surface of electrodes. Factors that need to be considered while developing solid state ECL systems include a sufficient amount of ruthenium complex,⁶⁰ as the ECL intensity is directly proportional to the luminophore concentration and conductivity of the composite matrix in which the ruthenium species are immobilized.⁶¹ $[\text{Ru}(\text{bpy})_3]^{2+}$ has been incorporated into ion exchange polymer composite films like nafion⁶¹⁻⁶³, Eastman AQ55D^{64,65} through electrostatic attachment, self assembled using layer by layer^{14,59} techniques and Langmuir Blodgett techniques.^{61,66} These methods ensures a high luminophore concentration. The use of carbon nanotube^{64,67} or platinum or gold nanoparticles⁶⁸ in the composite film have shown to increase the conductivity of the matrix. However, in all the above cases the luminophore is not covalently attached to the electrode surface and hence it is challenging to unambiguously confirm if the emission arises from the material on the electrode or from the solution very close to the electrode surface due to leaching of the material. This is a major obstacle which can be overcome by covalent immobilization of the luminophore to the electrode surface.¹⁶ There are examples of ruthenium being covalently embedded into sol-gel-based ruthenium-titania-nafion composite films⁵³ and these were shown to be stable in high contents of organic solvents with minimum leaching.

There has been extensive use of polymers in biosensors for testing and bio-regulation.^{69,70} Polymeric materials suitable for biosensor devices should be

biocompatible. Biocompatibility is imparted by the functional groups properly located on the polymer as well as its structure.^{71,72} Truly biocompatible polymers should be able to recognize and cooperate in harmony with bio assemblies and living cells without any undesired nonspecific interactions.⁷³

1.4.1 Metallopolymers

Metallopolymers are a very attractive option for use in biosensors due to their excellent deposition and easy synthesis.³⁸ These polymers are used in numerous applications like electrocatalysis,^{37,74} displays and electrochromic devices,^{75,76} membranes,⁷⁷ sensors,^{58,78} mechanical actuators,¹³ and battery electrodes to name a few. They are characterized by the presence of specific spatially isolated electrochemically active sites. Electroactivity in the polymer is highly localized with respect to voltage. A metallopolymer consists of redox active transition metal complex covalently bound to a polymer back bone. The polymer back bone however, may or may not be electroactive in nature.⁷⁶ These polymers are not only capable of being oxidized and reduced in a reversible manner, but also allow surface modification of electrodes so as to achieve tailored electrochemical properties. The synthetic procedures available for polymers containing covalently attached metal centers offer considerable flexibility in terms of the choice of solvent, reaction time or temperature.⁷⁹ For example by varying these parameters one can synthesise either mono or bis substituted product, *i.e.* $[M(bpy)_2(\text{polymer backbone})_nCl]^+$ or $[M(bpy)_2(\text{polymer backbone})_n]^{2+}$, where M is transition metal, bpy is 2,2'-bipyridyl. Polymer backbones that have been utilized include poly-(4-vinylpyridine) (PVP),^{80,81} poly (N-vinylimidazole) (PVI),⁸² poly-4-vinylpyridine/polystyrene copolymers (PVP/PS),⁸³ and polystyrene with amide linkage.⁸⁴ Different metal loadings ranging from 1:n (n = 5, one metal complex per 5 monomer units) to 1:25 have been produced though more dilute loadings can be created.⁸⁵

Amongst these different polymer backbones polyvinyl pyridine (PVP) has gained much attention as universal surface modifier⁸⁶ due to the strong affinity of pyridyl groups to metals and its ability to undergo hydrogen bonding with

polar species. In addition PVP can interact electrostatically in quaternized or protonated forms with charged surface.⁸⁶ The ECL properties of the metallopolymer, $[\text{Ru}(\text{bpy})_2\text{PVP}_{10}]^{2+}$, where PVP=poly 4-vinyl pyridine, has been studied in detail in the presence of oxalate and TPA co-reactant.^{58,75,78} Intense ECL is produced by these films as high concentrations of the luminophore (micro molar) are found within these films. However, at high concentrations it is observed that there is a decrease in the ECL efficiency of the films due to self absorbance and quenching.⁷⁵ Therefore, proper loading of the polymer is necessary to overcome this issue.

Many other transition metals like platinum,⁸⁷ iridium⁸⁸ and osmium¹⁴ have also been employed in ECL apart from ruthenium. Ruthenium complexes coordinated to a polypyridyl ligand are attractive options in ECL due to their photo and electrochemical potential,^{34,89} well-developed background of synthetic chemistry, chemical stability in a range of oxidation states, unique ground and excited state properties^{90,91} and facile electrochemistry.^{42,55} The motive behind deliberately immobilizing an ECL active polymer onto the electrode surface is that the electrode then exhibits chemical, electrochemical and other properties of the surface confined species. The surface confined electroactive species can then undergo electron transfer processes with the electrode. Rate limiting steps such as mass transfer of reactants or products, to and from, the surface of the electrode can be avoided. Figure 1.3 represents a pathway for a general electrode reaction.⁹²

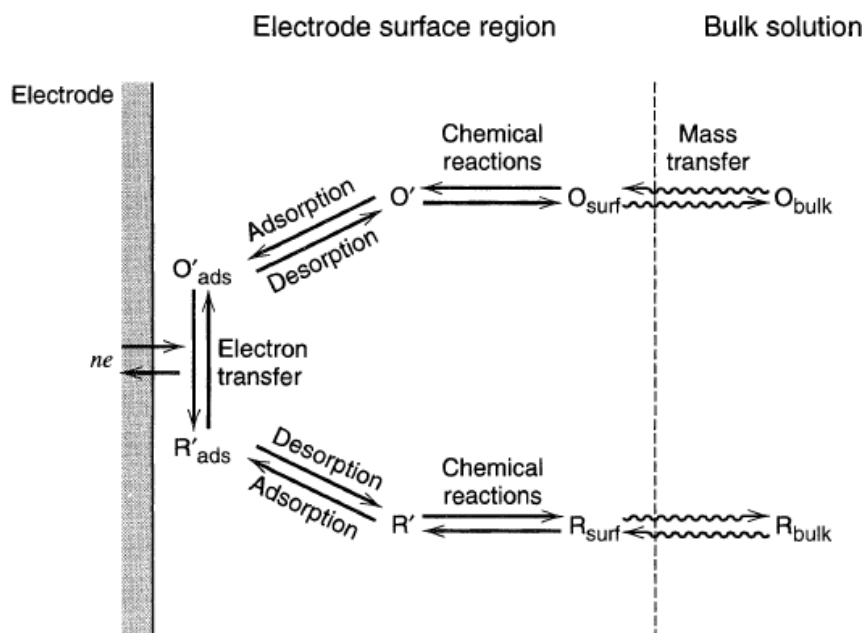


Figure 1.11: Pathway for general electrode reaction. Reprinted with permission from Bard, A. J.; and Faulkner, L. R.; *Electrochemical Methods: Fundamentals and Applications*, John Wiley & Sons Inc, New York, 1980

Electropolymerisation is another attractive method to produce polymer modified electrodes. It enables *in situ* production of thin and stable films of controlled thickness and is applicable to all sizes and shapes of electrodes. This aspect is especially important when considering mass production. Biosensors based on electropolymerised films can have significantly improved diffusional properties due to the thinness of the film, can effectively block interferences and prevent fouling⁹³. However, they have not been used in the context of ECL sensors. There have been few reports where polyluminol films⁹⁴ have been used for the detection of flavin and enhanced ECL with detection limit of $8.3 \times 10^{-8} \text{ mol L}^{-1}$ was achieved for riboflavin. The authors reported very little interference from water soluble vitamins and other fluorescent compounds. Thus, ECL from electropolymerised films and their application in biosensors is another field that remains unexplored.

1.4.2 Carbon nanotubes

Amperometry is the one of the most sensitive detection techniques available today but its limit of detection is in the range of (10^{-7} - 10^{-8}) M.¹¹ There is a need in the clinical environment to accurately detect certain analytes and cardiac biomarkers whose concentration in the blood plasma is 0.3-0.8 nM. Hence, there is a necessity to decrease the limits of detection and increase the sensitivity of the sensors available. This can be achieved by increasing the transducer surface area. Carbon nanotubes have been widely used in sensor fabrication due to their high surface area to weight ratio ($\sim 300 \text{ m}^2\text{g}^{-1}$) which is accessible for both electrochemistry and surface immobilization.⁹⁵ They also possess very good electrical conductivity, chemical stability and extremely high mechanical strength.⁵⁹

Following the discovery of carbon nanotubes by Iijima,^{96,97} nanotubes have captured the attention of researchers worldwide. A significant amount of work has been done in the past decade to understand the unique structural, electrical, mechanical and chemical properties of carbon nanotubes.^{95,98-104} The main interest in nanotubes arises due to their electro catalytic property and small size which make them the smallest electrodes capable of penetrating proteins and cells.¹⁰⁴ However, the electro catalytic property of carbon nanotubes has been questioned after the findings by Compton and co workers.^{105,106} Their work showed that the electro catalytic performance of carbon nanotubes was similar to that observed at the edge planes of pyrolytic graphite and was not anyway superior. These findings were further supported by Chou *et.al.*,¹⁰⁷ who provided direct evidence that the favourable electrochemistry of carbon nanotubes comes from carboxylic acid and quinone moieties at the ends of the tubes, the same functional groups responsible for the good electrochemistry of edge planes of graphite. Nevertheless, since the discovery of low potential detection of NADH on carbon nanotube modified electrode by Wang and co-workers,¹⁰⁸ the past 5 years has seen tremendous growth in the use of carbon nanotubes especially in ECL detection.^{14,32,59, 109}

Carbon nanotubes are basically graphene sheets rolled into a cylinder with their edges joined. They can be either one-atom thick called single walled nanotube (SWCNT) or a group of concentric tubes called multi walled carbon nanotube (MWCNT). Their lengths however, can be up to hundreds of microns or even centimetres. Figure 1.3 (A)¹¹⁰ shows the tunnelling electron microscopic image of chiral SWCNT whereas (B) and (C) show the TEM image of MWCNT and SWCNT bundle respectively.¹¹¹

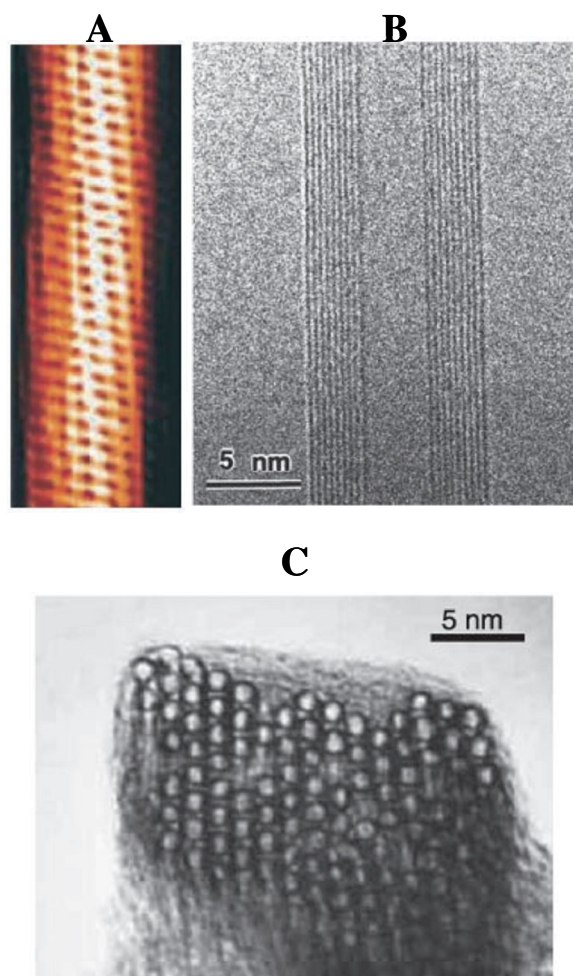


Figure 1.12: Tunnelling electron microscope image showing the helical structure of a 1.3-nm-diameter chiral SWNT (A). Reprinted with permission from Wilder, J.W.G.; Venema, L.C.; Rinzler, A.G.; Smalley, R.E.; Dekker, C., *Electronic structure of atomically resolved carbon nanotubes*, Nature, 1998, 391, 6662, 59-62. Transmission electron microscope (TEM) image of a MWNT containing a concentrically nested array of nine SWNTs (B). TEM micrograph showing the lateral packing of 1.4-nm-diameter SWNTs in a bundle (C). Reprinted from Thess, A.; Lee, R.; Nikolaev, P.; Dai, H.; Petit, P.; Robert, J.; Xu, C.; Lee, Y.H.; Kim, S.G.; Rinzler, A.G.; Colbert, D.T.; Scuseria, G.E.; Tomanek, D.; Fischer, J.E.; Smalley, R.E., *Crystalline Ropes of Metallic Carbon Nanotubes*, Science, 1996, 273, 5274, 483-487.

Many chemical strategies to tune the electronic properties of carbon nanotubes have been developed. These allow better solubilisation of nanotubes and also make them biocompatible. Once functionalized, the nanotubes can be used as electrodes and/or immobilization phase in many applications. Polymer composites have been prepared by compounding poly (ethylene vinyl acetate) (PEVA) with carbon nanotubes to produce a robust and electrically conducting substrate. The carbon nanotube–PEVA–antibody (specific to α -fetoprotein) composite sheet of 50 nm thickness was used to carry out sandwich design immunoassay.⁹⁵ The composites were exposed to samples containing α -fetoprotein (AFP) and anti-AFP antibodies conjugated with colloidal gold or $[\text{Ru}(\text{bpy})_3]^{2+}$. The electrochemiluminescence (ECL) signal was found to be linearly dependant on the concentration of AFP up to 30 nM with a LOD of about 0.1 nM. However, in this sensor the size and length of the nanotubes was not controlled. For applications in biosensors short and discrete nanotubes are required⁹⁹ as they exhibit faster electron transport properties. An ECL sensor possessing low detection limit of 8×10^{-7} M for TPA was developed by Ying *et.al.*,⁶⁷ using acid functionalized MWCNT and $[\text{Ru}(\text{bpy})_2(5\text{-NH}_2\text{-1,10-phenanthroline})]^{2+}$ covalently coupled to one another.⁶⁷ However, it was reported that drop coating of MWCNT- Ru composite caused a decrease in sensor response by 60% within a month of storage. Amine functionalization of single walled nanotubes has also been explored.^{112,113}

Significantly, vertically aligned carbon nanotubes are more advantageous for sensor application than non-aligned ones, since the edges of the nanotubes are exposed. This orientation of the nanotube has been shown to exhibit the highest electro catalytic activity coupled with fast electron transfer.¹⁰¹ Selective functionalization of SWCNTs with thiol groups and their attachment to pre-organized gold surfaces allowed vertical assembly of CNTs and most importantly, provide low-resistance contacts of CNTs to other electronic components.¹¹⁴ However, the thiol functionalized SWCNTs displayed slow adsorption kinetics compared to conventional alkane thiols and formed aggregates as adsorption progressed.

Growing high density of aligned tubes still poses a significant challenge. Several attempts have been made to generate high density of aligned tubes on conductive and non conductive substrates including thermal chemical vapour deposition,¹¹⁵ photolithography¹¹⁶ and electron beam lithography.¹¹⁷ Also, it is essential that the nanotubes are securely in contact with the conducting support with low contact resistance between the array and the support.¹¹⁵ However, most of the methodologies mentioned above usually involve transferring of the nanotubes from the substrate of growth to another substrate of interest as shown in Figure 1.16, where a SEM micrograph of patterned films of aligned nanotubes prepared by photolithography on quartz substrate is shown. These approaches are cumbersome and result in poor transfer efficiency and thereby poor device performances.

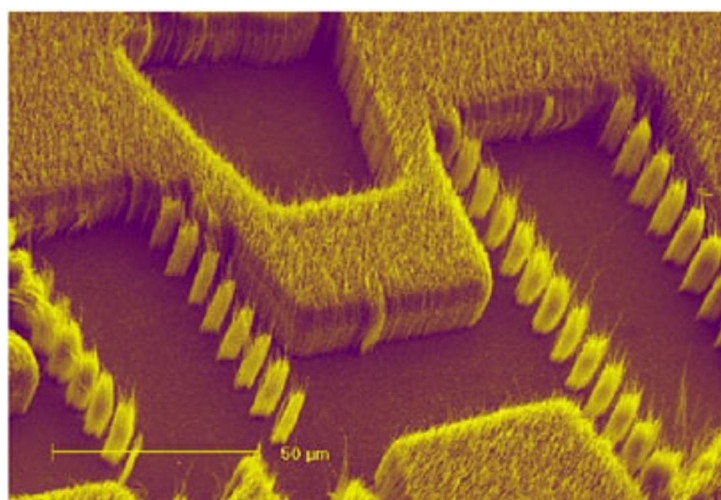


Figure 1.13: SEM micrograph of patterned films of aligned nanotubes prepared by the pyrolysis of FePc onto a photolithographically pre-patterned quartz substrate. Reprinted with permission from Liming, D.; Pingang, H.; Sinan, L., *Functionalized surfaces based on polymers and carbon nanotubes for some biomedical and optoelectronic applications*, Nanotechnology, 2003, 14, 1081-1097.

Amperometric immunosensors based on the adsorption of antibodies onto perpendicularly oriented assemblies of SWCNT forests on conductive substrates have been developed by Connor and co-workers.¹¹⁸ The forests were self-

assembled from oxidatively shortened SWCNTs onto Nafion/iron oxide-coated pyrolytic graphite electrodes. Anti-biotin antibody was strongly adsorbed to the SWCNT forests. In the presence of a soluble mediator, the detection limit for horseradish-peroxidase labelled biotin was 2.5 nM. Improved fabrication of SWCNT forests utilizing aged nanotube dispersions provided higher nanotube density and conductivity.¹¹⁹ Unmediated sandwich immunosensor achieved a detection limit of 75 nM using HRP labels. However, mediation dramatically lowered the detection limit to 1 nM. The authors concluded that the difference between mediated and unmediated assays was due to the fact that the average distance between HRP labels and nanotube ends was too large for efficient direct electron exchange. Mediation helped to overcome this distance effect. The ECL capabilities of these CNT forests are yet to be explored. Combined with the sensitivity of ECL detection system, these self assembled forests, without doubt can help to further lower detection limits and achieve higher sensitivity (down to few target molecules).

1.5 ELECTROCHEMICAL TECHNIQUES

1.5.1 Fundamentals of ECL

ECL involves simultaneous measurement of the current and light in response to the concentration of the target analyte when a potential is applied to the working electrode.

The standard potential, $E^\circ (A, A^{\bullet-})$, of the electrode reaction Equation 1.9 is measure with respect to a given reference electrode, based on a redox pair O/R given by Equation 1.10, and represents the Gibbs free energy, ΔG° , of the reaction Equation 1.11.¹²⁰



where, O and R are the oxidized and reduced forms of the electrochemically active species. The potential of the redox couple represents the energy needed at equilibrium to add an electron to A or to remove an electron from A^{•-}. For ECL reactions the ΔG° of the reaction,¹²⁰ Equation 1.12, is of utmost importance. ΔG° is given by Equation 1.13 and E°_{rxn} is given by Equation 1.14, where, n the number of electrons transferred in the reaction, and F the Faraday constant.



$$\Delta G^\circ = -nFE^\circ_{\text{rxn}} \quad 1.13$$

$$E^\circ_{\text{rxn}} = E^\circ(A^{\bullet-}, A) - E^\circ(A, A^{\bullet+}) \quad 1.14$$

For ECL reactions ΔG° is typically in the range of 2-3 eV.¹²⁰

Figure 1.17 illustrates the electrochemical and mass transport events that can occur at a polymer modified electrode surface. For monolayers in contact with a supporting electrolyte, the principal process is heterogeneous electron transfer across the electrode | monolayer interface. Mass transfer and reaction kinetics must be considered to fully understand the properties of these thin films. The following assumptions are made for an ideally responding redox polymer immobilized on an electrode surface, where, A_{Ox} and B_{Red} represent a reducible and oxidizable species in solution:³⁸

1. The redox couple, O/R, is adsorbed on the electrode surface and is not present in solution, or its concentration is sufficiently low such that its contribution to the Faradaic current is negligible.
2. All adsorption sites on the surface are equivalent and the oxidized and reduced forms occupy equal areas on the surface.
3. The free energy of adsorption and maximum or limiting surface coverage, assumed to be equal to the surface activity, are independent of the applied potential.

4. In order to observe an ideal response, the entire potential drop occurs at the electrode|polymer interface and the adsorbates do not interact laterally.
5. And finally, the Faradaic and capacitive currents can be separated.

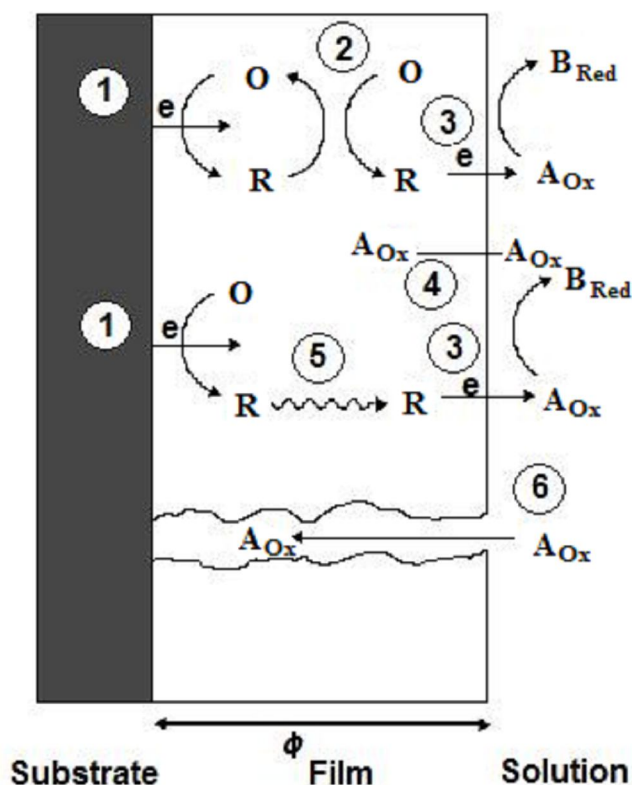


Figure 1.14: Schematic illustration of the processes that can occur at a modified electrode, where O represents a reducible substance in a film on the electrode surface and A_{Ox} a species in solution. The processes shown are as follows: (1) heterogeneous electron transfer to O to produce the reduced form R ; (2) electron transfer from R to another O in the film (electron diffusion or electron hopping in the film); (3) electron transfer from R to A_{Ox} at the film/solution interface; (4) penetration of A_{Ox} into the film (where it can also react with R or at the substrate/film interface); (5) movement (mass transfer) of R within the film; (6) movement of A_{Ox} through a pinhole or channel in the film to the substrate, where it can be reduced. From A.J. Bard and L.R. Faulkner, *Electrochemical Methods: Fundamentals and Applications*, John Wiley & Sons Inc, New York, 1980

Electrochemical techniques like voltammetry and AC impedance can provide powerful insight into the thermodynamics and kinetics of electron transfer across the electrode | polymer interface and within the polymer film.

Cyclic voltammetry (CV) involves monitoring the current response of a small stationary electrode in an unstirred solution, which is excited by a triangular potential waveform, such as that shown in Figure 1.15.¹²¹

In cyclic voltammetry, the potential applied to the working electrode is first swept in a forward direction, stopped at a desired potential, then a reverse sweep returns the potential to its initial value. In the absence of a redox couple, which is capable of electron transfer to or from the electrode surface, at the applied potential, one still observes a background current, as shown in Figure 1.15. This background current appears because the electrode-solution interface now behaves like a parallel plate capacitor. As the potential is varied the electrode surface gets charged and the ions move to the surface of the electrode and form an electrical double layer. Although strictly speaking an electrode-solution interface in the absence of a redox couple is not a pure parallel plate capacitor, this model is adequate to describe most of the electrochemical systems.

Helmholtz described the electrochemical capacitance C by Equation 1.15

$$\frac{C}{A} = \frac{\epsilon\epsilon_0}{\ell} \quad 1.15$$

where, ϵ is the dielectric constant of the medium between the plates, ϵ_0 is the permittivity of free space, ℓ is the separation between the plates and A is the area of the electrode. Capacitance is a crucial factor for electrochemical systems as this gives rise to current during the charging of the capacitor. The magnitude of this charging current, i_C , is given by Equation 1.16

$$|i_C| = AC_{dl}v \quad 1.16$$

where, v is the potential scan rate and C_{dl} is the double layer capacitance and A is the area of the electrode.

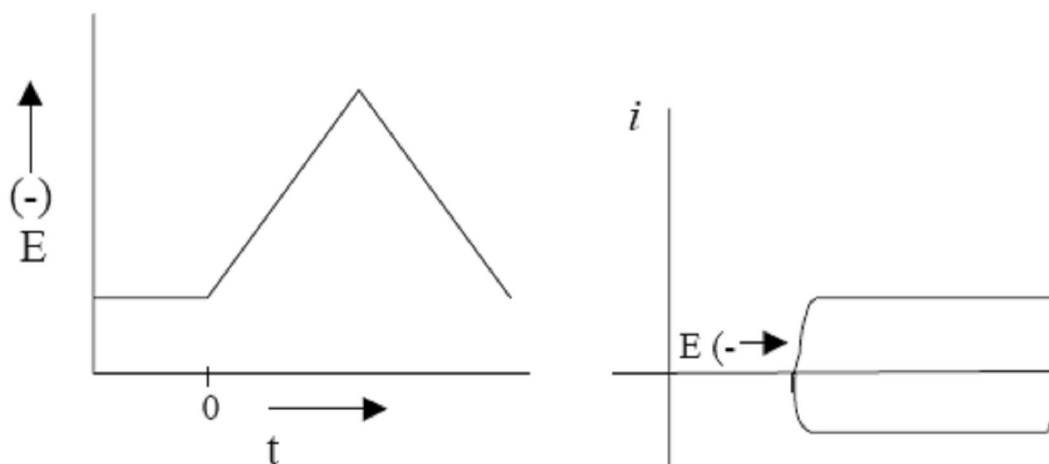


Figure 1.15: Schematic diagram showing a cyclic voltammetry experiment in the absence of a redox couple. Reprinted from Southampton.; *Electrochemistry group: Instrumental methods in electrochemistry*, Chapter 2, 1985, pg 49.

For a potential step experiment at a stationary constant area electrode, like the one described above, the charging current i_C dies away after a time equivalent to a few time constants $R_U C_{dl}$, where R_U is the uncompensated resistance. When an electroactive couple is present in solution the current, I_{Total} , observed during the cyclic voltammetric scan is a sum of the current due to electron transfer (Faradaic current i_F) and background charging current, i_C .

$$I_{Total} = i_C + i_F = AC_{dl} v + i_F \quad 1.17$$

The magnitude of the charging current depends on the scan rate and Faradaic current in the above case is always measured from a baseline of charging current.

The i vs. E output denotes flow of electrons between the redox active species and the electrode and is associated with a change in the oxidation state of the redox couple.⁸⁹ The significant values in this i vs. E plot are the anodic and cathodic peak potentials E_{PA} and E_{PC} ; the anodic and cathodic peak currents i_{PA} and i_{PC} , and the half-peak potentials, which are the potentials $E_{1/2A}$ and $E_{1/2C}$, at which the cathodic and anodic currents reach half their peak values. The independent variables are voltage, scan rate and the range of potential over which the scan is made. The former is the most important parameter in a diagnostic sense, although proper selection of scan range can often eliminate interferences from other processes.¹²² These parameters are depicted in Figure 1.16.

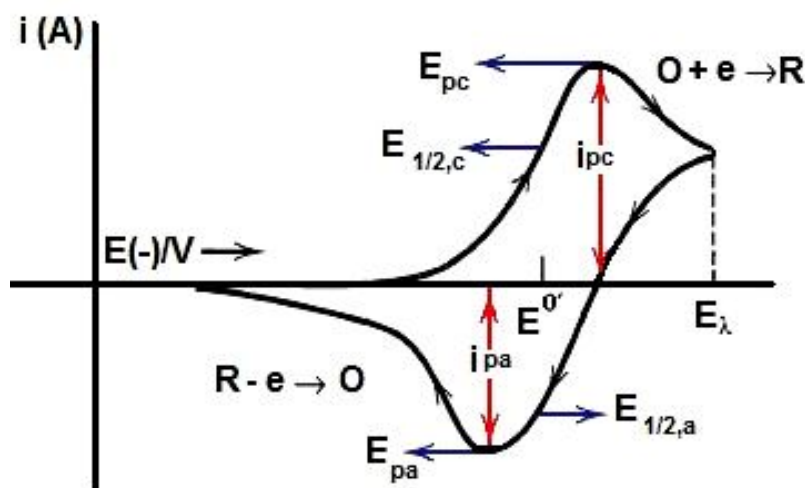


Figure 1.16: Reversible cyclic voltammogram obtained for freely diffusing redox specie in solution depicting the most important parameters measured during a cyclic voltammetric experiment. Adapted from Bard, A. J.; Faulkner, L. R.; *Electrochemical Methods: Fundamentals and Applications*, John Wiley & Sons Inc, New York, 1980.

Consider a solution containing the oxidized form of the redox couple, O. As the applied potential is scanned in the negative potential direction, initially no current due to Faradaic processes is observed. When the potential approaches the point where the reduction of the species can occur, a cathodic current

develops due to the reduction of the redox couple. A rapid increase in current occurs as the concentration of the oxidized species at the electrode surface becomes smaller. At the formal potential, there exists a 50% oxidized and 50% reduced species at the electrode surface. Past the peak potential, the current decays' as the diffusion layer extends farther away from the surface. When the potential is switched, the current remains cathodic as the potential is still negative enough to reduce the redox couple. Once the potential becomes sufficiently negative so that reduction can no longer occur, the Faradaic current goes to zero and then oxidation process begins. The anodic current resulting from the oxidation of the reduced species within the depletion zone, peaks and then decreases as this reduced species is consumed by the oxidation reaction.

The response observed for a surface confined redox active species can differ markedly from that observed for a solution phase species. For example, the theoretical response for a slow scan, cyclic voltammogram of an electrochemically reversible couple that is confined on the electrode surface is as shown in Figure 1.17. The peaks for surface confined species are sharp and symmetrical unlike those for freely diffusing species.³⁸ This behaviour is due to the presence of a fixed amount of redox active species at the electrode, which is not hindered by the complications of mass transfer. When a potential is applied to a surface modified electrode the current rises to a peak value and then returns to the baseline. For an ideal system no peak-to-peak separation is expected.⁹² Under the conditions of finite diffusion in which the redox composition of the layer is in thermodynamic equilibrium with the electrode potential, (*i.e.*, the Nernst condition), this behaviour will be observed for all electrochemically reversible reactions at sufficiently slow scan rates such that all electroactive centers undergo redox transformations on the experimental time-scale.

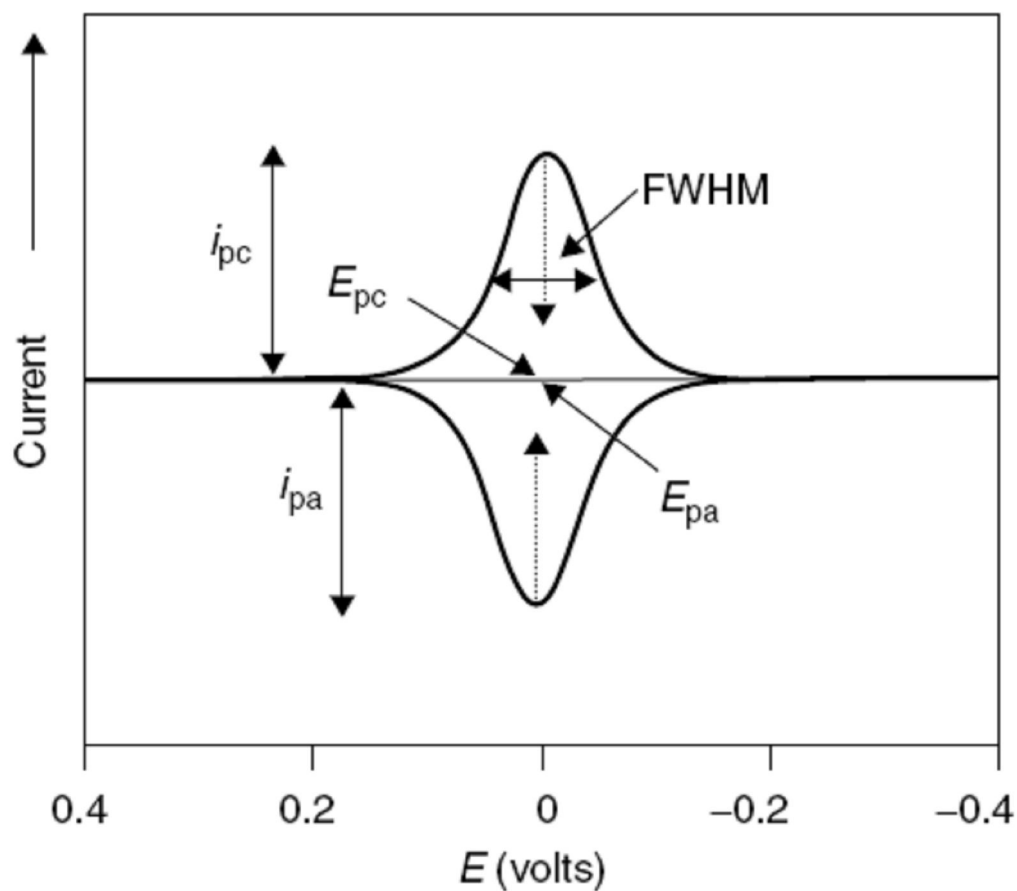


Figure 1.17: Current- potential curves obtained from cyclic voltammetry measurements for the reduction and oxidation of an adsorbed interfacial supramolecular assembly under finite diffusion conditions. Reprinted from Forster, R. J.; Keyes T. E.; Vos, J. G.; *Interfacial Supramolecular Assemblies*, John Wiley & Sons, Ltd, England, 2003.

The ideal reversible voltammogram under such conditions has the following features:

$$i_p = \frac{n^2 F^2}{4RT} v A \Gamma \quad 1.16$$

$$E_{pc} = E_{pa} \quad 1.17$$

$$FWHM = \frac{90.6}{n} \text{ mV} \quad 1.18$$

$$\frac{i_{p,c}}{i_{p,a}} = 1 \quad 1.19$$

where, FWHM is the full width at half maximum, n is the number of electrons passed, F is Faraday constant, Γ the surface coverage or concentration of the redox-active adsorbate (molcm^{-2}) total electroactive coverage, A is the electrode area (cm^2), v is the scan rate, R the gas constant and T is absolute temperature. These parameters are illustrated in Figure 1.17 and Figure 1.18.

Under these conditions of exhaustive oxidation/reduction of the modifying layer, the Faradaic charge, Q , under the current potential curve gives the quantity Γ (molcm^{-2}) according to the expression;

$$\Gamma = \frac{Q}{nFA} \quad 1.20$$

For a polymer or thicker film under these conditions of finite diffusion, a plot of scan rate versus peak current will be linear.

In most films of redox polymers, charge transport occurs by electron self exchange reactions between neighbouring oxidized and reduced sites. This electron hopping process is mathematically representable by diffusion laws in which the homogeneous charge transport diffusion coefficient, D_{CT} , is introduced as a measure of its rate.

The concentration profile of fixed oxidized and reduced sites within the film depend on the dimensionless parameter $D_{CT}t/d^2$, where t is the experimental time scale, (related to the time for a potential scan to traverse the wave), and d is the polymer layer thickness. When $D_{CT}t/d^2 \gg 1$, all electroactive sites within the film are in equilibrium with the electrode potential, and the surface type behaviour described previously for finite diffusion is observed. In contrast, when $D_{CT}t/d^2 \ll 1$, the oxidizing scan direction is switched before reduced sites at the films outer boundary are oxidized. This is the semi-infinite electrochemical charge diffusion condition. Here the $v^{1/2}$ dependence of the peak current is seen and the peak current itself is given by the same equation as that used for species dissolved in solution and diffusing to the electrode surface, the Randles-Sevcik equation;

$$i_p = 2.69 \times 10^5 n^{3/2} A D_{CT}^{1/2} C v^{1/2} \quad 1.21$$

where, C is the concentration of electroactive sites within the film. This equation is routinely used for evaluation of D_{CT} using cyclic voltammetry at relatively high scan rates (typically > 50 mV/s) where D_{CT} is of the order of 10^{-11} cm²s⁻¹ and the film thickness is few hundred nanometers.³⁸

A variety of factors can influence the shape and the various peak parameters in a cyclic voltammogram. For example, in an actual experiment in the finite diffusion regime, the oxidation and reduction peaks may not centre on a single potential even though they may be almost symmetric with peak heights approximately equal. While the ideal separation ΔE_p is predicted to be zero, there is almost always a finite separation of a few mV to tens of mV. In such cases, E^0 is usually taken to be the midpoint between the two peak potentials. Broadening or narrowing of CV peaks with respect to the ideal value of $90.6/n$ mV for surface bound redox couples suggests a breakdown of the assumption that there are no interactions between redox sites in the film and that all of them have the same E^0 . In films, which are ‘diluted’ with electrochemically inert material, lateral interactions are minimized but often peak widths are larger than ideal theoretical value.

1.5.2 Lockin detection

Signal modulation is a powerful technique for measuring small amplitude signals which are embedded in large amount of background or interference. The modulation can be achieved in a number of ways with the simplest method being amplitude modulation.¹²³ As electrochemiluminescence experiments can be controlled using potential, this can also be used for modulation purposes. Noise reduction is usually achieved using synchronous “lockin-in” detection.¹²⁴

Lockin detection is used to measure the amplitude and phase of narrow band amplitude modulated signals. This detection technique requires reference signals that are modulated at the same frequency as their signals of interest to use phase sensitive detection.¹²⁵ This enables “locking in” to the frequency of

interest while simultaneously ignoring all other frequencies. In this way, measuring very small AC signals that are buried in the noise can be accomplished.

Lockin amplifiers usually consist of a phase locked loop, a demodulator and a low-pass filter. The phase locked loop is usually responsible for creating precise, well-defined reference signal *i.e.*, sine wave or square wave, which has fixed amplitude.¹²⁴ A typical sine wave is as shown Figure 1.19. Additionally it also includes a phase shift circuit which precisely matches the phase of the reference signal to that of the analytical signal. The demodulator multiplies the reference signal by the input signal and the low pass filter then filters the output of the demodulator.^{125,126}

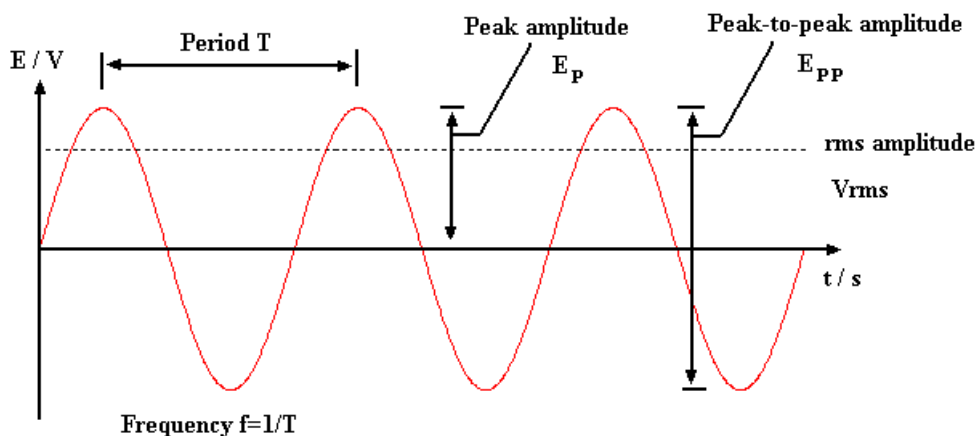


Figure 1.18: Typical sine wave showing important parameters. Reprinted from Meade, M. L.; *Lock-In amplifiers: Principles and Applications*, 2007, 1, 232.

Lock-in detection was usually used to achieve phase sensitive detection for the fundamental harmonic response of the cell, measurement of phase angle and second harmonic response. Apart from sine waves other periodic wave forms like saw-tooth, square wave and white noise have also been used as waveforms for the measurement of the total alternating current at the fundamental frequency.¹²⁷ Until recently, the theory of sinusoidal modulation existed only for amplitudes small in comparison with RT/nF .¹²⁸ However, advancement in computer simulations and Fourier transform methods have not only helped in modelling of modulated voltammetry¹²⁹ but also helped in the development of

voltammetric instrumentation.¹³⁰ High speed computation has also provided means of testing and implementing new analytical solutions proposed for modulated voltammetry.¹³¹ Modulated voltammetry is now widely used in the fields of electrochemical impedance spectroscopy^{132,133}, polymer technology^{134,135} and kinetic studies of electron transfer reactions in an electrochemical cell.¹³⁶

1.5.3 AC impedance

1.5.3.1 Basic principles of impedance

Impedance spectroscopy is a powerful technique to investigate electrochemical processes and interfacial phenomena. Techniques like cyclic voltammetry, described above, usually drive the electrodes to a condition far from equilibrium. However, impedance methods are based on perturbing the electrochemical cell with an alternating signal of small amplitude allowing measurements to be made essentially at equilibrium.¹³⁷

The alternating perturbation applied in an electrochemical impedance spectroscopy (EIS) experiment is usually sinusoidal, *e.g.* a sinusoidal potential. Consider a sinusoidal perturbation of applied potential¹³⁷ given by Equation 1.22:

$$\dot{E}(t) = E_0 \sin \omega t \quad 1.22$$

where, $\dot{E}(t)$ is the voltage at time t , E_0 is the voltage amplitude and ω is the radial frequency (rads^{-1}). The relationship between radial frequency and frequency¹³⁷ is given by Equation 1.23:

$$\omega = 2\pi f \quad 1.23$$

The current response $\dot{I}(t)$ will be sinusoidal at the same frequency f (Hz) but shifted in phase, ϕ ,¹³⁷ given by Equation 1.24.

$$I(t) = I_0 \sin(\omega t + \phi) \quad 1.24$$

Analogous to Ohm's law for DC circuits, for AC circuits' impedance is defined as the ratio of voltage phasor and current phasor¹³⁷ and is given by Equation 1.25:

$$Z = \dot{E}(t) / \dot{I}(t) \quad 1.25$$

It is well known that the surface characteristics and interfacial phenomena of a polymer-modified electrode can be studied by studying its impedance characteristics at different experimental conditions. Numerous models have been proposed for describing the impedance characteristics of electronically conducting polymers.¹³⁷⁻¹⁴⁰

The reversible electrochemical oxidation of conducting and redox polymers has been extensively studied with no redox couple in solution, symmetric configuration.^{80,138-140} When a redox couple is present in electrolyte solution, *e.g.* ECL polymer on electrode with a co-reactant in solution, the situation is slightly different. Multiple interfaces exist, metal|polymer interface, where electron transfer occurs and polymer|electrolyte interface, where ion and electron transfer occurs. This is called asymmetric configuration and is encountered frequently in ECL reactions. Many research groups have attempted to understand the charge transport properties at these interfaces as it is very crucial for the development of polymer modified electrodes.^{133,136,141-143} The analytical impedance functions have been already derived for asymmetric systems with redox couple in solution.^{133,143} Therefore, in order to study the kinetics and mechanisms of charge transfer and ion transport in the metal|polymer film interface and polymer film|electrolyte interface, these analytical functions have been used in conjunction with electrochemical impedance spectroscopy.

1.5.3.2 Impedance theory applied to polymer films

The kinetics of electron transport for polymer modified electrode without an additional redox species in solution at polymer|solution interface can be analyzed using the classical Butler-Volmer equation, Equation 1.26.^{144,145} The exchange current density I_0 is given by Equation 1.26:

$$I_0 = nFAk_s C_O^{(1-\alpha)} C_R^\alpha \quad 1.26$$

However in the presence of redox species in solution, I_0 is given by Equation 1.27:¹³³

$$I_0 = nFAk_s C_O \exp[-\alpha nF(E_{DC} - E^{0'})/RT] \quad 1.27$$

where, k_s is the heterogeneous rate constant, α is the transfer coefficient, E_{DC} is the equilibrium DC potential of the electrode, $E^{0'}$ is the formal potential of the oxalate in PBS and the rest of the symbols have their usual meaning. α is assumed to be 0.5. Under applied DC potential (E_{DC}), the mean surface concentration of O and R defined by the E_{DC} applied to the electrode is used as effective bulk values for AC perturbation.

The charge transfer resistance, R_{CT} , of the Faradaic process at over-potentials, $|\eta| < 118$ mV and in the high frequency kinetic control regime, is then given by Equation 1.28:¹⁴⁵

$$R_{CT} = \frac{RT}{nFI_0} \quad 1.28$$

Substituting Equation 1.28 into Equation 1.26 and 1.27, k_s is obtained.

The impedance Z for an equivalent electrical circuit is calculated as the ratio between the system voltage phasor, (\dot{E}) , and the current phasor, (\dot{I}) . These are generated by a lock-in amplifier during the experiment. Z can also be written in terms of Equation 1.29 where X is given by Equation 1.30. The term $j=\sqrt{-1}$, R is the resistance in Ω , X is reactance, C is capacitance in Farads (F) and ω is

angular frequency (rad s^{-1}) and f is applied frequency in Hz, respectively. The complex plane impedance, $Z(\omega)$, can then be represented as the sum of real, Z_{RE} and imaginary, Z_{IM} , components that originate mainly from the resistance and capacitance of the cell, respectively.

$$Z(\omega) = Z_{\text{RE}} + j Z_{\text{IM}} = R - j X \quad 1.29$$

$$X = 1/\omega C \quad 1.30$$

where, $\omega = 2\pi f$

The maximum angular frequency ω_{max} obtained from the complex plane plot is equal to the inverse of product of R_{CT} and double layer capacitance of the polymer|electrolyte interface, C_{D} . Equation 1.31 then gives the expression of ω_{max} and it is called the characteristic relaxation frequency.

$$\omega_{\text{max}} = \frac{1}{R_{\text{CT}} C_{\text{D}}} \quad 1.31$$

The inverse of ω_{max} is τ , which is the characteristic time constant for the charge transfer process

$$\tau = R_{\text{CT}} C_{\text{D}} \quad 1.32$$

At lower frequency, diffusion control (D.C) regime, diffusion of charge in the polymer film dominates impedance. The polymer resistance (R_{film}) and polymer capacitance (C_{film}) are related to charge transfer diffusion coefficient (D_{CT}) by Equation 1.33 and 1.34.^{144,146}

$$R_{\text{film}} = \frac{\phi^2}{3C_{\text{film}}D_{\text{CT}}} \quad 1.33$$

$$\frac{1}{C_{\text{film}}} = d(-Z_{\text{IM}})/d(\omega^{-1}) \quad 1.34$$

1.6 CONCLUSIONS

In conclusion, this chapter presents a review of relevant literature related to electrochemiluminescent biosensors. The chapter initially briefly introduces the basic concepts of biosensor and electrochemiluminescence followed by citing relevant literature related to transducer surface modification with metallopolymers and carbon nanotubes. Few key concepts regarding AC impedance is also introduced.

It is clear that ECL provides a powerful tool for developing new assays for clinical diagnosis. Currently, nearly 100 assays for a wide variety of biomarkers are available, like for prostate cancer, cardiac diseases, tumour and thyroid diseases. Compared to solution phase, solid state ECL exhibits several advantages. The vast number of literature available shows that a number of methods have been developed to fabricate solid state ECL sensors. Though much progress has been made to improve the sensitivity, robustness and regenerability of solid state ECL sensors, many new methods and materials are still needed to further improve the sensor performance and realize practical applications. Design and development of new materials, advancement in the field of instrumentation, novel signal amplification strategies, increase in conductivity of composite films through the use of carbon nanotubes and metallic nanoparticles and miniaturization will all play a significant role in this respect. But as the dynamics of ECL sensor greatly depends on reaction kinetics and electron transfer a fundamental understanding of the ECL processes is also highly essential for the development of portable, highly sensitive, selective, point of care devices.

1.7 REFERENCES

- (1) Blake, G. J.; Ridker, P. M. *J. Am. Coll. Cardiol.* **2003**, *41*, S37-S42.
- (2) Zhan, W.; Bard, A. J. *Anal. Chem.* **2007**, *79*, 459-463.
- (3) Zakynthinos, E.; Pappa, N. *J. Cardiol.* **2009**, *53*, 317-333.
- (4) Verma, S.; Szmitko, P. E.; Ridker, P. M. *Nat. Clin. Pract.* **2005**, *2*, 29-36.
- (5) Wolf, M.; Juncker, D.; Michel, B.; Hunziker, P.; Delamarche, E. *Biosensors and Bioelectronics* **2004**, *19*, 1193-1202.
- (6) Yu, X.; Munge, B.; Patel, V.; Jensen, G.; Bhirde, A.; Gong, J. D.; Kim, S. N.; Gillespie, J.; Gutkind, J. S.; Papadimitrakopoulos, F.; Rusling, J. F. *J. Am. Chem. Soc.* **2006**, *128*, 11199-11205.
- (7) Mani, V.; Chikkaveeraiah, B. V.; Patel, V.; Gutkind, J. S.; Rusling, J. F. *ACS Nano* **2009**, *3*, 585-594.
- (8) Antman, E. M.; Milenko, J. T.; Thompson, B.; Schactman, M.; McCabe, C. H.; Cannon, C. P.; Fischer, G. A.; Fung, A. Y.; Thompson, C.; Wybenga, D.; Braunwald, E. *N. Engl. J. Med.* **1996**, 1342.
- (9) Wujian, M.; Bard, A. J. *Anal. Chem.* **2004**, *76*, 7109-7113.
- (10) Palmisano, F.; Zambonin, P. G.; Centonze, D. *J Anal Chem* **2000**, *366*, 586-601.
- (11) Mohanty, S. P. **2001**, Biosensors: A survey report.
- (12) Zhou, M. **2004**, Online discussion forums, created 23/06/2009.
- (13) Gregory, K. **2008**, In *Micromachined transducers: Sourcebook*; W.C.B. / McGraw Hill, Inc.
- (14) Richter, M. M. *Chem. Rev.* **2004**, *104*, 3003-3036.
- (15) Hercules, D. M. *Science* **1964**, *145*, 808.
- (16) Miao, W. *Chem. Rev.* **2008**, *108*, 2506-2553.
- (17) Andrew, W. K. *Tr. Anal. Chem* **1999**, *18*, 47-62.

- (18) Bard, A. J., Ed.; *Electrogenerated Chemiluminescence*; Marcel Dekker, Inc: United States of America, 2004; , pp 540.
- (19) Andrew, W. K.; Gillian, M. G., *Analyst* **1994**, *119*, 879-890.
- (20) Kazuo, U.; Makoto, K., *Analyt. Sci.* **1991**, *7*, 803-804.
- (21) Michel, P. E.; Fiaccabrino, G. C.; Rooij, N. F.; Hep, M. K., *Analyticachim. Acta.* **1999**, *392*, 95-103.
- (22) Jilin, Y.; Xiurong, Y.; Erkang, W., *Anal. Chem.* **2005**, *77*, 5385-5388.
- (23) Hsueh, Y.; Collins, S. D.; Smith, R. L., *Sensors and Actuators B: Chemical*, **1998**, *49*, 1-4.
- (24) Preston, J. P.; Nieman, T. A., *Anal. Chem.* **1996**, *68*, 966-970.
- (25) Pyati, R.; Mark, R. M., *Annu. Rep. Prog. Chem. , Sect C* **2007**, *103*, 12-78.
- (26) Bard, A. J., *Fundamentals of ECL: Co-reactants*; Electrogenerated Chemiluminescence; Marcel Dekker, Inc: United States of America, 2004; pp 19.
- (27) Bernhardt, K.; Trissl, H. W., *Biochim. Biophys. Acta. Bioenergetics* **1999**, *1409*, 125-142.
- (28) Bezman, R.; Faulkner, L. R., *J. Am. Chem. Soc.* **1972**, *94*, 6324-6330.
- (29) Chang M. M.; Saji T.; Bard, A. J., *J. Am. Chem. Soc.* **1977**, *99*, 5399-5403.
- (30) Miao, W.; Choi, J. P.; Bard, A. J., *J. Am. Chem. Soc.* **2002**, *124*, 14478-14485.
- (31) Wightman, R. M.; Forry, S. P.; Maus, R.; Badocco, D.; Pastore, P., *J. Phys. Chem. B* **2004**, *108*, 19119-19125.
- (32) Forster, R. J.; Bertoncello, P.; Keyes, T. E., *Ann. Rev. Anal. Chem* **2009**, *2*, 359-385.
- (33) Kanoufi, F.; Bard, A. J., *J. Phys. Chem. B* **1999**, *103*, 10469-10480.
- (34) Sato, Y.; Uosaki, K., *J Electroanal Chem* **1995**, *384*, 57-66.
- (35) Lakowicz, J. R., *Long-Lifetime Metal-Ligand Complexes*; Principles of Fluorescence Spectroscopy; Plenum Publisher, New York, 1999; pp 573-594.

- (36) Balzani, V.; Scandola, F., In *Supramolecular Photochemistry*; Ellis Horwood series in physical chemistry; Ellis Horwood: New York, 1990.
- (37) Kalyanasundaram. K.; Grätzel. M., Eds.; In *Photosensitization and photocatalysis using inorganic and organometallic compounds*; Kluwer Academic Publishers: Netherlands, 1993; Vol. 14, pp 449.
- (38) Forster, R. J.; Keyes, T. E.; Vos, J. G. In *Interfacial Supramolecular Assemblies*; John Wiley & Sons, Ltd: 2003; .
- (39) Caspar J. V.; Kober, E. M.; Sullivan, B. P.; Meyer, T. J. *J. Am. Chem. Soc.* **1982**, *104*, 630-632.
- (40) Caspar, J. V.; Meyer, T. J. *J. Phys. Chem.* **1983**, *87*, 952-957.
- (41) Meso scale discovery Immunogenicity assays using MSD's multiarray technology.
http://www.mesoscale.com/CatalogSystemWeb/WebRoot/literature/not/es/pdf/Immunogenicity_Applications.pdf(2010).
- (42) Pellegrin, Y.; Forster, R. J.; Keyes, T. E. *Inorg. Chim. Acta* **2009**, *362*, 1715-1722.
- (43) Li, J.; Yan, Q.; Gao, Y.; Ju, H. *Anal. Chem.* **2006**, *78*, 2694-2699.
- (44) Morita, H.; Konishi, M. *Anal. Chem.* **2002**, *74*, 1584-1589.
- (45) Morita, H.; Konishi, M. *Anal. Chem.* **2003**, *75*, 940-946.
- (46) Massay, R. J.; Blackburn, G. F.; Wilkins, E. W.; Leland, J. K. U.S. Patent 5,746,974, 1995.
- (47) Deaver, D. R., *Nature* **1995**, *377*, 758-760.
- (48) Yang, M.; McGovern, M. E.; Thompson, M. *Anal. Chim. Acta.* **1997**, *346*, 259-275.
- (49) Shelton, D. R.; Higgins, J. A.; Van Kessel, J. S.; Pachepsky, Y. A.; Belt, K.; Karns, J. S., *J. Microbiol. Methods* **2004**, *58*, 223-231.
- (50) Verschraegen, I.; Anckaert, E.; Schiettecatte, J.; Mees, M.; Garrido, A.; Hermesen, D.; Lentjes, E. G. W. M.; Liebert, A.; Roth, H.; Stamminger, G.; Smits, J. *Clin. Chim. Acta* **2007**, *380*, 75-80.
- (51) Zhou. M.; Roovers. J.; Robertson. G. P.; Grover. C. P. *Anal. Chem.* **2003**, *75*, 6708-6717.
- (52) Jie, G.; Huang, H.; Sun, X.; Zhu, J. *Biosensors and Bioelectronics*, **2008**, *23*, 1896-1899.

- (53) Choi, H. N.; Cho, S.; Park, Y.; Lee, D. W.; Lee, W. *Anal. Chim. Acta* **2005**, *541*, 47-54.
- (54) Debad, J. D.; Glezer, E. N.; Wohlstadter, J.; Sigal, G. B. In *Clinical and biological applications of ECL*; Electrogenerated Chemiluminescence; Marcel Dekker, Inc: United States of America, 2004; pp 19.
- (55) Tfouni, E.; Doro, F. G.; Gomes, A. J.; Silva, R. S. d.; Metzker, G.; Benini, P. G. Z.; Franco, D. W. *Coord. Chem. Rev.* **2010**, *254*, 355-371.
- (56) Keener, W. K.; Rivera, V. R.; Cho, C. Y.; Hale, M. L.; Garber, E. A. E.; Poli, M. A. *Anal. Biochem.* **2008**, *378*, 87-89.
- (57) Wilson, R.; Clavering, C.; Hutchinson, A. *J Electroanal Chem* **2003**, *557*, 109-118.
- (58) Forster, R. J.; Hogan, C. F. *Anal. Chem.* **2000**, *72*, 5576-5582.
- (59) Su, M.; Liu, S. *Anal. Biochem.* , *In Press*, *Corrected Proof*.
- (60) Taylor, F. R.; Schultz, J. S. In *Immobilization methods*; Taylor, F. R., Schultz, J. S., Eds.; Handbook of Chemical and Biological Sensors; CRC Press: United Kingdom, 1996; pp 203.
- (61) Moretto, L. M.; Kohls, T.; Badocco, D.; Pastore, P.; Sojic, N.; Ugo, P. *J. Electroanal. Chem* **2010**, *640*, 35-41.
- (62) Ding, S.; Xu, J.; Zhang, W.; Chen, H. *Talanta* **2006**, *70*, 572-577.
- (63) Rubinstein, I.; Bard, A. J. *J. Am. Chem. Soc* **1981**, *103*, 5007-5013.
- (64) Zhang, L.; Guo, Z.; Xu, Z.; Dong, S. *J Electroanal Chem* **2006**, *592*, 63-67.
- (65) Wang, H.; Xu, G.; Dong, S. *Anal. Chim. Acta* **2003**, *480*, 285-290.
- (66) Bertoncello, P.; Dennany, L.; Forster, R. J.; Unwin, P. R. *Anal. Chem.* **2007**, *79*, 7549-7553.
- (67) Tao, Y.; Lin, Z.; Chen, X.; Huang, X.; Oyama, M.; Chen, X.; Wang, X. *Sensors Actuators B: Chem.* **2008**, *129*, 758-763.
- (68) Piao, M.; Yang, D.; Yoon, K.; Lee, S.; Choi, S. *Sensors* **2009**, *9*, 1662-1677.
- (69) Mao, L.; Yamamoto, K. *Anal. Chim. Acta* **2000**, *415*, 143-150.

- (70) Shi, G.; Luo, M.; Xue, J.; Xian, Y.; Jin, L.; Jin, J. *Talanta* **2001**, *55*, 241-247.
- (71) Ahuja, T.; Ahmad, I. M.; Kumar, D.; Rajesh. *Biomater.* **2007**, *28*, 791-805.
- (72) Guimard, N. K.; Gomez, N.; Schmidt, C. E. *Progress in Polymer Science* **2007**, *32*, 876-921.
- (73) Jagur-Grodzinski, J. *React Funct Polym* **1999**, *39*, 99-138.
- (74) Andrieux, C. P.; Haas, O.; Saveant, J. M. *J. Am. Chem. Soc.* **1986**, *108*, 8175-8182.
- (75) Dennany, L.; Hogan, C. F.; Keyes, T. E.; Forster, R. J. *Anal. Chem.* **2006**, *78*, 1412-1417.
- (76) Mortimer, R. J. *Electrochim. Acta* **1999**, *44*, 2971-2981.
- (77) Belanger, S.; Stevenson, K. J.; Mudakha, S. A.; Hupp, J. T. *Langmuir* **1999**, *15*, 837-843.
- (78) Dennany, L. Electrochemiluminescent & amperometric detection of DNA & DNA damage, Dublin City University, Dublin, 2004.
- (79) Seddon, E. A.; Seddon, K. R. In *Chapter 15; The Chemistry of Ruthenium*; Elsevier: NewYork, 1984; pp 1180.
- (80) Larsson, H.; Sharp, M. *J Electroanal Chem* **1995**, *381*, 133-142.
- (81) Doherty, A. P.; Forster, R. J.; Smyth, M. R.; Vos, J. G. *Anal. Chim. Acta* **1991**, *255*, 45-52.
- (82) Forster, R. J.; Vos, J. G. *Macromolecules* **1990**, *23*, 4372-4377.
- (83) Luxton, A. R.; Quig, A.; Delvaux, M. -.; Fetters, L. J. *Polymer* **1978**, *19*, 1320-1324.
- (84) Friesen, D. A.; Kajita, T.; Danielson, E.; Meyer, T. J. *Inorg. Chem.* **1998**, *37*, 2756-2762.
- (85) Geraty, S. M.; Vos, J. G. *J. Chem. Soc. , Dalton Trans.* **1987**, 3073-3978.
- (86) Malynych, S.; Luzinov, I.; Chumanov, G. *J. Phys. Chem. B* **2002**, *106*, 1280-1285.
- (87) Long, T. R.; Richter, M. M. *Inorg. Chim. Acta* **2005**, *358*, 2141-2145.
- (88) Muegge, B. D.; Richter, M. M. *Anal. Chem.* **2004**, *76*, 73-77.

- (89) Calvert, J. M.; Meyer, T. J. *Inorg. Chem* **1981**, 20, 27-33.
- (90) Kitamura, N.; Sato, M.; Kim, H.; Obata, R.; Tazuke, S. *Inorg. Chem.* **1988**, 27, 651-658.
- (91) Hughes, H. P.; Martin, D.; Bell, S.; McGarvey, J. J.; Vos, J. G., *Inorg. Chem* **1993**, 32, 4402-4408.
- (92) Bard, A. J.; Larry, R. F., *Electrochemical methods: Fundamentals and applications*; John Wiley & Sons Inc: New York, 1980; , pp 718.
- (93) Daly, D. J.; O'Sullivan, C. K.; Guilbault, G. G. *Biochem. Soc. Trans.* **2000**, 28, 89-93.
- (94) Zhang, G.; Chen, H. *Anal. Chim. Acta* **2000**, 419, 25-31.
- (95) Wohlstadter. J. N.; Wilbur. J. L.; Sigal. G. B.; Biebuyck. H. A.; Billadeau. M. A.; Dong. L.; Fischer. A. B.; Gudibande. S. R.; Jameison. S. H.; Kenten. J. H.; Leginus. J.; Leland. J. K.; Massey. R. J.; Wohlstadter. S. J. *Adv Mater* **2003**, 15, 1184-1187.
- (96) Iijima, S. *Nature* **1991**, 354, 56-58.
- (97) Iijima, S.; Ichihashi, T. *Nature* **1993**, 363, 603-605.
- (98) Jacobs, C. B.; Peairs, M. J.; Venton, B. J. *Anal. Chim. Acta* **2010**, 662, 105-127.
- (99) Wang, J. *Electroanalysis* **2005**, 17, 7-14.
- (100) Belin, T.; Epron, F. *Mater. Sci. Engg. B* **2005**, 119, 105-118.
- (101) Balasubramanian, K.; Burghard, M. *Anal Bioanal Chem* **2006**, 385, 452-468.
- (102) Pumera, M.; Sánchez, S.; Ichinose, I.; Tang, J. *Sensors Actuators B: Chem.* **2007**, 123, 1195-1205.
- (103) Colomer, J. F.; Benoit, J. M.; Stephan, C.; Lefrant, S.; Van Tendeloo, G.; B. Nagy, J. *Chem. Phys. Lett.* **2001**, 345, 11-17.
- (104) Li, J.; Cassell, A.; Delzeit, L.; Han, J.; Meyyappan, M. *J. Phys. Chem. B* **2002**, 106, 9299-9305.
- (105) Banks, C. E.; Davies, T. J.; Wildgoose, G. G.; Compton, R. G. *Chem. Commun.* **2005**, 829-841.
- (106) Moore, R. R.; Banks, C. E.; Compton, R. G. *Anal. Chem.* **2004**, 76, 2677-2682.

- (107) Chou, A.; Bocking, T.; Singh, N. K.; Gooding, J. J. *Chem. Commun.* **2005**, 842-844.
- (108) Musameh, M.; Wang, J.; Merkoci, A.; Lin, Y. *Electrochem. Commun.* **2002**, 4, 743-746.
- (109) Guo, S.; Wang, E. *Electrochem. Commun.* **2007**, 9, 1252-1257.
- (110) Wilder, J. W. G.; Venema, L. C.; Rinzler, A. G.; Smalley, R. E.; Dekker, C. *Nature* **1998**, 391, 59-62.
- (111) Thess, A.; Lee, R.; Nikolaev, P.; Dai, H.; Petit, P.; Robert, J.; Xu, C.; Lee, Y. H.; Kim, S. G.; Rinzler, A. G.; Colbert, D. T.; Scuseria, G. E.; Tomanek, D.; Fischer, J. E.; Smalley, R. E. *Science* **1996**, 273, 483-487.
- (112) Awasthi, K.; Singh, D. P.; Singh, S. K.; Dash, D.; Srivastava, O. N. *New Carbon Materials* **2009**, 24, 301-306.
- (113) Ramanathan, T.; Fisher, F. T.; Ruoff, R. S.; Brinson, L. C. *Chem. Mater.* **2005**, 17, 1290-1295.
- (114) Liu, Z.; Shen, Z.; Zhu, T.; Hou, S.; Ying, L.; Shi, Z.; Gu, Z. *Langmuir* **2000**, 16, 3569-3573.
- (115) Liu, X.; Baronian, K. H. R.; Downard, A. J. *Carbon* **2009**, 47, 500-506.
- (116) Liming, D.; Pingang, H.; Sinan, L. *Nanotech* **2003**, 14, 1081.
- (117) Guillorn, M. A.; McKnight, T. E.; Melechko, A.; Merkulov, V. I.; Britt, P. F.; Austin, D. W.; Lowndes, D. H.; Simpson, M. L. *AIP* **2002**, 91, 3824-3828.
- (118) O'Connor, M.; Kim, S. N.; Killard, A. J.; Forster, R. J.; Smyth, M. R.; Papadimitrakopoulos, F.; Rusling, J. F. *Analyst* **2004**, 129, 1176-1180.
- (119) Yu, X.; Kim, S. N.; Papadimitrakopoulos, F.; Rusling, J. F. *Mol. Biosyst.* **2005**, 1, 70-78.
- (120) Bard, A. J., Ed.; *Electrogenerated Chemiluminescence*; Introduction; Marcel Dekker, Inc: United states of America, 2004; , pp 10.
- (121) Zhang, T., Southampton Electrochemistry Group- *Instrumental Methods in Electrochemistry*; John Wiley & Sons, Inc: 1985; pp 49.
- (122) Skoog, D. A.; Holler, F. J.; Nieman, T. A., *Principles of Instrumental Analysis*; Harcourt Brace & Company: 1998; pp 650-660.
- (123) Carlsson, K. *Micron* **1995**, 26, 317-322.

- (124) Ametek signal recovery Low level optical detection using lock-in amplifier techniques. www.signalrecovery.com (accessed Oct, 2009).
- (125) Stoltenberg, J.; Pengra, D.; Van Dyck, R.; Vilches, O. The phase sensitive Lockin-In detector. <http://courses.washington.edu/phys431/lockin.pdf> (2009).
- (126) Meade, M. L., In *Lockin amplifiers*; Lockin amplifiers: Principles and applications; 2007; Vol. 1, .
- (127) Bond, A. M.; Fiego, U. S. *Anal. Chem* **1975**, *47*, 13, 2321-2324.
- (128) Engblom, S. O.; Myland, J. C.; Oldham, K. B., *J Electroanal Chem* **2000**, *480*, 120-132.
- (129) Gavaghan, D. J.; Bond, A. M., *J Electroanal Chem* **2000**, *480*, 133-149.
- (130) Gavaghan, D. J.; Elton, D.; Bond, A. M., *J Electroanal Chem* **2001**, *513*, 73-86.
- (131) Myland, J. C.; Oldham, K. B., *J Electroanal Chem* **2002**, *535*, 27-35.
- (132) Fernández-Sánchez, C.; McNeil, C. J.; Rawson, K. *Tr. Anal. Chem* **2005**, *24*, 37-48.
- (133) Sundfors, F.; Bobacka, J., *J Electroanal Chem* **2004**, *572*, 309-316.
- (134) Chen, W.; Wen, T.; Gopalan, A. *Synth. Met.* **2002**, *128*, 179-189.
- (135) Sabot, A.; Krause, S. *Anal. Chem.* **2002**, *74*, 3304-3311.
- (136) Sundfors, F.; Bobacka, J.; Ivaska, A.; Lewenstam, A. *Electrochim. Acta* **2002**, *47*, 2245-2251.
- (137) Holze, R. In *Impedance methods*; Bard, A. J., Stratmann, M., Eds.; Encyclopedia of electrochemistry; 2007; Vol. 3, pp 196-198.
- (138) Glarum, S. H.; Marshall, J. H. *J. Electrochem. Soc.* **1980**, *127*, 1467-1474.
- (139) Rosberg, K.; Paasch, G.; Dunsch, L.; Ludwig, S. *J Electroanal Chem* **1998**, *443*, 49-62.
- (140) Niu, L.; Li, Q.; Wei, F.; Chen, X.; Wang, H. *J Electroanal Chem* **2003**, *544*, 121-128.
- (141) Katz, E.; Willner, I. *Electroanalysis* **2003**, *15*, 913-947.

- (142) Bobacka, J.; Grzeszczuk, M.; Ivaska, A. *J Electroanal Chem* **1997**, 427, 63-69.
- (143) Bull, R. A.; Fan, F. F.; Bard, A. J. *J. Electrochem. Soc.* **1982**, 129, 1009-1015.
- (144) Hunter, T. B.; Tyler, P. S.; Smyrl, W. H.; White, H. S. *J. Electrochem. Soc.* **1987**, 134, 2198-2204.
- (145) Bard, A. J.; Faulkner, L. R. In *Approximated forms of i-n Equation*; Electrochemical methods: Fundamentals and applications; John Wiley & Sons, INC.: New York, 2001; pp 103.
- (146) Bott, W. A. *Curr. Separations* **2001**, 19-3, 71-75.

CHAPTER II

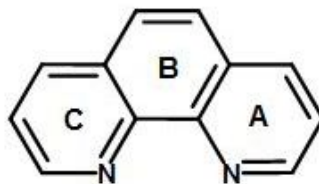
ELECTROCHEMILUMINESCENT NANOMATERIALS

2.1 INTRODUCTION

Electrochemiluminescence, where light-emitting species are produced by reactions between electrogenerated intermediates has become an important and powerful analytical tool in recent years. Since the first ECL experiments in 1964 by Hercules and co-workers¹ many ECL emitters including organic systems like 9,10-diphenylanthracene (DPA), anthracene, tetracene, phenothiazine, rubrene isobenzofurans, heterocyclic molecules like carbazoles and inorganic systems like $[\text{Ru}(\text{bpy})_3]^{2+}$, $[\text{Ir}(\text{ppy})_3]$, $[\text{Os}(\text{bpy})_3]^{2+}$, $[\text{Re}(\text{CO})_3\text{Cl}(\text{phen})]^+$ have been reported.²

Recent reviews have highlighted the use of metal chelate systems in ECL.³⁻⁷ For example, bipyridyl ruthenium complexes are of particular interest due to their solubility in a variety of solvent media, their stable redox chemistry, their long excited state lifetimes and their relatively strong photoluminescence and ECL.^{7,8} In fact, a $[\text{Ru}(\text{bpy})_3]^{2+}$ derivative containing a succinimide ester has been developed for use in clinical analyses (e.g., immunoassays, DNA probes).⁹ Another important class of chelating agent whose metal chelating properties have been utilized in a range of analytical reagents and probes is 1,10-phenanthroline ligand (Figure 2.1 A). One of the most important characteristics of this ligand is its rigid structure imposed by the central ring, B, which always keeps the two nitrogen atoms in juxtaposition to each other unlike in the 2,2'-dipyridyl system (Figure 2.1 B) where the two nitrogens are free to rotate about the linking bond.

(A)



(B)

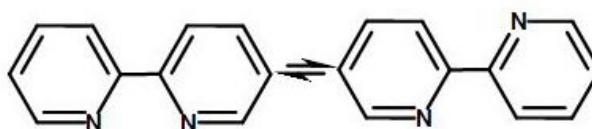


Figure 2.1: Structure of 1,10-phenanthroline ligand (A) and 2,2'-bipyridyl system (B).

In designing new ECL, probes several specific properties must be considered. Mainly, the probe must exhibit high luminescence efficiency that enables high detection sensitivity. Furthermore, for ECL-based assays, low redox potentials of the reagents and stability of their redox forms are mandatory. Thermal and photochemical stability, good solubility in water and synthetic accessibility are other important requirements for the probes.

Transition metal complexes, in particular those of the group 7 and 8 metals (Ru(II),^{8,10,12,13} Os(II),^{2,5} Re(I),⁸ Rh(III) and Ir(III)^{2,14}) and the lanthanides are a promising class of compounds for ECL sensor and probe technologies. Due to their long excited state lifetimes (hundreds of nanoseconds to tens of microseconds) transition metal complexes are more appealing than organic fluorophores (that usually have decay times of a few nanoseconds). Their luminescence quantum yields, although mostly modest compared to organic fluorophores, are adequate for a variety of applications. Furthermore, ruthenium polypyridyl complexes exhibit emissions with large Stokes shift which leads to

reduced background signal at the detection wavelength. They are less affected by oxygen quenching, compared to traditional fluorescent dyes and lanthanides.

The ECL characteristics of the transition metal complex strongly depend on the metals and the ligands of the complex. Various studies^{15,16} have shown that there exists an interesting relationship between the donor ability of the ligand and the ECL properties of the ruthenium (II) complexes and that it is possible to tune the ECL properties by introducing ligands with different donor abilities to metal complexes.

In the search for ECL probes with long-lived excited state, monomers containing two and three amino phenanthroline ligand *i.e.*, $[\text{Ru}(\text{aphen})_2\text{bpy}]^{2+}$ and $[\text{Ru}(\text{aphen}_3)]^{2+}$ respectively were prepared. The following chapter outlines the experimental methods and procedures used to synthesise and characterize these ruthenium polypyridyl complexes. These complexes are interesting to study in the context of electropolymerisation (Chapter 4) as they permit multidirectional polymer growth which leads to highly crossed linked polymers containing dispersed metal redox centers. Also they can be used as effective bio-immobilization platforms for the attachment of biomolecules like antibodies or proteins.

Recently, Forster and co-workers¹⁷⁻¹⁹ reported on the use of metallopolymer as a novel ECL platform. The ECL properties of $[\text{Ru}(\text{bpy})_2\text{PVP}]_{10}^{2+}$, where bpy is 2,2'-bipyridyl and PVP is poly(4-vinylpyridine), have been studied in some detail predominantly using oxalate, TPA and other small molecules as co-reactants. The synthesis and characterization of $[\text{Ru}(\text{bpy})_2\text{PVP}]_{10}^{2+}$ has also been reported in this chapter and the fabrication and characterization of $[\text{Ru}(\text{bpy})_2\text{PVP}]_{10}^{2+}$ modified electrodes has been described in detail in Chapter 3. These platforms have been used for potential modulation technique in Chapter 5.

In order to carry out biological assays another interesting monomeric ruthenium complex, $[\text{Ru}(\text{bpy})_2\text{PICH}_2]^{2+}$ where bpy is 2,2' bipyridine and PICH_2 is (2-(4-carboxyphenyl)imidazo[4,5-f][1,10]phenanthroline), was synthesised within the research group. This complex comprises of a phenanthroline chelate site linked

via a benzimidazole spacer to a benzoic acid terminus.^{20,21} Significantly, the imidazole moiety of this bridging ligand is capable of undergoing protonation/deprotonation reaction depending on the pH of the contacting electrolyte solution. Accordingly, $[\text{Ru}(\text{bpy})_2\text{PICH}_2]^{2+}$ possesses three ionisable sites depending on the pH of the contacting electrolyte and can exist in four states of protonation $[\text{Ru}(\text{bpy})_2\text{PICH}_3]^{3+}$, $[\text{Ru}(\text{bpy})_2\text{PICH}_2]^{2+}$, $[\text{Ru}(\text{bpy})_2\text{PICH}]^+$ and $[\text{Ru}(\text{bpy})_2\text{PIC}]^0$.²¹ Pellegrin *et.al.*,²⁰ reported that emission from the $[\text{Ru}(\text{bpy})_2\text{PICH}_2]^{2+}$ in aqueous solution occurs from the $^3\text{MLCT}$ excited state. $[\text{Ru}(\text{bpy})_2\text{PICH}_2]^{2+}$ is strongly luminescent, in its dicationic state with its emission maximum occurring at 605 nm at room temperature. Its luminescent lifetime λ_{EM} and quantum yield for emission ϕ^{455} in buffered aqueous solution (pH 5.5), were reported to be 975 ns and 0.067²⁰ (*i.e.*, 30% higher than the quantum yield of $[\text{Ru}(\text{bpy})_3]^{2+}$).

This complex is extremely attractive for use in biological assays due to its capacity to bind to DNA,²² its participation in interfacial self assembled monolayers (SAM),²³ peptide conjugates for luminescence and luminescence lifetime cellular imaging,²⁴ and its ability to bind to proteins through its carboxyl terminus. Furthermore, it can be readily functionalised through the carboxyl terminus making it an attractive complex for producing extended supramolecular structures.²⁰ Therefore, it serves as an excellent candidate to be used as ECL label in the antibody assay as described in Chapter 6.

2.2 EXPERIMENTAL

2.2.1 Apparatus

Electrochemical measurements were carried out with a CH instruments, model 660 potentiostat. Cyclic voltammetry was conducted using a typical three-electrode cell configuration. Electropolymerisation in anhydrous acetonitrile and aqueous sulphuric acid was performed using a 1.5 mm radius glassy carbon electrode as a working electrode. An aqueous or non-aqueous Ag/AgCl electrode was used as a reference depending on the solvent and a platinum wire was used as counter electrode. All solutions were deaerated for 20 min by purging with nitrogen prior to electrochemical experimentation. All potentials are quoted versus Ag/AgCl reference electrode, and all measurements were made at room temperature.

Absorbance spectra were recorded on a Shimadzu UV-Vis-NIR 3100 spectrophotometer and emission spectra on a Perkin-Elmer LS50-B spectrophotometer using 1 cm optical path length quartz cuvette.

Analytical ^1H and ^{13}C NMR spectra were recorded on Bruker Advance 400 NMR spectrometer and the free induction decay (FID) profiles processed using XWIN-NMR software package. Deuterated d_8 -dimethylsulfoxide (d_8 -DMSO) was supplied from Sigma-Aldrich.

The fluorescence properties of the electropolymerised films were investigated with a Zeiss LSM 510 Meta laser module confocal microscope using an excitation wavelength of 488 nm and 10x magnification objective.

Resonance Raman spectra were recorded on a HORIBA Jobin-Yvon Labram HR 2000 confocal Raman microscope. An argon ion laser (Coherent) was used to excite at 488 nm. The laser was focused onto the film using a 10x objective.

Time correlated single photon counting (TCSPC) lifetime measurements were made on PicoQuant PDL-800B pulsed diode laser controller and Fluo Time 100 TCSPC with a 450 nm pulsed laser source with a cut-off filter of 530 nm.

TCSPC analysis was performed using PicoQuant FluoFit software. Prior to measurement all samples were degassed for 30 min with nitrogen.

2.2.2 Materials and reagents

The ruthenium monomers, $[\text{Ru}(\text{aphen})_2\text{bpy}]^{2+}$ and $[\text{Ru}(\text{aphen})_3]^{2+}$ were kindly provided by Dr. Yann Pellegrin of the Tia Keyes research group following the synthesis procedure elsewhere described.²⁵ The metallopolymer, $[\text{Ru}(\text{bpy})_2(\text{PVP})_{10}]^{2+}$, was kindly provided by Ms. Anitha Devdoss of the Robert Forster research group and was synthesised using a modified literature procedure.¹⁸ Finally, $[\text{Ru}(\text{bpy})_2\text{PICH}_2]^{2+}$ was kindly provided by Dr. Ellena Lestini of Tia Keyes research group and was synthesised as described previously.²⁰ The structures of the complexes was confirmed using ^1H -NMR spectra that were recorded on Bruker Advance 400 NMR spectrometer and the free induction decay (FID) profiles processed using XWIN-NMR software package. The structures, ^1H -NMR, CHN data and mass spectra data of these compounds are given in Appendix 3. All chemicals and solvents were purchased from Sigma Aldrich and were of analytical grade. All solutions were made using deionised water purified with a Milli -Q plus 18.5 Millipore installation. The solvents used for spectroscopic measurements were of HPLC grade.

2.3 RESULTS AND DISCUSSION

2.3.1 $[\text{Ru}(\text{bpy})_2\text{PICH}_2]^{2+}$

$[\text{Ru}(\text{bpy})_2\text{PICH}_2]^{2+}$ was synthesised within the research group as described previously.²⁰ The product was characterized by cyclic voltammetry, UV-vis spectroscopy and NMR. Figure 2.2 shows representative cyclic voltammogram of a spontaneously adsorbed film of $[\text{Ru}(\text{bpy})_2\text{PICH}_2]^{2+}$ on indium tin oxide (ITO) electrode. Spontaneously adsorbed monolayers were formed according to a previously published procedure.²¹ Briefly, ITO electrodes were immersed 1

mM solution of the metal complex in methanol/water (50/50, v/v) mixture for 12 hrs. Before electrochemical measurements were performed, the electrodes were rinsed with acetone followed by washing with 0.1 M LiClO₄ (electrolyte solution) to remove any unbound material. The CV shown in Figure 2.2 was performed in blank solution of 0.1 M LiClO₄ (pH 6.5±0.1) which had no dissolved ruthenium monomer. The CV shows that the formal potential of Ru^{2+/3+} couple is at +0.9 V vs. Ag/AgCl, which is lower than that reported by Forster *et.al.*,²¹(1.04 ± 0.015 V vs. Ag/AgCl) for this compound under identical conditions. However, lower oxidation potential implies that the ruthenium complex can be easily oxidized when immobilized. This aspect is important as this compound will be immobilized onto the surface of silica nanospheres, to form ECL labels for IgG immunoassay in Chapter 6. The monolayer exhibits close to ideal surface confined behaviour with peak-to-peak separation of 0.1 V between anodic and cathodic waves. Apart from the formal oxidation and reduction potentials the compound was very similar to one previously reported.²¹ Figure 2.3 shows the associated emission decay which follows mono exponential kinetics, with a lifetime of 682±5 ns in nitrogen purged PBS (pH 7). This lifetime is some what shorter than that reported earlier for this compound by Pellegrin *et.al.*²³ This is however expected as the emission of the ruthenium PICH₂ compound is highly pH dependent. Pellegrin and co-workers reported that the both lifetime and luminescence quantum yield of [Ru(bpy)₂ PICH₂]²⁺ decreased to 550±10 ns and 0.038 respectively, when the complex was deprotonated at pH 11.²³ As the lifetime of 975±5 ns was reported for the complex at pH 5.5 one can expect that at PBS buffer of pH 7 there would be a slight decrease in the lifetime. These results along with UV spectrum (Figure 2.4) confirm the identity of the complex.

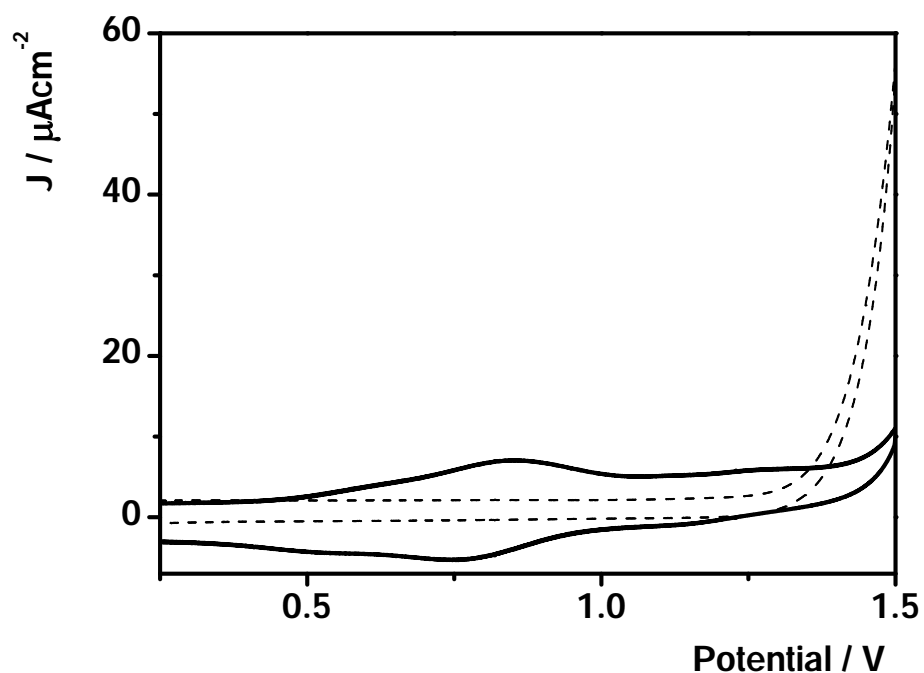
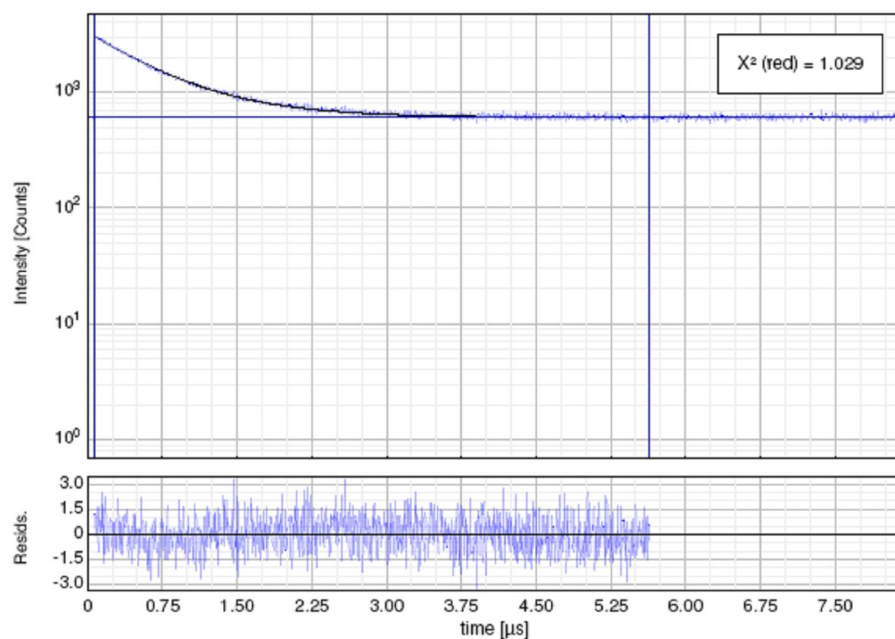


Figure 2.2: Cyclic voltammogram of monolayer formed by dissolving 1 mM $[\text{Ru}(\text{bpy})_2\text{PICH}_2]^{2+}$ in 50:50 Methanol: H_2O mixture and self assembling it on ITO (1 cm x 1 cm x 0.1 cm; 1 x b x h). The CV was performed in blank 0.1 M LiClO_4 (pH 6.5 ± 0.1) at scan rate 0.1 Vs^{-1} , potential range +0.0 V to +1.5 V.



$$I(t) = \sum_{i=1}^n A_i e^{-\frac{t}{\tau_i}}$$

Parameter	Value	Conf. Lower	Conf. Upper	Conf. Estimation
A ₁ [Cnts]	2427.5	-29.2	+29.2	Fitting
τ ₁ [μs]	0.68231	-0.00888	+0.00888	Fitting
Bkgr. Dec [Cnts]	614.64	-4.44	+4.44	Fitting

Figure 2.3: Typical fluorescence emission decay of $[\text{Ru}(\text{bpy})_2\text{PICH}_2]^{2+}$ in degassed aqueous PBS buffer (pH 7) when pulsed with a 450 nm laser source with a long pass cut-off filter of 530 nm, mono exponential decay.

2.3.2 Characterization

We know from the previous sections that one can tune the spectroscopic and electrochemical properties of metal complexes by appropriate choice of ligands.²⁵ The nature of the ligand can influence the energy of the lowest MLCT excited state, which is the emitting excited state responsible for the photoluminescence and electrochemiluminescence of the compounds studied herein. The presence of the MLCT excited state can be verified by absorption spectroscopy.

Figure 2.4 illustrates the absorption spectra of all four ruthenium polypyridyl complexes synthesised. The spectra shows that all three complexes *i.e.*, $[\text{Ru}(\text{bpy})_2\text{PICH}_2]^{2+}$, $[\text{Ru}(\text{aphen})_3]^{2+}$ and $[\text{Ru}(\text{aphen})_2\text{bpy}]^{2+}$ exhibit intense ligand centered (LC) $\pi \rightarrow \pi^*$ transition peaks in the 200-300 nm range. Also the three compounds show strong absorption maximum of the $d \rightarrow \pi^*$ MLCT^{25, 29} at 460, 467 and 450 nm respectively. Significantly, the MLCT absorption maxima of $[\text{Ru}(\text{aphen})_2\text{bpy}]^{2+}$ is identical to the lowest energy absorption maxima of $[\text{Ru}(\text{bpy})_3]^{2+}$ in aqueous solution.⁸

In addition to this, $[\text{Ru}(\text{aphen})_3]^{2+}$ and $[\text{Ru}(\text{aphen})_2\text{bpy}]^{2+}$ also show a peak 360 nm confirming the presence of amino phenanthroline ligand.³⁰ The absorption spectrum of $[\text{Ru}(\text{bpy})_2(\text{PVP})_{10}]^{2+}$ illustrated by a thin line (—), shows metal centered (MC) transition at 344 nm and $d \rightarrow \pi^*$ MLCT^{25,29} absorption maxima at 465 nm.⁷ The spectrum obtained below corresponds to that obtained previously for this metallopolymer.³¹

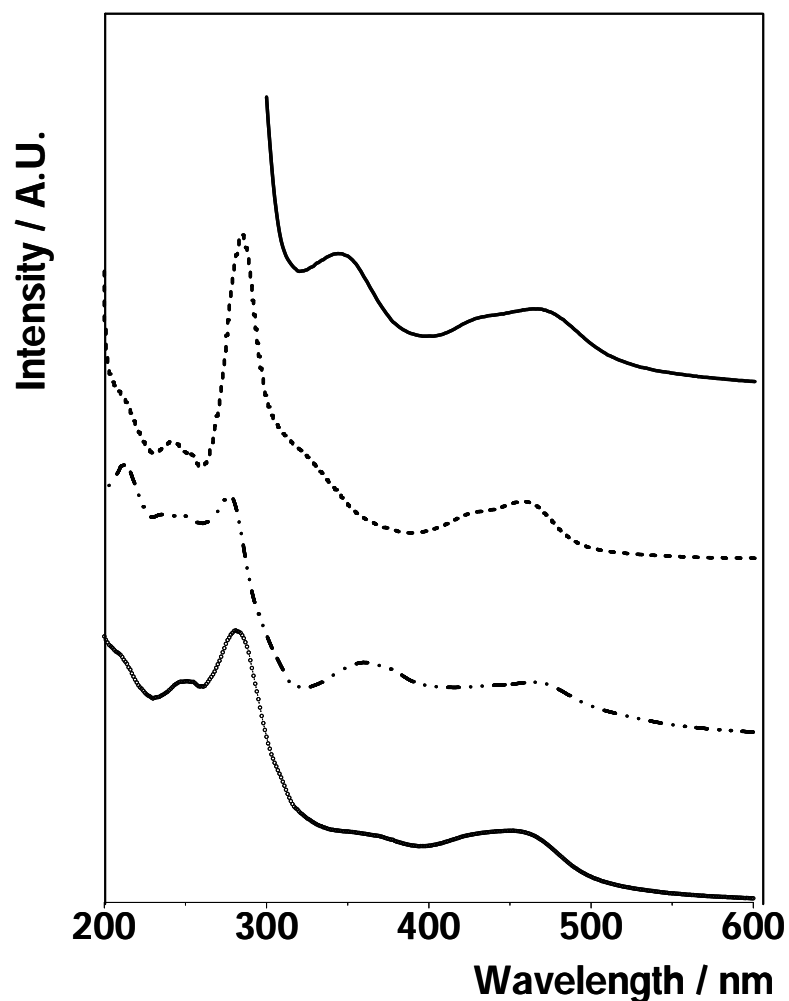


Figure 2.4: Absorption spectra of ruthenium polypyridyl complexes used. The spectra of the complexes were taken in the respective solvents in which they were used in the thesis. 60 μM $[\text{Ru}(\text{bpy})_2(\text{PVP})_{10}]^{2+}$ polymer in 1:1 mixture of Ethanol: DMF (.....), 15 μM $[\text{Ru}(\text{bpy})_2\text{PICH}_2]^{2+}$ in 10 mM PBS buffer pH 7 (----) , 31 μM $[\text{Ru}(\text{aphen})_3]^{2+}$ in spectroscopic grade CH_3CN (- · -) and 125 μM $[\text{Ru}(\text{aphen})_2\text{bpy}]^{2+}$ in spectroscopic grade CH_3CN (—). A quartz cuvette with 1 cm path length was used. The spectra have been offset for clarity.

All compounds, *i.e.*, $[\text{Ru}(\text{bpy})_2(\text{PVP})_{10}]^{2+}$, $[\text{Ru}(\text{bpy})_2\text{PICH}_2]^{2+}$, $[\text{Ru}(\text{aphen})_3]^{2+}$ and $[\text{Ru}(\text{aphen})_2\text{bpy}]^{2+}$, dissolved in acetonitrile, showed intense emission around 610 nm when excited at 465, 460, 467 and 450 nm respectively, as shown in Figure 2.5. This emission wavelength is identical to that of $[\text{Ru}(\text{bpy})_3]^{2+}$ in aqueous solution.^{8,32} The MLCT absorption, emission wavelengths and extinction coefficients of all the compounds in different solvents have been summarised in Table 2.1.

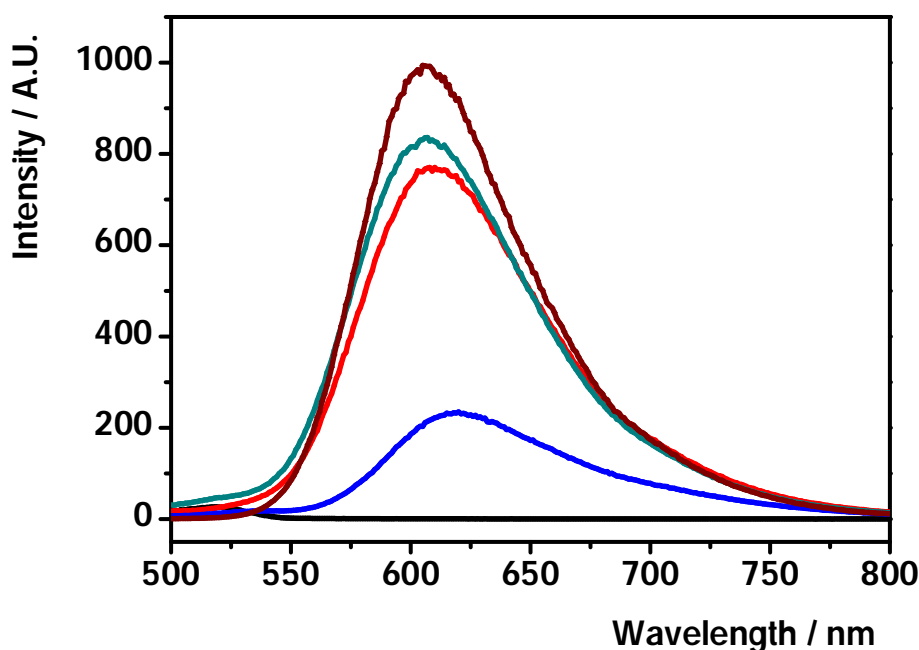


Figure 2.5: Emission spectra of all the ruthenium polypyridyl complexes used. The polymer, $[\text{Ru}(\text{bpy})_2(\text{PVP})_{10}]^{2+}$ (—), 60 μM was in 1:1 mixture of ethanol:DMF as it is not soluble in pure spectroscopic grade CH_3CN . The rest of the monomers, 15 μM $[\text{Ru}(\text{bpy})_2\text{PICH}_2]^{2+}$ (—), 31 μM $[\text{Ru}(\text{aphen})_3]^{2+}$ (—) and 125 μM $[\text{Ru}(\text{aphen})_2\text{bpy}]^{2+}$ (—) were present in spectroscopic grade CH_3CN . The compounds $[\text{Ru}(\text{bpy})_2(\text{PVP})_{10}]^{2+}$, $[\text{Ru}(\text{bpy})_2\text{PICH}_2]^{2+}$, $[\text{Ru}(\text{aphen})_3]^{2+}$ and $[\text{Ru}(\text{aphen})_2\text{bpy}]^{2+}$ were excited at 465, 460, 467 and 450 nm respectively with a slit width of 10 nm. Blank CH_3CN is represented by (—).

Table 2.1: Absorption and emission data of ruthenium polypyridyl complexes in different solvents.

Complex	MLCT absorption at rt, nm	λ_{max} (emission) at rt, nm	log ϵ
$[\text{Ru}(\text{bpy})_2(\text{PVP})_{10}]^{2+}$	465 ^a	620 ^c	3.8
$[\text{Ru}(\text{bpy})_2 \text{PICH}_2]^{2+}$	460 ^b	606 ^c	4.4
$[\text{Ru}(\text{aphen})_3]^{2+}$	467 ^c	606 ^c	3.9
$[\text{Ru}(\text{aphen})_2\text{bpy}]^{2+}$	450 ^c	610 ^c	3.5

^a Measured in (1:1;ethanol:DMF). ^b Measured in PBS (pH 7). ^c Measured in acetonitrile. rt –room temperature

It has been established that in ECL annihilation pathway, both the oxidized and reduced forms of the luminophore are produced electrochemically within the depletion zone by application of a potential step or sweep. These species then interact to produce both a ground state and an electronically excited state, which then relaxes by emission of a photon.¹⁵ The corresponding free energy for the reaction can then be calculated using Equation 2.1:¹⁵

$$\Delta G = nF(E_{\text{DONOR}}^0 - E_{\text{ACCEPTOR}}^0) \quad 2.1$$

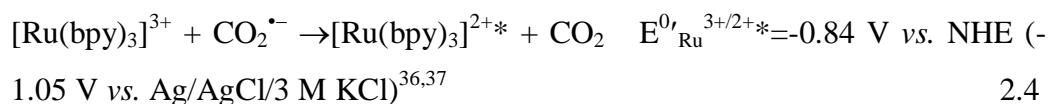
where, E_{DONOR}^0 , E_{ACCEPTOR}^0 are formal potentials for ground state reduction and oxidation processes respectively. For ECL reactions, ΔG is typically in the range of 2-3 eV. But in case of co-reactant ECL, establishing the energetics of ECL reactions is more difficult, because the energies of the reactive intermediates, such as $\text{CO}_2^{\bullet-}$, may not be accurately known.¹³ However, the fundamental principles are the same as with annihilation reaction in terms of the energy of the electron transfer step. Bock and co-workers³³ have estimated the formal reduction potential of $E^0_{\text{Ru}}(\text{Ru}^{3+/2+*})$ to be -0.84 V vs. NHE in H_2O . Knowing this value, co-reactant ECL can be explained following similar lines to that of annihilation ECL. For example the following reactions are known to occur in the $[\text{Ru}(\text{bpy})_3]^{2+}/[\text{C}_2\text{O}_4]^{2-}$ co-reactant ECL system.³⁴



The oxidizing potential also oxidizes the ECL luminophore $[\text{Ru}(\text{bpy})_3]^{2+}$:



$[\text{Ru}(\text{bpy})_3]^{3+}$ and $\text{CO}_2^{\bullet-}$ may then react according to Equation 2.4, to produce the excited state $[\text{Ru}(\text{bpy})_3]^{2+*}$ which is capable of emitting light. Given the values of E_{DONOR}^0 and E_{ACCEPTOR}^0 are +1.26 V and -0.84 V respectively, ΔG is of the order of 2.1 eV. Also, the wavelength of maximum emission obtained for $[\text{Ru}(\text{bpy})_3]^{2+*}$ at 298 K following photo excitation is 610 nm (~ 2.03 eV).³⁵ Therefore, the free energy of the above ECL reaction exceeds that required to create the electronically excited state, and ECL becomes possible.



Cyclic voltammetry (CV) is a convenient method for determining the potentials at which the desired reactants are generated. Also, CV is an excellent probe of the stability of the oxidized and reduced forms of the complex (*i.e.*, the radical

anions or cations) and their ability to undergo electron transfer reactions. Stable, “reversible” redox processes as well as high photoluminescence lifetimes are often used¹³ to determine whether a compound shows promise as an ECL luminophore or not.⁸

Figure 2.6 illustrates the cyclic voltammogram obtained when a 1.5 mm radius glassy carbon electrode is immersed in a 1.5 mM solution of $[\text{Ru}(\text{apen})_2\text{bpy}]^{2+}$ dissolved in 0.1 M acetonitrile with TBATFB as supporting electrolyte. In acetonitrile, consistent with previous reports,^{25,38} two oxidation processes are observed during the first scan. These processes correspond to irreversible oxidation of the 5-amino-1,10-phenanthroline ligand at approximately +0.85 V^{39, 40} and the electrochemically reversible $\text{Ru}^{2+/3+}$ couple at +1.01 V. Amine-based oxidation is essential for the initiation of polymerization as explained in detail in Chapter 4. The oxidation of $\text{Ru}^{2+/3+}$ couple occurs at +1.01 V from which we can calculate ΔG to be 2.06 eV. For oxalate co-reactant ECL this is an energy sufficient system.

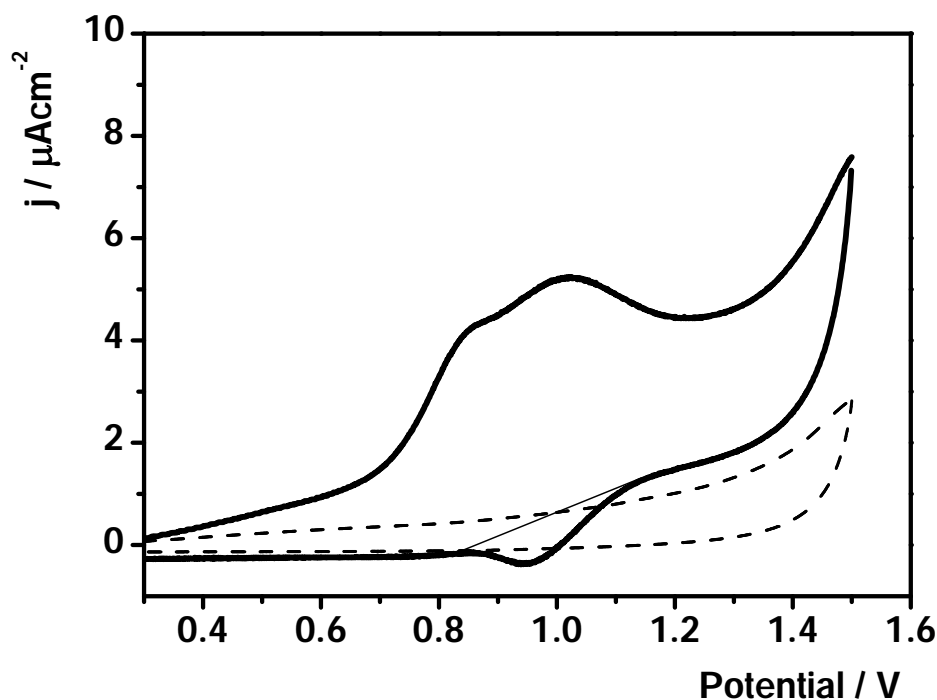


Figure 2.6: Cyclic voltammogram of 1.5 mM solution $[\text{Ru}(\text{aphen})_2\text{bpy}]^{2+}$, represented by solid line (—), on a 3 mm diameter glassy carbon electrode at a scan rate of 0.1 V s^{-1} . The potential range is from +0.3 V to +1.5 V in 0.1 M CH_3CN / TBATFB. CV of blank 0.1 M CH_3CN / TBATFB on GCE is represented by dashed line (---).

In acetonitrile, the $\text{Ru}^{2+/3+}$ couple shows reversible behaviour but it is observed that in 0.5 M H_2SO_4 (pH 0.3) it exhibits irreversible or quasi reversible behaviour.⁴¹ As shown in Figure 2.7, the CV of $[\text{Ru}(\text{aphen})_2\text{bpy}]^{2+}$ on a 3 mm diameter glassy carbon electrode shows oxidation and reduction peaks at +1.6 V and +0.6 V respectively. The value of $I_{\text{PA}}/I_{\text{PC}}$ lies in the range of 0.20-0.40 compared to the expected value of unity for a reversible response. No pre-peak for amine based oxidation is observed. The irreversible behaviour is explained in detail in Chapter 4. In spite of the above observations, a high ΔG value of 2.65 eV is obtained when half wave potential for Ru^{2+} oxidation is used. Hence,

this film may show higher ECL intensity when compared to its acetonitrile counter part.

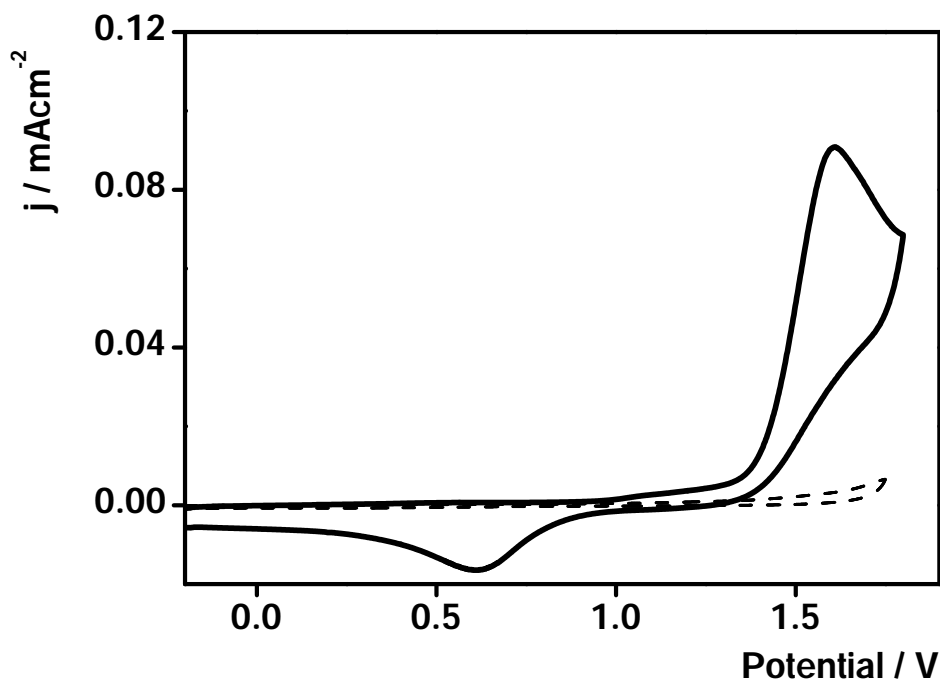
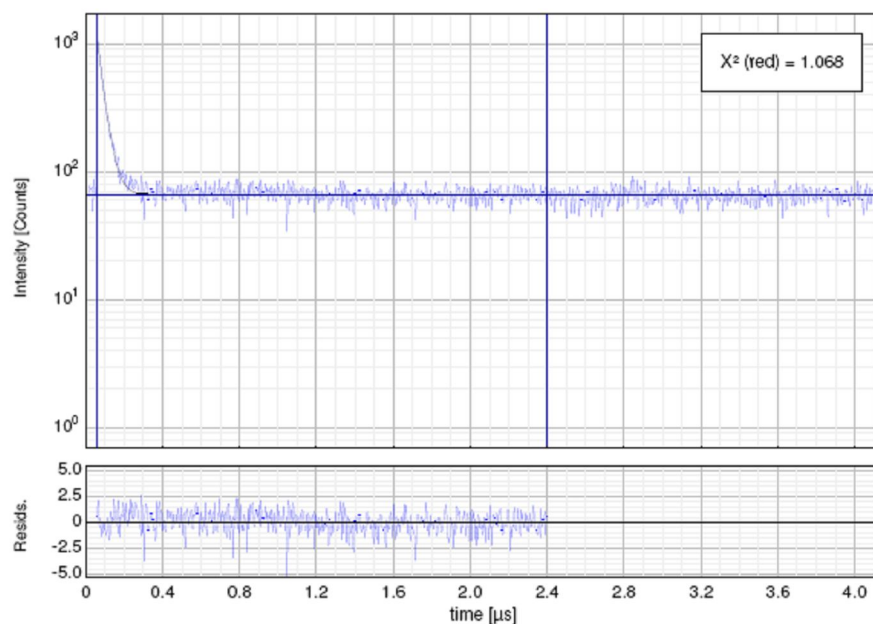


Figure 2.7: Cyclic voltammogram of 1.5 mM solution $[\text{Ru}(\text{aphen})_2\text{bpy}]^{2+}$, represented by solid line (—), on a 3 mm diameter glassy carbon electrode at a scan rate of 0.1 V s^{-1} . The potential range is from -0.2 V to +1.75 V in 0.5 M H_2SO_4 (pH 0.3). CV of blank 0.5 M H_2SO_4 (pH 0.3) on GCE is represented by dashed line (---).

Figure 2.8 shows the excited state lifetime of $[\text{Ru}(\text{aphen})_2\text{bpy}]^{2+}$ in acetonitrile under deoxygenated condition. The solution was deoxygenated for 30 min prior to measurements as it is well known that oxygen is an excellent quencher of excited state lifetime. The bis-aminophenanthroline complex shows a very short lifetime of 33 ns.



$$I(t) = \sum_{i=1}^n A_i e^{-\frac{t}{\tau_i}}$$

Parameter	Value	Conf. Lower	Conf. Upper	Conf. Estimation
A ₁ [Cnts]	1036.8	-47.4	+47.4	Fitting
τ ₁ [μs]	0.03273	-0.00143	+0.00143	Fitting
Bkgr. Dec [Cnts]	66.10	-1.37	+1.37	Fitting

Figure 2.8: Typical fluorescence emission decay of degassed [Ru(aphen)₂bpy]²⁺ in acetonitrile when pulsed with a 450 nm laser source with a long pass cut-off filter of 530 nm, single exponential decay.

Though [Ru(aphen)₂bpy]²⁺ exhibits a very short excited state lifetime compared to [Ru(bpy)₃]²⁺, the film formed both in acetonitrile and H₂SO₄ satisfy the energy requirement (ΔG value) needed to create the electronically excited state for ECL. Hence it is expected that these films might exhibit electrochemiluminescence.

Similar studies were conducted with 1.0 mM solution of [Ru(aphen)₃]²⁺ in 0.1 M acetonitrile with TBATFB as the supporting electrolyte and 0.5 M H₂SO₄ (pH 0.3). Figures 2.9 and 2.10 shows the cyclic voltammogram of 1.0 mM [Ru(aphen)₃]²⁺ in acetonitrile and in 0.5 M H₂SO₄ (pH 0.3) respectively.

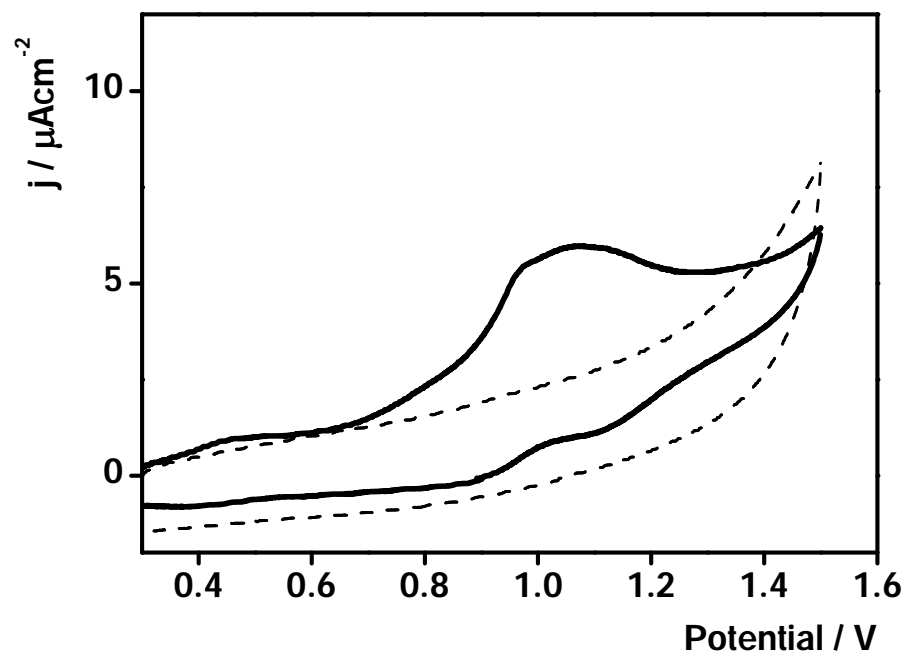


Figure 2.9: Cyclic voltammogram of 1.0 mM solution $[\text{Ru}(\text{aphen})_3]^{2+}$, represented by solid line (—), on a 3 mm diameter glassy carbon electrode at a scan rate of 0.1 Vs^{-1} . The potential range is from +0.3 V to +1.5 V in 0.1 M CH_3CN / TBATFB. CV of blank 0.1 M CH_3CN / TBATFB on GCE is represented by dashed line (---).

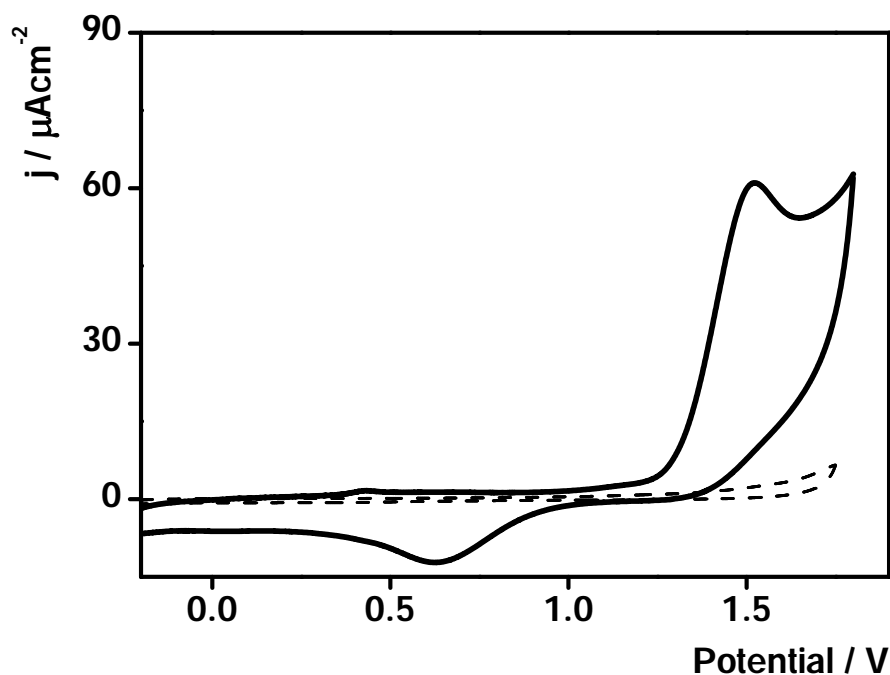
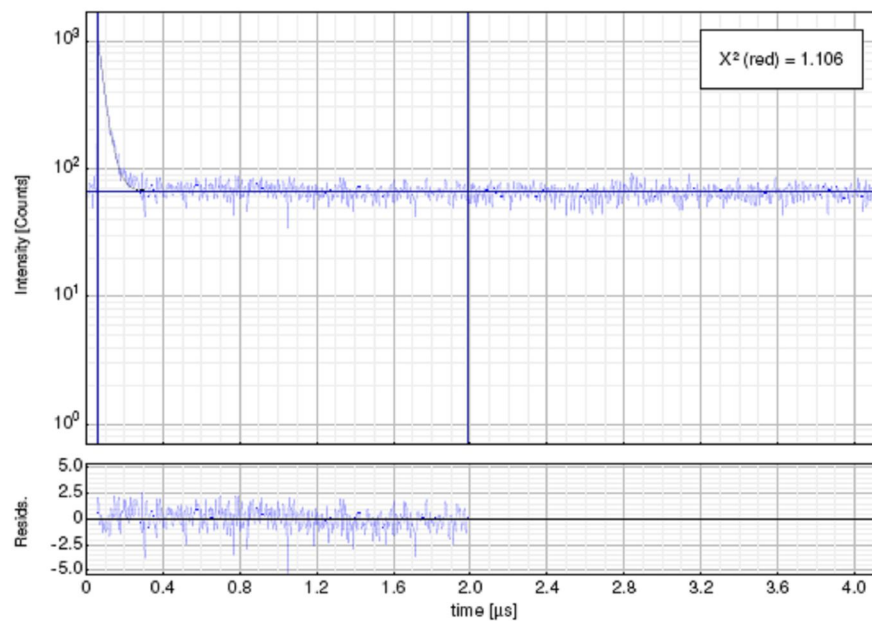


Figure 2.10: Cyclic voltammogram of 1.0 mM solution $[\text{Ru}(\text{aphen})_3]^{2+}$, represented by solid line (—), on a 3 mm diameter glassy carbon electrode at a scan rate of 0.1 V s^{-1} . The potential range is from -0.2 V to +1.75 V in 0.5 M H_2SO_4 (pH 0.3). CV of blank 0.5 M H_2SO_4 (pH 0.3) on GCE is represented by dashed line (---).

The cyclic voltammogram of $[\text{Ru}(\text{aphen})_3]^{2+}$ in acetonitrile shows a redox peak corresponding to the oxidation of electrochemical $\text{Ru}^{2+/3+}$ couple at +1.05 V.³⁹ Redox peaks at +0.5 V and +0.88 V are also seen which could be attributed to corresponding oxidation and reduction of 5-amino-1,10-phenanthroline ligand.^{39,42} The oxidation potential of the $\text{Ru}^{2+/3+}$ couple in H_2SO_4 lies at +1.5 V.

Figure 2.11 shows the excited state lifetime of $[\text{Ru}(\text{aphen})_3]^{2+}$ in acetonitrile under deoxygenated condition. The tris-aminophenanthroline complex also shows a very short lifetime of 33 ns.



$$I(t) = \sum_{i=1}^n A_i e^{-\frac{t}{\tau_i}}$$

Parameter	Value	Conf. Lower	Conf. Upper	Conf. Estimation
A_1 [Cnts]	1037.5	-43.8	+43.8	Fitting
τ_1 [μs]	0.03265	-0.00132	+0.00132	Fitting
Bkgr. Dec [Cnts]	66.42	-1.41	+1.41	Fitting

Figure 2.11: Typical fluorescence emission decay of degassed $[\text{Ru}(\text{aphen})_3]^{2+}$ in acetonitrile when pulsed with a 450 nm laser source with a long pass cut-off filter of 530 nm, mono exponential decay kinetics.

2.4 CONCLUSIONS

In conclusion, the synthesis and characterization of ruthenium polypyridyl complexes, used in this thesis *i.e.*, $[\text{Ru}(\text{aphen})_2\text{bpy}]^{2+}$, $[\text{Ru}(\text{aphen}_3)]^{2+}$, $[\text{Ru}(\text{bpy})_2\text{PVP}]_{10}^{2+}$ and $[\text{Ru}(\text{bpy})_2\text{PICH}_2]^{2+}$, have been reported herein.

Spectroscopic and electrochemical characterization of $[\text{Ru}(\text{aphen})_2\text{bpy}]^{2+}$ and $[\text{Ru}(\text{aphen}_3)]^{2+}$ monomers showed that these two complexes exhibit very short excited state lifetime. However, the films formed both in acetonitrile and H_2SO_4 satisfy the energy requirement (ΔG value) needed to create the electronically excited state for ECL. Hence, they are expected to possess electrochemiluminescent properties. The synthesised polymer, $[\text{Ru}(\text{bpy})_2\text{PVP}]_{10}^{2+}$, was characterized using UV-vis absorption spectroscopy. The emission values obtained correspond very well with ones reported earlier for this compound.³¹ This compound was used in the fabrication of polymer modified glassy carbon electrode platforms. These platforms have been used in modulated potential ECL, explained in Chapter 5. Finally, a high brightness luminophore $[\text{Ru}(\text{bpy})_2\text{PICH}_2]^{2+}$ with a lifetime of 682 ± 5 ns in degassed PBS buffer (pH 7) was also synthesised. This compound showed reduced lifetime than that reported in literature but the reduction in the lifetime is attributed to the high pH of the contacting electrolyte. The silica microspheres used in Chapter 6 were decorated with this novel ECL luminophore and used in the pico molar detection of IgG.

2.5 REFERENCES

- (1) Hercules, D. M. *Science* **1964**, *145*, 808.
- (2) Bard, A. J., In *Metal Chelate Systems*; Electrogenerated Chemiluminescence; Marcel Dekker, Inc: United States of America, 2004; pp 345.
- (3) Andrew, W. K. *Tr. Anal. Chem* **1999**, *18*, 47-62.
- (4) Fahrnich, K. A.; Pravda, M.; Guilbault, G. G. *Talanta* **2001**, *54*, 531-559.
- (5) Pyati, R.; Mark, R. M. *Annu. Rep. Prog. Chem. , Sect C* **2007**, *103*, 12-78.
- (6) Andrew, W. K.; Gillian, M. G. *Analyst* **1994**, *119*, 879-890.
- (7) Juris, A.; Balzani, V.; Barigelletti, F.; Campagna, S.; Belser, P.; von Zelewsky, A. *Coord. Chem. Rev.* **1988**, *84*, 85-277.
- (8) Richter, M. M. *Chem. Rev.* **2004**, *104*, 3003-3036.
- (9) Meso scale discovery Immunogenicity assays using MSD's multiarray technology.
http://www.mesoscale.com/CatalogSystemWeb/WebRoot/literature/notes/pdf/Immunogenicity_Applications.pdf(2010).
- (10) Lee, W. *Microchim. Acta* **2005**, *127*, 19-39.
- (11) Miao, W.; Choi, J. P.; Bard, A. J. *J. Am. Chem. Soc.* **2002**, *124*, 14478-14485.
- (12) Wang, H.; Xu, G.; Dong, S. *Anal. Chim. Acta* **2003**, *480*, 285-290.
- (13) Bard, A. J., In *Fundamentals of ECL: Coreactants*; Electrogenerated Chemiluminescence; Marcel Dekker, Inc: United States of America, 2004; pp 19.
- (14) Muegge, B. D.; Richter, M. M. *Anal. Chem.* **2004**, *76*, 73-77.
- (15) Forster, R. J.; Bertoncello, P.; Keyes, T. E. *Annu. Rev. Anal. Chem* **2009**, *2*, 359-385.

- (16) Forster, R. J.; Keyes, T. E.; Vos, J. G. In *Interfacial Supramolecular Assemblies*; John Wiley & Sons, Ltd: 2003; .
- (17) Forster, R. J.; Hogan, C. F. *Anal. Chem.* **2000**, 72, 5576-5582.
- (18) Hogan, C. F.; Forster, R. J. *Anal. Chim. Acta* **1999**, 396, 13-21.
- (19) Forster, R. J.; Vos, J. G. *Macromolecules* **1990**, 23, 4372-4377.
- (20) Pellegrin, Y.; Forster, R. J.; Keyes, T. E. *Inorg. Chim. Acta* **2009**, 362, 1715-1722.
- (21) Forster, R. J.; Pellegrin, Y.; Keyes, T. E. *Electrochem. Commun.* **2007**, 9, 1899-1906.
- (22) Bai, G.; Dong, B.; Lü, Y.; Wang, K.; Jin, L.; Gao, L. *J. Inorg. Biochem.* **2004**, 98, 2011-2015.
- (23) Pellegrin, Y.; Forster, R. J.; Keyes, T. E. *Inorg. Chim. Acta* **2008**, 361, 2683-2691.
- (24) Neugebauer, U.; Pellegrin, Y.; Devocelle, M.; Forster, R. J.; Signac, W.; Moran, N.; Keyes, T. E. *Chem. Commun* **2008**, 5307-5309.
- (25) Charles, D. E.; Lawrence, D. M.; Royce, W. M.; Thomas, J. M. *Inorg. Chem* **1983**, 22, 1283-1291.
- (26) Sullivan, B. P.; Salmon, D. J.; Meyer, T. J. *Inorg. Chem.* **1978**, 17, 3334-3341.
- (27) Bodige, S.; MacDonnell, F. M. *Tetrahedron Lett.* **1997**, 38, 8159-8160.
- (28) Kunishima, M.; Kawachi, C.; Monta, J.; Terao, K.; Iwasaki, F.; Tani, S. *Tetrahedron* **1999**, 55, 13159-13170.
- (29) Hughes, H. P.; Martin, D.; Bell, S.; McGarvey, J. J.; Vos, J. G., *Inorg. Chem* **1993**, 32, 4402-4408.
- (30) Pickup, P. G.; Osteryoung, R. A., *Inorg. Chem.* **1985**, 24, 2707-2712.
- (31) Dennany, L. Electrochemiluminescent & amperometric detection of DNA & DNA damage, Dublin City University, Dublin, 2004.
- (32) Li, C.; Hatano, T.; Takeuchi, M.; Shinkai, S. *Tetrahedron* **2004**, 60, 8037-8041.

- (33) Bock, C. R.; Connor, J. A.; Gutierrez, A. R.; Meyer, T. J.; Whitten, D. G.; Sullivan, B. P.; Nagle, J. K. *J. Am. Chem. Soc.* **1979**, *101*, 4815-4824.
- (34) Kanoufi, F.; Bard, A. J. *J. Phys. Chem. B* **1999**, *103*, 10469-10480.
- (35) Lu, M.; Whang, C. *Anal. Chim. Acta* **2004**, *522*, 25-33.
- (36) Rodgers, B. Potentials of common reference electrodes. <http://www.consultrsr.com/resources/ref/refpotls.htm> (accessed 10 april, 2010).
- (37) Brett, C. M. A.; Brett, A. M. O., In *Electrochemistry: Principles, methods and applications*; Oxford University Press Inc: NewYork, 1993; pp 427.
- (38) Osteryoung, R. A; Pickup, P. G., *Inorg. Chem.* **1984**, *24*, 2707-2712.
- (39) Belanger, S.; Stevenson, K. J.; Mudakha, S. A.; Hupp, J. T. *Langmuir* **1999**, *15*, 837-843.
- (40) Gregori, I.; Bedioui, F.; Devynck, J., *J. Electroanal. Chem* **1987**, *238*, 197-214.
- (41) Bard, A. J.; Faulkner, L. R., In *Electrochemical responses of adsorbed monolayers*; Electrochemical methods: Fundamentals and applications; John Wiley & Sons Inc: New York, 1980; pp 718.
- (42) Pinter, J. S.; Brown, K. L.; DeYoung, P. A.; Peaslee, G. F. *Talanta* **2007**, *71*, 1219-1225.

CHAPTER III

FABRICATION AND CHARACTERIZATION OF SUBSTRATES

3.1 INTRODUCTION

This chapter deals with the immobilization of ECL luminophores and biomolecules onto the surface of electrodes. The sensitive detection of proteins is critical in diagnostics and the transduction platform therefore plays a vital role.¹ Various immobilization techniques like drop / spin casting,¹ Langmuir-Blodgett,^{2,3} electropolymerization⁴⁻⁸ and self assembly exist.^{9,10,11,12} The following chapter deals with three such techniques *i.e.*, electropolymerization, drop casting and self assembly.

The immobilization of ECL reagents onto conducting substrates eliminates several disadvantages associated with solution phase detection including loss of signal due to diffusion of reagent out of the detection zone, high reagent consumption and limited ability to continuously cycle an individual luminophore.¹³

The method of forming the polymer films is a significant factor to bear in mind when considering them for different applications like immobilization of bio-components. Techniques like solvent evaporation and spin coating,¹⁴ though widely used to deposit polymer films on electrode surfaces, often do not produce homogeneous coatings. They may not possess good reproducibility in layer thickness and three-dimensional structure. Other techniques like Langmuir-Blodgett and electrostatic assembly on the other hand are associated with poor mechanical and thermal stability and substantial interpenetration.¹⁵

Dennany and co-workers¹⁶ have shown that drop casting of the ECL luminophore, $[\text{Ru}(\text{bpy})_2\text{PVP}_{10}]^{2+}$, increases the overall efficiency of the ECL reaction by four times when compared to the same material in solution. Hence, this technique has been employed in this chapter to create $[\text{Ru}(\text{bpy})_2\text{PVP}_{10}]^{2+}$ film electrodes for potential modulated ECL reported in Chapter 5.

One of the major challenges in designing biosensor platforms faced by many researchers today is the establishment of good electrical communication between the biomolecule and the sensor surface. The various characteristics of CNT make them excellent candidates to overcome this issue.¹⁷⁻¹⁹ They are conducting and can be derivatized with functional groups for the attachment of

biomolecules and they have a very high surface area to weight ratio ($\sim 300 \text{ m}^2 \text{ g}^{-1}$) which is accessible for both electrochemistry and surface immobilization.²⁰ The method for self assembling of SWCNTs in the form of vertically aligned forests is described herein. The nanotubes have been derivatized with carboxyl groups which were used to covalently link primary antibodies to give a functionalized surface for performing immunoassays. The performance of this assay is reported in Chapter 6.

3.2 EXPERIMENTAL

3.2.1 Apparatus

Electrochemical measurements were carried out with a CH instruments, model 660 potentiostat. Cyclic voltammetry was conducted using a typical three-electrode cell.

Impedance spectroscopy was performed using conventional three electrode cell and CH instruments, model 760B potentiostat. An excitation signal of 60 mV (peak amplitude) was applied to the electrodes and the frequency of the signal was varied between 1 mHz -100 kHz.

An aqueous Ag/AgCl/saturated KCl (3M) electrode (0.21 V vs. NHE)²¹ was used as reference for electrochemical measurements with a platinum wire counter electrode. All solutions were deaerated for 20 minutes by purging with nitrogen prior to electrochemical experimentation. All potentials are quoted versus Ag/AgCl reference electrode, and all measurements were made at room temperature.

Profilometry was performed using Dektak stylus surface profiler with a stylus tip radius of 12.5 μm . The stylus was on precision balanced cantilever coupled to a highly sensitive and repeatable Linear Variable Differential Transformer (LVDT). The Dektak has a vertical range of 25 Å to 2620 Å and a vertical resolution of 1 Å. The horizontal scan length range was 50 μm to 200 mm and the horizontal scan resolution was 775 pm.

Absorbance spectra were recorded on a Shimadzu UV-Vis-NIR 3100 spectrophotometer and emission spectra on a Perkin-Elmer LS50-B spectrophotometer using 1 cm optical path length quartz cuvette.

Resonance Raman spectra were recorded on a HORIBA Jobin-Yvon Labram HR 2000 confocal Raman microscope. Vertically aligned SWCNT forests were assembled on Si wafers for resonance Raman spectroscopy and AFM. A Helium-Neon laser was used to excite at 633 nm. The laser was focused onto the silica wafer using a 10x objective.

Atomic force microscopy was performed on NANOSCOPE IIIa /Dimensions 3100 microscope at National University of Ireland Galway (NUIG) and on Digital Instrument Bioscope II with a Nanoscope 7.30 controller operating in air. AFM images were taken in tapping mode configuration with a commercial non-conductive silicone nitride cantilever tip.

Field emission scanning electron microscopy (FSEM) was performed on a Hitachi 5500, magnification x 1000 k and resolution 0.5 nm. Image analysis was carried out using Image J version 1.37d image analysis software.

Transmission electron microscopy was performed using Hitachi H-7500 transmission electron microscope. Image analysis was carried out using Image J version 1.37d image analysis software.

Ink jet printing was done on Dimatrix DMP-2811 inkjet deposition system located in the National Center for Sensor Research (NCSR), research laboratory of Dr. Tony Killard. The Dimatrix DMP-2811 inkjet deposition system has 16 nozzles with 254 μm nozzle spacing, single row and drop volume of 10 pL. Squares of $1 \times 1 \text{ cm}^2$ were printed with a printing resolution of 40 μm , angle 9.1° .

3.2.2 Materials

$[\text{Ru}(\text{bpy})_2(\text{PVP})_{10}]^{2+}$ was synthesised within the group as described in Chapter 2, Section 2.3.1.3. Single walled carbon nanotubes (SWCNT-HiPco) were obtained from Prof. James F. Rusling's group (University of Connecticut) and carboxyl functionalized as described in Section 3.3.3. Silver-filled conductive epoxy and epoxy adhesive, Araldite Rapid, was purchased from Radionics. $0.8\ \mu\text{m}$ NH_2 functionalized silica microspheres were purchased from Bangs Laboratories, Inc. G1.5 acid terminated PAMAM dendrimers were purchased from Sigma-Aldrich. All chemicals and solvents were purchased from Sigma Aldrich and were of analytical grade. All solutions were made using deionized water purified with a Milli-Q plus 18.5 $\text{M}\Omega$ Millipore installation. The solvents used for spectroscopic measurements were of HPLC grade.

3.3 RESULTS AND DISCUSSIONS

3.3.1 $[\text{Ru}(\text{bpy})_2(\text{PVP})_{10}]^{2+}$ film electrode: Preparation and Characterization

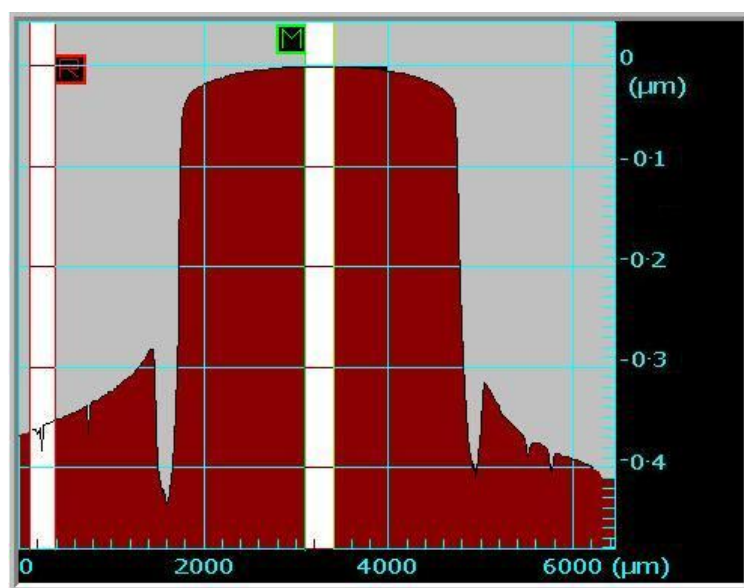
In order to form $[\text{Ru}(\text{bpy})_2(\text{PVP})_{10}]^{2+}$ films, glassy carbon electrodes were first polished with an aqueous slurry of $0.3\ \mu\text{m}$ alumina for 10 minutes, rinsed thoroughly with deionized water and then polished again for 10 minutes with $0.05\ \mu\text{m}$ alumina. After polishing, the electrodes were thoroughly rinsed, first with deionized water and then with acetone to remove all traces of alumina from the surface and dried under a nitrogen stream. A 1% (w/v) metallopolymer solution was prepared by dissolving 1 mg of polymer in 1 mL ethanol/DMF mixture (1:1; ethanol: DMF). A 50 μL drop of this 1% (w/v) metallopolymer solution was drop casted onto

the cleaned and polished electrode surface. These electrodes were then allowed to dry in the dark for 10-12 hrs.

3.3.1.1 Film thickness by profilometry

The film thickness was calculated using profilometry and it is as shown in Figure 3.1. It was found that the films were not uniform with the film thickness being larger towards the centre of the electrode. Hence, measurements were averaged over 5 different films and in all cases similar profiles were observed.

(A)



(B)

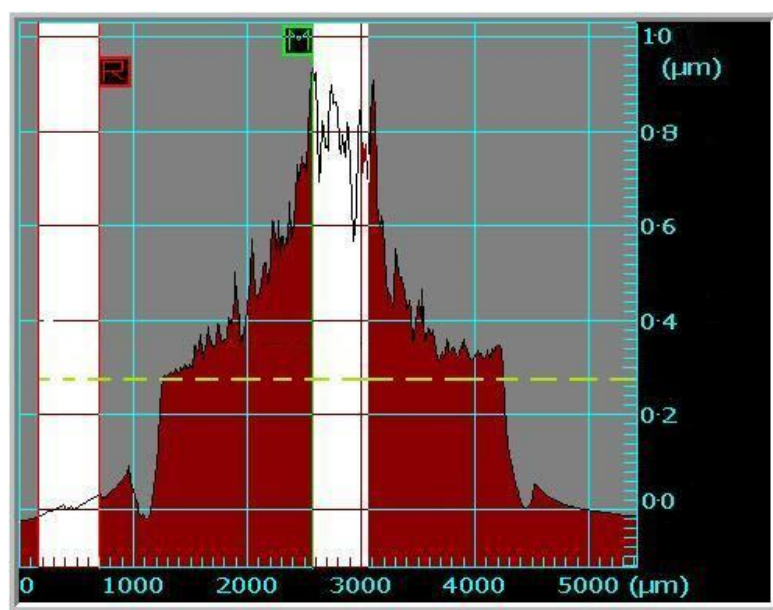


Figure 3.1: Profilometry measurement of a bare glassy carbon electrode (A) and the same glassy carbon electrode following evaporation to dryness of a 50 μL drop of 1% (w/v) $[\text{Ru}(\text{bpy})_2(\text{PVP})_{10}]^{2+}$ in 1:1; Ethanol: DMF mixture (B). The electrode radius is 1.5 mm.

The average thickness, ϕ , of the ruthenium films was found to be (0.8 ± 0.2) μm . It has to be noted that the thickness reported here is the dry thickness of the polymer film. It has already been reported by many researchers^{16, 22} that when these PVP systems are dipped in electrolyte, they tend to swell and the thickness during the experiment is significantly different, up to several hundred fold when compared to dry thickness.

3.3.1.2 Cyclic voltammetry characterization

The surface coverage, Γ , was determined by graphical integration of the background-corrected cyclic voltammogram ($\nu = 1 \times 10^{-3}$ Vs^{-1}). Figure 3.2 illustrates the voltammetric behaviour of thin 1% (w/v) $[\text{Ru}(\text{bpy})_2(\text{PVP})_{10}]^{2+}$ films on glassy carbon electrodes of 3 mm diameter. The metallopolymer has a formal oxidation potential at 1.15 ± 0.01 V vs. Ag/AgCl/KCl (3 M). This agrees well with the formal oxidation potential reported for this compound earlier by Denanny *et.al.*²³ For all scan rates, the ratio of the anodic peak current to cathodic peak current was found to be unity. This implies electron transfer reaction is reversible. The CV exhibits several characteristics of surface bound redox species.²⁴ The peak to peak separation between anodic and cathodic curve was found to be 0.02 V which is very close to zero, as expected for surface confined species.²⁴ The full width at half maximum (FWHM) is 95 ± 3 mV which is close to the theoretical value of 90.6 mV expected for a reaction involving the transfer of single electron. The ruthenium PVP film shows electrochemical characteristics similar to ones reported earlier by Hogan and co-workers¹² for this compound in H_2SO_4 . The surface coverage, Γ , was determined using Equation 1.20.

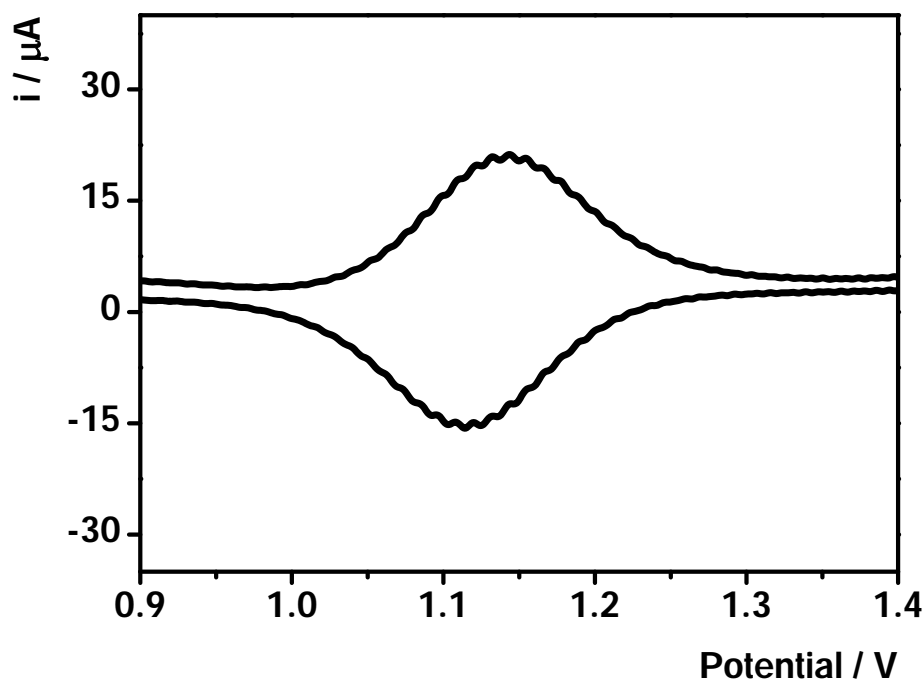


Figure 3.2: Cyclic voltammogram of a 3 mm diameter glassy carbon electrode following modification with a thin film of $[\text{Ru}(\text{bpy})_2(\text{PVP})_{10}]^{2+}$. The film was formed with a 50 μL drop of 1% (w/v) $[\text{Ru}(\text{bpy})_2(\text{PVP})_{10}]^{2+}$ in 1:1; Ethanol: DMF mixture. The scan rate was $1 \times 10^{-3} \text{ V s}^{-1}$ and the electrolyte used was 0.1 M aqueous LiClO_4 , and the surface coverage is $4.39 \pm 0.06 \times 10^{-8} \text{ mol cm}^{-2}$.

The surface coverage, Γ , was calculated to be $(4.39 \pm 0.06) \times 10^{-8} \text{ mol cm}^{-2}$. This value compares very well with that reported in literature.¹²

From the thickness and surface coverage measurements, the approximate concentration of ruthenium sites was found to be 0.55 M. This is slightly lower than that reported the literature (0.8 M) for this compound by Hogan *et.al.*¹²

At sufficiently slow scan rates, all electroactive centers undergo redox transformations on the experimental time-scale, and the redox composition of the film is in thermodynamic equilibrium with the electrode potential. The film is then said to be under finite diffusion condition and a plot of scan rate vs. peak current will be linear.

However, at higher scan rates the term $D_{CT}t/d^2$ (where D_{CT} is the charge transfer diffusion coefficient, t is the experimental time scale and d is the polymer layer thickness) will be far less than unity. This is referred to as semi-infinite diffusion condition and the peak current varies linearly with the square root of the scan rate. Figure 3.3 shows the scan rate dependence of the voltammetric response of $[Ru(bpy)_2(PVP)_{10}]^{2+}$ film. Table 3.1 gives the peak currents at different scan rates for the ruthenium film. The inset shows that the peak current varies linearly with the square root of the scan rate and therefore the response is dominated by semi-infinite diffusion. This response can be analyzed using Randles-Sevcik equation, Equation 1.21.

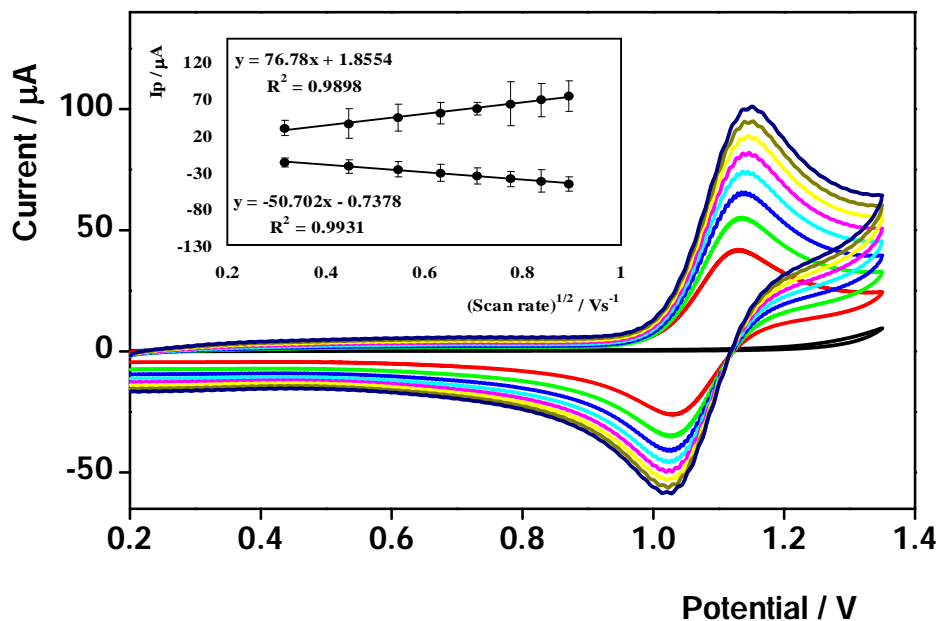


Figure 3.3: Scan rate dependence of the voltammetric response for a thin film of $[\text{Ru}(\text{bpy})_2(\text{PVP})_{10}]^{2+}$ (0.55 M) obtained by drop casting 50 μL of 1% (w/v) polymer in 1:1 DMF: Ethanol mixture on a 3 mm diameter glassy carbon electrode. The inset shows peak current dependence vs. root of scan rate. The CV was performed in PBS buffer (pH 7), with blank GCE (—), and $[\text{Ru}(\text{bpy})_2(\text{PVP})_{10}]^{2+}$ film, coloured lines, at different scan rates *i.e.*, 0.1 (—), 0.2 (—), 0.3 (—), 0.4 (—), 0.5 (—), 0.6 (—), 0.7 (—) and 0.8 (—) Vs^{-1} . The surface coverage is $4.39 \pm 0.06 \times 10^{-8} \text{ mol cm}^{-2}$.

Table 3.1: Peak currents and standard errors for 50 μL drop of 1% (w/v) $[\text{Ru}(\text{bpy})_2(\text{PVP})_{10}]^{2+}$ film on a 3 mm diameter glassy carbon electrode, 0.1 M PBS buffer (pH 7). The surface coverage is $4.39 \pm 0.06 \times 10^{-8} \text{ mol cm}^{-2}$.

v / Vs^{-1}	$I_{\text{PA}} / \mu\text{A}$	$I_{\text{PC}} / \mu\text{A}$
0.1	28.8 ± 1.6	-17.9 ± 0.6
0.2	35.0 ± 2.0	-24.0 ± 0.9
0.3	43.0 ± 1.8	-27.0 ± 1.1
0.4	49.0 ± 1.5	-32.0 ± 1.2
0.5	55.0 ± 0.8	-36.0 ± 1.1
0.6	62.0 ± 3.0	-40.0 ± 1.0
0.7	67.0 ± 2.2	-43.0 ± 1.5
0.8	72.0 ± 2.0	-47.0 ± 0.9

The charge transport diffusion coefficient was calculated to be $(4.48 \pm 0.2) \times 10^{-11} \text{ cm}^2 \text{ s}^{-1}$ from cyclic voltammetry. Assuming no swelling of the polymer film, Equation 3.1 can be used in conjunction with the homogeneous charge transport diffusion coefficient of this film to calculate the time taken to fully oxidize this layer and regenerate the Ru^{3+} mediating centers. This was found to be around 26 s.

$$t = \frac{\varphi^2}{\pi D_{\text{CT}}} \quad 3.1$$

Hogan *et.al.*,¹² reported a value of 10 s for a 250 nm thick film in H_2SO_4 . It is known from earlier work²⁵ that when the pH of the contacting electrolyte is greater than ~ 3.5 , the mass transport through the PVP matrix is impeded due to the absence of swelling which is favoured at low pH due to the repulsive interactions between the protonated pyridines. However, significant impedance to mass transport through PVP is not observed in this case. The thickness of the film reported here is at least double the thickness of the film reported by Hogan

and co-workers.¹² Not surprisingly the time taken to fully oxidize this film is also roughly double the value of 10 s.

3.3.1.3 Impedance studies

Generally, drop cast films do not have very good adhesion to the electrode surface and tend to come off the surface.³⁴ Hence, in order to check the stability of the films and its adhesion properties, A.C. impedance studies were carried out in PBS buffer (pH 7) on the polymer film to investigate if the polymer film underwent any degradation due to the application of a sinusoidal potential. Potential modulation experiments on the film are reported in detail in Chapter 5.

As seen in Figure 3.4, a Bode plot of logarithm Z vs. logarithm of frequency depicts the various phases present when a potential is applied to the polymer modified electrode system under consideration. According to Hunter *et.al.*²⁶ for an electrode | conducting polymer | electrolyte arrangement the following regions in the impedance spectra, shown in Figure 3.5, can be expected. At high frequency charge transfer dominated behaviour is observed. The semicircle corresponds to the bulk resistance of the polymer layer in parallel to its geometric capacitance. The bulk resistance reflects the concentration and mobility of charge carriers in the conducting polymer.²⁷ This is referred to as kinetic control (K.C) in this report. At low frequencies diffusion of charge in the polymer film dominates and a diffusion limited region is observed.^{27,28} This is referred to as diffusion control (Diff.C). In Figure 3.4 a small region between the two regions, K.C and Diff.C, which probably represents a transition from one region to the other is also observed.

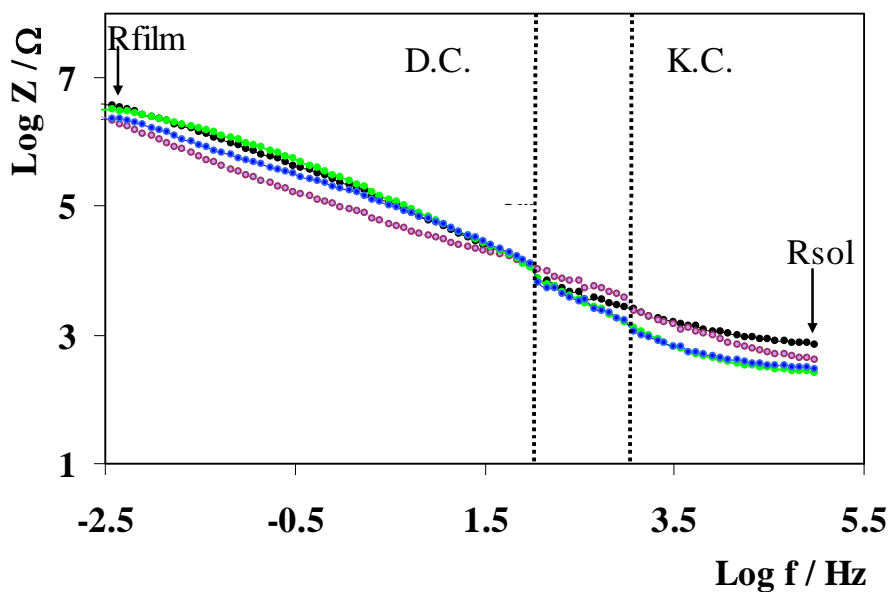


Figure 3.4: Bode plot recorded for $[\text{Ru}(\text{bpy})_2(\text{PVP})_{10}]^{2+}$ film $[\Gamma=(4.39\pm0.06)\times 10^{-8} \text{ molcm}^{-2}]$ on GCE with an A.C. sine modulation of 60 mV (peak amplitude), over a range of D.C. center potentials, 1.0 V (●), 1.08 V (●), 1.2 V (●) and 1.3 V (●) vs. Ag/AgCl, at frequency range of 1 mHz-100 KHz, in PBS buffer electrolyte (pH 7). The diffusion control (Diff.C) and kinetic control (K.C) have been separated with a dotted line.

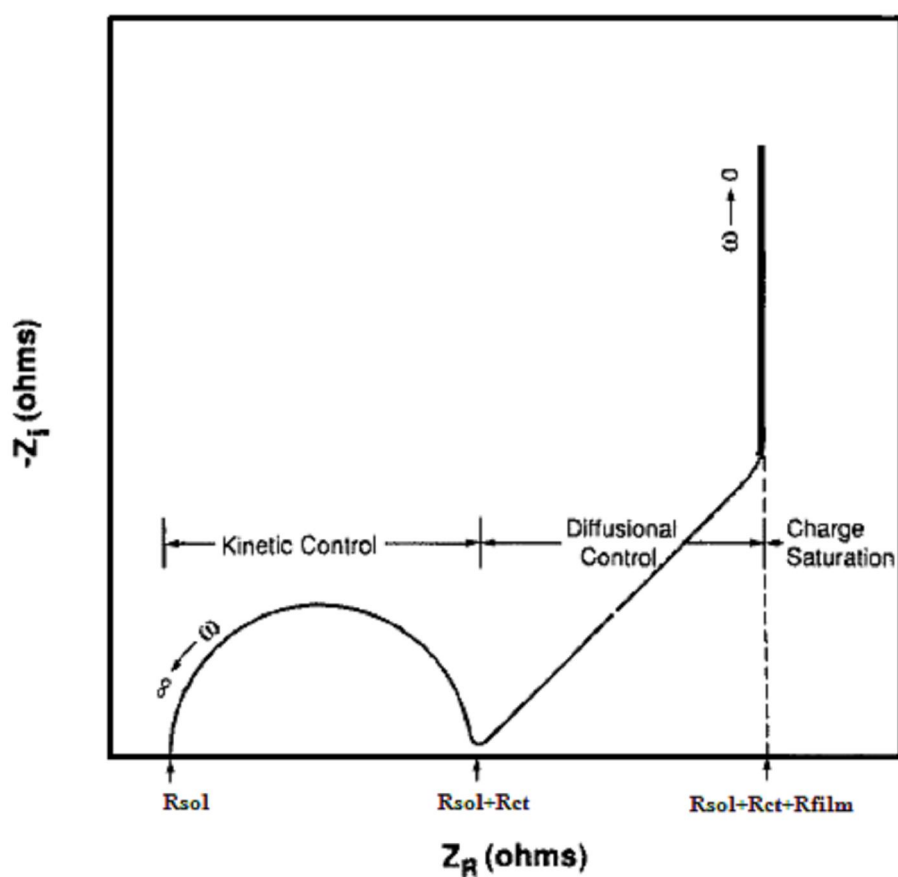


Figure 3.5: Ideal Nyquist plot of a redox polymer film. From Impedance analysis of poly vinyl ferrocene Hunter, T. B.; Tyler, P. S.; Smyrl, W. H.; White, H. S.; *Impedance analysis of poly(vinylferrocene) films*, J.Electrochem.Soc,1987, 134,9,2198-2204.

Fernandez-Sanchez and co-workers²⁸ have suggested a simple equivalent circuit, shown in Figure 3.6(a), which can satisfactorily describe a polymer coated transducer surface.

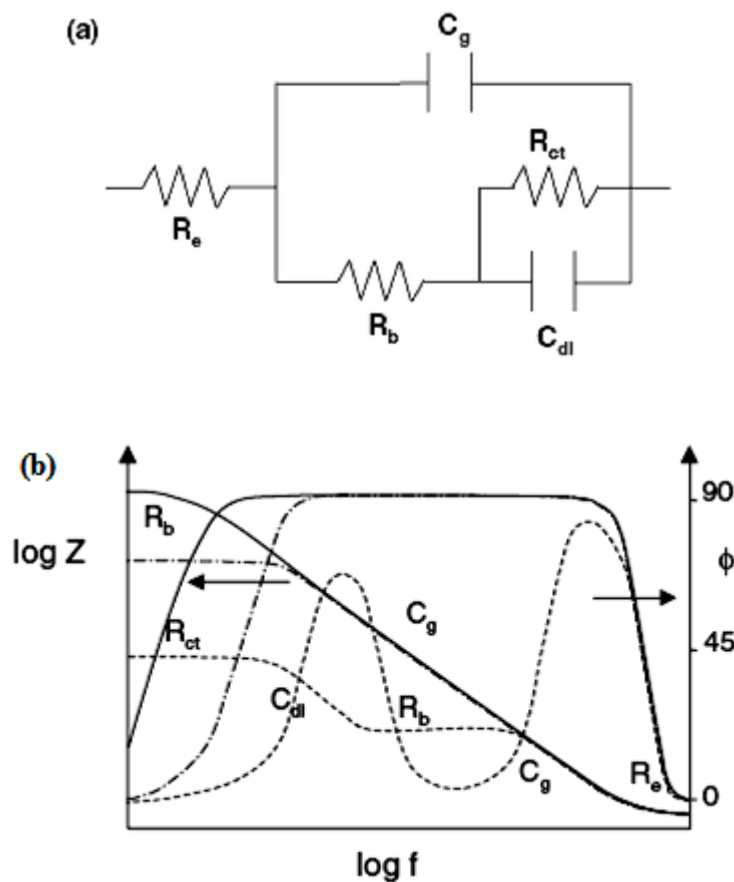


Figure 3.6: Equivalent circuit (a) that best describes the impedance behaviour of a polymer-coated transducer and its corresponding Bode Plot (c) where, C_g and R_b refer to capacitance and resistance of the film, R_{ct} is charge transfer resistance, C_{dl} is double layer capacitance and R_e is electrolyte resistance between working and reference electrodes. Reprinted from Fernandez-Sanchez, C.; McNeil, C.J.; Rawson, K.; *Electrochemical impedance spectroscopy study of polymer degradation: application to biosensor development*, Trends in Analytical Chemistry, 2005, 24, 1, pg 37-48.

The circuit described by Fernandez-Sanchez can be applied to the current situation and thus from the Bode plot, Figure 3.4, we can obtain film resistance (R_{FILM}) and film capacitance (C_{FILM})²⁸ values which are tabulated in Table 3.2. From the Table 3.2 it is seen that the R_{FILM} decreases with increasing potential but the C_{FILM} remains almost constant.

As already mentioned in the literature review, redox polymers like $[\text{Ru}(\text{bpy})_2\text{PVP}_{10}]^{2+}$ are characterized by the presence of specific spatially isolated electrochemically active sites. Electro-activity in these polymers is highly localized. They characteristically exhibit significant conductivity only over a very narrow potential range, with maximum conductivity occurring when the concentrations of the oxidized and reduced forms are equal in the film *i.e.*, at the formal potential, E^{or} , of the redox centres.²⁹ It is commonly held that redox conduction in polymers occurs by the electron hopping process proposed by Kaufman and co-workers^{30,31} whereby electron transfer proceeds as a process of sequential self-exchange steps between adjacent redox groups. In the polymer film where the total amount of redox species must be fixed (*i.e.*, $C_{\text{OX}} + C_{\text{RED}} = C_{\text{TOTAL}}$) the self-exchange rate will reach a maximum when the concentration of both species is equal, *i.e.*, $C_{\text{OX}} = C_{\text{RED}}$. Hence, maximum conductivity occurs at E^{or} . The sequential self-exchanges which give rise to the conductivity throughout the thickness of the film involves two processes. Charge injection at the polymer| electrode interface, (*i.e.*, at a distance of around 1 nm to the surface).³² This is a potential-driven process and conforms to Butler-Volmer kinetics.¹⁵ The second process is the percolation of charge through the film which is (to a first approximation) driven by concentration gradients and is quantifiable as a quasi-diffusional process.²⁹

As the applied potential is increased, the concentration of Ru^{3+} centers within the film also increases. Since electro-neutrality in the film must be maintained, the generation of charge at the electrode and the motion of the charge throughout the polymer is accompanied by the ingress and motion of charge compensating counter-ions into the film. As the conductivity of the film increases a reduction in the R_{FILM} is observed.

Delamination is one possible degradation pathway for a polymer-modified electrode.^{28,33} After application of high potential, the polymer-coated electrodes were removed from the cell and examined visually. It was observed that the polymer layer was still intact and present on the surface of the electrode. No significant reduction in the surface coverage (<2%) of polymer was detected. The electrolyte solution was also clear with no signs of polymer particles. Also,

had it been degradation of the polymer due to delamination, the capacitance of the electrode would increase due to decrease in thickness of the polymer film. The C_{FILM} values for the $[\text{Ru}(\text{bpy})_2(\text{PVP})_{10}]^{2+}$ film remains almost constant as seen in Table 3.2. Hence, degradation of the polymer layer by delamination can be excluded.

Table 3.2: Film resistance (R_{FILM}) and film capacitance (C_{FILM}) at different potentials, in diffusion control region of the Bode plot for 1% (w/v) $[\text{Ru}(\text{bpy})_2(\text{PVP})_{10}]^{2+}$ film ($\Gamma=(4.39 \pm 0.06) \times 10^{-8} \text{ molcm}^{-2}$) on a 3 mm diameter glassy carbon electrode, 0.1 M PBS buffer (pH 7).

Applied potential / V	$R_{\text{FILM}}/\text{M}\Omega$	$C_{\text{FILM}} / \mu\text{F}$
1.0	5.01 ± 0.01	0.51 ± 0.01
1.08	1.99 ± 0.01	0.54 ± 0.03
1.2	3.16 ± 0.04	0.51 ± 0.01
1.3	2.5 ± 0.03	0.47 ± 0.04

A decrease in R_{FILM} is also seen when pinholes are created in the polymer film and the depth of these pinholes increase in response to the applied perturbation. Failure of the polymer layer is observed when these pinholes become so deep that they reach the electrode surface causing the electrolyte to seep in and spread. This leads to detachment of the polymer layer from the surface of the electrode.²⁸ This can be confirmed by analysing the Bode and the Nyquist plots, Figure 3.7 and Figure 3.8 respectively, at lower applied potentials. The horizontal line observed in Figure 3.7 (1.0 V •) in the low frequency region represents the initial conductive pathway through the polymer layer.^{27,34} As the potential is increased to 1.2 V, we observe the horizontal line gradually disappears and further increase in potential leads to a peak formation. Similar change was observed by Armstrong *et.al.*,³⁵ for polyester films when they were exposed to UV radiation. The film degraded and failed due to pinholes.

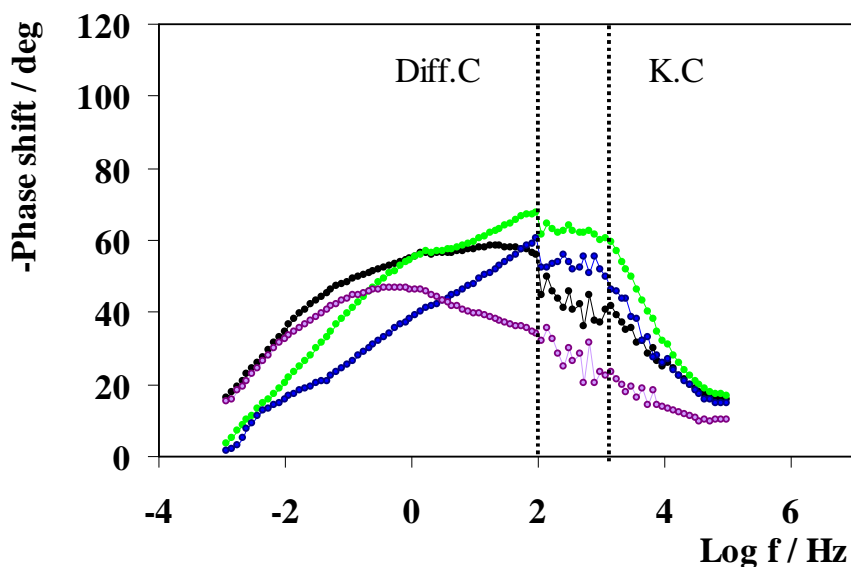


Figure 3.7: Bode plots recorded for 1% (w/v) $[\text{Ru}(\text{bpy})_2(\text{PVP})_{10}]^{2+}$ film $[\Gamma = (4.39 \pm 0.06) \times 10^{-8} \text{ mol cm}^{-2}]$ on GCE with an A.C. sine modulation of 60 mV (peak amplitude), over a range of D.C. center potentials, 1.0 V (●), 1.08 V (●), 1.2 V (●) and 1.3 V (●) vs. Ag/AgCl, at frequency range of 1 mHz-100 KHz, in pbs buffer electrolyte (pH 7). The diffusion control (Diff.C.) and kinetic control (K.C) have been separated with a dotted line.

However, the Bode plot does not give a definitive evidence of presence of pores. Therefore, examination of the Nyquist plot, Figure 3.8, is essential. With the increase in potential, there is no appearance of a second semicircle in the Nyquist plot. This second semicircle is seen only when there are pinholes in the film and the depth of these pinholes increases so much that it exposes the surface of the underlying electrode causing a new electrode | electrolyte interface to be identified.^{27,28}

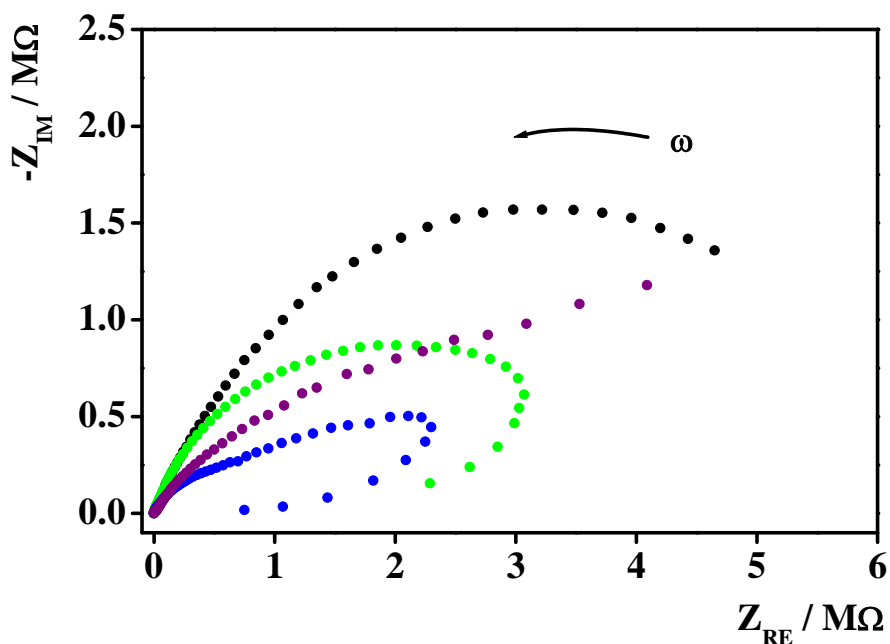


Figure 3.8: Impedance plane plots recorded for 1% (w/v) $[\text{Ru}(\text{bpy})_2(\text{PVP})_{10}]^{2+}$ film $[\Gamma=(4.39\pm0.06)\times 10^{-8} \text{ molcm}^{-2}]$ on GCE with an A.C. sine modulation of 60 mV (peak amplitude), over a range of D.C. center potentials, 1.0 V (●), 1.08 V (●), 1.2 V (●) and 1.3 V (●) vs. Ag/AgCl, at frequency range of 1 mHz-100 KHz, in PBS buffer electrolyte (pH 7).

Hence, from the two plots, Bode and Nyquist, it is clear that the $[\text{Ru}(\text{bpy})_2(\text{PVP})_{10}]^{2+}$ film ($\Gamma=(4.39\pm0.06)\times10^{-8} \text{ molcm}^{-2}$) shows high conductivity evidenced by the decrease in film resistance. Significantly, its structure allows for efficient penetration of the ions and solvent thereby improving the rates of charge transfer. Since the success of ECL sensors ultimately depends on high charge transfer rates, this would result in a tremendous increase not only in signal intensity but also improve the sensors sensitivity. Application of high over-potentials does not lead to the formation of a second semi-circle in the Nyquist plot. Thus, it can be confirmed that there is no breach in the continuity of the film and a new electrode|electrolyte interface is not formed. The

polymer layer remains intact and strongly attached to the electrode surface even at positive potentials.

3.3.2 Fabrication of ITO array electrode

Recent advances in genomics and proteonomics are due to the widespread application of microarray technology. A microarray is a tool for analyzing protein or gene expression. It basically consists of a small membrane or glass slide containing samples of many proteins or genes arranged in a regular pattern.³⁶ They allow screening of biologically important binding events in a parallel and high throughput fashion.³⁷ As most solid supports on which microarrays are built, are non-conductive, applications involving them are limited to fluorescence type assays. ECL on the other hand is an electrochemical, two channel detection method where both light and current signal can be measured simultaneously. This type of measurement enables one to separate current signal produced by interferences from that produced by analyte. The interferences may be capable of reducing the catalytic Ru^{3+} centers without creating the emitting Ru^{2+*} or they may quench the Ru^{2+*} centers by energy or electron transfer.²⁵ By detecting both light and current simultaneously better selectivity may be obtained. In order to perform electrochemical analysis, the solid support needs to be conductive. Indium tin oxide (ITO) films have been used widely due to their conductive and optically transparent characteristics.³⁸ This section describes the fabrication of vertically aligned, self-assembled, 25–75 nm long terminally carboxylated single-wall carbon nanotube (SWNT) forests on nafion and iron oxide decorated transparent ITO surfaces. These platforms have been used for ultrasensitive detection of proteins (IgG) by a novel approach using G1.5 acid terminated PAMAM dendrimers as size selective protein linkers. The performance of this ECL immunosensor is the topic of Chapter 6.

In order to form these platforms, ITO electrodes were cleaned by sonicating them first in deionised water for 20 minutes, then in acetone for 20 minutes followed by sonication in chloroform for 20 minutes.

Electrical contact was made to cleaned ITO slide (7.5 x 1 x 0.1) cm by fixing a copper wire to the conducting side of the ITO with commercially available silver-filled conductive epoxy. This was allowed to cure for 10 hrs. The contact was made waterproof by covering it with commercially available epoxy adhesive. Once cured, spots of self-assembled SWCNT arrays as shown in Figure 3.10 were formed on these electrodes as described in Section 3.3.4.

3.3.3 Functionalization of SWCNT

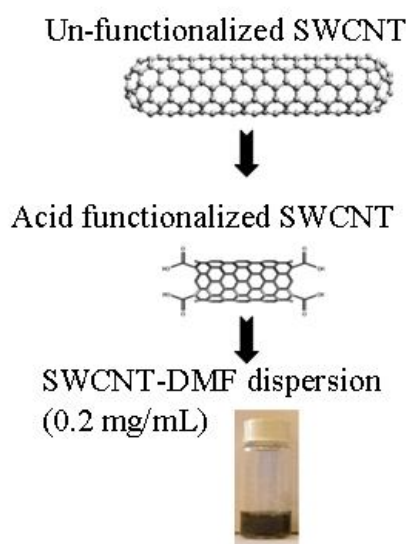
Commercially available SWCNTs were functionalized with carboxyl end groups according to a previously published procedure.³⁹ Briefly, 5 mg of SWCNT were weighed and taken up in 5 mL of 3: 1, HNO₃: H₂SO₄ and sonicated for 4 hrs at 70 °C.⁴⁰ These dispersions were filtered (Amicon Ultra-15, 30 kDa), centrifuged at 3220 rpm and washed with deionized water. The washing step was repeated until the pH of the filtrate was neutral. The sample was then dried and dispersed in a DMF suspension at 0.2 mg/mL and used after allowing this dispersion to stabilize for a week.

3.3.4 Fabrication and characterization of SWCNT-ITO array sensors

Carboxyl functionalized SWCNT dispersions which were produced as described above, were used to form SWCNT forest assemblies on ITO array electrodes. A two well silicone separator containing 3 mm diameter wells was used as a mask to form SWCNT array spots. The silicone separator was pressed tightly against the ITO electrode to form a waterproof seal such that there was no intermixing of liquids. 200 µL drop of nafion solution (1 mg/mL (9:1; methanol: water)) was dropped into each well and allowed to stand for 30 min. Care was taken to avoid complete drying of the any solution placed in the well by covering the electrode with a wetted petridish. The nafion layer results in the formation of a uniform negatively charged spot.⁴⁰ These spots were then washed with deionized water and 200 µL of aqueous FeCl₃ solution (pH 1.7) was dropped onto the nafion layer and allowed to stand for 15 min. After 15 min the spots

were washed in aqueous HCl ($\text{pH} < 4$) to remove loosely bound Fe^{3+} ions, followed by a quick wash in DMF to remove excess water. The HCl and DMF wash facilitate the transformation of Fe^{3+} ions into their basic hydroxide form. This is then followed by dropping 200 μL of aged SWCNT dispersions in DMF (0.2 mg/mL) prepared earlier. The solution was allowed to stand for 4 hrs followed by washing with methanol and air drying. An overall scheme describing the various steps followed in the fabrication of SWCNT-ITO array electrode is as shown in Figure 3.9.

Functionalisation of SWCNT



Assembly of SWCNT-ITO array electrode

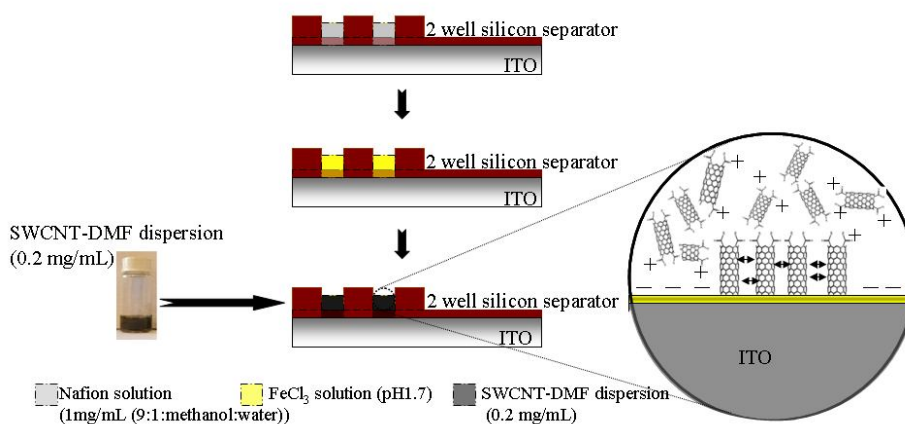


Figure 3.9: Schematic showing the various steps followed in the fabrication of SWCNT-ITO array electrode.

It has been reported^{40,41} that the initial driving force for the formation of vertically aligned SWNT forests originates from acid–base neutralization between one of the two COOH ends of the SWNT with basic $\text{Fe}(\text{OH})^{x+}_{3-x}$ ($x = 1, 2$ and 3) domains. The iron oxide domains are formed by the slow precipitation on nafion-adsorbed Fe^{3+} ions involving trace amounts of water during the DMF washing step. Figure 3.10 shows an image of the drop casted SWCNT-ITO array electrode after air drying.

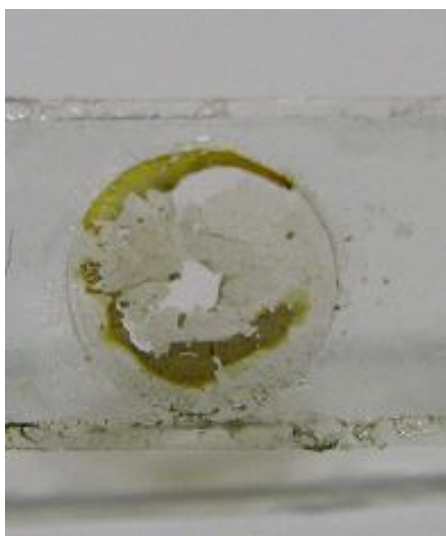


Figure 3.10: Digital image of drop casted ITO electrode with vertically aligned SWCNT forests. Spot size is 3 mm in diameter.

It can be seen that this technique yields a very patchy and uneven SWCNT forest coverage. The total number of active acid sites present on the SWCNT-ITO array can be electrochemically determined by forming amide bonds between NH_2 terminated $[\text{Ru}(\text{bpy})_2\text{PICNH}_2]^{2+}$ dye and the COOH ends of the SWCNT-ITO array electrode. Conventional NHS-EDC coupling chemistry was used to covalently bind NH_2 terminated $[\text{Ru}(\text{bpy})_2\text{PICNH}_2]^{2+}$ to the COOH ends of the SWCNT-ITO array electrode. After coupling, the SWCNT-ITO electrode was washed thoroughly with deionized water to remove physisorbed ruthenium pic complex. Cyclic voltammetry was then performed on this ITO sensor and is as shown in Figure 3.12. The voltammograms show large currents from which we can infer that the SWCNT have good electronic communication with the ITO surface. The total amount of coupled dye for drop casted electrode was

determined by integrating the area under the cyclic voltammogram peak at 1.3 V, Figure 3.12, and substituting appropriate values in Equation 1.20. This is one of the methods of directly calculating the total number of acid sites that are available for covalent coupling to protein on the surface of the SWCNT-ITO. Alternatively, ruthenium labelled antibody could also be used along with NHS-EDC coupling chemistry. But, the former approach avoids complications due to nonspecific binding of antibodies on the glass surface and hence, was chosen as a more accurate technique.

With the drop cast electrodes, the total number of carboxyl sites involved in the covalent coupling with anti-IgG was found to be $(10.8 \pm 5.8) \times 10^{-10} \text{ molcm}^{-2}$. The huge error of $\pm 6 \times 10^{-10} \text{ molcm}^{-2}$ indicates that the surface area varies a lot and hence, in order to have more precise control over the vertically aligned nanotube forest assembly, inkjet printing was tried.

Inkjet printing technology is gaining popularity in the formation of micro patterned surfaces for the development of biosensors,⁴² DNA arrays,³⁷ and protein sensor electrodes.⁴³ It is a form of non contact deposition technique which is highly attractive due to its simplicity, precision and commercial ability. Significantly, it allows very small volume droplets *i.e.*, 2-12 picoL, to be deposited on virtually any flat surface with high precision and reproducibility. A high degree of resolution of 1200 drops per inch (dpi) with a mean dot diameter of about 15-40 μm can be achieved.⁴² Also, as there is no physical contact between the print head and the printed support, spraying nanotubes could enable self assembly of vertically aligned SWCNT.

Ink jet printing was performed on ITO slides instead of the layer-by-layer technique. First the ITO was placed in marked locations on a graduated printer stage and 15 layers of nafion solution were printed on them. The ITO was then removed and washed with deionized water and placed back in the exact same position as before. 15 layers of FeCl_3 were then printed on their surface followed by washing with HCl and DMF. Finally 8 layers of nanotube dispersion were printed (0.2 mg/mL). The ITO slides were then removed and washed with methanol and air dried. This technique resulted in uniform and precise pattern as shown in Figure 3.11.



Figure 3.11: Digital image of inkjet printed ITO electrode with vertically aligned SWCNT forests. Square size is $1 \times 1 \text{ cm}^2$, $40 \text{ }\mu\text{m}$ resolution with an angle of 9.1° .

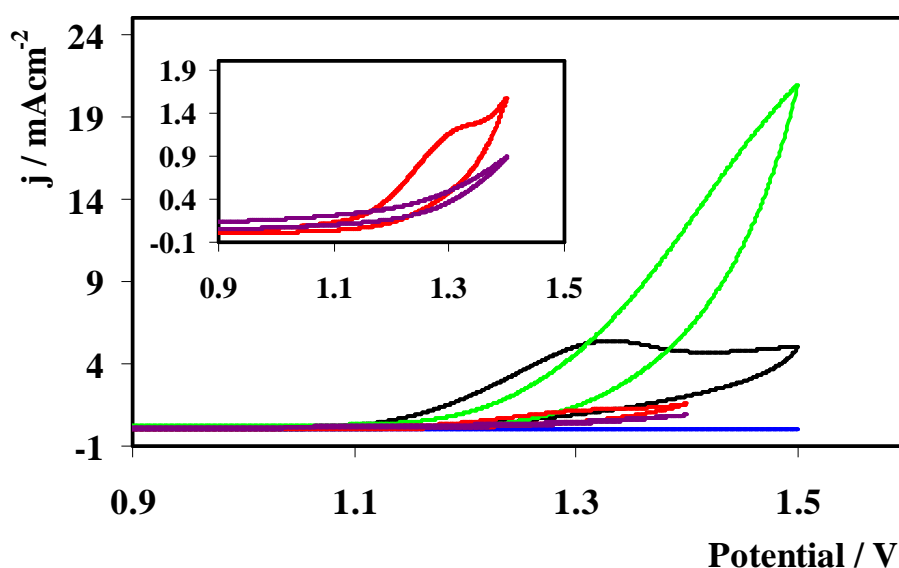


Figure 3.12: Cyclic voltammetry of drop casted ITO (—) and inkjet printed (—) vertically aligned SWCNT forests covalently bound to $[\text{Ru}(\text{bpy})_2\text{PICNH}_2]^{2+}$. Uncoupled SWCNT forests for drop coated (—) and inkjet printed (—) ITO and bare ITO (—) are also shown. The inset gives an enlarged view of drop casted SWCNT forests with and without $[\text{Ru}(\text{bpy})_2\text{PICNH}_2]^{2+}$. 0.01 M PBS buffer ($\text{pH } 7$) was used as supporting electrolyte with 0.002 Vs^{-1} scan speed.

Significantly, ITO electrodes with inkjet printed SWCNTs had three orders of magnitude higher active acid sites. For inkjet printed ITOs, surface coverage of covalently coupled $[\text{Ru}(\text{bpy})_2\text{PICNH}_2]^{2+}$ dye was found to be $(1.82 \pm 0.03) \times 10^{-6} \text{ mol cm}^{-2}$.

Commercial SWCNT are often synthesised⁴⁴ in the form of entangled bundles with a diameter distribution of 0.8-1.3 nm as seen in Figure 3.13. The lengths of these bundles are typically in micrometers as seen in Figure 3.15. For applications in biosensors,¹⁸ short and discrete nanotubes are required and hence, the nanotubes are usually subjected to solution-phase chemical oxidation techniques like the one mentioned in Section 3.3.3. This technique not only enables shortening of nanotubes but also improves its solubility and functionalizes the ends of nanotubes with carboxyl groups. Liu. *et.al.*,⁴⁵ suggested that oxidative shortening takes place via a two step mechanism. The first being the introduction of sidewall damage followed by cutting at damaged sites. A later work by Ziegler *et.al.*,⁴⁶ suggested that during oxidative shortening the tubes are consumed from the ends. Though the exact mechanism of tube shortening is unclear it is important to quantitatively determine the dimensions of SWCNT after oxidative treatment. Raman spectroscopy is one of the most powerful tools to characterize carbon nanotubes without sample preparation.⁴⁷

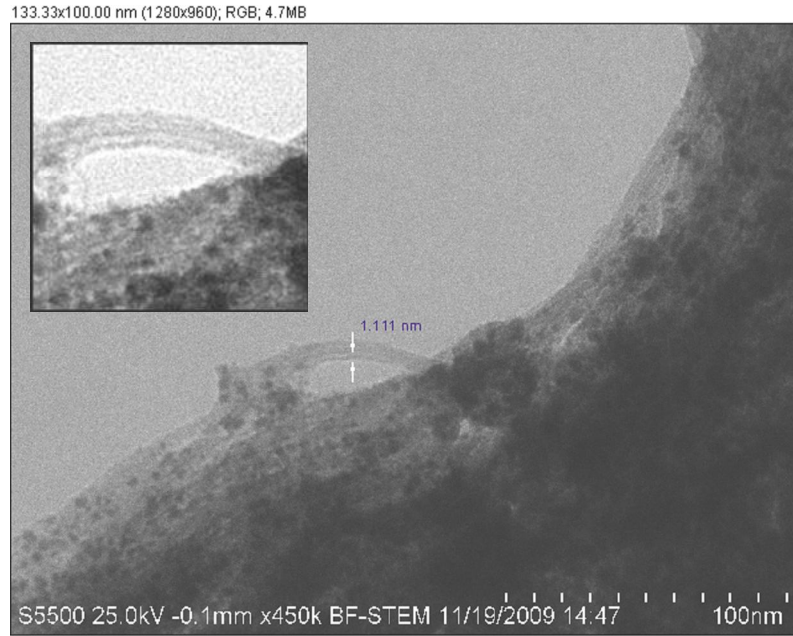


Figure 3.13: Field emission SEM image of drop casted pristine SWCNT (0.2 mg/mL suspension in deionized water) on Si wafer. White arrows show the diameter of one single nanotube. The diameter was determined using Image J version 1.37d image analysis software. The inset shows a zoomed-in image of 3 individual single walled carbon nanotubes.

Figure 3.14 shows the resonance Raman spectra of pristine and cut and functionalized SWCNT (0.2 mg/mL suspension in DMF). The diameter of the nanotubes can be determined from the radial breathing modes (RBM) present in the Raman spectra by applying Equation 3.2.⁴⁷ The RBM usually lies in the frequency range of 100-300 cm^{-1} and strongly depends on the nanotube diameter (d). Its resonance effects are due to semi-conducting and metallic behaviour of the SWCNT.⁴⁷

$$\omega_{\text{RBM}} = \frac{A}{d} + B \quad 3.2$$

where, A and B are determined experimentally. For SWCNT bundles with tube/tube interactions Milnera *et.al.*,⁴⁸ obtained a value of $A=234 \text{ nmcm}^{-1}$ and $B= 10 \text{ cm}^{-1}$. In this study it is assumed that pristine, cut and self assembled SWCNT all experience tube/tube interactions and hence, the values estimated by

Milnera *et.al.*,⁴⁸ apply. Table 3.3 gives the calculated diameter values for RBM for pristine and cut nanotubes.

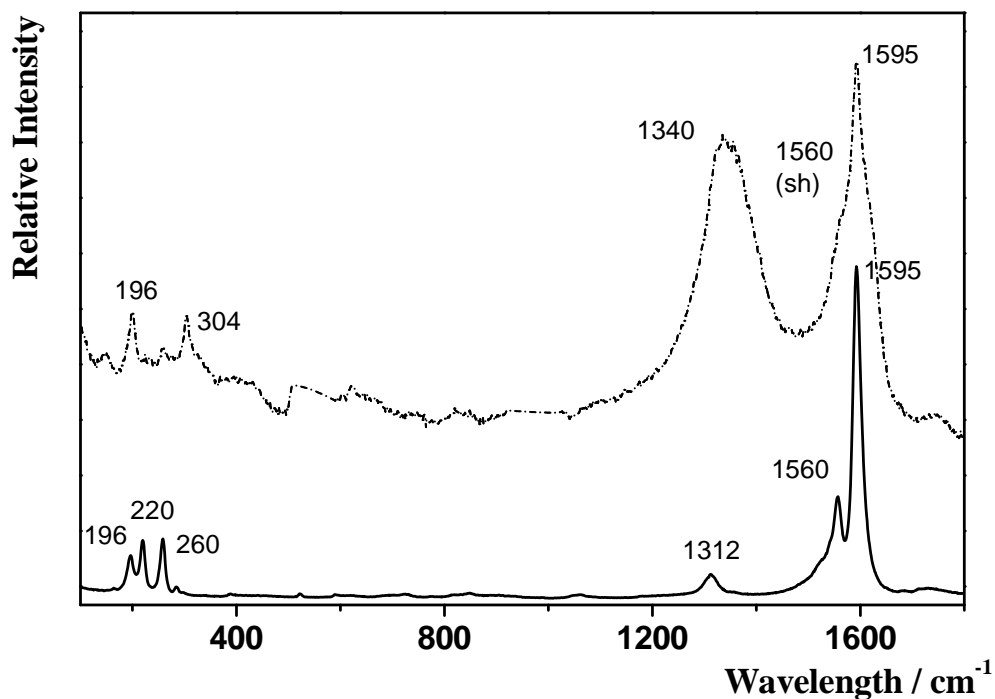


Figure 3.14: Resonance Raman spectra of pristine SWCNT (0.2 mg/mL suspension in DMF, —), cut and functionalized SWCNT (0.2 mg/mL suspension in DMF, ----) drop cast on a Si wafer. The samples were irradiated using laser excitation at 633 nm, 10x objective. The relative intensity has been offset for clarity.

Table 3.3: Calculated diameters of pristine and cut and functionalized SWCNT.

Pristine SWCNT		Cut SWCNT	
RBM/ cm^{-1}	d / nm	RBM/ cm^{-1}	d / nm
196	1.26 \pm 0.03	196	1.26 \pm 0.07
220	1.12 \pm 0.01	304	0.79 \pm 0.3
260	0.94 \pm 0.04	—	—
Average	1.11	Average	1.03

The spectra in Figure 3.14 show the presence of radial breathing modes for nanotubes after oxidative treatment. This observation confirms that the oxidation procedure does not comprehensively destroy the nanotube structure. The spectrum also contains tangential graphite like mode (TM) characteristic of SWCNTs⁴⁷ and observed in the frequency range of 1450- 1700 cm^{-1} . The presence of G band in the spectrum of cut tubes at 1560 (sh) cm^{-1} and 1595 cm^{-1} also suggests that intact nanotubes are present in the sample.⁴⁹ From the Table 3.3, an average diameter of 1.11 nm is obtained for pristine and 1.03 nm for cut and functionalized SWCNT. No significant change in the diameter of the tubes is observed and hence, it can be assumed that the oxidative shortening takes place via the two step mechanism suggested by Liu *et.al.*⁴⁵

The D band or the defect band is typically observed between 1250 and 1450 cm^{-1} and originates from the first order scattering by in-plane hetero-atoms, grain boundaries, vacancies or other defects.³⁹ The cut and functionalized SWCNT show large D: G ratio compared to pristine SWCNT suggesting that there is a substantial increase in the number of defects after oxidation.

The nature of the TM peaks at 1560 (sh) cm^{-1} and 1595 cm^{-1} after oxidation provides information about the electronic structure of the tubes. A strong peak

for cut tubes at 1595 cm^{-1} suggests that the cut tubes are predominantly semi-conducting.⁵⁰ The appearance of a shoulder at 1560 cm^{-1} suggests that there is also a weak contribution from metallic tubes.⁵¹

Having determined the diameter of the nanotubes using Resonance Raman spectroscopy, the length of the SWCNT after oxidative treatment can be determined from TEM images using IMAGEJ software and the length contours of cut SWCNT were individually traced as shown in Figure 3.16 and measured. Figure 3.17 shows the histogram of all the nanotubes measured. From the histogram it is evident that the majority of the nanotubes are around 25-75 nm in length.

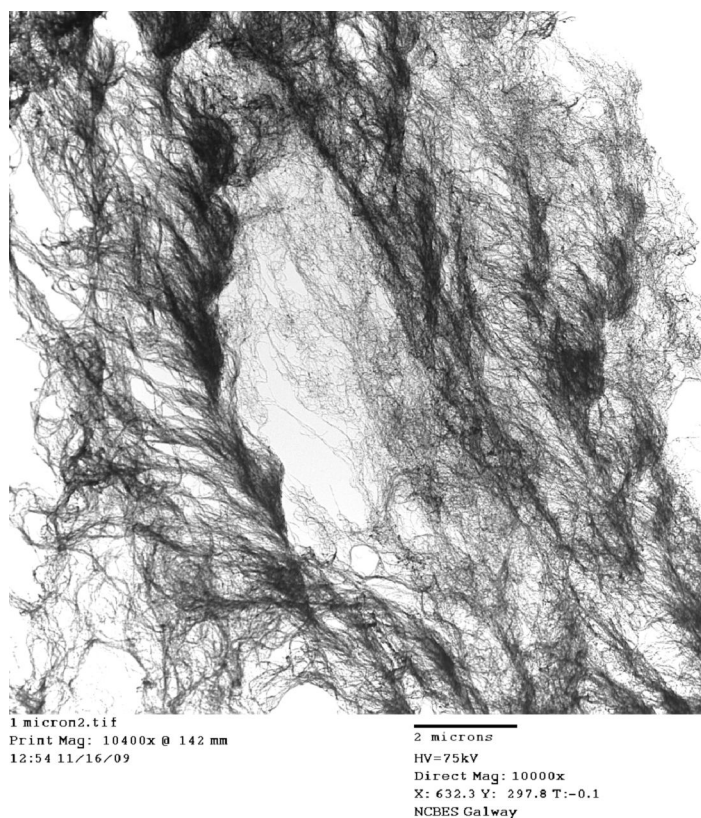


Figure 3.15: TEM image of pristine un-functionalized SWCNT.

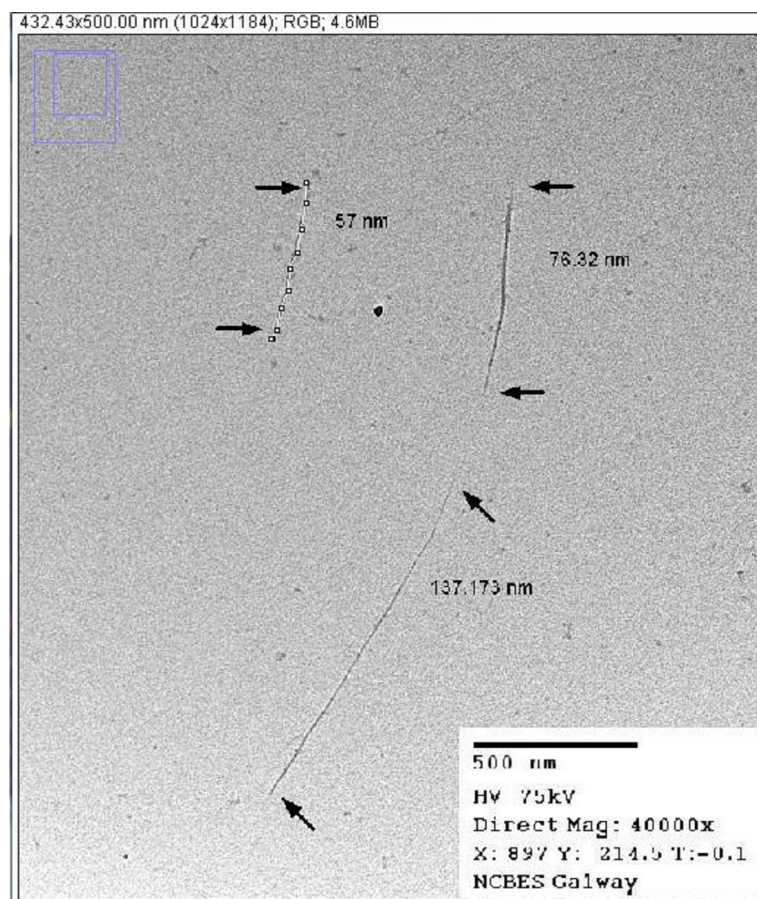


Figure 3.16: TEM image of cut and COOH functionalized SWCNT after oxidative shortening of commercial SWCNT in 3: 1, HNO₃: H₂SO₄ for 4 hrs at 70 °C. Black arrows show the length of individual SWCNT. SWCNT were measured individually using IMAGE J software by tracing out the length contours. One such measurement is shown in the form of white line with black circles.

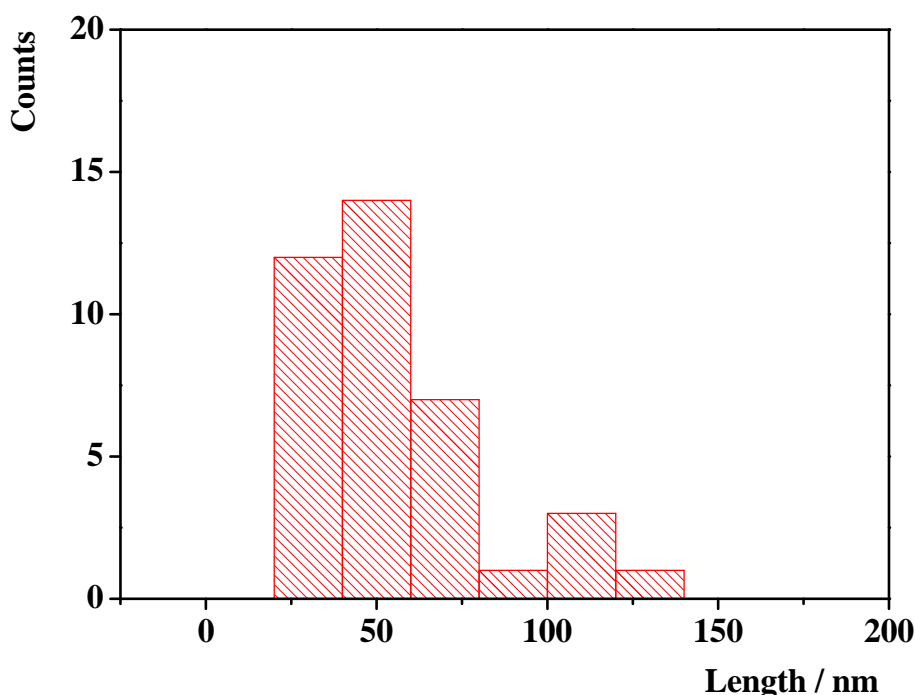


Figure 3.17: Length distribution for SWCNT after oxidative treatment from TEM images. Commercially available and un-functionalized SWCNT were shortened using 3: 1, HNO_3 : H_2SO_4 for 4 hrs at 70°C . Lengths of SWCNT were measured from the TEM images, individually using IMAGE J software by tracing out the length contours.

The self assembled vertically aligned SWCNT forests formed as described in Section 3.3.4, were also investigated using atomic force microscopy (AFM). Figure 3.18 shows the AFM image of SWCNT forest formed on ITO electrode by drop casting method. The AFM image shows that uniform coverage is not obtained on the surface rather; small islands of vertically aligned CNTs are formed. The height of the self assembled CNTs from AFM image is also found to be between 50-70 nm. However, Figure 3.19 shows an AFM image of an inkjet printed ITO electrode. It can be clearly seen that a dense and uniform SWCNT forest coverage is obtained. As the printer head prints line by line to form $1 \times 1 \text{ cm}^2$ square, due to the set resolution of the printer a banded appearance on the ITO is seen. This is also observed when the substrate is inspected by naked eye as shown in Figure 3.11. However, from the AFM

image, Figure 3.15, it is clear that this lined appearance does not drastically affect the coverage as vertical nanotubes can be seen in both regions.

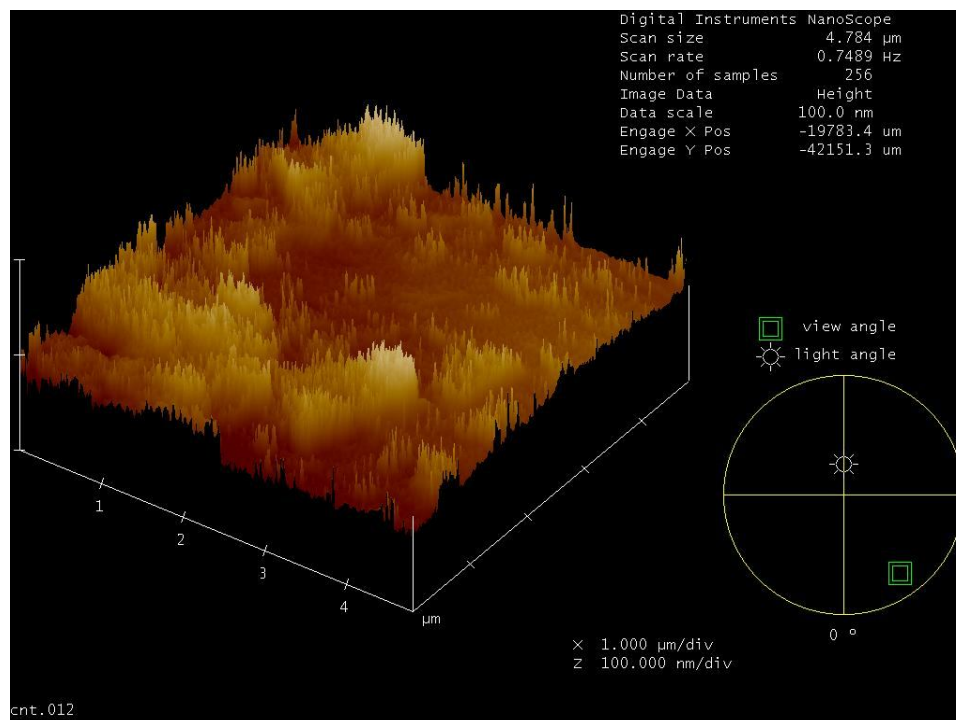


Figure 3.18: Tapping mode atomic force micrograph of self assembled, vertically aligned SWCNT forests formed on ITO electrode by drop casting. A commercial non-conductive silicone nitride cantilever was used.

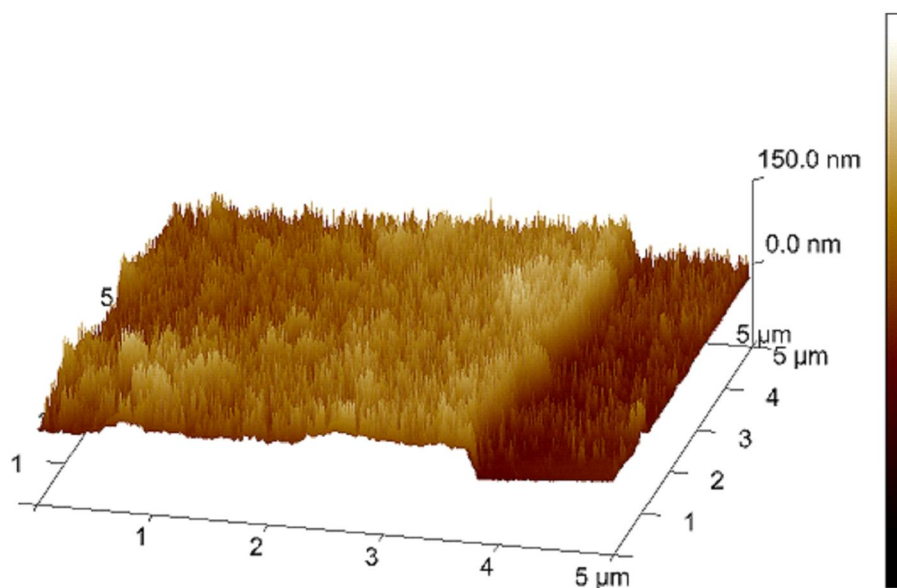


Figure 3.19: Tapping mode atomic force micrograph of self assembled, vertically aligned SWCNT forests formed on ITO electrode by inkjet printing method. A commercial non-conductive silicone nitride cantilever was used.

The primary antibody, anti-IgG (Ab_1) was attached onto the surface of the SWCNT forest using conventional NHS N-(3-dimethylaminopropyl)-N'-ethylcarbodiimide hydrochloride (EDC) chemistry.⁵² 30 μ L of freshly prepared NHS-EDC solution (1:10 ratio in 1 ml PBS buffer (pH 7)) was placed onto the vertically aligned SWCNT spots and washed off after 10 minutes. This was immediately followed by a 3 hrs incubation at 37°C with 20 μ L of 5 mg/mL Ab_1 in PBS buffer (pH 7) containing 0.05% Tween-20. The electrodes were then washed with 0.05% Tween-20 and PBS buffer. This anti-IgG SWCNT -ITO sensor was then treated with 20 μ L of 5% casein + 0.05% Tween-20, followed by washing with 0.05% Tween-20 and PBS buffer for 20 minutes. The casein wash was essential to block non-specific binding (NSB) to obtain a sensitive response. Figure 3.20 shows AFM images of SWCNT immunosensor with anti-IgG covalently attached to the carboxyl sites of the vertical nanotubes. The sensor was formed by inkjet printing. It can be clearly seen that the spiky forest appearance is lost and a globular coating, generally reminiscent of protein coatings⁴¹ is observed. Moreover, a four fold increase in domain height is also

observed after covalent coupling on anti-IgG. Wide area views showed that there were also regions of uncoated SWCNT forests.

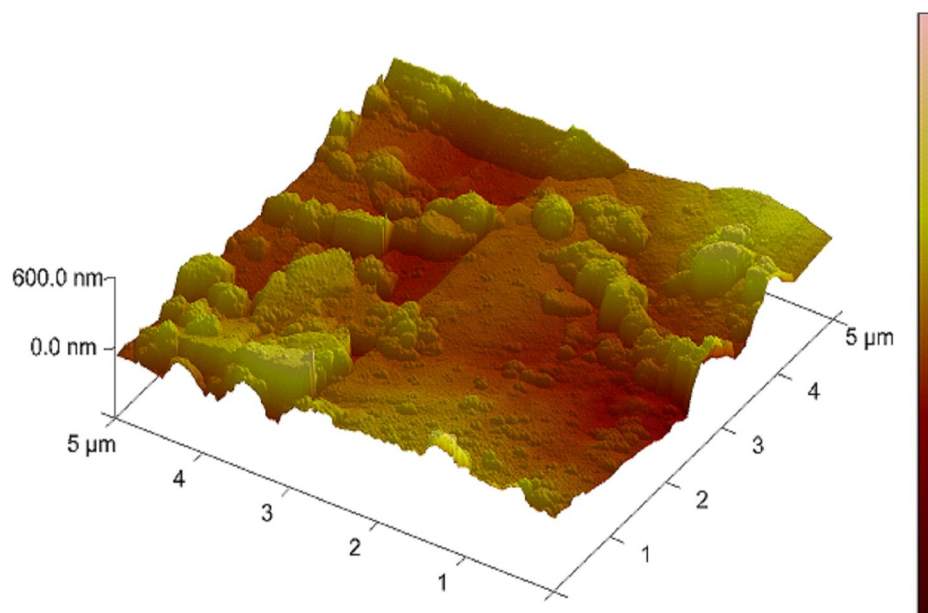


Figure 3.20: Tapping mode atomic force micrograph of self assembled, vertically aligned SWCNT forests formed on ITO electrode by the inkjet printing method. A commercial non-conductive silicone nitride cantilever was used.

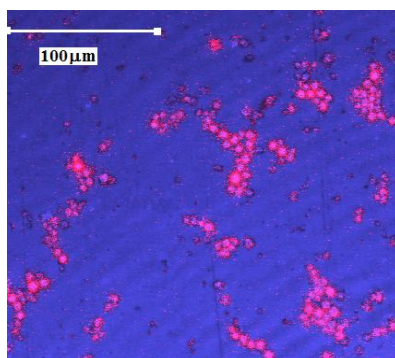
Thus, by printing the carbon nanotubes, high degree of precision, control and active acid sites were obtained. The coverage was uniform even though banding due to the resolution of the printer could still be seen, and the method was found to be very reproducible. The standard error, defined as standard deviation / number of trials, on the surface coverage was found to be only $\pm 0.03 \text{ molcm}^{-2}$.

3.3.5 IgG-G1.5-[Ru(bpy)₂PICH₂] bio-conjugate: Fabrication and characterization

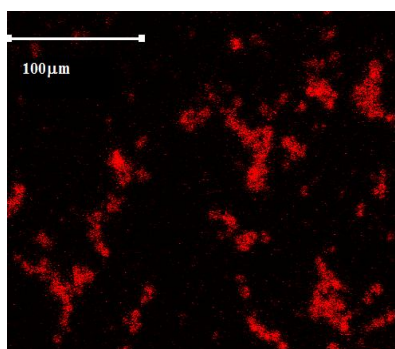
Particle based assays are widely used as signal enhancement tools as they offer a large surface area for the attachment of biomolecules.¹³ Metal¹ and silica nanoparticles⁵³ have been shown to decrease detection limits down to 0.5 picogmL⁻¹ for prostate specific antigen and 2.98 nM for TPA respectively. Commercially available amine functionalized silica nanospheres were decorated with the [Ru(bpy)₂PICH₂]²⁺ complex in order to achieve ECL signal enhancement.

Commercially available amine functionalized silica nanospheres of 800 nm diameter were coated with [Ru(bpy)₂(PICH₂)]²⁺ using conventional NHS-EDC coupling chemistry.⁵² Firstly, 500 μ L of 2 mg/mL silica nanospheres were washed by centrifuging at 3000 RPM in 10 mM PBS buffer (pH 7). Then a 1:10 molar ratio of NHS: EDC solution was freshly prepared in 1 ml of 10 mM PBS buffer (pH 7). To this solution, 1 mM of [Ru(bpy)₂(PICH₂)]²⁺ was added and allowed to stir for 5 minutes. Once the acid groups of the dye were activated, the amine functionalized silica nanospheres were added. This was allowed to stir for 4 hrs, and then washed with 10 mM PBS (pH 7) by centrifuging at 3000 RPM. The washing step was repeated till the supernatant turned colourless. The ruthenium coated spheres, as shown in Figure 3.23 (A), were suspended in 1 mL of 10 mM PBS (pH 7) and stored at 4°C until further use. Figure 3.21 (A) shows confocal images of ruthenium coated spheres. It is clear from the confocal image, Figure 3.21 (B), that only the spheres emit when excited with a 458 nm laser.

(A)



(B)



(C)

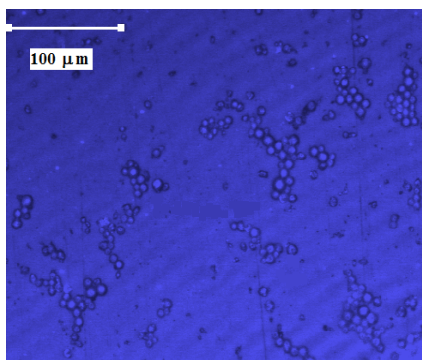


Figure 3.21: Fluorescence microscopy image of 500 μL of 2 mg/mL, 800 nm silica nanospheres coated with 1mM [Ru(bpy)₂(PICH₂)]²⁺ (A). 5 μL of the coated spheres were drop casted on a glass slide and excited with 458 nm laser, 60 x magnification. The fluorescence Image (A) was split into two channels such that Image (B) represents the channel with only fluorescence emission from the spheres whereas Image (C) represents the channel with only the reflectance image.

In order to determine the total concentration of ruthenium covalently bound to the surface of the silica nano particles, UV-vis absorption spectroscopy was performed. First, the total number of nanospheres in 3 mL of 2 mg/mL commercially available nanosphere suspension was calculated using Equation 3.3.⁵⁴

$$N = \frac{6 \times 10^{10} S \rho_L}{\pi \rho_s d^3} \quad 3.3$$

where, N is the number of nanospheres/mL (3.64×10^{12}) of suspension, S is the weight% solids *i.e.* 5 for 5% solid suspension, ρ_L is the density of nanosphere suspension (0.039 g/mL) and was calculated using Equation 3.4⁵⁴, ρ_s is the density of solid sphere (2×10^{-3} g/cm³) and d is the mean diameter in μm (0.8 μm). N was found to be 10.9×10^{12} spheres/mL.

$$\rho_L = \frac{100 \times \rho_s}{[S(1 - \rho_s) + (100\rho_s)]} \quad 3.4$$

The total number of charge groups/ nanosphere can be calculated using Equation 3.5 where, P is the occupied area in \AA^2 , given by Equation 3.6 and D_c is the surface charge density. Given D_c for 0.8 μm spheres is 2 nmol/mg, (specification provided by Bangs Laboratories, Inc), Equation 3.5 and Equation 3.6 yield parking area or surface charge density $P = 311.3 \text{ \AA}^2$ and charge groups per nanosphere $C_M = 645.9 \times 10^3$.

$$P = \frac{1}{1.004 D_c \rho_s d} \quad 3.5$$

$$C_M = \frac{\pi d^2 10^8}{P} \quad 3.6$$

Thus, ideally 10.9×10^{12} spheres have a maximum of 7.1×10^{18} surface charge groups *i.e.*, roughly 11.7 μmol of $[\text{Ru}(\text{bpy})_2(\text{PICH}_2)]^{2+}$ dye molecules. The degree of coating on the micro spheres can be confirmed using UV-vis absorption spectroscopy. Figure 3.22 shows the absorption spectrum of 15 μM $[\text{Ru}(\text{bpy})_2(\text{PICH}_2)]^{2+}$ dye (black line) and the spectrum of 1 mL of 2 mg/mL $[\text{Ru}(\text{bpy})_2(\text{PICH}_2)]^{2+}$ coated nanospheres (red line) in PBS buffer (pH 7)

respectively. Care was taken to minimise settling of the spheres by agitating the solution and quickly measuring the UV spectra. The spectrum of $[\text{Ru}(\text{bpy})_2(\text{PICH}_2)]^{2+}$ coated nanospheres appears to be rather noisy. It is most likely due to the scattering of incident light by the nanosphere suspension.

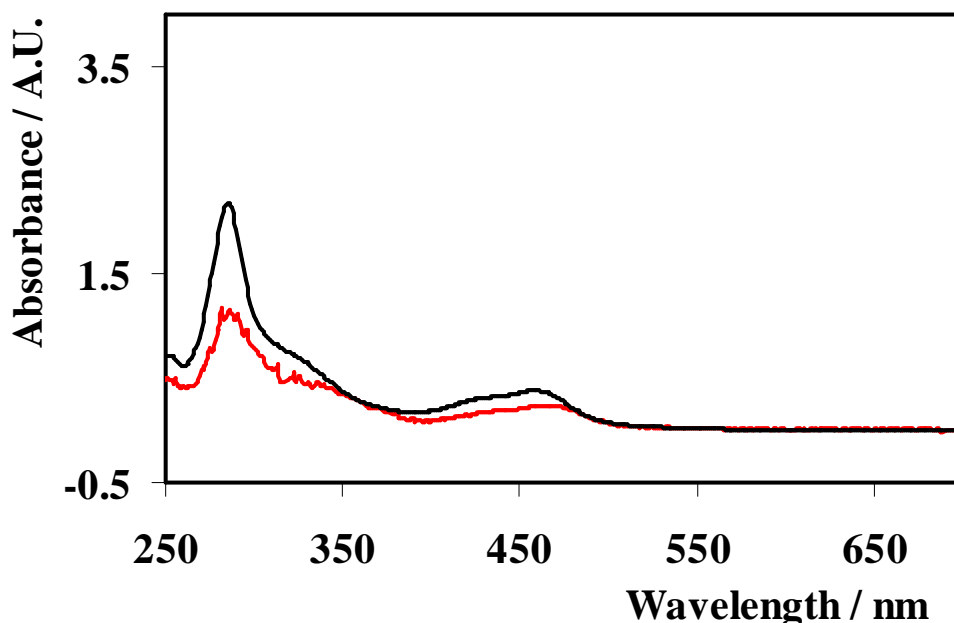


Figure 3.22: Background corrected absorption spectra of 15 μM $[\text{Ru}(\text{bpy})_2(\text{PICH}_2)]^{2+}$ (—) and 1 mL $[\text{Ru}(\text{bpy})_2(\text{PICH}_2)]^{2+}$ coated, 800 nm, amine functionalized silica nanospheres (—) in PBS buffer (pH 7). Quartz cuvette of 1 cm path length with 20 nm slit width was used.

Using Beer –Lamberts law, Equation 3.7, the total concentration of ruthenium present on the surface of 1 mL of 2 mg/mL spheres was calculated to be $10.6 \pm 0.2 \mu\text{mol}$.

$$A = \epsilon l C \quad 3.7$$

where, A is absorbance, ϵ is extinction coefficient in $\text{M}^{-1}\text{cm}^{-1}$, l is the path length in cm and C is the concentration of absorbers in M.

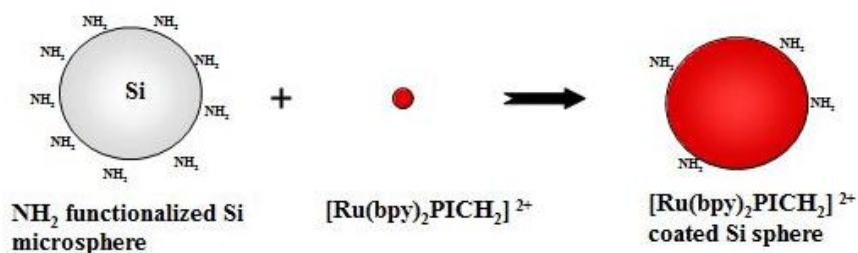
In order to couple secondary antibody *i.e.*, IgG to the ruthenium coated spheres, 20% G1.5 acid terminated PAMAM dendrimers were activated along with 400 μL of 25 mg/mL ruthenium coated spheres using EDC: NHS coupling

chemistry.⁵² To this 200 μ L of 10 mg/mL IgG was added and stirred for 4 hrs. The G1.5 dendrimer has a total of 16 sites.⁵⁵ It is expected that some of these sites will be involved in coupling with IgG, whereas others will couple to the remaining amine sites on the silica spheres, as shown in Figure 3.23 (D). These were then washed and suspended in 1 mL PBS (pH 7).

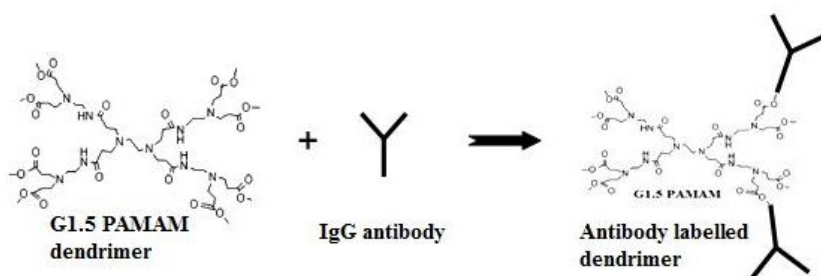
G1.5 acid terminated PAMAM dendrimers were chosen for binding IgG to spheres because they have COOH ends and it has been previously shown that the best interaction between a dendrimer and a protein will occur when they have similar interfacial /addressable area.⁵⁶ G1.5 acid terminated PAMAM dendrimers have flexible structures and their carboxylate terminals can interact with a positive surface across their full diameter. The surface area that each dendrimer can address is roughly 80 nm. Chiba. *et.al.*,⁵⁶ have also shown experimentally that even though larger dendrimers possess larger surface area for binding of proteins, they bind weakly to their protein targets due to increased surface crowding and rigidity. Therefore, in order to achieve efficient binding; the size of the dendrimer should be optimized depending on the protein target. In this study, though different dendrimer sizes were not explored, G1.5 dendrimer was chosen because it possesses similar interfacial area⁵⁶ to that of an IgG molecule.

In order to determine the number of antibodies attached to each sphere, UV- vis absorption spectroscopy was used and Cy-5 labelled IgG were coupled to G1.5 dendrimer (Figure 3.23 (C)) instead of unlabelled IgG and the same procedure as stated earlier, was followed. Care was taken to minimise settling of the spheres by agitating the solution and quickly measuring the UV spectra. The Cy-5-IgG-G1.5-[Ru(bpy)₂PICH₂]² bio-conjugate is as shown in Figure 3.23 (E).

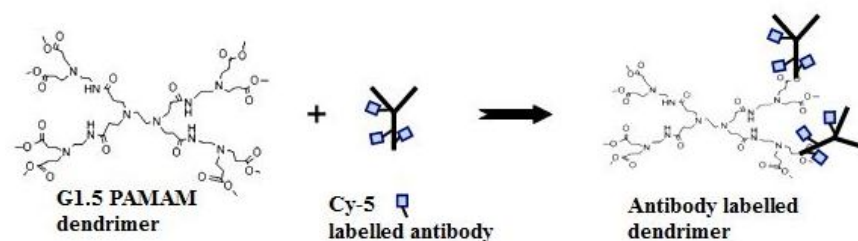
(A)



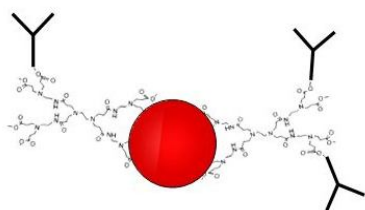
(B)



(C)



(D)



(E)

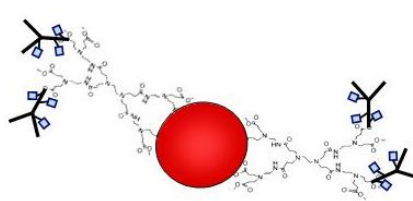


Figure 3.23: Schematic showing various labels and bio-conjugates synthesised. $[\text{Ru}(\text{bpy})_2\text{PICH}_2]^{2+}$ coated silica spheres (A), IgG antibody labelled G1.5 PAMAM dendrimer (B) Cy-5 labelled antibody coated G1.5 PAMAM dendrimer (C), IgG-G1.5- $[\text{Ru}(\text{bpy})_2\text{PICH}_2]$ bio-conjugate (D) and Cy-5-IgG-G1.5- $[\text{Ru}(\text{bpy})_2\text{PICH}_2]$ bio-conjugate (E).

Figure 3.24 shows the absorption spectrum of commercial Cy-5 dye labelled IgG (black line) and 1 mL of Cy-5 labelled IgG coupled to [G1.5 dendrimer-ruthenium nanosphere] bio-conjugate (red line), respectively.

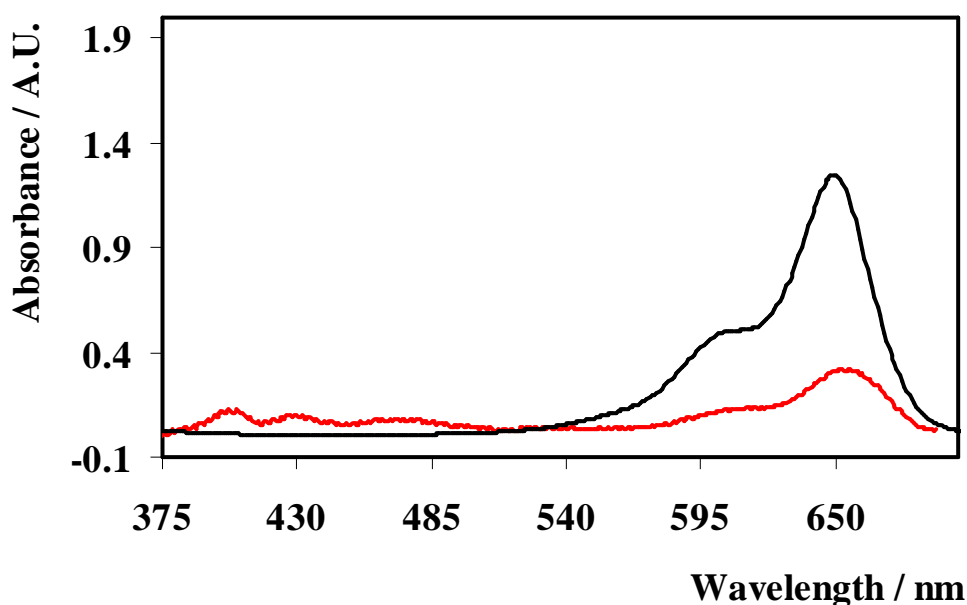


Figure 3.24: Background corrected absorption spectra of 5 μ M Cy-5 labelled IgG, with dye: protein ratio of 3 (—) and Cy-5 labelled IgG-[G1.5 dendrimer-Ru(bpy)₂(PICH₂)²⁺ coated, 800 nm silica nanosphere] bio-conjugate (—) in PBS buffer (pH 7). Quartz cuvette of 1 cm path length and 20 nm slit width was used.

The UV spectra shows that the peak at 650 nm shifts slightly to 655 nm and additional peaks at 400 nm, 430 nm and a broad peak at 470 nm appear, after coupling with nanospheres. This slight shift in the peak at 650 nm could be due to surface confinement of the Cy-5 labelled IgG. It is known that the UV absorption peak of nanospheres and conjugated polymers shift towards blue or red region when their microenvironment is perturbed.^{9, 57} Also this spectrum appears noisy just like Figure 3.22 due to the scattering of incident light by the non-transparent nanosphere suspension. The extinction coefficient ϵ for

commercial Cy-5 dye⁵⁸ is given to be 250000 M⁻¹cm⁻¹ with a dye: protein ratio of 3 and molecular weight of IgG is 150 kDa (2.5x10⁻¹⁹ g). From the UV spectrum, Figure 3.24, the Cy-5 concentration on 1 mL of 25 mg/mL ruthenium coated silica spheres was found to be 1.3 μM (1.3x10⁻⁹ mol). Thus, taking dye to protein ratio under consideration the concentration of IgG on 3.64x10¹² ruthenium coated nanospheres was calculated to be 0.44 nmol (440 nM). The coupling efficiency^{52, 59} (η_{IgG}) can be determined by comparing the amount of protein in the reaction solution prior to coupling to the amount of protein left in solution after coupling. Thus η_{IgG} ⁵² is given by Equation 3.8:

$$(\eta_{\text{IgG}}) = \text{Conc. of (Cy-5-IgG left AFTER COUPLING)} / \text{Conc. of (Cy-5-IgG added)} \quad 3.8$$

$$(\text{Cy-5-IgG}_{\text{TOTAL}}) = (\text{Cy-5-IgG}_{\text{BOUND}}) - (\text{Cy-5-IgG}_{\text{UNBOUND}}) \quad 3.9$$

$$(\eta_{\text{IgG}}) = (\text{Cy-5-IgG}_{\text{TOTAL}} - \text{Cy-5-IgG}_{\text{BOUND}}) / (\text{Cy-5-IgG}_{\text{TOTAL}}) \quad 3.10$$

Substituting the values obtained from the UV-vis absorption spectra, Figure 3.24, coupling efficiency was calculated to be 74%.

The surface area of a 800 nm sphere is calculated to be 8.04x10⁶ nm². It is known from Section 3.3.5, that the concentration of IgG on 3.64x10¹² ruthenium coated nanospheres is 440 nM. This implies that there are roughly 73 molecules of IgG on a single ruthenium coated sphere containing G1.5 dendrimer. The projected area of a single human IgG molecule depends on its configuration at the interface.⁶⁰ In an end-on configuration the area is 20 nm² whereas with side-on, its 103 nm². Thus 73 IgG molecules per silica sphere is a clearly an overestimation of the actual numbers present. The presence of high IgG numbers could be partly attributed to the presence of G1.5 acid terminated dendrimers. It has been previously shown⁵⁶ that G1.5 acid terminated PAMAM dendrimer have flexible structures. The flexibility of smaller dendrimers allows them to “stretch” or “squeeze” onto or into protein surfaces which allows each dendrimer to be able to address an area, referred to as the addressable area, of 80 nm².⁵⁶ Thus the dendrimers tend to not only act as protein linkers, linking the IgG to the surface of the nanospheres but also help to increase the number of contact points for the IgG on the nanosphere surface. However, this alone

cannot account of the high IgG numbers. It is important to note that these calculations are based on UV-vis absorption spectroscopy technique. Though it is widely used and is precise when dealing with fluorescent liquid samples, it is not the best method to be used when dealing with colloidal suspensions. The presence of non-transparent nanospheres and their orientation during measurement, shielding of light due to the presence of proteins attached to the sphere surfaces and settling of the spheres during measurement all introduce errors. However, the above calculated values are used in this thesis assuming the contribution of these errors to the final ECL assay is minimal.

3.4 CONCLUSIONS

The fabrication and characterization of various substrates used in this thesis has been described in detail in this chapter. $[\text{Ru}(\text{bpy})_2(\text{PVP})_{10}]^{2+}$ film electrodes have been successfully developed and the polymer layer, characterized using profilometry, cyclic voltammetry and A.C. impedance. The thickness of the films was found to be around $0.8 \pm 0.2 \text{ } \mu\text{m}$ with D_{CT} being $(4.48 \pm 0.2) \times 10^{-11} \text{ cm}^2 \text{ s}^{-1}$. Cyclic voltammetry was used to determine the surface coverage (Γ) which was found to be $(4.39 \pm 0.06) \times 10^{-8} \text{ mol cm}^{-2}$. A.C. impedance studies show that the films allow efficient penetration of ions and stay attached to the electrode surface even at positive potentials. These films have been extensively used in Chapter 5 for modulated potential studies. Pristine SWCNT were successfully functionalized with carboxyl groups and characterized by TEM and resonance Raman microscopy. The average length of the cut and functionalized nanotubes were determined to be 50-70 nm. Fabrication of vertically aligned SWCNT forests on ITO electrodes has also been described in this chapter. As drop casting proved inefficient with regard to uniform forests being formed, inkjet printing was employed instead. Inkjet printing resulted in 3 orders of magnitude increase in the number of active acid sites involved in covalent coupling. The forests were characterized using AFM and cyclic voltammetry. Finally, IgG-G1.5- $[\text{Ru}(\text{bpy})_2\text{PICH}_2]^{2+}$ bio-conjugates were synthesised with a labelling efficiency of 74%. Using the Beer –Lambert law, the total concentration of ruthenium present on the surface of 3 mL of 2

mg/mL silica nanospheres was calculated to be (10.6 ± 0.2) μmol . These carboxyl functionalized SWCNT forest platforms and ruthenium dye coated silica nanospheres are used for bioassay studies in Chapter 6 where pico molar detection of secondary antibodies (IgG) is achieved.

3.5 REFERENCES

- (1) Mani, V.; Chikkaveeraiah, B. V.; Patel, V.; Gutkind, J. S.; Rusling, J. F. *ACS Nano* **2009**, 3, 585-594.
- (2) Bertoncello, P.; Dennany, L.; Forster, R. J.; Unwin, P. R. *Anal. Chem.* **2007**, 79, 7549-7553.
- (3) Aoki, A.; Miyashita, T. *Colloids. Surf. A: Physicochem. Eng. Aspects* **2002**, 198-200, 671-676.
- (4) Masaki, T.; Tomoki, Y.; Atsushi, S.; Yuji, T.; Hiroki, M.; Yuji, M.; Kenichi, M.; Mikito, Y.; Junko, M. *Analyt. Sci.* **2007**, 23.
- (5) Johan, H.; Robyn, W. H.; Anders, H.; Edwin, C. C.; Catherine, E. H.; Forester, R. J. *Inorg. Chem.* **2005**, 44, 1073-1081.
- (6) Takada. K.; Naal. Z.; Abruna. H. D. *Langmuir* **2003**, 19, 5402-5406.
- (7) Charles, D. E.; Lawrence, D. M.; Royce, W. M.; Thomas, J. M. *Inorg. Chem* **1983**, 22, 1283-1291.
- (8) Nyasulu, F. W. M.; Mottola, H. A., *J. Electroanal. Chem.* **1988**, 239, 175-186.
- (9) Hong, H.; Davidov, D.; Chayet, H.; Faraggi, E. Z.; Tarabia, M.; Avny, Y.; Neumann, R.; Kirstein, S. *Supramol. Sci.* **1997**, 4, 67-73.
- (10) Forster, R. J.; Pellegrin, Y.; Keyes, T. E. *Electrochem. Commun.* **2007**, 9, 1899-1906.
- (11) Forster, R. J.; Kelly, A. J.; Vos, J. G.; Lyons, M. E. G. *J Electroanal Chem* **1989**, 270, 365-379.
- (12) Hogan, C. F.; Forster, R. J. *Anal. Chim. Acta* **1999**, 396, 13-21.
- (13) Forster, R. J.; Bertoncello, P.; Keyes, T. E. *Annu. Rev. Anal. Chem* **2009**, 2, 359-385.
- (14) Daly, D. J.; O'Sullivan, C. K.; Guilbault, G. G. *Biochem. Soc. Trans.* **2000**, 28, 89-93.
- (15) Forster, R. J.; Keyes, T. E.; Vos, J. G. In *Interfacial Supramolecular Assemblies*; John Wiley & Sons, Ltd: 2003; .
- (16) Dennany, L.; Hogan, C. F.; Keyes, T. E.; Forster, R. J. *Anal. Chem.* **2006**, 78, 1412-1417.
- (17) Patolsky, F.; Weizmann, Y.; Willner, I. *Angew. Chem. Int. Ed.* **2004**, 43, 2113-2117.
- (18) Wang, J. *Electroanalysis* **2005**, 17, 7-14.
- (19) Jacobs, C. B.; Peairs, M. J.; Venton, B. J. *Anal. Chim. Acta* **2010**, 662, 105-127.
- (20) Wohlstadter. J. N.; Wilbur. J. L.; Sigal. G. B.; Biebuyck. H. A.; Billadeau. M. A.; Dong. L.; Fischer. A. B.; Gudibande. S. R.; Jameison. S. H.; Kenten. J. H.; Leginus. J.; Leland. J. K.; Massey. R. J.; Wohlstadter. S. J. *Adv Mater* **2003**, 15, 1184-1187.
- (21) Friis, E. P.; Andersen, J. E. T.; Madsen, L. L.; Bonander, N.; Møller, P.; Ulstrup, J. *Electrochim. Acta* **1998**, 43, 1114-1122.
- (22) Larsson, H.; Sharp, M. *J Electroanal Chem* **1995**, 381, 133-142.
- (23) Dennany, L., *Electrochemiluminescent & amperometric detection of DNA & DNA damage*, Dublin City University, Dublin, 2004.

- (24) Bard, A. J.; Faulkner, L. R. In *Electrochemical responses of adsorbed monolayers*; Electrochemical methods: Fundamentals and applications; John Wiley & Sons Inc: New York, 1980; pp 718.
- (25) Forster, R. J.; Hogan, C. F. *Anal. Chem.* **2000**, *72*, 5576-5582.
- (26) Hunter, T. B.; Tyler, P. S.; Smyrl, W. H.; White, H. S. *J. Electrochem. Soc.* **1987**, *134*, 2198-2204.
- (27) Holze, R. In *Encyclopedia of electrochemistry* (A.J. Bard and M. Stratmann eds), vol 3: instrumentation and electroanalytical chemistry (P.R. Unwin ed); 2007; Vol. 11, pp 134-135.
- (28) Fernández-Sánchez, C.; McNeil, C. J.; Rawson, K. *Tr. Anal. Chem* **2005**, *24*, 37-48.
- (29) Cameron, C. G., *Enhanced rates of electron transport in conjugated-redox polymer hybrid*, University of Ottawa, Canada, 1992.
- (30) Kaufman, F. B.; Engler, E. M. *J. Am. Chem. Soc.* **1979**, *101*, 547-549.
- (31) Kaufman, F. B.; Schroeder, A. H.; Engler, E. M.; Kramer, S. R.; Chambers, J. Q. *J. Am. Chem. Soc.* **1980**, *102*, 483-488.
- (32) Lyons, M. E. G., Ed.; In *Electroactive polymer electrochemistry*; On Yeh, A. G., Mikolajuk, Z., Eds.; Fundamentals; Plenum press: NewYork, 1994; Vol. 1.
- (33) Sabot, A.; Krause, S. *Anal. Chem.* **2002**, *74*, 3304-3311.
- (34) Brett, C. M. A.; Brett, A. M. O., In *Electrochemistry: Principles, methods and applications*; Oxford University Press Inc: NewYork, 1993; , pp 427.
- (35) Armstrong, R. D.; Jenkins, A. T. A.; Johnson, B. W. *Corros. Sci.* **1995**, *37*, 1615-1625.
- (36) National Center for Biotechnology Information, *A science primer*, <http://www.ncbi.nlm.nih.gov/About/primer/index.html> (accessed April, 2010).
- (37) Schena, M.; Heller, R. A.; Theriault, T. P.; Konrad, K.; Lachenmeier, E.; Davis, R. W. *Tr. Biotechnol.* **1998**, *16*, 301-306.
- (38) Penza, M.; Cozzi, S.; Tagliente, M. A.; Mirengi, L.; Martucci, C.; Quirini, A. *Thin Solid Films* **1999**, *349*, 71-77.
- (39) Yu, X.; Munge, B.; Patel, V.; Jensen, G.; Bhirde, A.; Gong, J. D.; Kim, S. N.; Gillespie, J.; Gutkind, J. S.; Papadimitrakopoulos, F.; Rusling, J. F. *J. Am. Chem. Soc.* **2006**, *128*, 11199-11205.
- (40) Chattopadhyay, D.; Galeska, I.; Papadimitrakopoulos, F. *J. Am. Chem. Soc.* **2001**, *123*, 9451-9452.
- (41) Yu, X.; Kim, S. N.; Papadimitrakopoulos, F.; Rusling, J. F. *Mol. BioSyst.* **2005**, *1*, 70-78.
- (42) Setti, L.; Fraleoni-Morgera, A.; Ballarin, B.; Filippini, A.; Frascaro, D.; Piana, C. *Biosensors and Bioelectronics* **2005**, *20*, 2019-2026.
- (43) Hart, A. L.; Turner, A. P. F.; Hopcroft, D. *Biosensors and Bioelectronics* **1996**, *11*, 263-270.
- (44) Zhang, M.; Yudasaka, M.; Iijima, S. *J. Phys. Chem. B* **2004**, *108*, 149-153.
- (45) Liu, Z.; Shen, Z.; Zhu, T.; Hou, S.; Ying, L.; Shi, Z.; Gu, Z. *Langmuir* **2000**, *16*, 3569-3573.
- (46) Ziegler, K. J.; Gu, Z.; Peng, H.; Flor, E. L.; Hauge, R. H.; Smalley, R. E. *J. Am. Chem. Soc.* **2005**, *127*, 1541-1547.
- (47) Belin, T.; Epron, F. *Mater. Sci. Engg. B* **2005**, *119*, 105-118.

- (48) Milnera, M.; Kürti, J.; Hulman, M.; Kuzmany, H. *Phys. Rev. Lett.* **2000**, *84*, 1324.
- (49) Forrest, G. A.; Alexander, A. J. *J. Phys. Chem. C* **2007**, *111*, 10792-10798.
- (50) Colomer, J. F.; Benoit, J. M.; Stephan, C.; Lefrant, S.; Van Tendeloo, G.; B. Nagy, J. *Chem. Phys. Lett.* **2001**, *345*, 11-17.
- (51) Corio, P.; Temperini, M. L. A.; Santos, P. S.; Romero, J. V.; Huber, J. G.; Luengo, C. A.; Brown, S. D. M.; Dresselhaus, M. S.; Dresselhaus, G.; Dantas, M. S. S.; Leite, C. F.; Matinaga, F.; Gonzalez, J. C.; Pimenta, M. A. *Chem. Phys. Lett.* **2001**, *350*, 373-380.
- (52) Bangs laboratories.Inc Tech note 205 Covalent coupling. <http://www.bangslabs.com/literature/technotes>2008).
- (53) Zhang, L.; Dong, S. *Anal. Chem.* **2006**, *78*, 5119-5123.
- (54) Bangs laboratories.Inc Tech note 206. <http://www.bangslabs.com/literature/technotes>2008).
- (55) Kitchens, K. M.; El-Sayed, M. E. H.; Ghandehari, H. *Adv. Drug Deliv. Rev.* **2005**, *57*, 2163-2176.
- (56) Chiba, F.; Chou Hu, T.; Twyman, J. L.; Wagstaff, M. *Chem. Comm* **2008**, 4351-4353.
- (57) Chen, X.; Chen, Z.; Lu, G.; Bu, W.; Yang, B. *J. Colloid Interface Sci.* **2003**, *264*, 266-270.
- (58) Clontech Laboratories **2008**, *Protocol number PT3648-1*.
- (59) Hermanson, G. T.; Mattson, G. R.; Krohn, R. I. *J. Chromatogr. A* **1995**, *691*, 113-122.
- (60) Elaissari, A., Ed.; In *Colloidal biomolecules, biomaterials and biomedical applications*; Surfactant science series; Marcel Dekker, Inc: USA, 2004; Vol. 116, pp 55.

CHAPTER IV

OXIDATIVE ELECTROPOLYMERISATION OF RUTHENIUM AMINO PHENANTHROLINE COMPLEXES

4.1 INTRODUCTION

Films of functional polymers play pivotal roles in diverse areas ranging from advanced sensors to reactive coatings and displays.^{1,2} Incorporating transition metal complexes within these coatings are desirable because of their redox, catalytic and optical properties.³⁻⁵ Moreover, the metal complex can sometimes simultaneously fulfil several roles. For example, complexes of the type $[M(\text{aphen})_n\text{bpy}_m]^{2+}$, where M is Ru, Os, Co or Fe, $n=2,3$ and $m=1,0$ have the potential to covalently bind an enzyme through peptide bond formation, shuttle electrons to the active site and produce an interfacial polymer film through oxidative electropolymerisation of the amino functionality. The resulting films are superior to those involving an electrostatically immobilized luminophore in a polymer such as Nafion where leaching from the film can occur over time. Hence, they are very attractive for creating biosensors. Moreover, electropolymerisation has the advantage that it enables *in situ* production of thin and stable films of controlled thickness.⁶⁻⁹ For example fundamental studies on amino-phenanthroline polymers have been previously reported by others for ruthenium,¹⁰ iron¹¹ and osmium¹² complexes.

The 5-NH₂ -1, 10- phenanthroline ligand (aphen) is especially attractive for electropolymerisation as it provides both a readily oxidizable amino moiety and a metal coordination site. Studies investigating the electrochemical film forming ability of this compound with other transition metal complexes showed that, of the various transition metals, Ru^{II} and Fe^{II} were the best in regard to the electroactivity of the film and its surface coverage.¹²⁻¹⁵ Also, Bachas *et.al.*,¹² have shown that electroactive film growth only occurs when both metal center and the amine group are present and without the initiation of the electropolymerisation reaction by the amine group of the ligand, no film growth is observed. They state that as Ru^{II} has redox potentials close to that of the amine oxidation potential of the ligand (+1.35 V vs. Ag/AgCl),¹² electropolymerisation of this complex is very effective. The metal center serves as the means to transport the electrons between the polymer film and the surface of the electrode.

In this chapter, the electrodeposition of $[\text{Ru}(\text{aphen})_2\text{bpy}]^{2+}$ and $[\text{Ru}(\text{aphen})_3]^{2+}$ from aqueous sulphuric acid and acetonitrile where aphen is 5-amino-1,10-phenanthroline and bpy is 2,2'-bipyridine, is reported. These complexes are interesting to study as this arrangement of ligand amino groups effectively ensures that the film growth can occur in all directions rather than unidirectional mode of growth. Hence, a highly crossed linked polymer containing dispersed metal redox centers can be obtained. Another impressive advantage of these types of metal-ligand complexes is that the amine linkages can be used to attach antibodies, amino acids or proteins to the surface of the electroactive polymer film, forming an excellent method of biological immobilization. This is because not all the amino groups are used in coupling and are available for biomolecule binding. Furthermore, it is known that the ECL characteristics of the transition metal complex strongly depend on the metals–ligand interactions and it is possible to tune the ECL properties by introducing ligands with different donor abilities to metal complexes.

Hence, oxidative electropolymerisation has been employed to form electroactive films in both aqueous and organic media. Scanning electron microscopy (SEM) was performed to study the morphology of the two films deposited in acetonitrile and sulphuric acid. Moreover, these electrodeposited films were also investigated for electrochemiluminescence (ECL) in the presence of tripropylamine (TPA) and sodium oxalate as co-reactant. The various electrochemical, photophysical and ECL properties and pH dependency results of the electropolymerised ruthenium films have been investigated and are reported.

4.2 EXPERIMENTAL

4.2.1 Apparatus

Electrochemical measurements were carried out with a CH instruments, model 660 Potentiostat. Cyclic voltammetry was conducted using a typical three-electrode cell. An aqueous or non-aqueous Ag/AgCl electrode was used as reference depending on the solvent and a platinum wire was used as a counter

electrode. The electrodes used were first polished with 0.3 μm alumina for 10 min, rinsed thoroughly with deionized water and then polished again for 10 min with 0.05 μm alumina. After polishing, the electrodes were thoroughly rinsed, first with deionized water and then with acetone to remove all traces of alumina from the surface and dried under nitrogen stream. All potentials are quoted versus an Ag/AgCl reference electrode, and all measurements were made at room temperature.

ECL measurements, utilized an Oriel 70680 photo multiplier tube (PMT) equipped with a high voltage power supply, (Oriel, model 70705), which was used at a bias of -850 V, and amplifier / recorder (Oriel, model 70701). During experiments, the cell was placed inside a specially constructed holder, which positioned the working electrode in a reproducible manner directly opposite the face of a fiber optic bundle, the other end of which was coupled to the PMT.

The morphology of the electropolymerised films were investigated using the Hitachi S-3000N scanning electron microscope. Image analysis was carried out using Image J version 1.37d image analysis software.

4.2.2 Materials

All chemicals and solvents were purchased from Sigma Aldrich and were of analytical grade. All solutions were made using deionized water purified with a Milli-Q plus 18.5 M Ω Millipore installation. The solvents used for spectroscopic measurements were of HPLC grade. All deposition solvents were deaerated for 20 min using nitrogen prior electrodeposition. The surface coverages were estimated by integration of charge under slow sweep rate ($v < 0.01 \text{ Vs}^{-1}$) in the deposition solvent in the absence of the metal complex.

4.2.3 Oxidative electropolymerisation

4.2.3.1 In acetonitrile

Films were deposited from a 1.5 mM solution of $[\text{Ru}(\text{aphen})_2\text{bpy}]^{2+}$ or 1.0 mM solution of $[\text{Ru}(\text{aphen})_3]^{2+}$ (*i.e.*, 3 mM of polymerisable amine groups) dissolved in HPLC grade anhydrous acetonitrile using 0.1 M tetrabutylammonium-tetrafluoroborate (TBATFB) as the supporting electrolyte on a 3 mm diameter glassy carbon electrode at a scan speed of 0.1 Vs^{-1} for 10 cycles. Activated alumina (5 mg) was added to the acetonitrile to ensure removal of trace water from the electrolyte solution.

4.2.3.2 In aqueous sulphuric acid

Similarly, films from 2 mM solution of $[\text{Ru}(\text{aphen})_2\text{bpy}]^{2+}$ and 1.33 mM solution of $[\text{Ru}(\text{aphen})_3]^{2+}$ (*i.e.*, 4 mM of polymerisable amine groups) dissolved in HPLC grade 0.5 M sulphuric acid, pH 0.3 were also deposited on 3 mm glassy carbon electrode at a scan rate of 0.1 Vs^{-1} and 60 cycles.

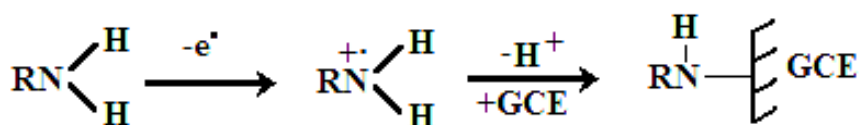
4.3 RESULTS AND DISCUSSIONS

The electropolymerised films prepared as described in Section 4.2.3 were characterised using cyclic voltammetry, UV-Vis spectroscopy, resonance Raman spectroscopy and SEM. In order to perform UV-Vis and Raman measurements the polymer films were dissolved off the electrode surface using prolonged sonication in acetonitrile and sulphuric acid. The results comparing the monomers described in Chapter 2, Section 2.3.1.1 and 2.3.1.2, to the electrochemically synthesised polymers are summarized below.

4.3.1 Electrochemical characteristics of films

Figure 4.1 illustrates the effect of repeated voltammetric cycling of a 1.5 mm radius glassy carbon electrode immersed in a 1.5 mM solution of $[\text{Ru}(\text{aphen})_2\text{bpy}]^{2+}$ dissolved in 0.1 M acetonitrile with TBATFB as supporting electrolyte. Consistent with previous reports,^{10,11} this figure shows that two oxidation processes are observed during the first scan. These correspond to irreversible oxidation of the 5-amino-1,10-phenanthroline ligand at approximately +0.85 V^{8,14} and the electrochemically reversible $\text{Ru}^{2+/3+}$ couple at +1.02 V. The presence of the pre-peak implies that electropolymerisation occurs when the amino phenanthroline ligand is oxidized. This result suggests that the electro-oxidation of the amine containing compound proceeds via the one-electron oxidation of the amine functionality^{10,16} to its corresponding cation radical, as shown in Scheme 1. This species subsequently forms a carbon-nitrogen linkage at the glassy carbon surface.

Scheme 1.



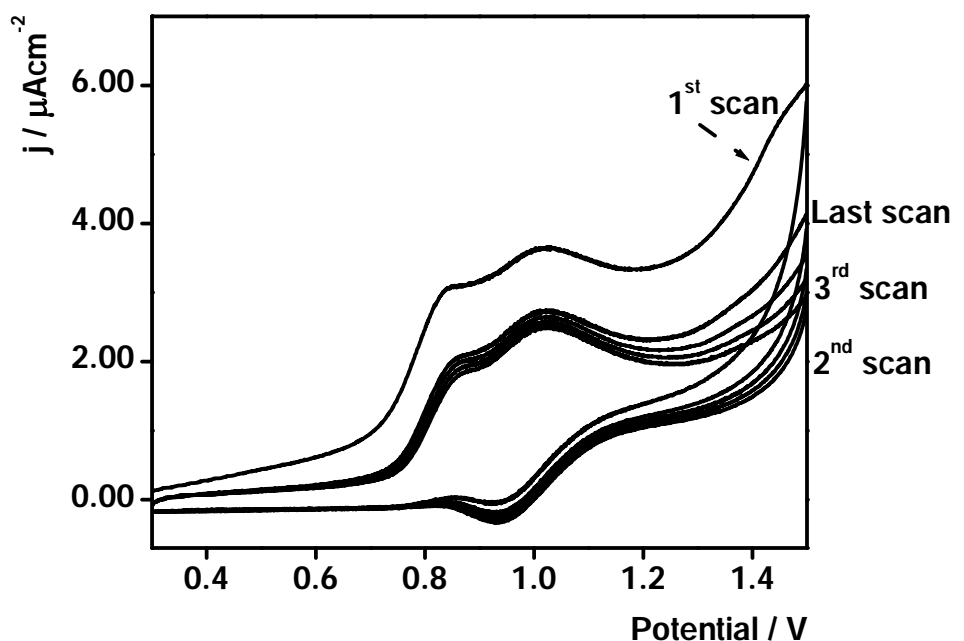


Figure 4.1: Interfacial electropolymerisation from a 1.5 mM solution $[\text{Ru}(\text{aphen})_2\text{bpy}]^{2+}$ on a 3 mm diameter glassy carbon electrode for 10 scans at a scan rate of 0.1 Vs^{-1} . The deposition medium was 0.1 M $\text{CH}_3\text{CN/TBATFB}$.

Significantly, for $[\text{Ru}(\text{aphen})_2\text{bpy}]^{2+}$, the peak current associated with the $\text{Ru}^{2+/3+}$ couple increases modestly with an increasing number of voltammetric scans. However, the rate of growth rapidly decreases between successive scans. The increase in the peak current density is indicative of the formation of a redox active electropolymerised film on the electrode surface. However, the deposition efficiency decreases as the film grows. This may be due to the decrease in the rate of homogeneous charge transport through the film as the film thickness increases. Under these conditions, the rate of oxidation of the ruthenium complex at the interface becomes progressively slower and the rate of film deposition decreases.

Figure 4.2 shows that the behaviour of $[\text{Ru}(\text{aphen})_3]^{2+}$ under repeated cycling is slightly different when compared to $[\text{Ru}(\text{aphen})_2\text{bpy}]^{2+}$ under similar conditions.

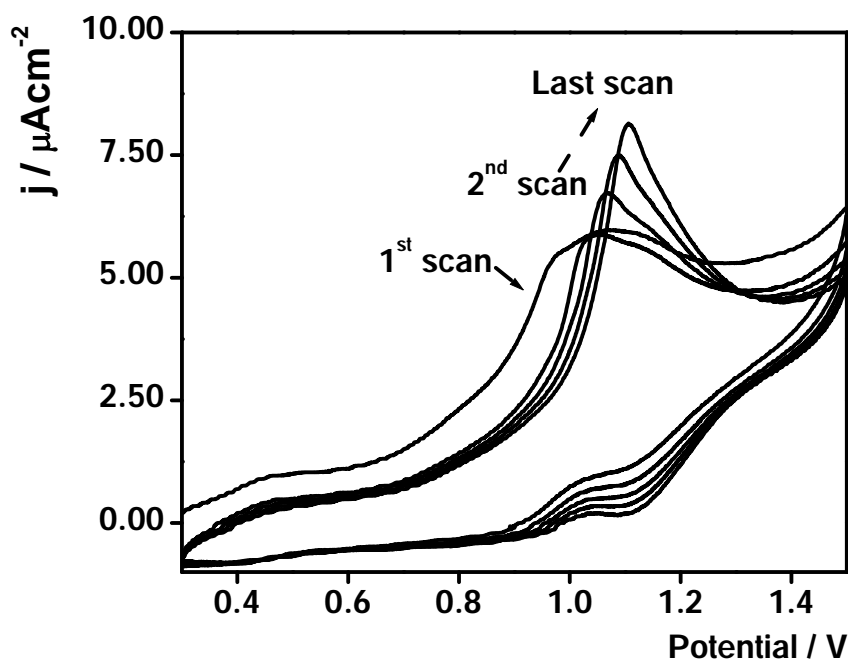


Figure 4.2: Interfacial electropolymerisation from a 1.0 mM solution of $[\text{Ru}(\text{aphen})_3]^{2+}$ on a 3 mm diameter glassy carbon electrode at a scan rate of 0.1 Vs^{-1} , for 10 cycles. The deposition medium was $0.1 \text{ M CH}_3\text{CN/TBATFB}$.

In Figure 4.2, no distinct pre-peak corresponding to the oxidation of aphen is observed, but there is a significant increase in the peak current density at $+1.05 \text{ V}$, which is associated with the electrochemically reversible $\text{Ru}^{2+/3+}$ couple. The absence of the pre-peak does not necessarily signify that there is no oxidation of the amino phenanthroline ligand but it could be due to a smaller difference in energies between the oxidation of amino phenanthroline ligand and oxidation of Ru^{2+} species.

Similar to previous reports,¹² significantly larger anodic charge compared to the cathodic charge is observed which suggests that both irreversible ligand oxidation and reversible metal center oxidation are involved. With the increase in the number of voltammetric scans, the half wave potential also shifts to a more positive value. Similar results were obtained by Belanger *et.al.*, for polypyridyl compounds of iron with amino phenanthroline ligand.⁸

After 10 scans at 0.1 Vs^{-1} , the electrode was removed from the cell and inspected visually. It revealed a reddish orange film, which remained even after

thorough rinsing with deionized water. Once the electrode was removed and thoroughly rinsed, it was transferred to a cell containing blank electrolyte solution (*i.e.*, 0.1 M CH₃CN with TBATFB as supporting electrolyte). Figure 4.3 shows that a persistent voltammetric response associated with the Ru^{2+/3+} couple was observed after electrodeposition of [Ru(aphen)₂bpy]²⁺, suggesting that a redox active film was formed on the electrode.

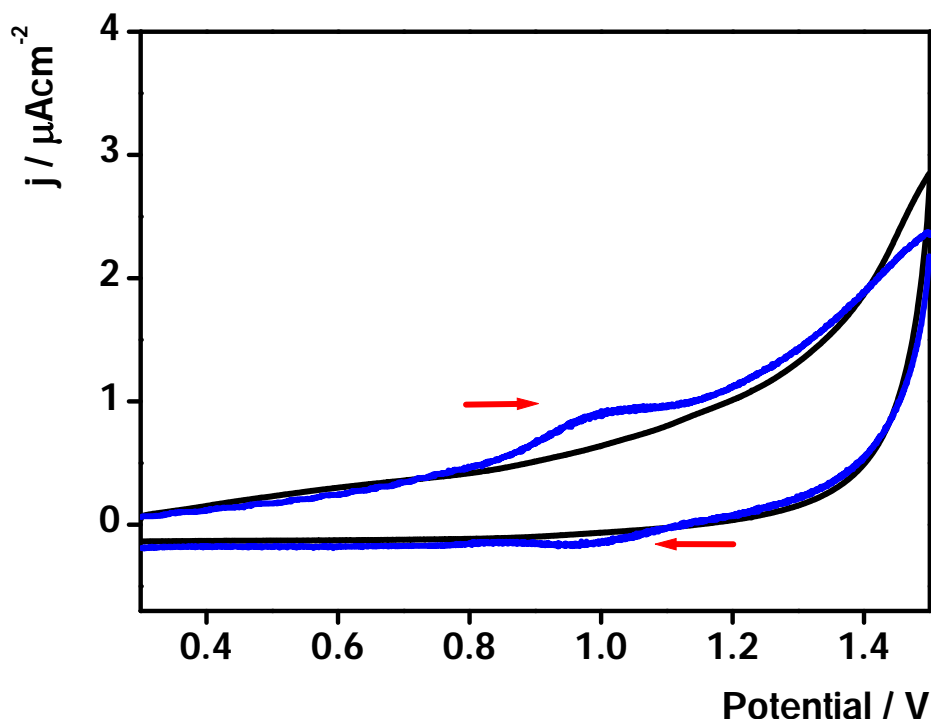


Figure 4.3: Voltammetric behaviour following electrodeposition, of [Ru(aphen)₂bpy]²⁺ (—), in blank 0.1 M CH₃CN/TBATFB after 10 cycles. The scan rate is at 0.1 Vs⁻¹. Blank GCE in 0.1 M CH₃CN/TBATFB is given by (—).

A similar behaviour was observed with tris amino phen complex. Figure 4.4 shows that a persistent voltammetric response associated with the Ru^{2+/3+} couple is observed.

Unusual sharp amine pre peaks are observed in Figure 4.2 and Figure 4.4. Similar peaks were observed by Calzón *et.al.* for oxidation process induced by 2-mercaptopyrimidine at mercury electrodes.⁵⁵ The sharp peaks are attributed to high concentration of 2-mercaptopyrimidine and are considered to be non-faradaic, corresponding to transition between the surface phases due to electro

oxidation product. $[\text{Ru}(\text{aphen})_3]^{2+}$ contains more amines compared to the bis compound and the sharp pre peaks are observed only for $[\text{Ru}(\text{aphen})_3]^{2+}$. Hence this sharp pre peak observed in Figure 4.2 and Figure 4.4 could be attributed to high amine concentration in the $[\text{Ru}(\text{aphen})_3]^{2+}$ compound and non-faradaic transition between surface phases due to oxidative electropolymerisation.

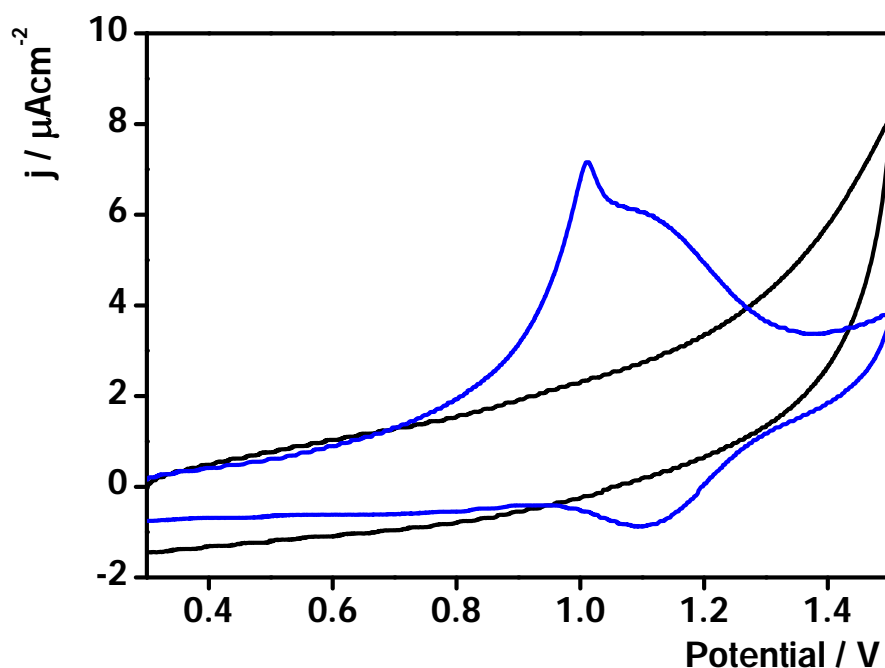


Figure 4.4: Voltammetric behaviour following electrodeposition, of $[\text{Ru}(\text{aphen})_3]^{2+}$ (—), in blank 0.1 M $\text{CH}_3\text{CN}/\text{TBATFB}$ after 10 cycles at scan rate 0.1 Vs^{-1} . Blank GCE in 0.1 M $\text{CH}_3\text{CN}/\text{TBATFB}$ is given by (—).

In order to check if increasing the number of scan cycles would increase the thickness of the film formed, keeping the $[\text{Ru}(\text{aphen})_2\text{bpy}]^{2+}$ concentration constant, the number of scans cycles was increased. Each time, after the set number of scans, the electrode was removed from the cell, thoroughly washed and placed in a cell containing blank electrolyte. The surface coverage of the electrodeposited film, in each case, was determined at 0.01 Vs^{-1} using Equation 1.20.

It can be clearly seen from Figure 4.5, increasing the number of cycles from 5 to 10, increases the amount of electrodeposited $[\text{Ru}(\text{aphen})_2\text{bpy}]^{2+}$ on the glassy

carbon electrode. This is indicated by the increase in the peak current density at +1.02 V. The various surface coverages obtained for different scan numbers is given in Table 4.1. However, increasing the number of cycles further to 15 and 20 does not show any measurable increase in the peak current or the surface coverage of ruthenium.

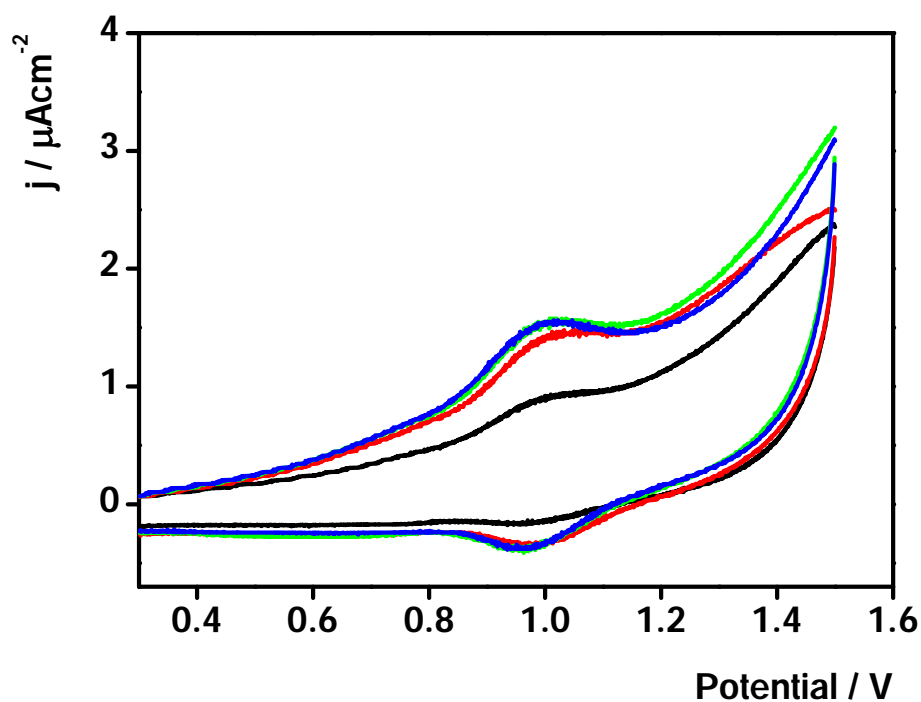


Figure 4.5: Voltammetric behaviour following electrodeposition of $[\text{Ru}(\text{aphen})_2\text{bpy}]^{2+}$ on 3 mm diameter glassy carbon electrode in blank 0.1 M $\text{CH}_3\text{CN}/\text{TBATFB}$, after 5 (—), 10 (—), 15 (—) and 20 (—) scan cycles at a scan rate of 0.1 V s^{-1} .

Table 4.1: Apparent film coverages and peak currents for the oxidative electropolymerisation of $[\text{Ru}(\text{aphen})_2\text{bpy}]^{2+}$ with different number of scan cycles and scan rate (v) 0.1 Vs^{-1} . Surface coverages were estimated by the integration of charge under slow sweep rate in the deposition solvent in the absence of the metal complex.

Scan cycles	$i_{\text{pc}} / \mu\text{A}$	$i_{\text{pa}} / \mu\text{A}$	$\Gamma / \text{nmolcm}^{-2}$
5	0.13	2.3	29 ± 3
10	0.22	5.5	37 ± 4
15	0.22	5.5	36 ± 7
20	0.21	4.6	32 ± 3

Galicía-Luis *et.al.*,^{18,19} and Gomez-Hernandez¹⁹ were able to establish that the 5 aphen ligand was fully protonated at $\text{pH} < 0.9$. According to the authors, this was the species responsible for the growth of the film formed during to electropolymerisation yielding best features and good stability.²⁰ This was the reason a very low pH range (*i.e.*, pH 0.2-0.3) was chosen for the present study.

In sharp contrast to the behaviour observed in acetonitrile, Figure 4.6 and 4.7 show that in aqueous sulphuric acid the voltammetric response for both $[\text{Ru}(\text{aphen})_2\text{bpy}]^{2+}$ and $[\text{Ru}(\text{aphen})_3]^{2+}$, are irreversible. For $[\text{Ru}(\text{aphen})_2\text{bpy}]^{2+}$, oxidation and reduction peaks are observed at +1.6 V and +0.6 V and for $[\text{Ru}(\text{aphen})_3]^{2+}$ at +1.5 V and +0.5 V, respectively. The value of $i_{\text{pa}}/i_{\text{pc}}$ for both these complexes lies in the range of 0.20-0.40 compared to the expected value of unity for a reversible response. Significantly, the response does not approach ideality at slow scan rates. This suggests that slow heterogeneous electron transfer is not the origin of the irreversibility but rather arises because of a following chemical reaction. This is also supported by the fact that during polymerisation, the growth cycles are characterised by an enhanced Ru(II)

oxidation current and a diminished Ru(III) reduction current suggesting that there may be some catalytic electrochemical/chemical reaction sequence taking place.¹⁷

Though a definitive conclusion cannot be reached with the data in hand, the most likely explanation would be that the pK_a of the amino phenanthroline functionalities depends on the oxidation state of the ruthenium centre. A change in protonation state upon electron transfer will change the electron density on the ruthenium thus causing the half-wave potentials for oxidation and reduction to be very different from one another.^{21,22} However, this issue has not been investigated in detail for metal complexes although it has been reported that addition of a few drops of concentrated sulphuric acid to a solution of $[Ru(bpy)_2(aphen)]^{2+}$ in phosphate buffer eliminated the oxidation peak associated with aphen oxidation and inhibited film formation.²³

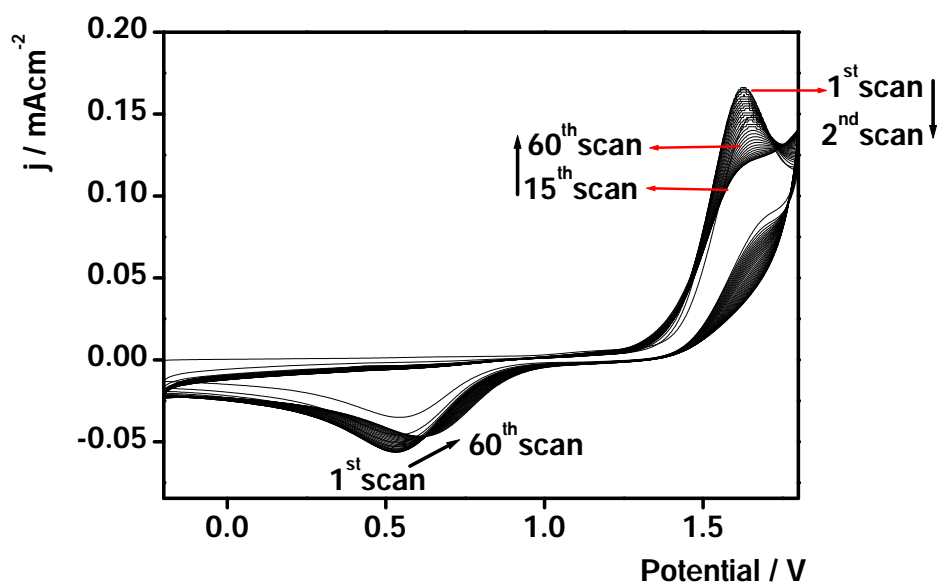


Figure 4.6: Interfacial electropolymerisation from a 1.5 mM solution $[\text{Ru}(\text{aphen})_2\text{bpy}]^{2+}$ on a 3 mm diameter glassy carbon electrode, at a scan rate of 0.1 Vs^{-1} . A total of 60 scanning cycles were applied and the deposition medium was aqueous $0.5 \text{ M H}_2\text{SO}_4$ (pH 0.3).

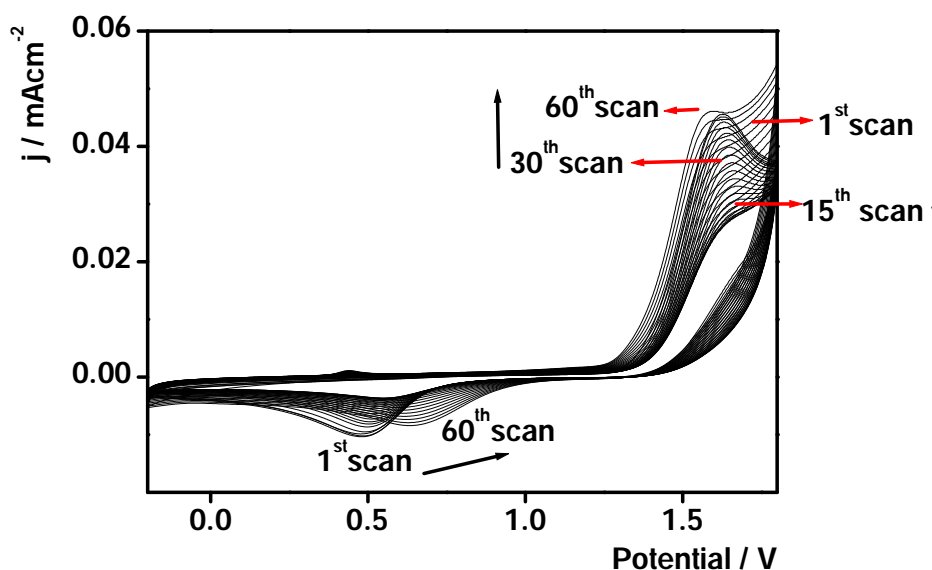


Figure 4.7: Interfacial electropolymerisation from a 1.0 mM solution $[\text{Ru}(\text{aphen})_3]^{2+}$ on a 3 mm diameter glassy carbon electrode at a scan rate of 0.1 Vs^{-1} . A total of 60 scanning cycles were applied and the deposition medium was aqueous $0.5 \text{ M H}_2\text{SO}_4$ (pH 0.3).

After 60 scans at 0.1 Vs^{-1} the electrodes were removed from their respective cells, rinsed thoroughly with deionized water and transferred to a cell containing blank electrolyte solution ($0.5 \text{ M H}_2\text{SO}_4$, pH 0.3). The presence of a persistent voltammetric response associated with the $\text{Ru}^{2+/3+}$ couple is observed, as shown in Figure 4.8 and 4.9, suggesting that redox active films are formed on the electrode surfaces in both cases. However, the response of the films is not consistent with that expected for a surface-confined species undergoing a reversible one-electron transfer reaction. For example, the ratio of anodic to cathodic current ($i_{\text{pa}}/i_{\text{pc}}$) for $[\text{Ru}(\text{aphen})_2\text{bpy}]^{2+}$ and $[\text{Ru}(\text{aphen})_3]^{2+}$, lies in the range of 0.2-0.4 compared to the value of unity expected for a reversible response. The charge passed under the peak at +1.5 V yields a surface coverage of $(1.6 \pm 0.8) \times 10^{-11} \text{ mol cm}^{-2}$ for the bis aminophen complex. It is interesting to note that despite using 6 times more scan cycles compared to the bis aminophen complex in acetonitrile, the surface coverage is almost an order of magnitude lower when the electropolymerisation is carried out in sulphuric acid rather than in acetonitrile. However, for ruthenium tris aminophen, increasing the number

of scan cycles from 10 in acetonitrile to 60 in sulphuric acid, almost doubles the surface coverage to $(4.4 \pm 0.6) \times 10^{-8} \text{ mol cm}^{-2}$. This suggests that for better film coverages, the type of solvent and the number of scan cycles are crucial factors.

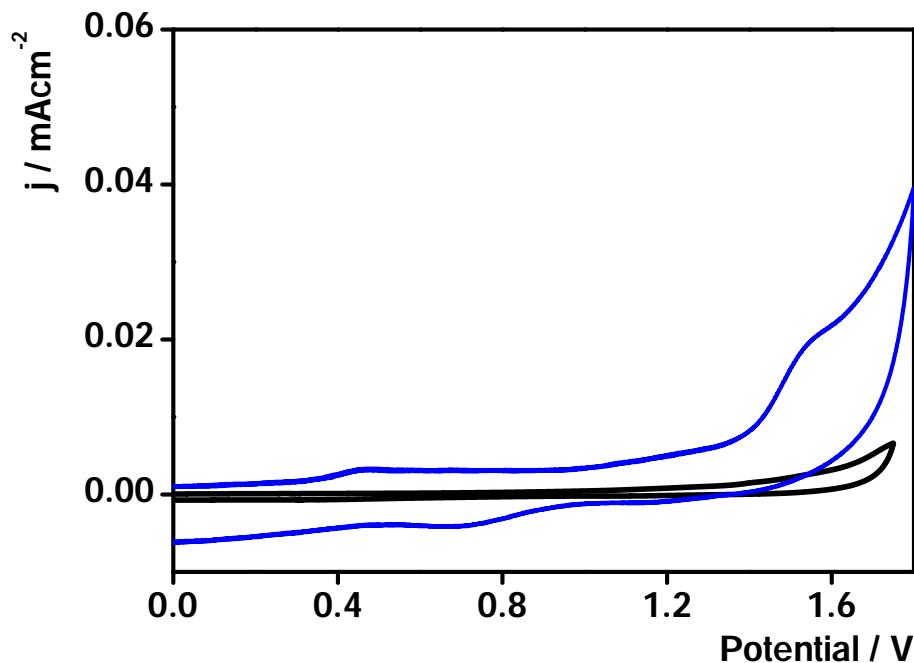


Figure 4.8: Voltammetric behaviour following electrodeposition, of $[\text{Ru}(\text{aphen})_2\text{bpy}]^{2+}$ (—), in blank aqueous 0.5 M H_2SO_4 (pH 0.3) after 60 cycles, at a scan rate of 0.1 Vs^{-1} . Cyclic voltammogram of blank GCE in aqueous 0.5 M H_2SO_4 (pH 0.3) is given by (—).

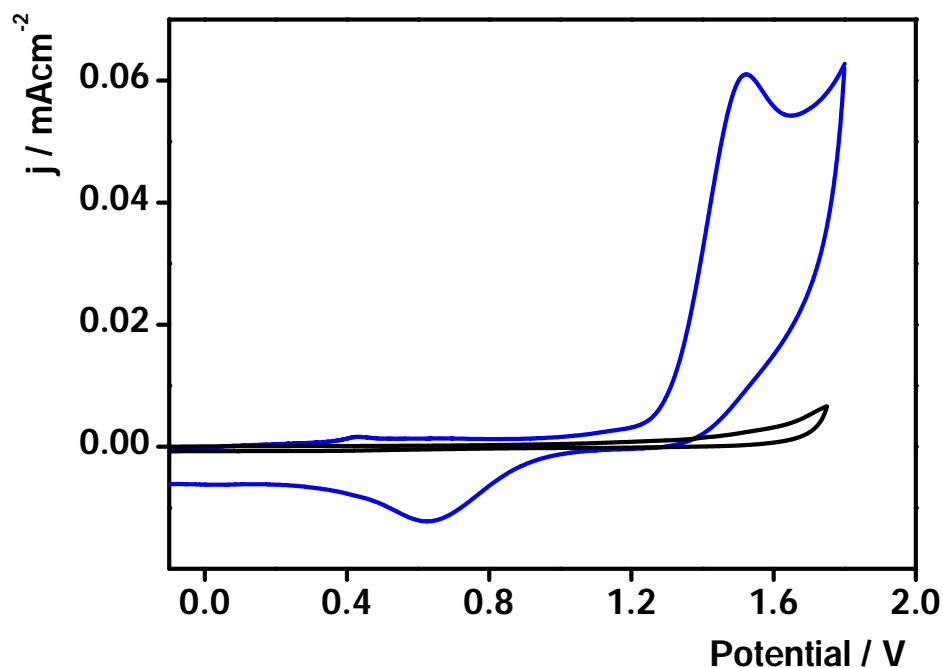
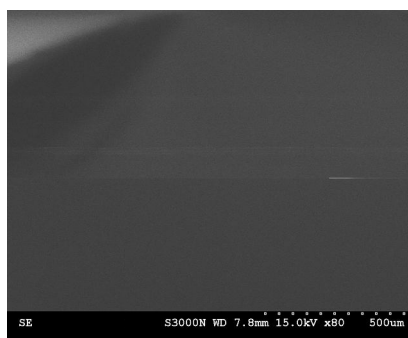


Figure 4.9: Voltammetric behaviour following electrodeposition, of $[\text{Ru}(\text{aphen})_3]^{2+}$ (—), in blank aqueous 0.5 M H_2SO_4 (pH 0.3) after 60 cycles at a scan rate of 0.1 V s^{-1} . Cyclic voltammogram of blank GCE in aqueous 0.5 M H_2SO_4 (pH 0.3) is given by (—).

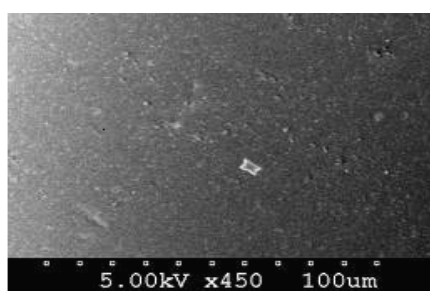
4.3.2 S.E.M

In order to probe the morphology of the films formed in the two different media, scanning electron microscopy (SEM) was performed on films of $[\text{Ru}(\text{aphen})_2\text{bpy}]^{2+}$ and $[\text{Ru}(\text{aphen})_3]^{2+}$ formed in both acetonitrile and sulphuric acid. Figure 4.10 shows SEM images of the bare glassy carbon electrode (A), electropolymerised $[\text{Ru}(\text{aphen})_2\text{bpy}]^{2+}$ film formed in acetonitrile (B) and sulphuric acid (C), respectively.

(A)



(B)



(C)

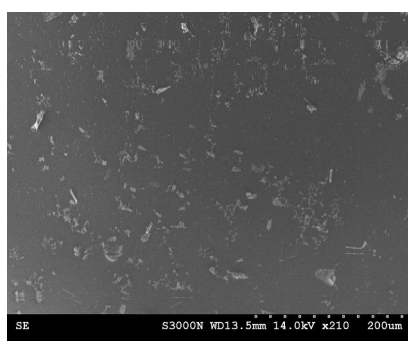
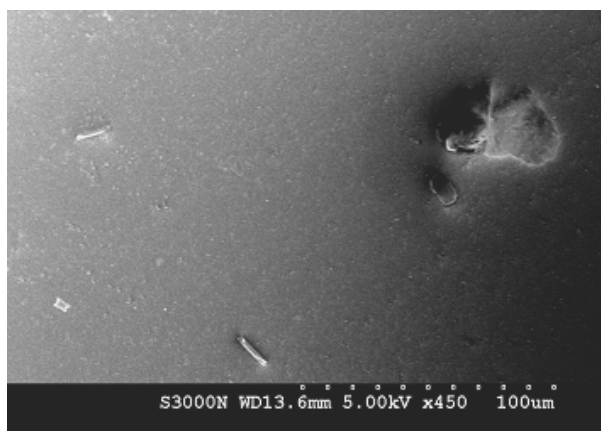


Figure 4.10: SEM images of bare glassy carbon electrode (A) and films of [Ru(aphen)₂bpy]²⁺ electropolymerised on a 1.5 mm radius glassy carbon electrode from anhydrous acetonitrile (B) and sulphuric acid (C).

(A)



(B)

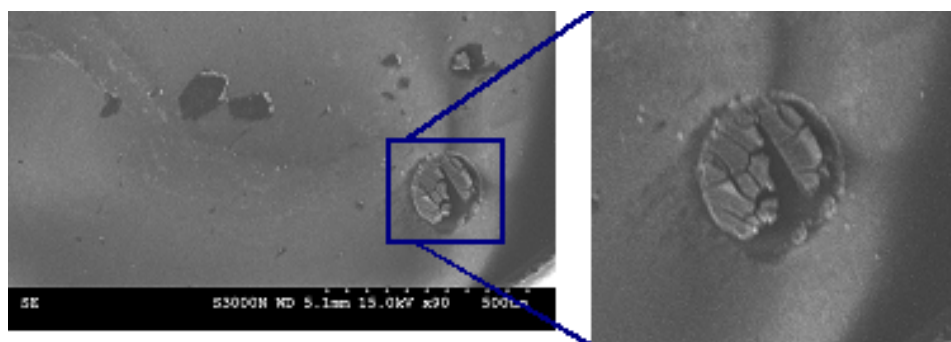


Figure 4.11: SEM images of films of $[\text{Ru}(\text{aphen})_3]^{2+}$ electropolymerised on 1.5 mm radius glassy carbon electrodes from anhydrous acetonitrile (A) and sulphuric acid (B). A small defect region has been enlarged for better clarity.

Figure 4.11 shows SEM of $[\text{Ru}(\text{aphen})_3]^{2+}$ films formed in acetonitrile and sulphuric acid and even they appear continuous and smooth, similar to the $[\text{Ru}(\text{aphen})_2\text{bpy}]^{2+}$ films.

From the SEM images, it is clear that both $[\text{Ru}(\text{aphen})_2\text{bpy}]^{2+}$ and $[\text{Ru}(\text{aphen})_3]^{2+}$ form rather smooth continuous films on the surface. Wide area views of films formed in both solvents confirm that a continuous film covers the whole electrode surface. Although the electropolymerised films cover the entire

electrode surface, SEM images show that they are not free from all defects. Some electrodes exhibit small patches of uncovered electrode surface and burst blisters as shown in Figure 4.11 (A) and enlarged view of Figure 4.11 (B). These defects could be due to the presence of some impurity adsorbed onto the surface of the carbon electrode prior to electropolymerisation. The surface of the carbon electrode is also not atomically smooth and hence it may have defects like dislocation lines or varying surface density¹⁷ which may again influence the continuous film formation on the electrode surface. Also, exposure of the films to vacuum while capturing scanning electron microscopic images may have caused the ‘burst blister’ like structures that we see in Figure 4.11(B). Irrespective of the presence of small defects, the majority of the electrode surface is defect free with a smooth and even electrochemically synthesised polymer layer being formed which is potentially useful for sensor applications.^{24,25}

4.3.3 Evaluation of charge transfer coefficients

The sensitivity of an ECL sensor will ultimately be dictated by the rate at which the Ru^{3+} sites can be regenerated. Therefore, it is important to determine the rate of charge transport through the film leading to the conversion of the inactive Ru^{2+} centres into the Ru^{3+} centres that can react with co-reactant to generate an electronically excited state, Ru^{2+*} . For semi-infinite electrochemical charge diffusion through surface confined redox layer, $v^{1/2}$ dependence of the peak current is seen and the peak current itself is given by the same equation as that used for species dissolved in solution and diffusing to the electrode surface, *i.e.*, Equation 1.21. It characterises the movement of charge through the film.¹⁷

The rate of charge transport through the electropolymerised film can be quantified by measuring the D_{CT} using cyclic voltammetry. The lower limit on the range of useful scan rates in cyclic voltammetry is dictated by the requirement that the depletion layer thickness be significantly less than the overall film thickness, while the upper scan rate is limited by the rate of heterogeneous electron transfer across the electrode layer interface.

Figure 4.12 shows the voltammetric response of the electrodeposited film of $[\text{Ru}(\text{aphen})_2\text{bpy}]^{2+}$ in blank 0.1 M $\text{CH}_3\text{CN}/\text{TBATFB}$ solution at scan rates 0.1-0.4 Vs^{-1} . The i_{pa} and i_{pc} values at various scan rates are given in Table 4.2 and the dependence of the voltammetric response on these scan rates is shown in Figure 4.13. It can be clearly seen that the peak current, i_{pa} , is proportional to the root of scan rate at higher scan rates and this is indicative of semi-infinite linear diffusion control for the surface bound redox species.²⁶ Therefore, for 0.1 $\text{Vs}^{-1} < \nu < 0.4 \text{ Vs}^{-1}$, Randles-Sevcik equation can be used to derive the charge transport diffusion coefficient, D_{CT} .^{11,27,28}

It is found that ΔE_p is 50 mV, which is slightly different when compared to the 57 mV value that is expected for an ideally reversible response. The charge passed is $3.1 \pm 0.05 \mu\text{C}$ corresponding to a surface coverage of $(4.6 \pm 0.5) \times 10^{-10} \text{ molcm}^{-2}$.

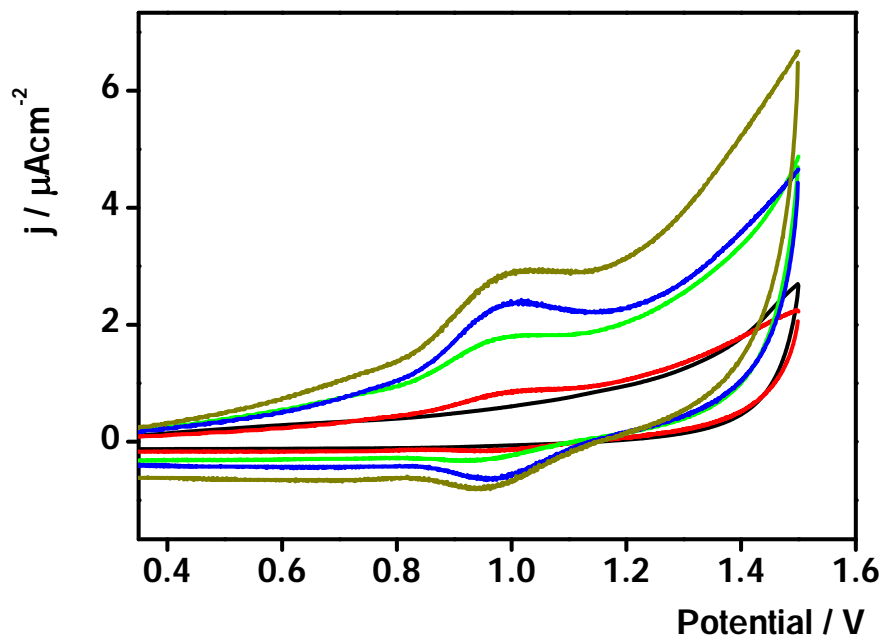


Figure 4.12: Scan rate dependence of the voltammetric response for a thin film of $[\text{Ru}(\text{aphen})_2\text{bpy}]^{2+}$ [$\Gamma = (4.6 \pm 0.5) \times 10^{-10} \text{ mol cm}^{-2}$] electropolymerised on a 3 mm diameter glassy carbon electrode. The supporting electrolyte is 0.1 M $\text{CH}_3\text{CN/TBATFB}$. The electrolyte used here and the deposition solution are the same. The scan rates are from top to bottom 0.4 (—), 0.3 (—), 0.2 (—) and 0.1 (—) Vs^{-1} . Blank glassy carbon electrode in 0.1 M $\text{CH}_3\text{CN/TBATFB}$ is given by (—).

Table 4.2: Peak currents and standard errors of electrodeposited film of $[\text{Ru}(\text{aphen})_2\text{bpy}]^{2+}$ on glassy carbon electrode, in blank 0.1 M $\text{CH}_3\text{CN}/\text{TBATFB}$ solution at scan rates 0.1-0.4 Vs^{-1} .

Scan rate / Vs^{-1}	$i_{\text{Pa mean}} / \mu\text{A}$	$i_{\text{Pc mean}} / \mu\text{A}$
0.1	6.2 ± 0.2	-9.5 ± 0.1
0.2	13.3 ± 0.3	-2.6 ± 0.6
0.3	17.6 ± 0.5	-4.8 ± 0.2
0.4	22.2 ± 0.1	-6.2 ± 0.3

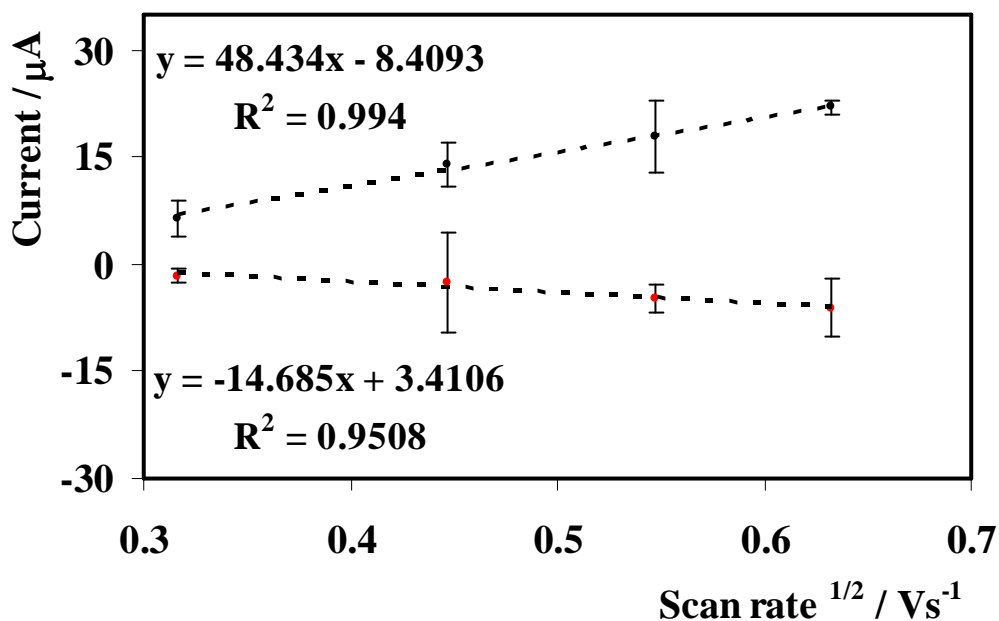


Figure 4.13: Peak current dependence vs. root of scan rate for $[\text{Ru}(\text{aphen})_2\text{bpy}]^{2+}$ electropolymerised film on a 3 mm diameter glassy carbon electrode in 0.1 M $\text{CH}_3\text{CN}/\text{TBATFB}$.

The slope of the Randles-Sevcik equation, Equation 1.21, was calculated by substituting appropriate values for various parameters and the charge transfer diffusion coefficient, D_{CT} , was found to be $(1.1 \pm 0.8) \times 10^{-11} \text{ cm}^2 \text{ s}^{-1}$.

Figure 4.14 shows the voltammetric response for electrodeposited films of $[\text{Ru}(\text{aphen})_3]^{2+}$ from 0.1 M $\text{CH}_3\text{CN}/\text{TBATFB}$ solution, at scan rates 0.1-0.4 Vs^{-1} . Figure 4.15 shows the dependence of the voltammetric response on the square root of the scan rates. Table 4.3 gives the values of i_{Pa} and i_{Pc} at these scan rates.

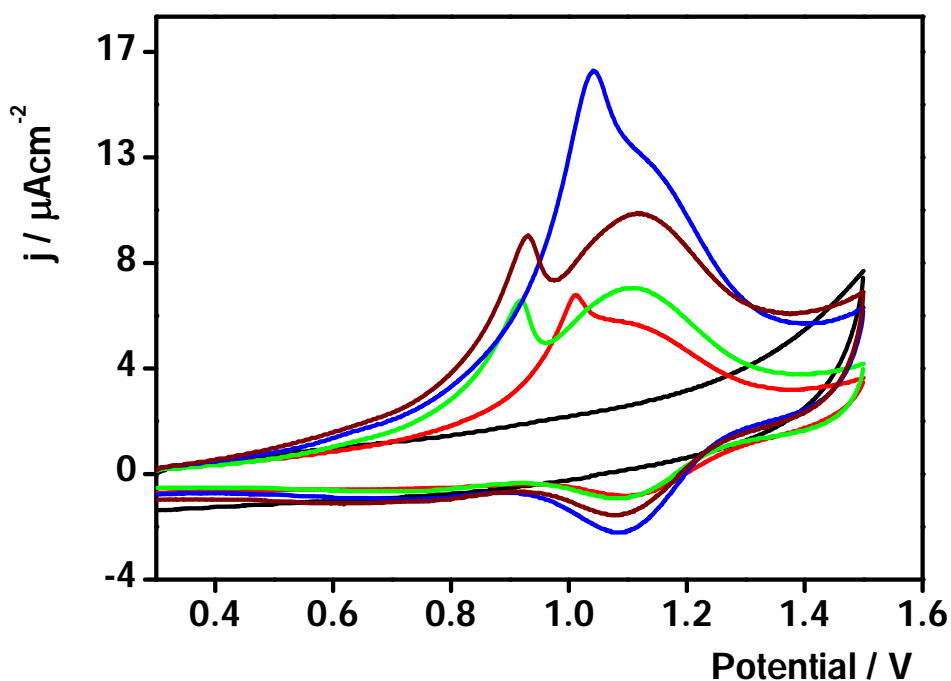


Figure 4.14: Scan rate dependence of the voltammetric response for a thin film of $[\text{Ru}(\text{aphen})_3]^{2+}$ ($\Gamma = 2.2 \pm 0.6 \times 10^{-8} \text{ mol cm}^{-2}$) electropolymerised on a 3 mm diameter glassy carbon electrode in 0.1 M $\text{CH}_3\text{CN}/\text{TBATFB}$. The scan rates are from top to bottom 0.4 (—), 0.3 (—), 0.2 (—) and 0.1 (—) Vs^{-1} . Blank glassy carbon electrode in 0.1 M $\text{CH}_3\text{CN}/\text{TBATFB}$ is given by (—).

Table 4.3: Peak currents and standard errors of electrodeposited film of $[\text{Ru}(\text{aphen})_3]^{2+}$ on glassy carbon electrode, in blank 0.1 M $\text{CH}_3\text{CN}/\text{TBATFB}$ solution at scan rates 0.1-0.4 Vs^{-1} .

Scan rate / Vs^{-1}	$i_{\text{Pa mean}} / \mu\text{A}$	$i_{\text{Pc mean}} / \mu\text{A}$
0.1	43.5±0.1	-5.7±0.6
0.2	52.8±0.1	-7.7±0.2
0.3	72.4±1.6	-11.0±1.4
0.4	82.5±9.2	-14.5±2.8

D_{CT} was found to be $(4.4 \pm 0.8) \times 10^{-11} \text{ cm}^2 \text{s}^{-1}$. It is perhaps important to note that the D_{CT} values stated above represent the lower bound of D_{CT} since any film swelling will decrease the ruthenium concentration causing D_{CT} to be underestimated.

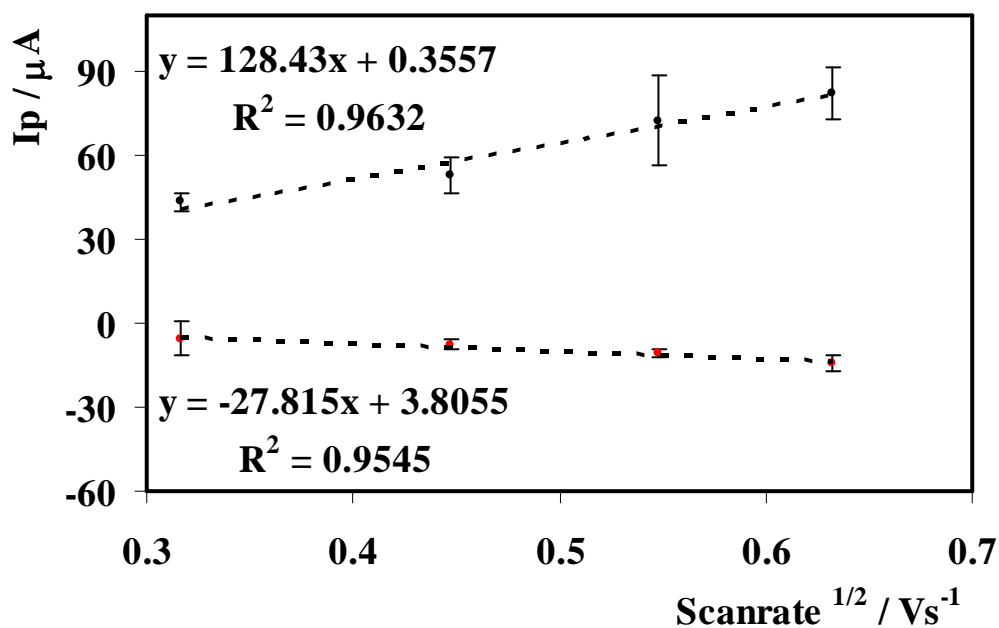


Figure 4.15: Peak current dependence vs. root scan rate for $[\text{Ru}(\text{aphen})_3]^{2+}$ electropolymerised film on a 3 mm diameter glassy carbon electrode in 0.1 M $\text{CH}_3\text{CN/TBATFB}$.

Figures 4.16 and 4.18 show voltammetric responses for electrodeposited films of $[\text{Ru}(\text{aphen})_2\text{bpy}]^{2+}$ and $[\text{Ru}(\text{aphen})_3]^{2+}$, in blank 0.5 M H_2SO_4 , pH 0.3, at scan rates 0.1-0.4 Vs^{-1} respectively. Figure 4.17 and 4.19 shows the dependence of the peak of the two films on the square root of the scan rates. The plot of i_p vs. root scan rate was found to be linear for both films and applying Randles-Sevcik equation, gave the homogeneous charge transport diffusion coefficient, D_{CT} to be $(6.9 \pm 0.4) \times 10^{-10} \text{ cm}^2 \text{ s}^{-1}$ for $[\text{Ru}(\text{aphen})_2\text{bpy}]^{2+}$, D_{CT} is $(9.6 \pm 0.6) \times 10^{-9} \text{ cm}^2 \text{ s}^{-1}$ for $[\text{Ru}(\text{aphen})_3]^{2+}$.

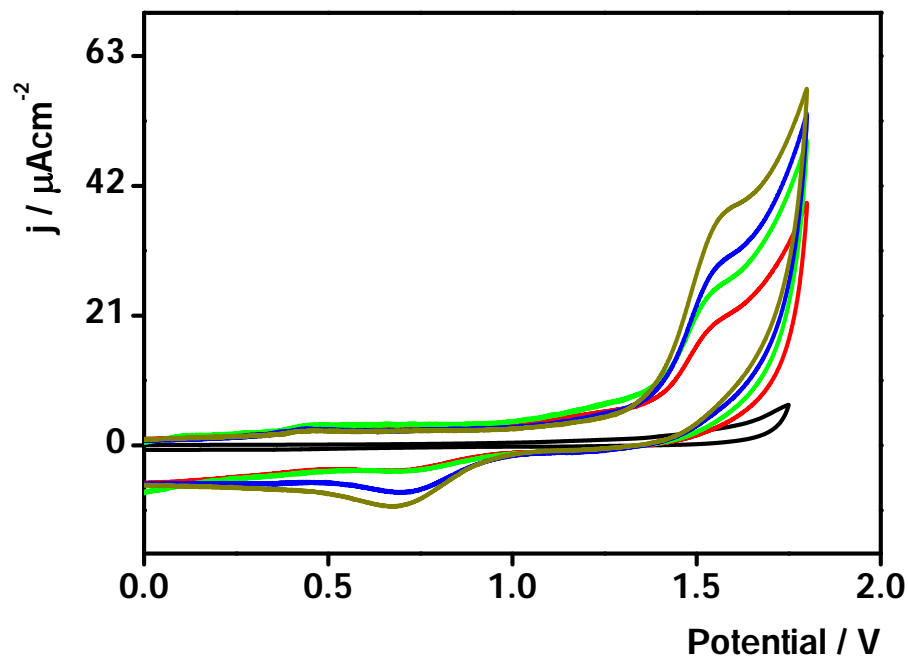


Figure 4.16: Scan rate dependence of the voltammetric response of a thin film of $[\text{Ru}(\text{aphen})_2\text{bpy}]^{2+}$ ($\Gamma=1.6\pm0.8\times10^{-11}\text{ molcm}^{-2}$) electropolymerised on a 3 mm diameter glassy carbon electrode in 0.5 M H_2SO_4 (pH 0.3). The scan rates are from top to bottom 0.4 (—), 0.3 (—), 0.2 (—) and 0.1 (—) Vs^{-1} . Blank glassy carbon electrode in 0.5 M H_2SO_4 (pH 0.3) is given by (—).

Table 4.4: Peak currents and standard errors of electrodeposited film of $[\text{Ru}(\text{aphen})_2\text{bpy}]^{2+}$ on glassy carbon electrode, in blank 0.5 M H_2SO_4 , pH 0.3, at scan rates 0.1-0.4 Vs^{-1} .

Scan rate / Vs^{-1}	$i_{\text{Pc mean}} / \mu\text{A}$	$i_{\text{Pa mean}} / \mu\text{A}$
0.1	137 ± 2	-27.8 ± 0.1
0.2	176 ± 0.1	-32.5 ± 0.2
0.3	205 ± 5	-55.2 ± 1.4
0.4	262 ± 7	-71.9 ± 1.5

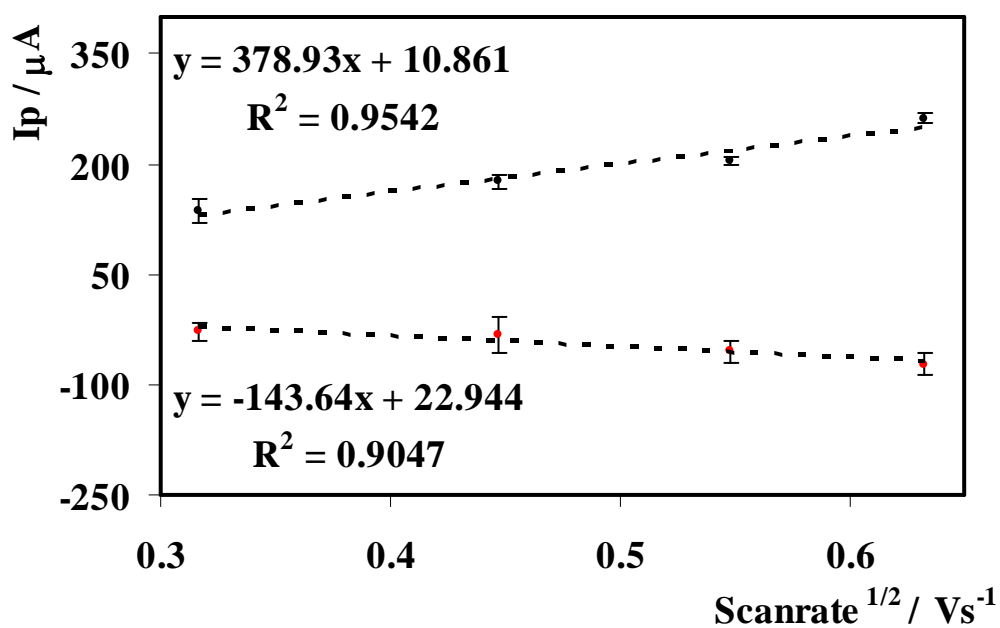


Figure 4.17: Peak current vs. square root of scan rate for $[\text{Ru}(\text{aphen})_2\text{bpy}]^{2+}$ electropolymerised film on a 3 mm diameter glassy carbon electrode in 0.5 M H_2SO_4 , electrolyte, pH 0.3.

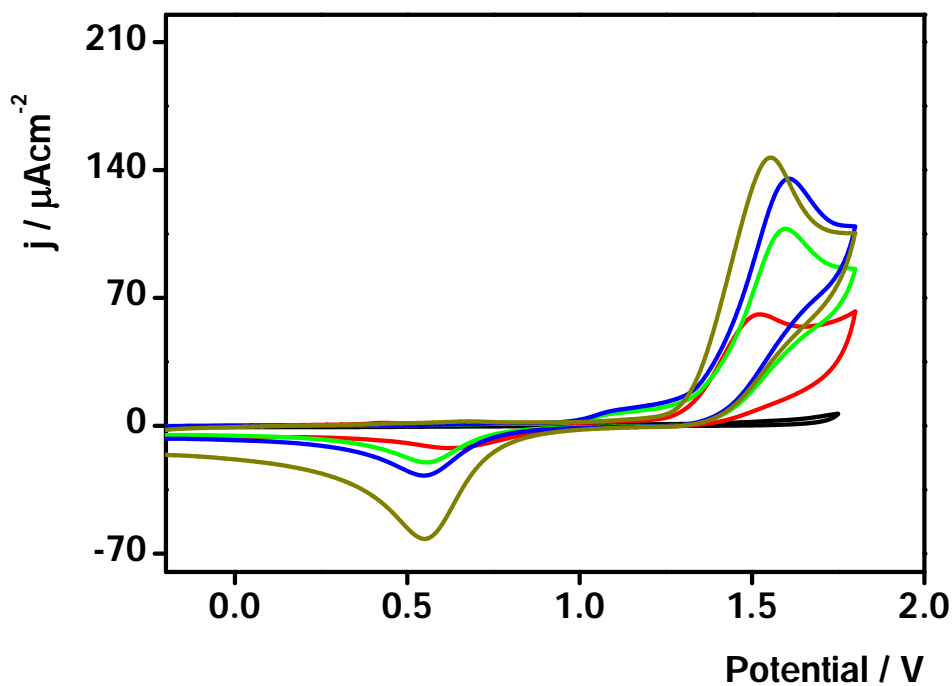


Figure 4.18: Scan rate dependence of the voltammetric response for a thin film of $[\text{Ru}(\text{apen})_3]^{2+}$, $[\Gamma=(4.4\pm0.6) \times 10^{-8}] \text{ molcm}^{-2}$, electropolymerised on a 3 mm diameter glassy carbon electrode in 0.5 M H_2SO_4 (pH 0.3). The scan rates are from top to bottom 0.4 (—), 0.3 (—), 0.2 (—) and 0.1 (—) Vs^{-1} . Blank glassy carbon electrode in 0.5 M H_2SO_4 (pH 0.3) is given by (—).

Table 4.5: Peak currents and standard errors of electrodeposited film of $[\text{Ru}(\text{aphen})_3]^{2+}$ on glassy carbon electrode, in blank 0.5 M H_2SO_4 , pH 0.3, at scan rates 0.1-0.4 Vs^{-1} .

Scan rate / Vs^{-1}	$i_{\text{Pa mean}} / \mu\text{A}$	$i_{\text{Pc mean}} / \mu\text{A}$
0.1	294 ± 14	-87.8 ± 0.5
0.2	435 ± 33	-185 ± 4
0.3	503 ± 45	-247 ± 5
0.4	566 ± 47	-400 ± 3

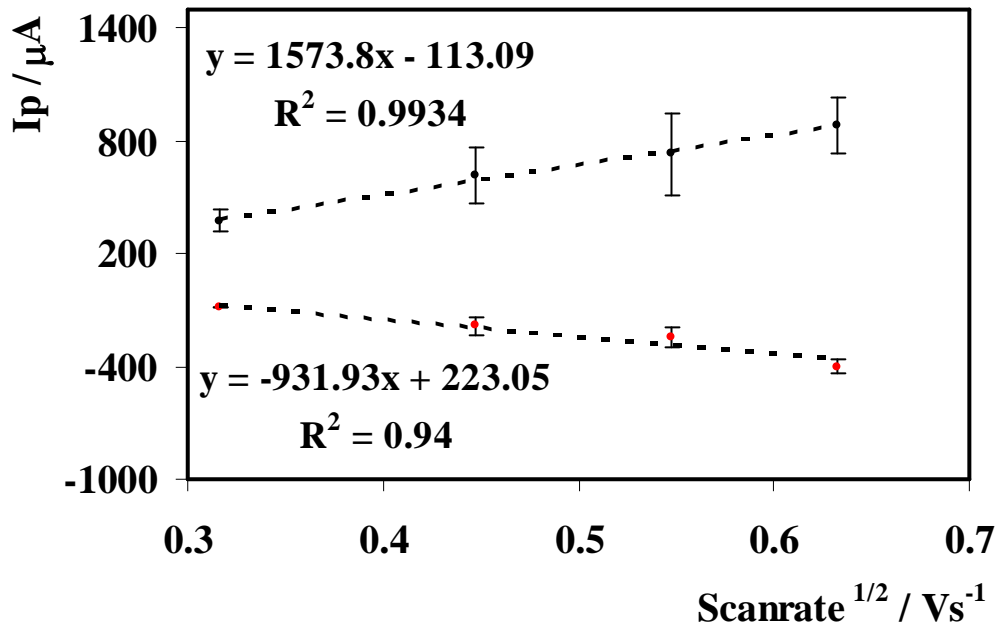


Figure 4.19: Peak current vs. square root of scan rate for a $[\text{Ru}(\text{aphen})_3]^{2+}$ electropolymerised film on a 3 mm diameter glassy carbon electrode in 0.5 M H_2SO_4 , electrolyte, pH 0.3.

Figure 4.16 shows the voltammogram of $[\text{Ru}(\text{apen})_2\text{bpy}]^{2+}$ in blank electrolyte (0.5 M H_2SO_4) in which the ligand oxidation peak at around +0.45 V can be identified.¹² The ΔE_P for the $\text{Ru}^{2+/3+}$ couple is very large, 80 mV, which is not consistent with a surface confined species undergoing reversible one-electron transfer reaction. This could be due to some following chemical reaction or slow heterogeneous charge transfer processes. However, when the charge transport values are compared for films deposited from the two media, the $[\text{Ru}(\text{apen})_2\text{bpy}]^{2+}$ films formed in sulphuric acid show a D_{CT} value which is roughly an order of magnitude faster than those found for films deposited from acetonitrile. Higher charge transport values may be due to swelling of the polymer matrix in the highly acidic medium.⁴⁹ Higher pH of the organic medium may impede charge transport through the polymer matrix due to absence of swelling of the polymer matrix which is usually favoured at low pH due to repulsive interactions between the protonated apen.

For $[\text{Ru}(\text{apen})_3]^{2+}$ films, the ratio i_{Pa}/i_{Pc} was found to be 0.6 instead of unity and the D_{CT} was $(9.6 \pm 0.6) \times 10^{-9} \text{ cm}^2 \text{ s}^{-1}$. In contrast, for $[\text{Ru}(\text{apen})_3]^{2+}$, increasing the number of scan cycles in sulphuric acid compared to acetonitrile, apparently increased the surface coverage also. However, the charge transfer coefficient was approximately two orders of magnitude higher than that found for the films of the same compound formed in acetonitrile. This behaviour in acid indicates that the lifetime of the cation radical of the amino-phenanthroline ligand may be large in sulphuric acid than in acetonitrile. Hence more polymer is formed per unit time. Both surface coverages and charge transfer coefficients have been summarized in Table 4.6. However, the observation that electropolymerisation proceeds in aqueous sulphuric acid is significant despite the non-ideal voltammetric responses.

Table 4.6: Apparent film coverages, formal potentials and D_{CT} values for oxidatively electropolymerised complexes at a scan rate 0.05 Vs^{-1} .

Complex/ /mM	Solvent	E_O/ V	E_R/ V	Scan cycles	Γ/ molcm^{-2}	D_{CT} / cm^2s^{-1}
[Ru(aphen)₂bpy] ²⁺ / 1.5	CH ₃ CN	+1.0	+0.94	10	4.6 ± 0.5 $\times 10^{-10}$	1.1 ± 0.8 $\times 10^{-11}$
[Ru(aphen)₂bpy] ²⁺ / 2.0	H ₂ SO ₄	+1.6	+0.5	60	1.6 ± 0.8 $\times 10^{-11}$	6.9 ± 0.4 $\times 10^{-10}$
[Ru(aphen)₃]²⁺ /1.0	CH ₃ CN	+1.1	+1.1	10	2.2 ± 0.6 $\times 10^{-8}$	4.4 ± 0.8 $\times 10^{-11}$
[Ru(aphen)₃]²⁺ /1.33	H ₂ SO ₄	+1.5	+0.6	60	4.4 ± 0.6 $\times 10^{-8}$	9.6 ± 0.6 $\times 10^{-9}$

For complexes of the general formula $[\text{Ru}(\text{bpy})_n(\text{aphen})_{3-n}]$, where $0 \leq n \leq 2$, monomer with $n=0$ gives better films²⁹ with respect to coverage and stability, compared to monomer with $n=2$. Indeed in this study, the ruthenium polypyridyl complex of the above general formula with $n=0$ gives better coverages compared to the one with $n=1$. The values of Γ obtained in acetonitrile media for $[\text{Ru}(\text{aphen})_3]^{2+}$ and $[\text{Ru}(\text{aphen})_2\text{bpy}]^{2+}$ compare very well with the values reported in literature.^{10,12}

4.3.4 Spectroscopic and photophysical studies

To investigate if the differences observed in the electrochemical behaviour of the polymers arise from structural differences in materials deposited from different solvents, the spectroscopic properties of the polymers were investigated using UV absorption, luminescence emission and Raman spectroscopies. Electronic spectroscopy has proved useful in characterisation of ruthenium containing polymers.³⁰ In particular the position of the lowest absorption maxima and the wavelength of emission are often characteristic of a particular ruthenium moiety.

Figures 4.20 and Figure 4.21 compare the absorption spectra of $[\text{Ru}(\text{aphen})_2\text{bpy}]^{2+}$ (—) and $[\text{Ru}(\text{aphen})_3]^{2+}$ (—) monomers with the electrochemically synthesised polymers dissolved into CH_3CN and H_2SO_4 respectively. The insets show an expanded view of the spectra of the electrochemically synthesised polymers. When the electrochemically synthesised polymers were dissolved off in acetonitrile, Figure 4.20, it is observed that all the electrochemically synthesised polymers show strong ligand centered $\pi \rightarrow \pi^*$ transition in the 200-300 nm range, the absorption maxima of the $d \rightarrow \pi^*$ MLCT transition around 450 nm similar to the monomers.^{10,31} All electrochemically synthesised polymers show strong amino phenanthroline peak at 355 nm,¹³ even though the bis monomer does not show strong peak at 355 nm. For ruthenium polypyridyl complexes the extinction coefficient, $\log \epsilon$, does not depend on the pH of the media and the value of $\log \epsilon$ of ruthenium monomers and polymers usually lies in the range of $\log \epsilon = 3$ to $\log \epsilon = 4$.^{17,24} Therefore, assuming the same extinction coefficient as the monomer and the Beer-Lambert law, the concentration of the metal centers in the polymer solution was calculated. These results have been tabulated in Table 4.7. Similarly, the electrochemically synthesised polymers were also dissolved off in sulphuric acid to investigate if the dissolution solvent had any effect on the absorption and emission properties of the electrochemically synthesised polymers. These results have been tabulated in Table 4.8.

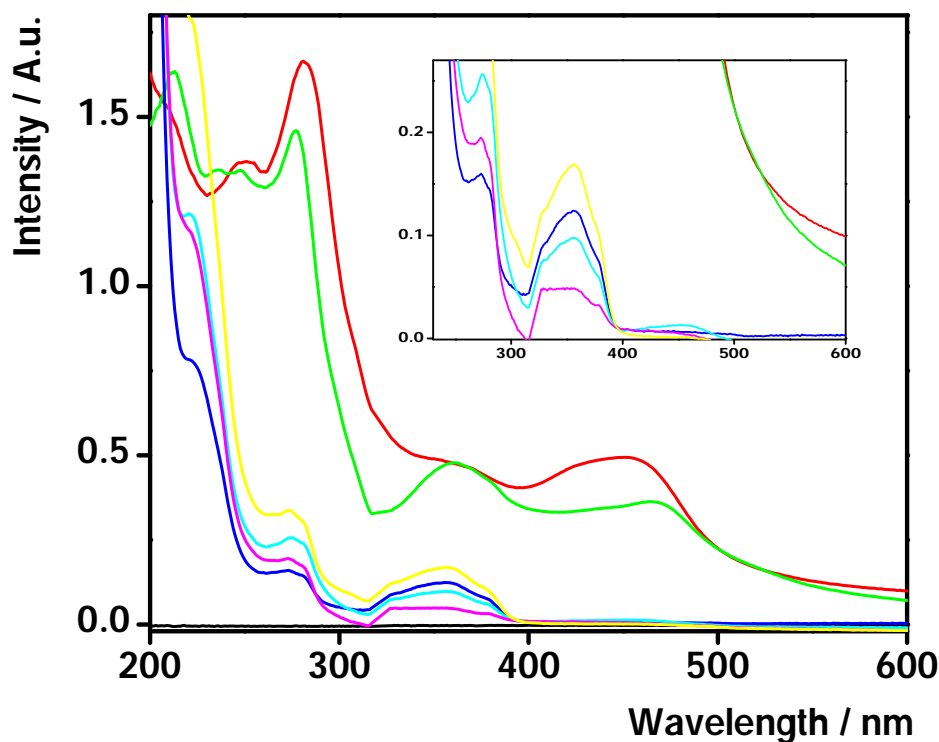


Figure 4.20: Absorption spectra of 125 μM $[\text{Ru}(\text{aphen})_2\text{bpy}]^{2+}$ (—) and 31.25 μM $[\text{Ru}(\text{aphen})_3]^{2+}$ (—) monomers and electrochemically synthesised polymers dissolved off from the GCE electrode surface into spectroscopic grade CH_3CN . A quartz cuvette with 1 cm path length was used. 0.63 μM $[\text{Ru}(\text{aphen})_2\text{bpy}]^{2+}$ in CH_3CN as deposition medium is given by (—), 3.20 μM $[\text{Ru}(\text{aphen})_2\text{bpy}]^{2+}$ in H_2SO_4 as deposition medium is given by (—), 0.76 μM $[\text{Ru}(\text{aphen})_3]^{2+}$ in CH_3CN as deposition medium is given by (—), 0.5 μM $[\text{Ru}(\text{aphen})_3]^{2+}$ in H_2SO_4 as deposition medium is given by (—) and blank CH_3CN is given by (—).

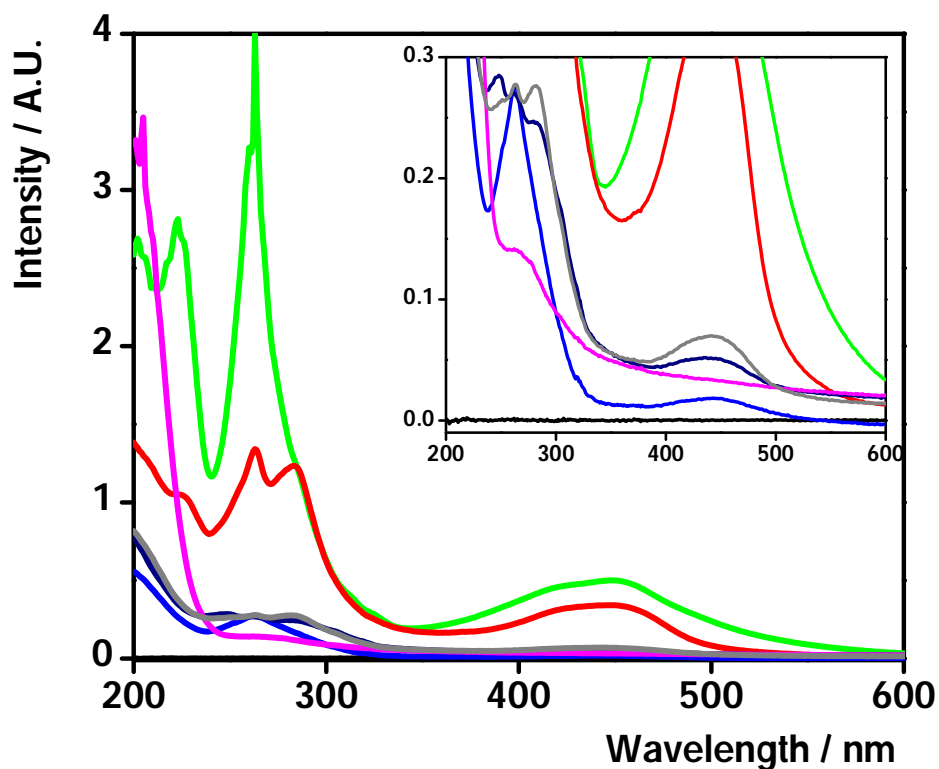


Figure 4.21: Absorption spectra of 125 μM $[\text{Ru}(\text{phen})_2\text{bpy}]^{2+}$ (—) and 31.25 μM $[\text{Ru}(\text{phen})_3]^{2+}$ (—) monomers and electrochemically synthesised polymers dissolved off from the GCE electrode surface into HPLC grade 0.5 M H_2SO_4 (pH 0.3). A quartz cuvette with 1 cm path length was used. $[\text{Ru}(\text{phen})_2\text{bpy}]^{2+}$ in CH_3CN as deposition medium is given by (—), 15.8 μM $[\text{Ru}(\text{phen})_2\text{bpy}]^{2+}$ in H_2SO_4 as deposition medium is given by (—), 2.5 μM $[\text{Ru}(\text{phen})_3]^{2+}$ in CH_3CN as deposition medium is given by (—), 8.8 μM $[\text{Ru}(\text{phen})_3]^{2+}$ in H_2SO_4 as deposition medium is given by (—) and blank 0.5 M H_2SO_4 (pH 0.3) is given by (—).

Table 4.7: Absorption and emission data of ruthenium monomers and electrochemically synthesised polymers. A known concentration of the monomer was used along with Beer-Lambert law to determine the extinction co-efficient. The electrochemically synthesised polymers were dissolved off into acetonitrile from the electrode surface by prolonged sonication. Assuming the same extinction co-efficient as their respective monomers, the concentration of the polymers was determined using Beer-Lambert law.

Complex / deposition solution	MLCT^a absorption at rt, nm	log ϵ	λ_{max}^a (emission) at rt, nm	C / μM
[Ru(aphen) ₂ bpy] ²⁺ / monomer in CH ₃ CN	450	3.5	610	125
[Ru(aphen) ₂ bpy] ²⁺ / polymer from CH ₃ CN	453	3.5	614	0.63
[Ru(aphen) ₂ bpy] ²⁺ / polymer from H ₂ SO ₄	445	3.5	610	3.20
[Ru(aphen) ₃] ²⁺ / monomer in CH ₃ CN	467	3.9	606	31.3
[Ru(aphen) ₃] ²⁺ / polymer from CH ₃ CN	454	3.9	606	0.76
[Ru(aphen) ₃] ²⁺ / polymer from H ₂ SO ₄	454	3.9	596	0.50

^a Measured in acetonitrile. rt –room temperature.

Table 4.8: Absorption and concentration data of ruthenium monomers and electrochemically synthesised polymers. A known concentration of the monomer was used along with Beer-Lambert law to determine the extinction co-efficient. The electrochemically synthesised polymers were dissolved off into 0.5 M H₂SO₄ (pH 0.3) from the electrode surface by prolonged sonication. Assuming the same extinction co-efficient as their respective monomers, the concentration of the polymers was determined using Beer-Lambert law.

Complex / deposition solution	MLCT^b absorption at rt, nm	log ϵ	C / μM
[Ru(aphen) ₂ bpy] ²⁺ / monomer in H ₂ SO ₄	445	3.5	125
[Ru(aphen) ₂ bpy] ²⁺ / polymer from CH ₃ CN	-	-	-
[Ru(aphen) ₂ bpy] ²⁺ / polymer from H ₂ SO ₄	435	3.5	15.8
[Ru(aphen) ₃] ²⁺ / monomer in H ₂ SO ₄	447	3.9	31.3
[Ru(aphen) ₃] ²⁺ / polymer from CH ₃ CN	443	3.9	2.5
[Ru(aphen) ₃] ²⁺ / polymer from H ₂ SO ₄	440	3.9	8.8

^bMeasured in 0.5 M H₂SO₄ (pH 0.3). rt –room temperature.

From Tables 4.7 and 4.8, it is clear that not much variation is observed in the position of the lowest absorption maxima and the wavelength of emission between the monomers and the electrochemically synthesised polymers. Also, the solvents do not seem to have any major effect. However, the bis electrochemically synthesised polymer formed in acetonitrile did not show any emission when dissolved off the electrode in sulphuric acid. But the polymer shows good emission when dissolved into acetonitrile, the lack of emission in sulphuric acid could just be due to solubility issues. There are also slight blue / red shifts observed in few of the electrochemically synthesised polymers as seen from the two tables. It is a well known fact that the absorption peaks of complexes tend to shift slightly towards blue or red regions when the micro environment of the molecule is perturbed.^{32,33} As the micro environment experienced by the monomer molecules in solution will be different from the polymer molecules due to the presence of oligomers of different monomeric units and longer polymer chains, a slight shift in the emission after polymerisation is quite expected.

Before dissolution of the polymers from the surface of the electrode, they were probed with confocal fluorescence microscope with a 458 nm laser. No emission was detected from the surface. The importance of oxygen containing functional groups to carbon electrode surface chemistry, particularly with respect to electrochemical processes is well known.^{34,35} Surface oxides form spontaneously on most carbon surfaces in air, and are unavoidable without special effort, such as ultra high vacuum (UHV) or heat treatment.³⁵⁻³⁷ There is a significant fraction of surface oxygen groups on glassy carbon electrode surface. The surface oxide distribution is highly sensitive to initial conditions and subsequent chemical treatment of the electrode.³⁷ However, it is known that the fluorescence is quenched on the GC surface unless the fluorescent label is a significant distance from the surface. But monolayers of ruthenium polypyridyl complexes have been shown to retain luminescence on metallic surfaces, which are also well known for quenching fluorescence.³⁸ In addition, polymer films such as those described here would not be expected to be completely quenched as the layers are thicker than a monolayer.³⁹

Murcia and co-workers,¹⁹ found that though N-C, C-C coupling play a key role in the electropolymerisation of aminophenanthroline ligand, aromatic C=C bonds also actively participate in the polymerisation process. Taking these two facts into account two possibilities exist. Loss of luminescence may arise because of the quenching by the surface oxide groups present on the glassy carbon electrode surface or there is loss of aromaticity of phenanthroline ligands upon electropolymerisation. Hence, to investigate these possibilities the pre-formed metallopolymers were dissolved off the electrode by prolonged sonication in acetonitrile.

The monomers used in this study contain two to three reactive apen ligands, which might be expected to lead to the formation of highly crosslinked network polymers. Based on degree of crosslinking two types of network polymers exists, covalent chemically crosslinked polymers and physically crosslinked polymers.⁴⁰ When the polymerisation process leads to covalent chemically crosslinked polymers, if previously soluble, it will no longer dissolve (except for some ionically crosslinked polymers) because crosslinking causes tremendous increase in their molecular weight.⁴¹ However, physically crosslinked polymers *i.e.*, polymer that are not heavily crosslinked, can usually be dissolved in some solvent.^{22, 41}

The fact that the electrochemically synthesised polymers could be dissolved off the electrode surface confirms that polymers are not extensively crosslinked. Cyclic voltammogram of the electrodes after dissolution of the electrochemically synthesised polymers did not show any redox peaks and resembled CV's of bare glassy carbon electrode in 0.1 M CH₃CN with TBATFB supporting electrolyte. This kind of behaviour is observed when there is very little electroactive material on the surface of the electrode *i.e.*, all the material is removed by prolonged sonication. Significantly, all polymer solutions exhibited the characteristic ruthenium polypyridine metal-to-ligand charge transfer (MLCT) emission peak at approximately 610 nm upon photo excitation, as shown in Figure 4.22. It also appears that the relative emission intensities do not depend strongly on the deposition medium. The fact that the polymers emit suggests that the aromaticity of the ligand is preserved upon

electropolymerisation and that the reaction mechanism is similar in both the solvents. Therefore, the absence of emission from the electrode surface is most likely due to quenching by the electrode surface.

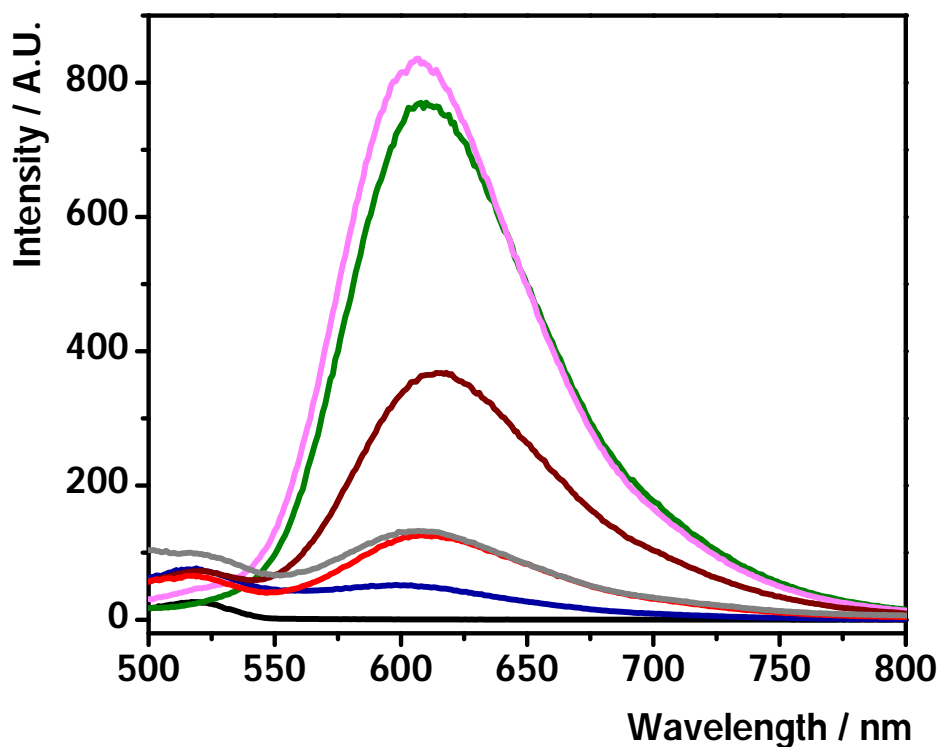


Figure 4.22: Emission spectra of 125 μM $[\text{Ru}(\text{aphen})_2\text{bpy}]^{2+}$ (—) and 31.3 μM $[\text{Ru}(\text{aphen})_3]^{2+}$ (—) monomers and electropolymerised films that were initially formed in the two different solvents *i.e.*, CH_3CN and H_2SO_4 , then dissolved off the electrode into acetonitrile. The electrochemically synthesised polymers were subjected to their respective excitation (*i.e.*, given by table 4.1), with a slit width of 10 nm, quartz cuvette, 1 cm path length. $[\text{Ru}(\text{aphen})_2\text{bpy}]^{2+}$ in CH_3CN as deposition medium is given by brown line (—), $[\text{Ru}(\text{aphen})_2\text{bpy}]^{2+}$ in H_2SO_4 as deposition medium is given by (—), $[\text{Ru}(\text{aphen})_3]^{2+}$ in CH_3CN as deposition medium is given by (—), $[\text{Ru}(\text{aphen})_3]^{2+}$ in H_2SO_4 as deposition medium is given by (—) and blank acetonitrile is given by (—).

The exact mechanism of the apen polymerisation reaction is not fully elucidated but is likely to involve an NH^\bullet radical.^{11,15} For the case of metal-bound 5-amino-1,10-phenanthroline, the initial step is a ligand-based one-electron oxidation to form an $\text{apen}^{\bullet+}$ radical cation. The radical cation thus formed is then thought to lose a proton to form active NH^\bullet radical species. This species may possess a number of contributing resonance structures as illustrated in Figure 4.23. These can then react with other apen ligands to form N-N, N=N (reaction of NH^\bullet) or N=C (reaction of 5-imino (iphen $^\bullet$)) linkages.¹⁰ For example, if we consider the complex $[\text{Ru}(\text{apen})_2\text{bpy}]^{2+}$, Figure 4.24, 1a and 1b depict the possible resonance structures of the apen^\bullet species and 2 and 3 depict how the radical species could react with the other apen ligands. Structure 3 on further oxidation with C-N or C-C coupling will propagate polymer growth.¹⁹

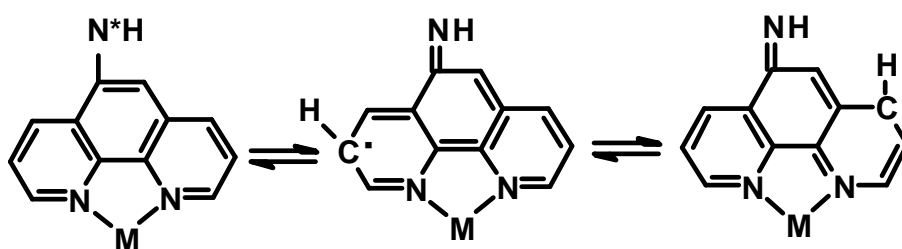


Figure 4.23: Resonance structures of apen^\bullet radical species

1)

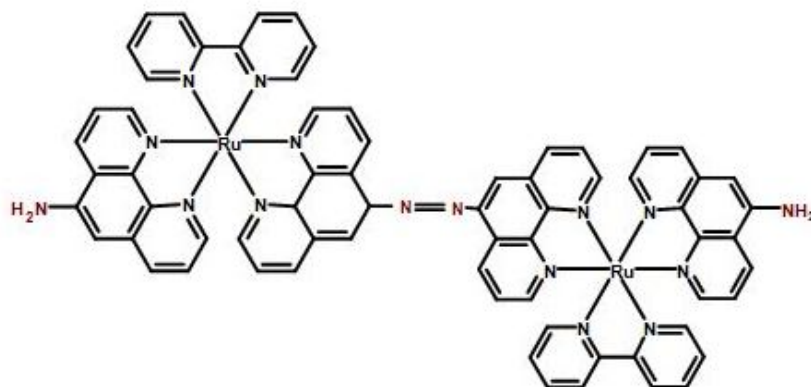
(a)



(b)



2)



3)

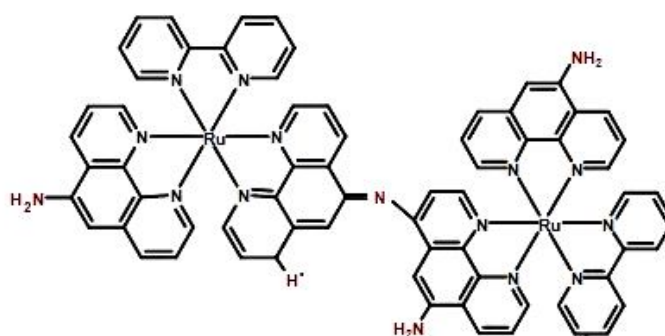


Figure 4.24: Resonance structures of apen[•] species of [Ru(apen)₂bpy]²⁺ complex (1a), (1b) and mechanism of polymer growth through N=N (2), N=C (3) linkages.

As all the electrochemically synthesised polymers exhibit MLCT transition states, they are also expected to exhibit ECL.

Thus, the metallopolymers exhibit similar absorption and emission spectra, irrespective of the deposition medium. However, vibrational spectroscopy can directly and sensitively probe subtle differences in the structure of the polymers formed.

4.3.5 Resonance Raman spectroscopy

Figure 4.25 (A) shows the resonance Raman spectra of $[\text{Ru}(\text{aphen})_2\text{bpy}]^{2+}$ monomer drop-cast onto glass (—), and thin electropolymerised film (—) while Figure 4.25 (B) illustrates that of $[\text{Ru}(\text{aphen})_3]^{2+}$ monomer (—) and electropolymerised film (—). Resonance Raman spectroscopy has increasingly become an important analytical technique in recent years³⁹ as it provides information about the vibrational characteristics of metal centres, leading to structural information. Using a laser excitation which matches an optical transition, resonant enhancement in the vibrational modes of the chromophoric units can be achieved yielding not only information about the vibrational frequencies of the chromophore in resonance with the incident frequency but also about the metal coordination geometry and the ligand environment.⁴²

Both the ruthenium monomers exhibit spectral features typical of resonance with an MLCT absorbance centered on a phenanthroline ligand. The $[\text{Ru}(\text{aphen})_2\text{bpy}]^{2+}$ monomer exhibits Resonance Raman spectral features attributable to both the bpy and the phen modes while signature phenanthroline modes are seen in the $[\text{Ru}(\text{aphen})_3]^{2+}$ monomer spectrum.^{31,43,44} The peaks at 1575 (sh), 1458 (sh), 1314.8, 1193.5, 520 and 437 cm^{-1} are signature phenanthroline peaks. Bipyridyl modes are observed at 1600 (sh), 1560, 1484 and 1170 cm^{-1} .^{31, 43, 44}

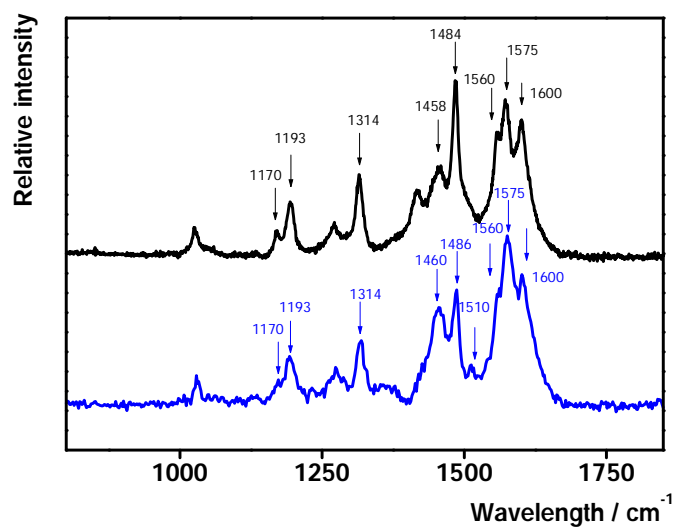
The assignments of principal peaks in the Raman spectra, Figure 4.25, has been summarised in Table 4.9.

Table 4.9: Assignment of the principal Raman spectra bands for bis and tris amino phenanthroline. The frequencies are in cm^{-1} and the intensity of the bands are assigned as follows; s-strong, m-medium, w-weak, sh-shoulder.

Bis Monomer / cm^{-1}	Bis Polymer / cm^{-1}	Tris Monomer / cm^{-1}	Tris Polymer / cm^{-1}	Mode
1193 (s)	1192(w)	1190(s)	1195(m)	Phenanthroline
1272(w)	1273(w)	1276(sh)		MLCT state of phenanthroline
1314(s)	1319(m)	1313	1318	Phenanthroline
1420(w)		1420		In plane ring stretch
			1430	In plane ring stretch
1458(sh)	1460	1451(sh)		In plane ring stretch
			1460	In plane ring stretch
1484 (s)	1486	1484	1486	In plane ring stretch
		1500(sh)		In plane ring stretch
	1510			In plane ring stretch
1575(s)	1575(sh)	1574	1574	C=C aromatic stretch
1600(sh)	1600(sh)		1615(sh)	C=C aromatic stretch

For both monomers, and their respective electrochemically synthesised polymers, the spectral features typical of resonance with an MLCT absorbance centered on a phenanthroline ligand remain, albeit with some small shifts in the frequency. In addition, there are some new features evident for each electrochemically synthesised polymer, and there are also small but significant differences between the various electrochemically synthesised polymers.

(A)



B)

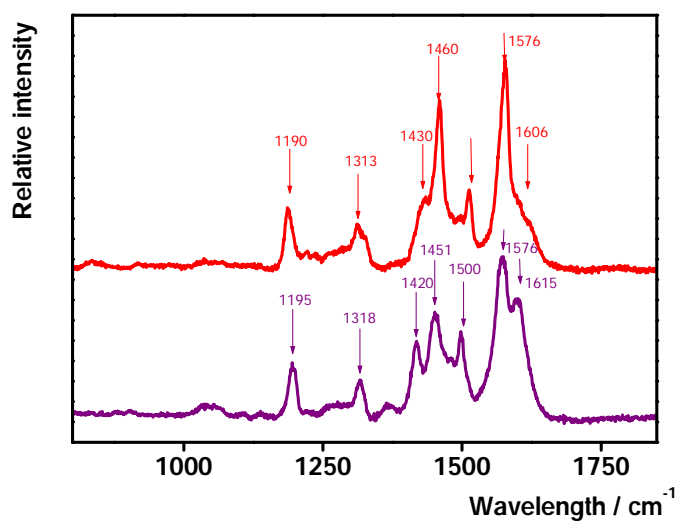


Figure 4.25: Resonance Raman spectra of $[\text{Ru}(\text{aphen})_2\text{bpy}]^{2+}$ (A) and $[\text{Ru}(\text{aphen})_3]^{2+}$ (B) obtained by irradiating the samples using argon laser excitation at 488 nm. The different spectra are of $[\text{Ru}(\text{aphen})_2\text{bpy}]^{2+}$ monomer drop-cast onto glass (—), $[\text{Ru}(\text{aphen})_2\text{bpy}]^{2+}$ metallopolymer after electrodeposition (—) in sulphuric acid, $[\text{Ru}(\text{aphen})_3]^{2+}$ monomer drop-cast onto glass (—) and $[\text{Ru}(\text{aphen})_3]^{2+}$ electrochemically synthesised polymer (—).

For $[\text{Ru}(\text{aphen})_2\text{bpy}]^{2+}$ electrochemically synthesised polymer, Figure 4.25 (—), the shoulder at 1600 cm^{-1} attributed to a C=C aromatic stretch mode remains unchanged compared with the monomer. The most intense C=C aromatic stretch mode in the parent, Figure 4.25 (—), appears at 1575 cm^{-1} . This is likely to be associated with a C=C ring stretch, since a C=N imine bond produced by reaction of 5-imino (iphen•) would be expected to appear below about 1630 cm^{-1} . This could be the reason for the enhanced intensity of this mode (1575 cm^{-1}) in the electrochemically synthesised polymer compared to its parent monomer. Also, the intensity of the bpy modes at 1484 and 1170 cm^{-1} in the electrochemically synthesised polymer film appear diminished when compared to that in the parent monomer compound. There are significant differences in the frequencies of the spectral features in region between 1400 and 1530 cm^{-1} where in-plane ring stretches occur. The parent compound has three distinct features at 1485 , 1458 and 1420 cm^{-1} . Electropolymerisation shifts these features to a lower frequency with peaks appearing at 1486 cm^{-1} and 1460 cm^{-1} with a new feature appearing at 1510 cm^{-1} .

In the case of $[\text{Ru}(\text{aphen})_3]^{2+}$, when compared to the parent monomer at 1576 cm^{-1} (—), a new shoulder (C=C aromatic stretch mode) at 1615 cm^{-1} is observed in the electrochemically synthesised polymer (—). This feature is superimposed on a weak shoulder centered around 1606 cm^{-1} in the parent complex. This is also likely to be associated with a C=C ring stretch, since a C=N imine bonds are produced here as well. The appearance of the 1615 cm^{-1} mode for the polymer is likely to arise from a change in conjugation of the phenanthroline C=C modes on polymerisation. The appearance of a new mode at 1171 cm^{-1} is tentatively attributed to a C-N azo stretch.⁴⁵ Similar to $[\text{Ru}(\text{aphen})_2\text{bpy}]^{2+}$ compounds, significant differences in the frequencies of the in-plane ring stretch mode for the parent and polymer spectra are observed. For the parent compound four features are observed at 1500 (sh), 1484 , 1451 (sh) and 1420 cm^{-1} . Electropolymerisation causes a significant shift in the highest energy ring stretch mode to 1460 cm^{-1} and the remaining features appear at 1486 and 1430 cm^{-1} . Broadly, they appear to be shifted to lower frequency on

electropolymerisation. Conversely, the phenanthroline modes at 1313 and 1190 cm^{-1} shift to higher frequency, 1318 cm^{-1} and 1195 cm^{-1} respectively, on electropolymerisation.

The origin of the differences between the polymers is not clear but it does not seem to affect the λ_{max} (emission) or the MLCT transition states. The small changes between the electrochemically synthesised polymers would suggest that polymerisation process does not affect the phenanthroline ligand directly but rather is localised on the substituent.

Overall, this data demonstrates that there are significant changes to the aromatic ring structures of the polymers when compared to the parent monomer. This is a consequence of changes in the extent of conjugation arising from the imine formation. In the $[\text{Ru}(\text{aphen})_3]^{2+}$ electrochemically synthesised polymer there is also evidence for azo bond formation. In contrast, these bands do not appear in the ruthenium bis aminophen electrochemically synthesised polymer, suggesting that the mechanism for polymer termination may be different for these two complexes. It could be speculated that due to the presence of more number of aminophen moieties in the tris complex compared to the bis substituted complex, the NH^\bullet radical facilitates both types of termination, *i.e.*, imine formation and azo formation, in $[\text{Ru}(\text{aphen})_3]^{2+}$ electrochemically synthesised polymer whereas imine formation dominates in $[\text{Ru}(\text{aphen})_2\text{bpy}]^{2+}$ electrochemically synthesised polymer.

Therefore, it can be concluded that electropolymerisation results in structural perturbation to the phenanthroline ligands. The general trend towards lower frequency ring and C-C stretch modes suggests lengthening of C-C bonds, perhaps due to some loss in aromaticity in the phenanthroline rings. The retention of luminescence without changing the emission wavelength suggests that for a given complex, electropolymerisation may involve reaction of a single amino-phenanthroline ligand. This conclusion is also consistent with the solubility of the polymer, which suggests that the polymers are not heavily cross-linked. These electrogenerated polymers are therefore attractive from the perspective of developing biosensors since the remaining amino-phen moieties can be used to bind biomolecules such as enzymes or antibodies.

4.3.6 ECL emission characteristics of films

One of the key objectives of this work was to investigate if electropolymerised films exhibit any ECL and to compare the generated ECL from the films electrodeposited from different solvents. Also, it is important to study how pH affects the ECL emission from the two-electropolymerised ruthenium complexes, since the redox behaviour, the protonation state and the photophysical characteristics of the amino phenanthroline ligand are deeply influenced by the pH of the electrolyte solution. In order to study this effect, the ECL generation properties of the polymer films formed in the two different media were tested at different pH values (5, 2.5, 8.5 and 11.5) in the presence of sodium oxalate and tripropylamine (TPA) as co-reactant in phosphate buffer and CH₃CN respectively.

The ECL mechanism of TPA/ [Ru(bpy)₃]²⁺ ECL system has been investigated by many workers. Many possible reaction pathways have been proposed for TPA/ [Ru(bpy)₃]²⁺ ECL system.⁴⁶ But in general it is believed that on oxidation a radical cation (TPA^{•+}) is produced which through loss of a proton from an α carbon, forms a strong reducing intermediate TPA[•]. This radical can reduced the electrogenerated Ru³⁺ species to the excited state reduced product Ru^{2+*} which then relaxes to the electronic ground state by emission. The oxidation of TPA can be via a “catalytic route” where electrogenerated Ru³⁺ species reacts with TPA (Figure 1.3, Chapter 1) or by direct reaction of TPA at the electrode described by Figure 1.4, Scheme 1, Chapter 1. The ECL intensity of the TPA/ [Ru(bpy)₃]²⁺ system is known to strongly depend not only on the concentration of both Ru²⁺ species and TPA species but also on solution pH, electrode material and surfactants. This suggests that direct TPA oxidation at the electrode surface plays a vital role in the light generation process. Miao and co-workers⁴⁶ proposed an alternate route involving the intermediacy of TPA cation radicals (TPA^{•+}) which has a half life of 0.2 ms in aqueous solutions at pH 8.5. They showed that at low concentrations of [Ru(bpy)₃]²⁺ (μ M) and 10-100 mM aqueous TPA, pH 8.5, the ECL emission vs. potential curves displayed two broad waves. Similar behaviour was observed for electropolymerised films of [Ru(aphen)₂bpy]²⁺ deposited in acetonitrile in the presence of 0.1 M TPA (pH

8.5) dissolved in acetonitrile, Figure 4.26. It is important to note that the deposition medium and the medium in which ECL experiment was carried out is the same in this case. The initial ECL signal started at potentials where the direct oxidation of TPA at the GC electrode occurs ($E_a \sim 0.5$ V vs. Ag/AgCl)⁴⁷ and reached a first maximum at a potential of about 0.8 V vs. Ag/AgCl, about 0.3 V more positive than the reported peak potential⁴⁷ for TPA oxidation in acetonitrile, and well before Ru^{2+} oxidation. The second ECL signal has a peak potential value of 1.17 V vs. Ag/AgCl, in the potential region of the direct oxidation of Ru^{2+} at a GC electrode.⁴⁶ The first ECL signal is relatively smaller compared to the second ECL signal.

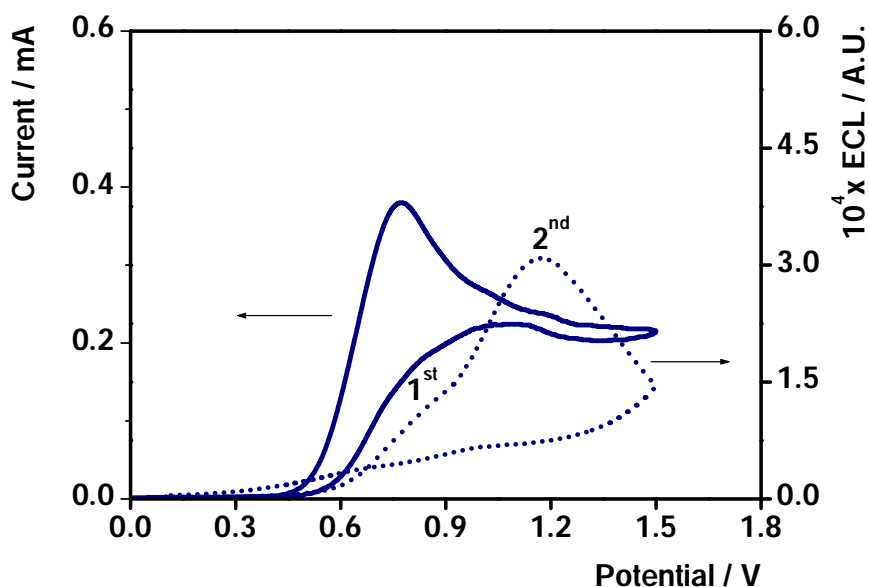


Figure 4.26: Cyclic voltammogram (—) and electrochemiluminescence response (····) for a 3 mm glassy carbon electrode ($A=0.71 \text{ cm}^2$) modified with $[\text{Ru}(\text{apen})_2\text{bpy}]^{2+}$ film electrodeposited from acetonitrile. The co-reactant used was 0.1 M TPA (pH 8.5) dissolved in acetonitrile. The scan rate was 0.1 Vs^{-1} and Γ is $(4.6 \pm 0.5) \times 10^{-10} \text{ mol cm}^{-2}$.

It has been reported earlier^{46,48} that the ECL intensity of the first peak is determined by the quantity of TPA derived radicals generated from the oxidation of TPA at the electrode surface. In the presence of excess Ru^{2+} , the ECL intensity of the first peak is governed by the concentration of TPA whereas

in the presence of excess TPA radicals compared to Ru^{2+} , the ECL intensity is governed by concentration of Ru^{2+} .

From the UV-Vis absorption data we already know that only micromolar amounts of ruthenium centers are present after electropolymerisation. Therefore, due to very low ruthenium concentrations, Figure 4.26 can be interpreted on similar terms to Miao and co-workers.⁴⁶ At 0.8 V vs. Ag/AgCl there is an excess of TPA radicals but as the electropolymerised film is not completely oxidized the concentration of Ru^{3+} is very low. The low concentration of ruthenium centers in general in the electrochemically synthesised polymer films compared to the concentration of TPA radicals also contribute significantly to this effect. In this situation, as the ECL intensity of the first peak is governed by Ru^{2+} concentration we observe a very low ECL signal. But as the potential is increased closer to the oxidation potential of Ru^{2+} , a higher ECL signal is observed which peaks at 1.17 V vs. Ag/AgCl.

Figure 4.27 shows simultaneously recorded CV (A) and ECL response (B) for a thin film of $[\text{Ru}(\text{aphen})_2\text{bpy}]^{2+}$ film electrodeposited from acetonitrile with TPA co-reactant dissolved in acetonitrile. The pH of TPA was adjusted to 8.5 (CV \cdots , ECL —) and 11.5 (CV \cdots , ECL —) by adding a few drops of perchloric acid to the electrolyte solution. This figure reveals that the ECL intensity of the $[\text{Ru}(\text{aphen})_2\text{bpy}]^{2+}$ film is higher at higher pH in organic medium.

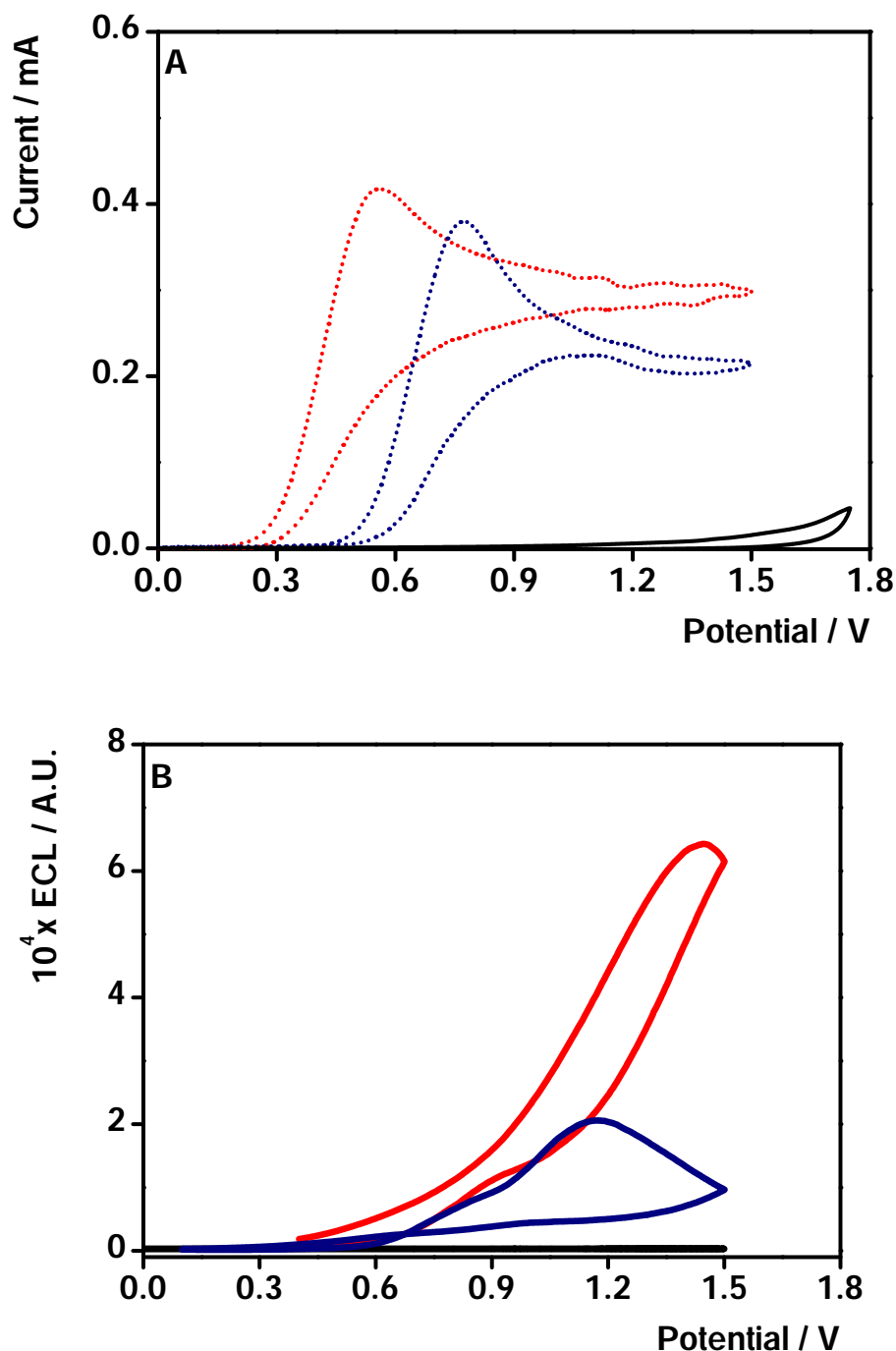


Figure 4.27: Cyclic voltammogram (A) and electrochemiluminescence response (B) for a 3 mm glassy carbon electrode ($A=0.71 \text{ cm}^2$) modified with $[\text{Ru}(\text{aphen})_2\text{bpy}]^{2+}$ film electrodeposited from acetonitrile. The co-reactant used was 0.1 M TPA dissolved in acetonitrile. The pH of TPA was adjusted to 8.5 (CV (A) \cdots , ECL (B) —) and 11.5 (CV (A) \cdots , ECL (B) —). — is the response of the film in blank acetonitrile with no TPA. The scan rate was 0.1 Vs^{-1} and Γ is $4.6 \pm 0.5 \times 10^{-10} \text{ molcm}^{-2}$.

Even at pH 11.5, two ECL peaks are observed, first one at 0.9 V *vs.* Ag/AgCl and second at 1.4 V. However, the ECL intensity at higher pH is almost 3 times the ECL intensity found at 8.5 pH.

Figure 4.28 illustrates the ECL behaviour of $[\text{Ru}(\text{apen})_2\text{bpy}]^{2+}$ film electrodeposited from acetonitrile, in aqueous PBS solution in the presence of oxalate co-reactant (pH 5.2). The pH of the oxalate solution was adjusted by adding few drops of oxalic acid.

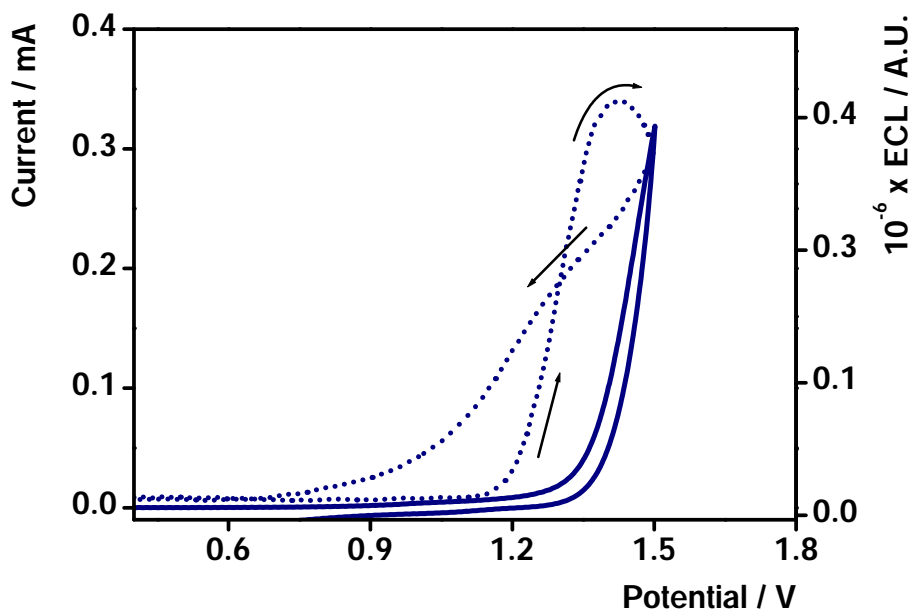


Figure 4.28: Cyclic voltammogram (—) and electrochemiluminescence response (····) for a 3 mm glassy carbon electrode ($A=0.71 \text{ cm}^2$) modified with $[\text{Ru}(\text{apen})_2\text{bpy}]^{2+}$ film electrodeposited from acetonitrile. The co-reactant used was sodium oxalate (pH 5.2) dissolved in PBS. The deposition medium and the medium in which ECL was performed are different. The scan rate was 0.1 Vs^{-1} and Γ is $(4.6 \pm 0.5) \times 10^{-10} \text{ molcm}^{-2}$.

From the Figure 4.28, it can be seen that there is a significant increase in the oxidation peak current in the presence of oxalate (pH 5.2) which is not seen when oxalate is not present in electrolyte solution *i.e.*, Figure 4.29. The oxidation of oxalate on bare glassy carbon electrode was found to occur at +1.2 V *vs.* Ag/AgCl in PBS buffer electrolyte. Consistent with previous reports, an

increased current is observed at the oxidation potentials of oxalate (~ 1.2 V vs. Ag/AgCl), Figure 4.28.⁴⁹ As the oxidation potential of $[\text{Ru}(\text{aphen})_2\text{bpy}]^{2+}$ film electrodeposited from acetonitrile occurs at +1.02 V (Figure 4.3), it can be concluded that the oxidation of oxalate is mediated by Ru^{3+} centers. This increased current is not observed in the absence of the ruthenium metallopolymer layer. Thus Figure 4.28 shows that the oxidation of oxalate is accompanied by ECL emission indicating that the Ru^{3+} centers are reduced to Ru^{2+*} , which then emits light and relaxes back to the electronic ground state. On reversal of the scan the intensity of ECL decreases as the current leading to the production of Ru^{3+} decreases.

Figure 4.29 shows simultaneously recorded CV (A) and ECL response (B) for a thin film of $[\text{Ru}(\text{aphen})_2\text{bpy}]^{2+}$ film electrodeposited from acetonitrile with oxalate co-reactant dissolved in PBS buffer. The pH of oxalate was adjusted to 2.5 (CV \cdots , ECL —) and 5.2 (CV \cdots , ECL —) by adding a few drops of oxalic acid to the electrolyte solution. This figure reveals that even in this case the ECL intensity of the $[\text{Ru}(\text{aphen})_2\text{bpy}]^{2+}$ film is higher at higher pH.

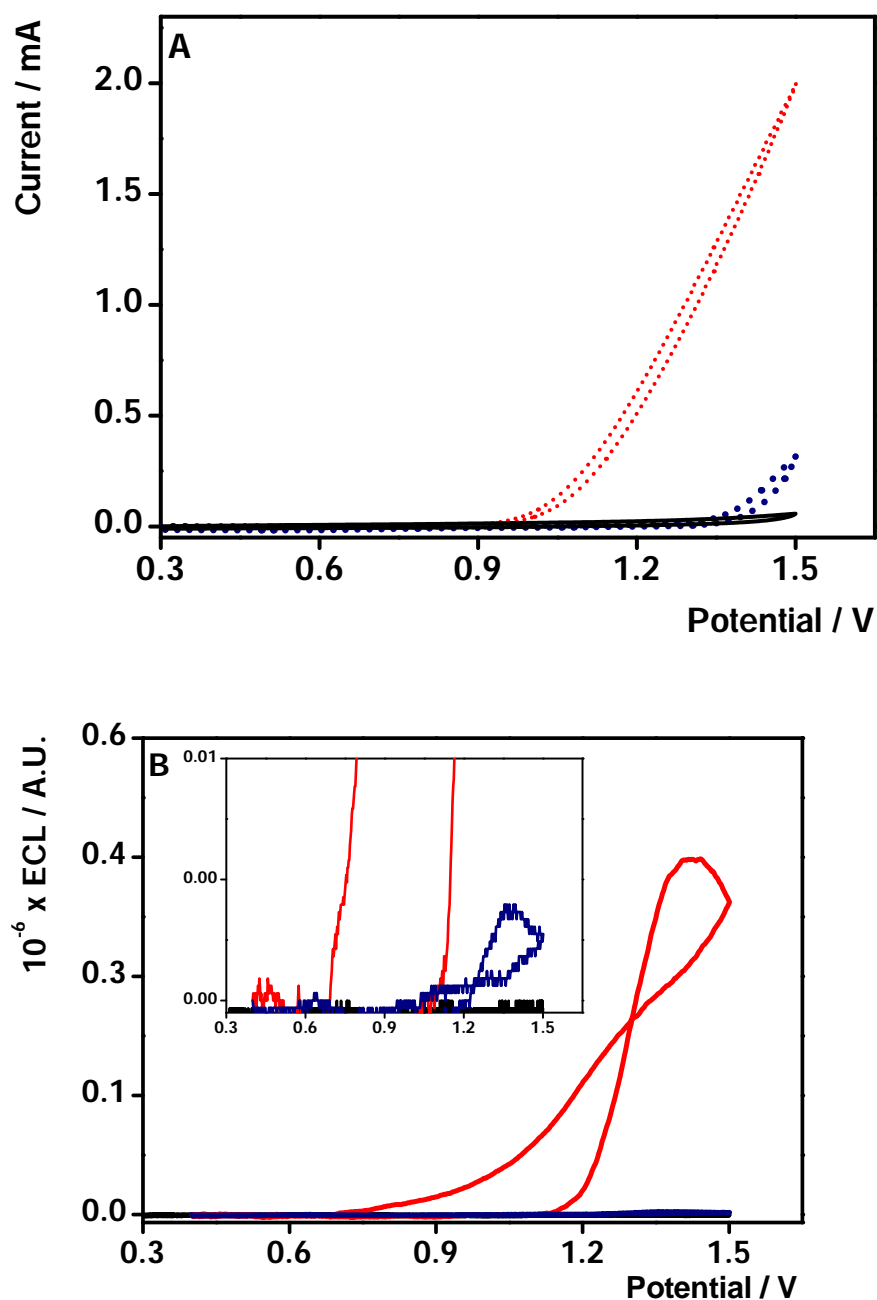


Figure 4.29: Cyclic voltammogram (A) and electrochemiluminescence response (B) for a 3 mm glassy carbon electrode ($A=0.71 \text{ cm}^2$) modified with $[\text{Ru}(\text{aphen})_2\text{bpy}]^{2+}$ film electrodeposited from acetonitrile. The co-reactant used was sodium oxalate dissolved in PBS. The pH of oxalate was adjusted to 2.5 (CV (A) \cdots , ECL (B) —) and 5.2 (CV (A) \cdots , ECL (B) —). — is the response of the film in blank PBS with no oxalate. The scan rate was 0.1 Vs^{-1} and Γ is $(4.6 \pm 0.5) \times 10^{-10} \text{ mol cm}^{-2}$. The ECL signal obtained at pH 2.5 has been enlarged for clarity.

It has already been established by many workers, that the ECL intensity of $[\text{Ru}(\text{bpy})_3]^{2+}$ / Oxalate system is strongly dependant on the pH.⁵⁰⁻⁵³ Lu et.al.,⁵¹ reported that for ITO electrodes modified with PVP bound $[\text{Ru}(\text{bpy})_3]\text{Cl}_2$, increase in pH increased ECL intensity. The authors concluded that at low pH (for oxalic acid $\text{pK}_1=1.23$ and $\text{pK}_2=4.19$) there is efficient penetration of the PVP film by the oxalate but neutral and mono-anionic oxalate will be the dominant species present. The protonated forms of the radical intermediates ($\text{HC}_2\text{O}_4^\bullet$) which are responsible for generation of the excited state luminophore are weak reducing agents compared to un-protonated form (CO_2^\bullet). Therefore, a low ECL emission is observed at low pH when compared to higher pH values. Similar observation is seen here with electropolymerised $[\text{Ru}(\text{aphen})_2\text{bpy}]^{2+}$ films. The ECL emission is higher at pH 5.2 when compared to pH 2.5. However, when the overall ECL intensity is considered, $[\text{Ru}(\text{aphen})_2\text{bpy}]^{2+}$ films electropolymerised in acetonitrile produce more intense ECL in organic electrolyte with TPA co-reactant than in aqueous electrolyte with oxalate co-reactant. This could also be because in the former case the deposition medium and the medium in which ECL was examined were both same, where as in the later case they differed. Hence, in addition to pH effects, electrolyte solution also seems to influence the ECL light emission process of the electropolymerised films.

Similar experiments were performed on $[\text{Ru}(\text{aphen})_2\text{bpy}]^{2+}$ films electrodeposited from sulphuric acid. Surprisingly, two ECL peaks like the ones observed in Figure 4.26 are not observed. A single peak beginning at 0.9 V, reaching its maximum at around 1.3 and decreasing in intensity with reverse scan is observed. The CV contains a broad irreversible anodic peak which begins to rise around 0.8 V vs. Ag/AgCl with a peak at 1.3 V.

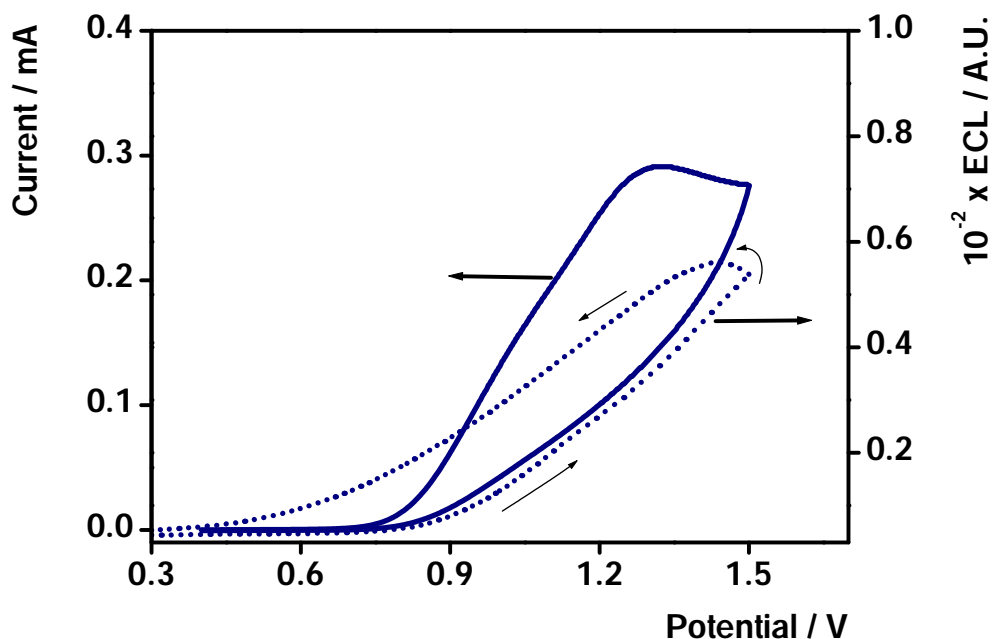


Figure 4.30: Cyclic voltammogram (—) and electrochemiluminescence response (····) for a 3 mm glassy carbon electrode ($A=0.71 \text{ cm}^2$) modified with $[\text{Ru}(\text{aphen})_2\text{bpy}]^{2+}$ film electrodeposited from sulphuric acid. The co-reactant used was TPA (pH 11.5) dissolved in acetonitrile. The deposition medium and the medium in which ECL was performed are different. The scan rate was 0.1 Vs^{-1} and Γ is $(1.6 \pm 0.8) \times 10^{-11} \text{ molcm}^{-2}$.

As the ruthenium concentration is very low, this peak is believed to be mainly due to the direct oxidation of TPA.⁴⁸ This behaviour is very consistent with that observed for small concentrations of $[\text{Ru}(\text{bpy})_3]\text{Cl}_2$ with TPA in acetonitrile solution and Pt electrode⁴⁸ and in basic solution with glassy carbon electrode.⁵⁴

Figure 4.31 shows simultaneously recorded CV (A) and ECL response (B) for a thin film of $[\text{Ru}(\text{aphen})_2\text{bpy}]^{2+}$ film electrodeposited from sulphuric acid with TPA co-reactant dissolved in acetonitrile. The pH of TPA was adjusted to 8.5 (CV····, ECL—) and 11.5 (CV····, ECL—) by adding a few drops of perchloric acid to the electrolyte solution. Here too the ECL intensity of the $[\text{Ru}(\text{aphen})_2\text{bpy}]^{2+}$ film is higher at higher pH.

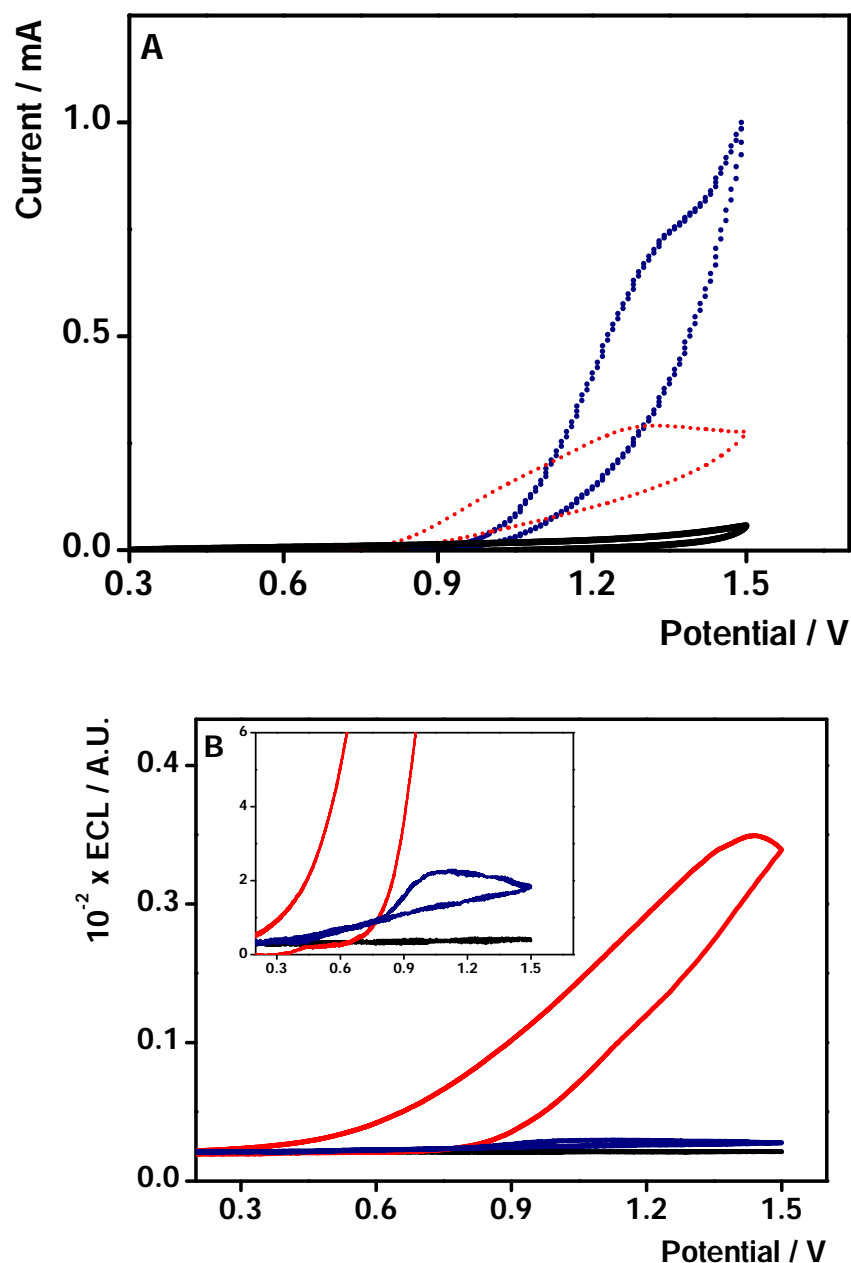


Figure 4.31: Cyclic voltammogram (A) and electrochemiluminescence response (B) for a 3 mm glassy carbon electrode ($A=0.71 \text{ cm}^2$) modified with $[\text{Ru}(\text{apen})_2\text{bpy}]^{2+}$ film electrodeposited from sulphuric acid. The co-reactant used was 0.1 M TPA dissolved in acetonitrile. The pH of TPA was adjusted to 8.5 (CV (A) \cdots , ECL (B) —) and 11.5 (CV (A) \cdots , ECL (B) —). — is the response of the film in blank acetonitrile with no TPA. The scan rate was 0.1 Vs^{-1} and Γ is $(1.6 \pm 0.8) \times 10^{-11} \text{ molcm}^{-2}$. Inset shows zoomed in image of the same graph for clarity.

At pH 8.5 it is observed that in spite of higher catalytic current very little ECL emission is observed. The reason for this response is unclear but it could be due to unfavourable pH conditions for radical formation.

Figure 4.32 shows simultaneously recorded CV (A) and ECL response (B) for a thin film of $[\text{Ru}(\text{aphen})_2\text{bpy}]^{2+}$ film electrodeposited from sulphuric acid with oxalate co-reactant dissolved in PBS buffer. The pH of oxalate was adjusted to 2.5 (CV \cdots , ECL —) and 5.2 (CV \cdots , ECL —). Similar to the previous case it is observed that ECL intensity increases with increase in pH. A similar study was conducted for $[\text{Ru}(\text{aphen})_3]^{2+}$ film and the relative ECL intensities, diffusion coefficients and pH for $[\text{Ru}(\text{aphen})_3]^{2+}$ film and $[\text{Ru}(\text{aphen})_2\text{bpy}]^{2+}$ film have been summarized in Table 4.10.

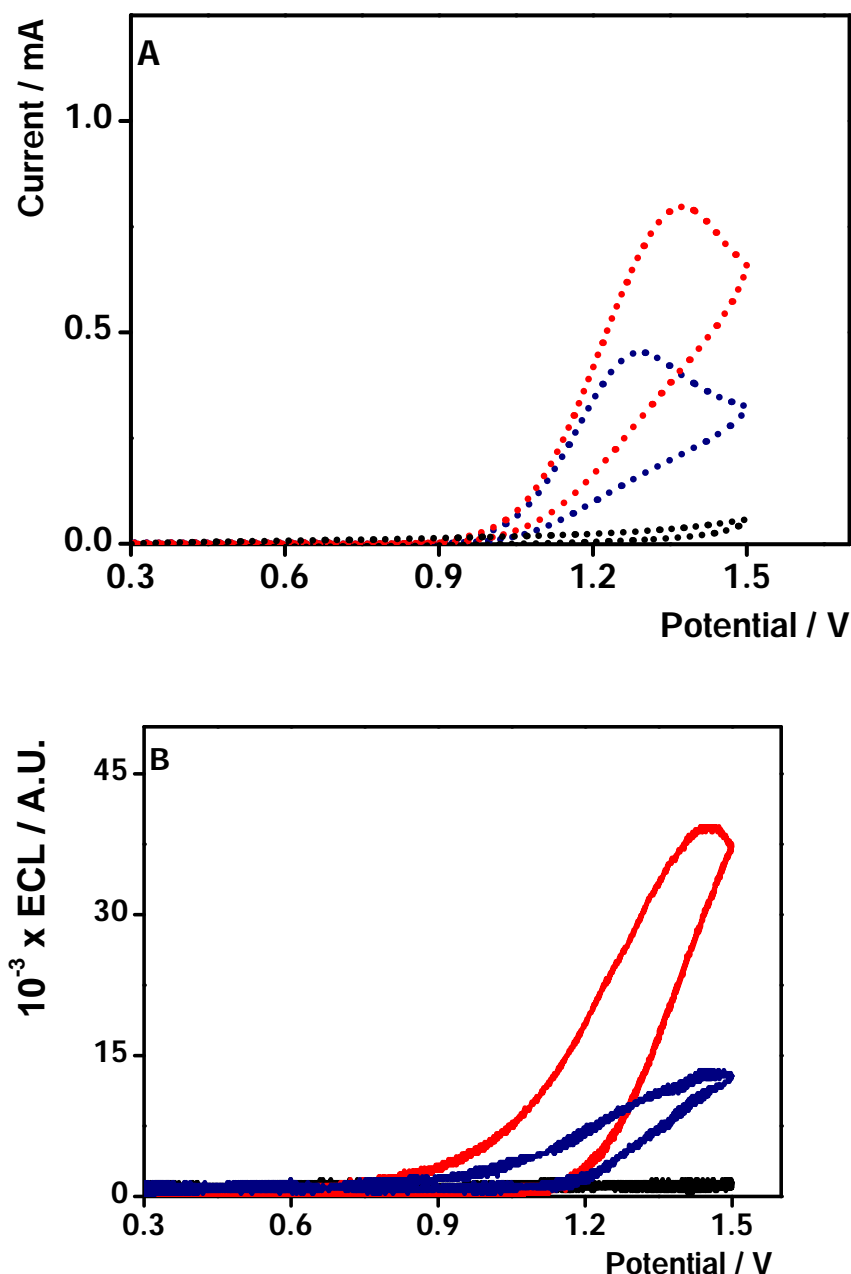


Figure 4.32: Cyclic voltammogram (A) and electrochemiluminescence response (B) for a 3 mm glassy carbon electrode ($A=0.71 \text{ cm}^2$) modified with $[\text{Ru}(\text{aphen})_2\text{bpy}]^{2+}$ film electrodeposited from sulphuric acid. The co-reactant used was sodium oxalate dissolved in PBS. The pH of oxalate was adjusted to 2.5 (CV (A) \cdots , ECL (B) —) and 5.2 (CV (A) \cdots , ECL (B) —). — is the response of the film in blank PBS with no oxalate. The scan rate was 0.1 Vs^{-1} and Γ is $(1.6 \pm 0.8) \times 10^{-11} \text{ molcm}^{-2}$.

Table 4.10: Relative ECL Intensity of the $[\text{Ru}(\text{aphen})_2\text{bpy}]^{2+}$ and $[\text{Ru}(\text{aphen})_3]^{2+}$ films formed in different media in the presence of TPA and sodium oxalate at various pH.

Complex	C mM	$D_{\text{CT}} / \text{cm}^2\text{s}^{-1} \times 10^{-10}$	Co-reactant	pH	ECL
$[\text{Ru}(\text{aphen})_2\text{bpy}]^{2+}$	1.5 ^a	0.11±0.1	TPA	11.5	6.4x10 ⁴
				8.5	1.8x10 ⁴
			Sodium oxalate	2.5	8.9x10 ⁻⁸
				5.2	0.45x10 ⁻⁶
	2.0 ^b	6.9±0.4	TPA	11.5	51.7x10 ⁻²
				8.5	2.1x10 ⁻²
			Sodium oxalate	2.5	13.5x10 ⁻³
				5.2	40x10 ⁻³
$[\text{Ru}(\text{aphen})_3]^{2+}$	1.0 ^a	0.44±0.08	TPA	11.5	4.8x10 ⁵
				8.5	3.1x10 ⁵
			Sodium oxalate	2.5	0.8x10 ²
				5.2	1.9x10 ²
	1.3 ^b	960±0.6	TPA	11.5	2.1x10 ⁶
				8.5	0.9x10 ⁶
			Sodium oxalate	2.5	No signal
				5.2	No signal

^aDeposition medium was CH₃CN. ^bDeposition medium was H₂SO₄

As predicted on the basis of cyclic voltammetry and spectroscopy data all electropolymerised films produced high ECL upon electrochemical oxidation of Ru^{3+} centres in acetonitrile in the presence of TPA. A general trend of increased ECL with increasing pH is observed. It is important to note that, $[\text{Ru}(\text{aphen})_3]^{2+}$ films deposited from sulphuric acid, showed an order of magnitude higher ECL intensity (2.1×10^6) than those deposited from acetonitrile (4.8×10^5). This result is consistent with the high D_{CT} values obtained for the films formed in sulphuric acid, compared to those obtained for the films deposited from acetonitrile. This suggests that the morphology of $[\text{Ru}(\text{aphen})_3]^{2+}$ films formed in lower pH favours high charge transfer and ECL emission properties. Also, $[\text{Ru}(\text{aphen})_3]^{2+}$ films show higher ECL compared to $[\text{Ru}(\text{aphen})_2\text{bpy}]^{2+}$ films. This also suggests faster diffusion of charges through the film helps to enhance ECL intensity. However, $[\text{Ru}(\text{aphen})_3]^{2+}$ films show negligible or no ECL in aqueous medium with sodium oxalate as co-reactant. Even though the charge transfer diffusion coefficient is faster for these films, the absence of ECL signal in the presence of sodium oxalate would suggest that D_{CT} is not the only governing factor but other factors like film structure, porosity, pH, co-reactant *etc.* also play important role and hence have to be considered.

4.4 CONCLUSIONS

The electropolymerisation of $[\text{Ru}(\text{aphen})_2\text{bpy}]^{2+}$ and $[\text{Ru}(\text{aphen})_3]^{2+}$ complexes and the properties of the electropolymerised films formed by oxidative electropolymerisation in two different media namely, anhydrous acetonitrile and sulphuric acid, has been reported in this chapter. Results show that electropolymerisation proceeds in both acetonitrile and in sulphuric acid and smooth films, which cover the entire electrode surface, can be obtained. Films formed in sulphuric acid have slightly higher surface coverages ($4.4 \pm 0.6 \times 10^{-8} \text{ mol cm}^{-2}$) compared to films formed in acetonitrile ($2.2 \pm 0.6 \times 10^{-8} \text{ mol cm}^{-2}$). These electrochemically synthesised polymers exhibit considerable ECL when oxidized to the Ru^{3+} state in the presence of TPA as a co-reactant. $[\text{Ru}(\text{aphen})_2\text{bpy}]^{2+}$ films deposited from acetonitrile also show high ECL in the presence of TPA co-reactant. However, the electrochemically synthesised

polymers (e.g. $\text{Ru(aphen)}_2\text{bpy}]^{2+}$ in CH_3CN and H_2SO_4 and $[\text{Ru(aphen)}_3]^{2+}$ in CH_3CN), do not exhibit open pore structure and have very low rates of charge transfer (e.g. $[\text{Ru(aphen)}_2\text{bpy}]^{2+}$ in CH_3CN has a D_{CT} of $1.1 \pm 0.8 \times 10^{-11}$). The exception to this was the $[\text{Ru(aphen)}_3]^{2+}$ film formed in H_2SO_4 . The $[\text{Ru(aphen)}_3]^{2+}$ films deposited from sulphuric acid have higher emission intensities than the ones deposited from acetonitrile. These results are consistent with the high D_{CT} values obtained for the films formed in sulphuric acid, compared to the substantially lower D_{CT} values obtained for the films deposited from acetonitrile. Hence, these films have a greater potential to be used as polymeric luminophores and they are capable of serving as an excellent immobilization matrix.

4.5 REFERENCES

- (1) Higgins, S. J. *Chem. Soc. Rev.* **1997**, 26, 247-257.
- (2) Johan, H.; Robyn, W. H.; Anders, H.; Edwin, C. C.; Catherine, E. H.; Forester, R. J. *Inorg. Chem.* **2005**, 44, 1073-1081.
- (3) Basudam, A.; Sarmishtha, M. *Prog. Polym. Sci.* **2004**, 29, 699-766.
- (4) Dennany, L.; Hogan, C. F.; Keyes, T. E.; Forster, R. J. *Anal. Chem.* **2006**, 78, 1412-1417.
- (5) Bertoncello, P.; Dennany, L.; Forster, R. J.; Unwin, P. R. *Anal. Chem.* **2007**, 79, 7549-7553.
- (6) Takada, K.; Naal, Z.; Abruna, H. D. *Langmuir* **2003**, 19, 5402-5406.
- (7) Oyama, N.; Anson, F. C. *J. Electrochem. Soc.* **1980**, 127, 247.
- (8) Belanger, S.; Stevenson, K. J.; Mudakha, S. A.; Hupp, J. T. *Langmuir* **1999**, 15, 837-843.
- (9) Hjelm, J.; Handel, R. W.; Hagfeldt, A.; Constable, E. C.; Housecroft, C. E.; Forster, R. J. *Electrochem. Commun.* **2004**, 6, 193-200.
- (10) Charles, D. E.; Lawrence, D. M.; Royce, W. M.; Thomas, J. M. *Inorg. Chem* **1983**, 22, 1283-1291.
- (11) Osteryoung.; Pickup, P. G.; Robert. A. *Inorg. Chem.* **1984**, 24, 2707-2712.
- (12) Bachas, L. G.; Cullen, L.; Hutchins, R. S.; Scott, D. L. *J. Chem. Soc.; Dalton Trans* **1997**, 1571-1577.
- (13) Pickup, P. G.; Osteryoung, R. A. *Inorg. Chem.* **1985**, 24, 2707-2712.
- (14) Gregori, I.; Bedioui, F.; Devynck, J., *J. Electroanal. Chem* **1987**, 238, 197-214.
- (15) Nyasulu, W. M.; Frazier.; Horacio, M. A. *J. Electroanal. Chem.* **1988**, 239, 175-186.
- (16) Deinhammer, R. S.; Ho, M.; Anderegg, J. W.; Porter, M. D. *Langmuir* **1994**, 10, 1306-1313.
- (17) Bard, A. J.; Faulkner, L. R. In *Electrochemical methods: Fundamentals and applications*; John Wiley & Sons Inc: New York, 1980; , pp 718.
- (18) Galicia, L. L.; Rojas, H. A.; Gomez, H. M.; Ramirez, S. M. T. *Sensors and Chemometrics* **2001**, 65-73.
- (19) J. A. Cobos-Murcia.; L. Galicia.; A. Rojas-Hernandez.; M. T. Ramirez-Silva.; R. Alvarez-Bustamante.; M. Romero-Romo.; G. Rosquete-Pina.; M. Palomar-Pardave. *Polymer* **2005**, 46, 9053-9063.
- (20) Ma. Teresa, R.; Martin, G. H.; Hernandez, Pacheco. Lourdes. M. A. De.; Hernandez, A. R.; Laura, G. *Spectrochim. Acta. A* **2004**, 60, 781-789.
- (21) Venkatanarayanan, A.; Spehar-Deleze, A.; Dennany, L.; Pellegrin, Y.; Keyes, T. E.; Forster, R. J. *Langmuir* **2008**, 24, 11233-11238.
- (22) Pinter, J. S.; Brown, K. L.; Deyoung, P. A.; Peaslee, G. F. *Talanta* **2007**, 71, 1219-1225.
- (24) Dennany, L.; Forster, R. J.; White, B.; Smyth, M.; Rusling, J. F. *J. Am. Chem. Soc.* **2004**, 126, 8835-8841.

- (25) O'Connor, M.; Kim, S. N.; Killard, A. J.; Forster, R. J.; Smyth, M. R.; Papadimitrakopoulos, F.; Rusling, J. F. *Analyst* **2004**, *129*, 1176-1180.
- (26) Forster, R. J., Walsh, D. A. In *Cyclic Voltammetry; Encyclopedia of Analytical Chemistry*; Academic Press: New York, 2003; .
- (27) Ikeda, T.; Schmehl, R.; Denisevich, P.; Willman, K.; Murray, R. W. *J. Am. Chem. Soc.* **1982**, *104*, 2683-2691.
- (28) Pickup, P. G.; Kutner, W.; Leidner, C. R.; Murray, R. W. *J. Am. Chem. Soc.* **1984**, *106*, 1991-1998.
- (29) Linford, R. G., Ed.; In *Electrochemical science and technology of polymers-1*; Elsevier applied science publishers ltd: NewYork, 1987; Vol. 1, pp Pg 162.
- (30) Forster, R. J.; Vos, J. G. *Macromolecules* **1990**, *23*, 4372-4377.
- (31) Hughes, H. P.; Martin, D.; Bell, S.; McGarvey, J. J.; Vos, J. G., *Inorg. Chem* **1993**, *32*, 4402-4408.
- (32) Hong, H.; Davidov, D.; Chayet, H.; Faraggi, E. Z.; Tarabia, M.; Avny, Y.; Neumann, R.; Kirstein, S. *Supramol. Sci.* **1997**, *4*, 67-73.
- (33) Chen, X.; Chen, Z.; Lu, G.; Bu, W.; Yang, B. *J. Colloid Interface Sci.* **2003**, *264*, 266-270.
- (34) Hu, I.; Karweik, D. H.; Kuwana, T. *J Electroanal Chem* **1985**, *189*, 59-72.
- (35) Wightman, R. M.; Deakin, M. R.; Kovach, P. M.; Kuhr, W. G.; Stutts, K. J. *J. Electrochem. Soc.* **1984**, *131*, 1578-1583.
- (36) Chen, P.; McCreery, R. L. *Anal. Chem.* **1996**, *68*, 3958-3965.
- (37) Ray, K. G.; McCreery, R. L. *J Electroanal Chem* **1999**, *469*, 150-158.
- (38) Brennan, J. L.; Keyes, T. E.; Forster, R. J. *Langmuir* **2006**, *22*, 10754-10761.
- (39) Forster, R. J.; Keyes, T. E.; Vos, J. G. In *Interfacial Supramolecular Assemblies*; John Wiley & Sons, Ltd: 2003; .
- (40) Stevens, M. P. In *Basic principles; Polymer chemistry: An introduction*; Oxford university press: New York, 1990; pp 11.
- (41) Stevens, M. P. In *Chemical structure and polymer morphology; Polymer chemistry: An introduction*; Oxford university press: New York, 1990; pp 99.
- (42) Andrikopoulos, P. C.; McCarney, K. M.; Armstrong, D. R.; Littleford Rachael, E.; Graham Duncan.; Ewen Smith, W. *J. Mol. Struct.* **2006**, *789*, 59-70.
- (43) Kumar, C. V.; Barton, J. K.; Gould, I. R; Turro, N. J.; Houten, J. V.; *Inorg. Chem* **1988**, *27*, 648-651.
- (44) Chang, Y. J.; Xu Xiaobing.; Yabe, T.; Yu Soo Chang.; Anderson, D. R.; Orman, L. K.; Hopkins, J. B. *J. Phys. Chem.* **1990**, *94*, 729-736.
- (45) Trotter, P. J. *Appl. Spectrosc.* , *31*, 1-53(january/february 1977)-30-35.
- (46) Miao, W.; Choi, J. P.; Bard, A. J. *J. Am. Chem. Soc.* **2002**, *124*, 14478-14485.
- (47) Long, T. R.; Richter, M. M. *Inorg. Chim. Acta* **2005**, *358*, 2141-2145.
- (48) Zu, Y.; Bard, A. J. *Anal. Chem.* **2000**, *72*, 3223-3232.
- (49) Forster, R. J.; Hogan, C. F. *Anal. Chem.* **2000**, *72*, 5576-5582.
- (50) Pyati, R.; Mark, R. M. *Annu. Rep. Prog. Chem.* , *Sect C* **2007**, *103*, 12-78.
- (51) Lu, M.; Whang, C. *Anal. Chim. Acta* **2004**, *522*, 25-33.

- (52) Bard, A. J. In *Fundamentals of ECL: Coreactants*; Electrogenerated Chemiluminescence; Marcel Dekker.Inc: United states of america, 2004; pp 19.
- (53) Debad, J. D.; Glezer, E. N.; Wohlstadter, J.; Sigal, G. B. In *Clinical and biological applications of ECL*; Electrogenerated Chemiluminescence; Marcel Dekker.Inc: United states of america, 2004; pp 19.
- (54) Mann, C. K. *Anal. Chem.* **1964**, 36, 2424-2426.
- (55) Calzón, J. A. G.; Álvarez, J. L. M.; Fonseca, J. M. L.; *J. Colloid Interface Sci*, 2005, 290, 2, 498-504.

CHAPTER V

MODULATED POTENTIAL ECL AND A.C. IMPEDANCE

5.1 INTRODUCTION

Electropolymerization plays a pivotal role in forming films of controlled thickness, but the films may not possess an open pore structure and may be cross-linked which significantly decreases the overall rate of charge transfer due to ion transport limitations. The electrochemically synthesised polymers described in the previous chapter, do not exhibit open pore structure and most of them have very low rates of charge transfer (e.g. $[\text{Ru}(\text{aphen})_2\text{bpy}]^{2+}$ in CH_3CN has a D_{CT} of $1.1 \pm 0.8 \times 10^{-11}$). Also, it was observed that it was very difficult to achieve relatively thick films. Usually, films with surface coverages greater than about $5 \times 10^{-8} \text{ mol cm}^{-2}$ or approximately $0.5 \text{ }\mu\text{m}$ thick, which might improve the limits of detection, are very desirable for analytical applications.^{1,2} This kind of surface coverage was achieved only for $[\text{Ru}(\text{aphen})_3]^{2+}$ in H_2SO_4 . However, these films require 60 scan cycles to form and they emit high ECL only in the presence of very basic TPA co-reactant (pH 8-11). Hence, in order to obtain more open, flexible films which would emit high ECL at physiological pH 7, a different approach, where one polymerizes appropriate polymer precursor, followed by the attachment of redox active groupings, can be used. Synthetic incorporation of redox sites onto PVP (poly (4-vinyl pyridine)) backbone³⁻⁶ is one such example. These films strongly interact with contacting electrolytes and allow for the efficient penetration of ions and solvent thereby greatly improving the rates of charge transfer.

Source modulation techniques coupled with synchronous detection are frequently encountered in the context of fluorescence^{7,8} and

absorbance.⁹ In this technique, the source signal is modulated at a particular frequency using a chopper wheel and the signal alone is then encoded as a magnitude of a carrier waveform. This approach eliminates background signals from the analytical response of interest.

In recent years, many research groups have focused their attention on better understanding of ECL mechanisms, biomolecular interactions with ECL reactants, kinetics and thermodynamics of the analyte.^{10,11} This knowledge can provide valuable insights into the phenomena of charge transport through molecular structures and intracellular components of bio-related species.¹²⁻¹⁶ The kinetics of ECL reactions mainly depends on the co-reactant chemistry and the cross reaction between an ECL generator *e.g.* $[\text{Ru}(\text{bpy})_3]\text{Cl}_2$ and co-reactant *e.g.* oxalate or TPA.¹⁷⁻²⁰ A better understanding of this co-reactant chemistry and how it affects the light emission is absolutely essential for optimisation of any biosensor device.

In ECL reactions, the electrode potential initiates the light generating reaction. Hence by controlling the electrode potential one can easily control the emission of light from the electrode surface. This means, one can easily turn the reaction “on” and “off” at will, adding an element of temporal control to the reaction not usually achievable with conventional chemiluminescence reactions.²¹

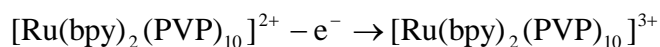
Thus, by using this temporal control inherent to the ECL process in conjunction with porous metallopolymer films and source modulation technique, it is possible to develop a unique detection approach.

The system considered here is the ECL reaction between $[\text{Ru}(\text{bpy})_2(\text{PVP})_{10}]^{2+}$ polymer film and oxalate.² The polymer is surface bound to a glassy carbon electrode and the oxalate is present in solution. For surface bound systems, the principal process is heterogeneous

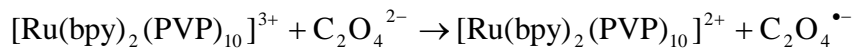
electron transfer across the electrode|polymer interface. Mass transfer and reaction kinetics through the polymer layer must be considered to fully understand the properties of such systems.

In an ECL reaction, the rate of conversion of surface bound Ru^{2+} to Ru^{3+} , Equation 5.1, is very facile. Also $\text{CO}_2^{\bullet-}$ arrives at the film|solution boundary by diffusion. It then enters the polymer layer where it gets oxidized to CO_2 . For the $[\text{Ru}(\text{bpy})_2(\text{PVP})_{10}]^{2+}$ / Oxalate ECL system considered, Scheme 1 represents the various reactions taking place.²²

Scheme 1:



5.1



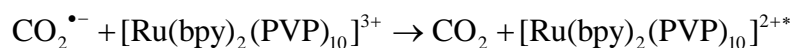
5.2

The oxalate anion radical rapidly decomposes according to Equation 5.3

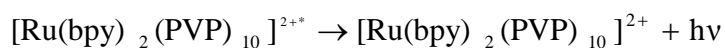


5.3

The intermediate radical ion, $\text{CO}_2^{\bullet-}$, is a strong reducing agent that can produce the ruthenium 2+ excited state, Ru^{2+*} , by directly reducing the 3+ species.

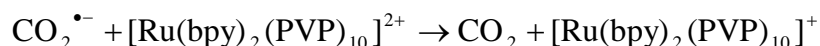


5.4

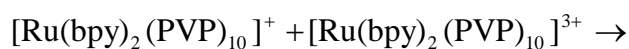


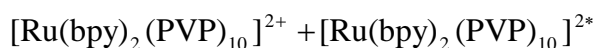
5.5

Alternatively, as described by Equations 5.6 and 5.7, the $\text{CO}_2^{\bullet-}$ anion radical may reduce the complex to the 1+ state, which can then produce Ru^{2+*} by reacting with electrogenerated Ru^{3+} .



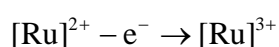
5.6



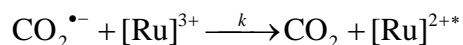


5.7

Let us consider a modified version of Equation 5.1 and 5.4 in Scheme 1. For convenience in this analysis $[\text{Ru}]^{2+}$ and $[\text{Ru}]^{3+}$ shall represent the surface oxidized and reduced forms of $[\text{Ru}(\text{bpy})_2(\text{PVP})_{10}]^{2+}$. It is known that the bimolecular cross-reaction between the substrate $[\text{CO}_2^{\bullet-}]$ and $[\text{Ru}]^{3+}$ is irreversible as oxalate acts as a sacrificial co-reactant.



5.1a



5.4a

Under the conditions presented here, oxalate ions cannot be effectively oxidized at the bare electrode surface and hence, it has to be oxidized by the Ru^{3+} . Also for sensitive analysis, it is desirable to have the analyte reacting with the mediating centers throughout the film thickness. This is indeed shown to be the case where Hogan and co-workers²² demonstrated that the emission of light in the ECL reaction between $[\text{Ru}(\text{bpy})_2(\text{PVP})_{10}]^{2+}$ and oxalate is controlled, not by the rate at which catalytic Ru^{3+} centers are regenerated or the rate at which the analyte reaches the electrode surface, but by the rate of cross reaction between the analyte and the Ru^{3+} centers.

The kinetics of $[\text{Ru}]^{2+} / [\text{Ru}]^{3+}$ redox transformation are facile and they can be described by the Nernst Equation 5.8:

$$E = E^{0'} + 2.303 \frac{RT}{nF} \ln \frac{[C_{OX}]}{[C_{RED}]}$$

5.8

where E is the electrode potential in volts, $E^{0'}$ is the formal potential of the reversible reaction, Equation 5.1, in volts, R is gas constant ($8.314 \text{ JK}^{-1} \text{ mol}^{-1}$), T is temperature in Kelvin, n is the stoichiometric number of electrons consumed in the electrode reaction ($n = 1$), F is the Faraday constant (96485 Cmol^{-1}), C_{OX} is concentration of oxidising specie O and C_{RED} is the concentration of reducing specie R , respectively.

The rate of the reaction described by Equation 5.4a follows second order kinetics and can be written as

$$r = k [Ru^{3+}] [CO_2^{\bullet}]$$

5.9

where r is the rate of the reaction, k is the reaction rate constant ($M^{-1}s^{-1}$), $[Ru^{3+}]$ is the concentration of Ru^{3+} species and $[CO_2^{\bullet}]$ is the concentration of CO_2^{\bullet} radical, respectively.

Given the rate constant²³ of $(3.2 \pm 1.0) \times 10^2 \text{ M}^{-1} \text{ s}^{-1}$ two limiting conditions exist. When the concentration of oxalate is sufficiently high e.g. 100 mM, the half-life of analyte will only be $\approx 32 \text{ ms}$ and the catalytic Ru^{3+} centers are consumed more rapidly than they can be regenerated by homogenous charge transport through the layer. Under these conditions the ECL reaction becomes independent of the analyte concentration and this gives the upper limit of linear calibration range. However, for low concentrations of oxalate e.g. $1 \text{ }\mu\text{M}$, the half-life of the analyte is in the order of 3000 s and hence the cross reaction between Ru^{3+} and oxalate

becomes the rate limiting reaction.²³ It has been previously reported that at such low concentrations substantial background emission is observed, *i.e.*, detection of non-zero photo current by the photo multiplier tube (PMT) even in the absence of co-reactant.²²

Most of the ECL apparatus^{10,17,28,29} used by researchers worldwide basically contains a photo detector that converts the ECL intensity to a voltage. This measures the D.C. current generated in an optical detector as a result of incidence of steady state light source. Such a detection system, though simple and economical, is associated with several flaws. Firstly, when very low light signals need to be measured, this kind of system becomes more susceptible to random events and noise from various sources. The offset control of the detector has to be adjusted correctly to compensate for the detector's D.C. leak. If this is not done properly then the detector will have a nonzero output even in the absence of an optical input like the one seen by Forster and co-workers.²² Also, these kinds of detectors cannot differentiate between stray light entering the system from analytical light signal and hence the whole apparatus needs to be confined to light tight environments.

In order to apply a modulation technique to an ECL detection system, a sine wave is used and the potential of the working electrode is modulated. The potential of the working electrode is chosen as the source for modulation as it is this potential that is ultimately responsible for producing light. This induced AC potential modulates the light emission. Thus, an AC signal is generated at the detector output, which can be measured synchronously using a lock-in amplifier. Lock-in amplifiers have inbuilt synchronous filter whose bandwidth can be adjusted.²⁷ By adjusting the bandwidth of the filter to those frequencies close to the modulation frequency, noise and stray light can be filtered out.

The advantages of this technique not only include sensitive detection of a very small change of the input signal exclusively induced by the modulation, but also the capability of tracking the kinetics, for example the phase shift of the output ac signal with respect to the input ac modulation directly reflects how fast the system follows the potential change.²⁴ In this chapter, modulated potential ECL, AC impedance spectroscopy and equivalent circuit theory are used to describe the kinetics of light generation at an electrode | polymer | electrolyte interface.

5.2 AC IMPEDANCE SPECTROSCOPY

The basic feature of any biosensor device is the interaction of the biomaterial with the conductive support and the electronic transduction of the biological function associated with the biological matrix. Therefore, many of these devices involve the formation of a recognition complex between the sensing biomaterial and the analyte in a monolayer or thin film configuration deposited on the electronic transducer.³⁰ Impedance spectroscopy is a very powerful tool for the analysis of the interfacial properties of modified electrodes. Faradic impedance spectroscopy allows the kinetics and mechanisms of bio-electro catalytic reactions at the modified electrode surfaces to be analyzed providing important information for the development of amperometric biosensors.^{18,31-34}

In general, in this technique an electrochemical cell is considered to represent an impedance to a small applied sinusoidal excitation.¹⁸ Hence, an equivalent electrical circuit consisting of resistors and capacitors can represent its performance. This circuit will pass current with the same amplitude and phase angle as the real electrochemical cell. When the voltage $V \cos(\omega t)$ is applied to a circuit element, the resulting alternating current is solely of frequency ω having an amplitude proportional to V . For a Faradaic circuit the electrode process is said to be linear when the applied potential (V) is very small in comparison to RT/nF (*i.e.*, 26×10^{-3} Volts).¹⁸ Hence, traditionally small

amplitude excitation signals (5-10 mV) were employed to maintain the linearity of the system.

Fast Fourier transform (FFT) techniques that help to interpret data have recently made using large amplitude sine waves possible.³⁵⁻³⁹ Large amplitude perturbations introduce non-linearity. In order to determine the current in such systems, one has to employ non-linear system analysis, which is usually quite complicated. However, one has to tread carefully when dealing with FFT. FFTs are useful when the analytical signal is stationary *i.e.*, signal whose frequency content does not change in time. However, in practice, most of the investigated electrochemical systems are non-stationary. Strictly speaking, the impedance of a non-stationary system is a function of both frequency and time.⁴⁰ Although the frequency components of the signal can be found with the Fourier techniques it does not give us information about the time at which these frequency components occur.⁴¹

Many groups have tried to address the issue of non-linear electrochemical impedance spectra in corrosion,^{40,42} hydrodynamics⁴³ and electro analytical chemistry using time accurate transient models. Zhu and Kee⁴⁴ also developed a model, which not only predicts the response of the system for small amplitude perturbations but also for large amplitude perturbations.

These techniques are very useful in dealing with large amplitude perturbations but they involve rigorous computational modelling and simulation. Hence, another popular method extensively used to interpret large amplitude electrochemical impedance spectroscopy data is the equivalent circuit model (ECM). The ECM is a phenomenological model and hence is easily accepted and understood. Idealized equivalent circuit models are often constructed to simulate the physical and chemical processes taking place at a modified electrode surface.⁴⁰ Also each discrete circuit element has a corresponding physical and chemical meaning, such as mass-transfer, electron transfer, electrolyte resistance,

electrochemical reaction conductance *etc.*⁴⁰ Due to this feature, its simplicity and ease in diagnosis, this method has been followed herein.

5.2.1 Equivalent circuit theory: Modified Randle-Ershler circuit

The impedance characteristics of polymer-modified electrode systems in the presence and absence of oxalate species in solution can be modelled using modified Randle-Ershler circuit.^{18,31} This circuit is very commonly used to model interfacial phenomena. It mainly consists of an ohmic resistance of the electrolyte solution, R_{SOL} , the Warburg impedance, Z_{W} , due to the diffusion of ions from the bulk electrolyte to the electrode interface, the double layer capacitance, C_{dl} , and electron transfer resistance, R_{CT} , that exists when a redox specie (co-reactant) is present in electrolyte solution. Though many studies use a generic model it is often difficult to get a good fit. Hence, it is necessary to include more circuit elements like resistors, capacitors, constant phase elements *etc.* to get a good fit. However, with this approach not all circuit elements can be given physical meaning unambiguously. Moreover, the situation gets more complicated when dealing with conducting polymer as charge transport through the polymer can occur either by charge hopping or diffusion.⁴⁵ On the basis of the impedance diagrams obtained, an equivalent circuit, as shown in Figure 5.1, has been suggested for this $[\text{Ru}(\text{bpy})_2(\text{PVP})_{10}]^{2+}$ film system. Even though major part of the Randle-Ershler circuit has been maintained, a few modifications have been made. A resistor representing the film resistance and constant phase element describing the roughness of electrode has been added.

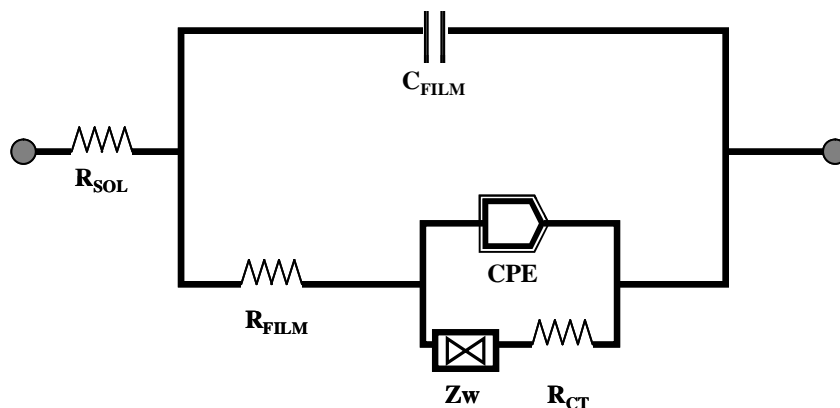


Figure 5.1: Modified Randle-Ershler model for polymer film electrode with a redox species (co-reactant) in solution where, R_{SOL} is electrolyte solution resistance, Z_W is Warburg impedance, CPE is the constant phase element, R_{FILM} and C_{FILM} are resistance and capacitance of the polymer film and R_{CT} is the electron transfer resistance.

The elements CPE, $R_{FILM} + C_{FILM}$ and $Z_W + R_{CT}$ are introduced in parallel as the total current through the working interface will be the sum of distinct contributions from the Faradaic process, I_F and the double layer charging I_C . R_{SOL} is introduced in series since all the current must pass through the uncompensated resistance of the electrolyte. The ligand in $[Ru(bpy)_2(PVP)_{10}]^{2+}$ film carries a charge under open circuit conditions due to unequal charge distribution in the ligand and pyridine units. Due to this a double layer around the redox center is formed. This makes the polymer-coated electrode behave as a pure capacitor given by C_{FILM} . R_{FILM} is interpreted as film resistance due to the penetration of electrolyte.

5.3 EXPERIMENTAL

5.3.1 Apparatus

Electrochemical measurements were carried out with a CH instruments, model 660 potentiostat. Cyclic voltammetry was conducted using a typical three-electrode cell. An aqueous Ag/AgCl/ saturated KCl (3 M) electrode was used as reference and a platinum wire was used as a counter electrode. The electrodes used were first polished with 0.3 μm alumina for 10 min, rinsed thoroughly with deionized water and then polished again for 10 min with 0.05 μm alumina. After polishing, the electrodes were thoroughly rinsed, first with deionized water and then with acetone to remove all traces of alumina from the surface and dried under nitrogen stream. All solutions were deaerated for 20 min by purging with nitrogen prior to electrochemical experimentation. All potentials are quoted versus an Ag/AgCl reference electrode, and all measurements were made at room temperature.

ECL measurements, utilized an Oriel 70680 photo multiplier tube (PMT) equipped with a high voltage power supply, (Oriel, model 70705), which was used at a bias of -850 V, and amplifier / recorder (Oriel, model 70701). During experiments, the cell was placed inside a specially constructed holder, which positioned the working electrode in a reproducible manner directly opposite the face of a fiber optic bundle, the other end of which was coupled to the PMT. The entire electrode assembly was contained inside a box and no extra measure was taken to avoid room light, as shown in Figure 5.2. The CH instruments potentiostat, model 660, which was connected via its external input jack to the internal oscillator sine wave output of a SR850–100 kHz DSP lock-in amplifier (Stanford Research Systems, Sunnyvale, CA), controlled the working electrode potential.

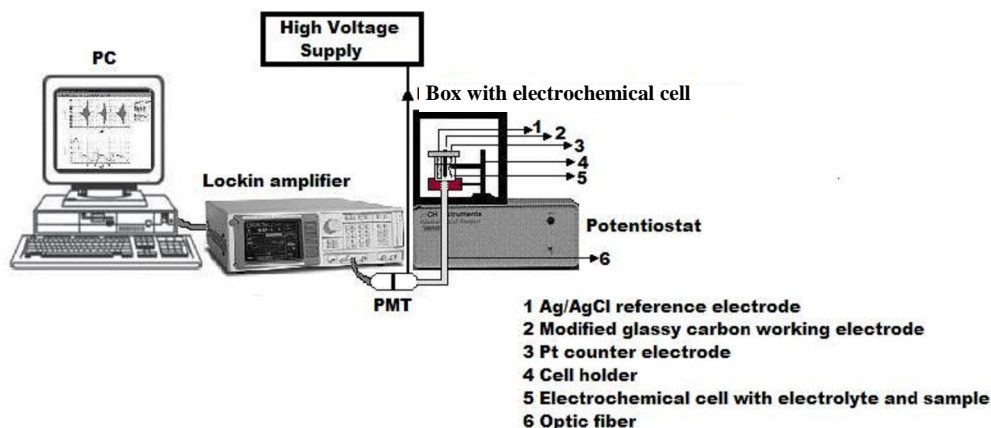


Figure 5.2: Experimental apparatus used for potential modulation experiments.

Impedance spectroscopy was performed using conventional three electrode cell and CH instruments, model 760B potentiostat. An excitation signal of 60 mV (peak amplitude) was applied to the electrodes in the presence of 24 dB filter, run time 30 s and the frequency of the signal was varied between 1 mHz -100 kHz. Modelling and curve fitting were also done using CH instruments, model 760B potentiostat.

5.4 RESULTS AND DISCUSSIONS

1% (w/v) $[\text{Ru}(\text{bpy})_2(\text{PVP})_{10}]^{2+}$ films (0.55 M of ruthenium sites and Γ $(4.39 \pm 0.06) \times 10^{-8} \text{ mol cm}^{-2}$), were formed as mentioned in Chapter 3, Section 3.3.1, on polished glassy carbon electrodes. The $[\text{Ru}(\text{bpy})_2(\text{PVP})_{10}]^{2+}$ films were characterised using profilometry, cyclic voltammetry and impedance spectroscopy and have been reported in Chapter 3. These techniques allowed the determination of various parameters of the film like thickness and charge transfer diffusion coefficient; D_{CT} . In this chapter, potential modulation coupled with synchronous detection was performed on both $[\text{Ru}(\text{bpy})_2(\text{PVP})_{10}]^{2+}$ films and $[\text{Ru}(\text{bpy})_3]^{2+}$ in solution. The analytical performances of D.C.

detection and the modulation technique are reported for both immobilised and solution phase reagents. The electrochemical impedance behaviour of the ECL polymer in the presence of co-reactant has also been studied. For the purpose of interpretation, the impedance characteristics of this polymer film at different potentials has been modelled using modified Randle-Ershler circuit.^{46,47} The impedance spectra and the charge transfer resistances obtained at different potentials from the model have also been reported.

5.4.1 Potential dependence of Ru^{3+} concentration in the film

It is known that for electrode processes involving fast heterogeneous charge transfer kinetics the surface concentrations of the oxidized and reduced species are related to the electrode potential by the Nernst equation¹⁸ *i.e.*, Equation 5.8. In the modulation experiment used here the surface potential is altered by ± 60 mV. This change is rapid at high-applied frequency and slow at low frequency. In order to evaluate how quickly the Faradaic system responds to this modulation it is important to know the number of electroactive Ru^{3+} present in the polymer film at a particular potential. The potential dependence of electroactive Ru^{3+} was calculated using formal potential, $E^{0'} = 1.08$, for $[\text{Ru}(\text{bpy})_2\text{PVP}_{10}]^{2+}$ film from Figure 5.5 and the Nernst equation at different potentials.

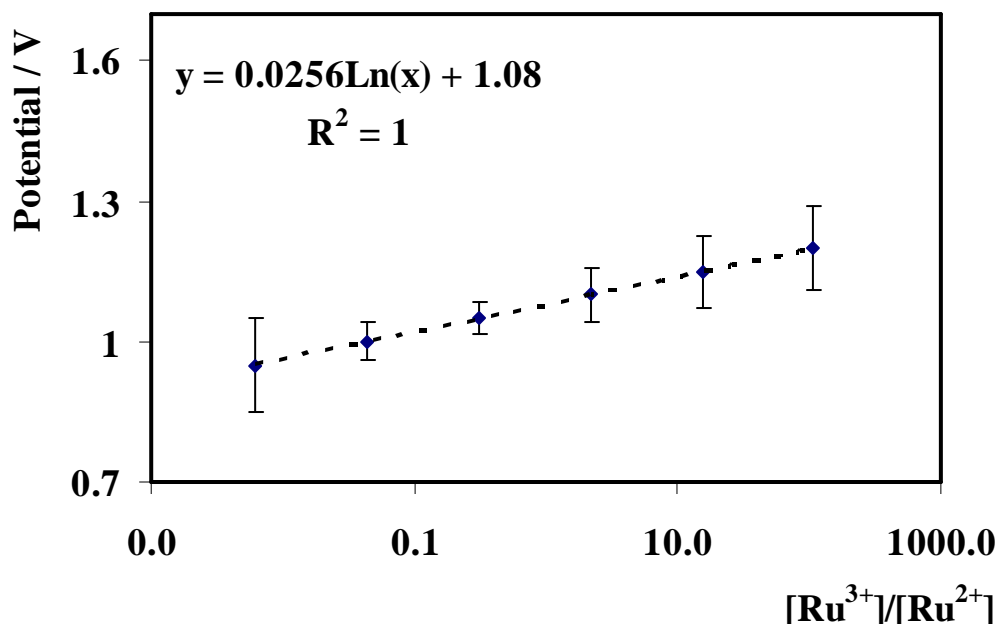


Figure 5.3: Potential dependence of the Ru^{3+} species present in a thin film of $[\text{Ru}(\text{bpy})_2(\text{PVP})_{10}]^{2+}$. The $[\text{Ru}(\text{bpy})_2(\text{PVP})_{10}]^{2+}$ film was obtained by drop casting 50 μL of 1% (w/v) polymer in 1:1 DMF: Ethanol mixture on a 3 mm diameter glassy carbon electrode and its surface coverage is $(4.39 \pm 0.06) \times 10^{-8} \text{ mol cm}^{-2}$. The curve is linear over potential range 0.95 V-1.2 V and the regression and slope for this region is reported in the inset.

From the Figure 5.3, it is observed that after 0.95 V the Ru^{3+} concentration increases linearly with applied potential between 1.0 V and 1.15 V. At potentials greater than 1.2 V all the Ru^{2+} reaching the electrode surface are converted to Ru^{3+} and hence, the concentration of Ru^{2+} can be assumed to be zero at the polymer | electrolyte interface.

It has been established that significant quenching of Ru^{2+*} by Ru^{3+} can occur in polymer films due to high concentration of the emitting centers within the film.⁴⁸ As shown earlier the emissive Ru^{2+*} state is created from the reduction of the electrogenerated Ru^{3+} state by the co-reactant. In the presence of high

Ru^{3+} concentration within the film, rather than the desired light emission process, Ru^{2+*} can be self quenched by electron transfer to Ru^{3+} .

Therefore, it is important to determine the relationship between ECL intensity and the ratio of $\text{Ru}^{3+}/\text{Ru}^{2+}$. Figure 5.4 illustrates relative ECL intensity as a function of % Ru^{3+} .

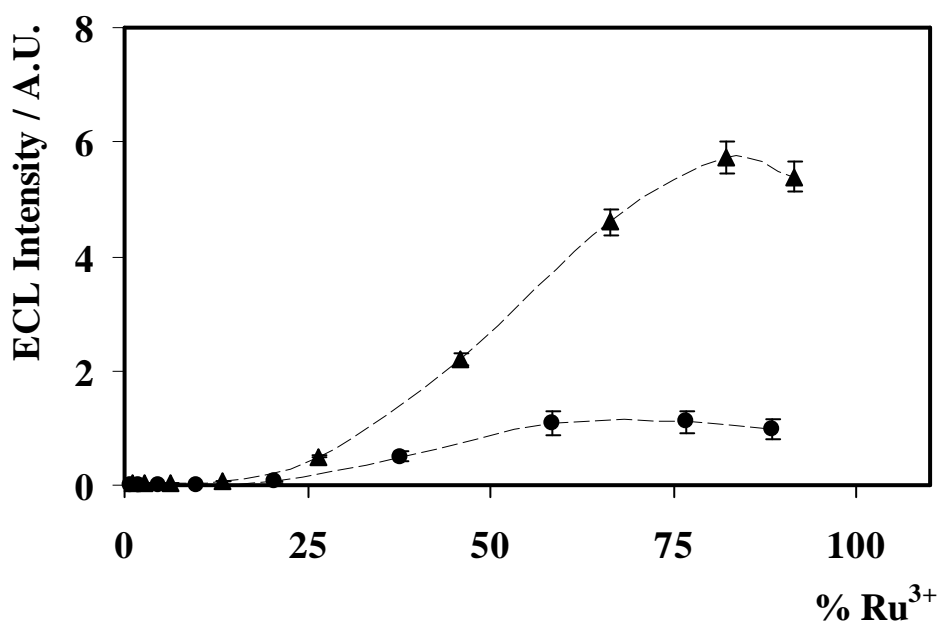


Figure 5.4: Dependence of ECL intensity on the percentage of oxidation of Ru^{2+} species present in the thin film of $[\text{Ru}(\text{bpy})_2(\text{PVP})_{10}]^{2+}$ on GCE (●) and in 1.0 mM $[\text{Ru}(\text{bpy})_3]\text{Cl}_2$ in solution (▲). 0.1 M PBS buffer (pH 7) was used as supporting electrolyte in the presence of 1 mM $\text{Na}_2\text{C}_2\text{O}_4$ co-reactant. A GCE working electrode was used and the surface coverage of $[\text{Ru}(\text{bpy})_2(\text{PVP})_{10}]^{2+}$ film was $(4.39 \pm 0.06) \times 10^{-8} \text{ mol cm}^{-2}$.

As expected, Figure 5.4 shows that ECL is absent at extremely low concentrations of Ru^{3+} and as the concentration of Ru^{3+} centers increases, ECL intensity also increases linearly, until a peak intensity is reached. Beyond this point, a drop in the ECL intensity is seen due to self quenching.

5.4.2 Potential modulation of solution phase & surface confined species

Source modulation coupled with synchronous detection when applied to surface bound $[\text{Ru}(\text{bpy})_2(\text{PVP})_{10}]^{2+}/\text{Oxalate}$ ECL system and solution phase $[\text{Ru}(\text{bpy})_3]^{2+}/\text{Oxalate}$ has the possibility of eliminating background and giving high S/N ratio and can also give valuable insight into the kinetics of the two systems. The results for solution phase $[\text{Ru}(\text{bpy})_3]^{2+}/\text{Oxalate}$ system have been published²¹ and hence it serves as a model system against which the results of the new surface confined system can be compared.

Figure 5.5 shows the D.C. potential dependence of current (A) and emission intensity (B) respectively of a thin $[\text{Ru}(\text{bpy})_2(\text{PVP})_{10}]^{2+}$ film $\{\Gamma (4.39 \pm 0.06) \times 10^{-8} \text{ mol cm}^{-2}\}$. The co-reactant used was 1 mM sodium oxalate dissolved in 0.1 M PBS buffer (pH 7).

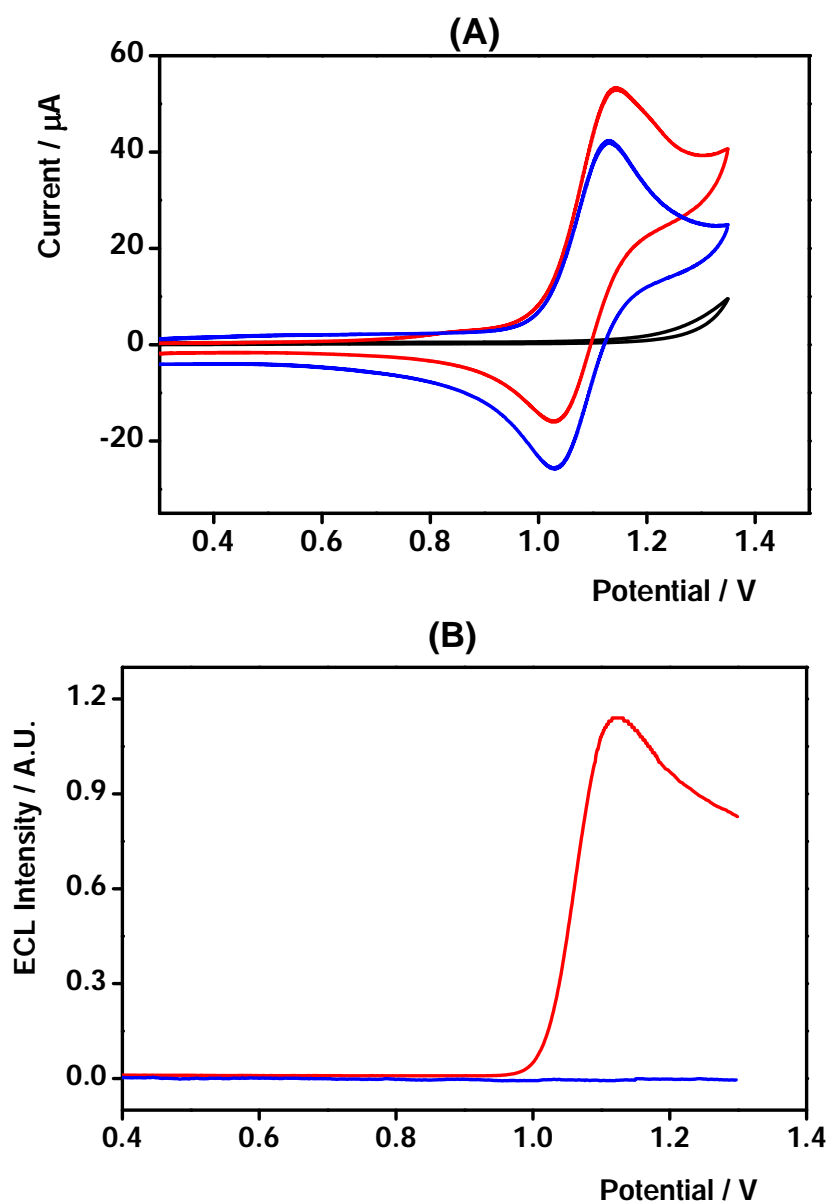


Figure 5.5: D.C. Potential dependence of current (A) and emission intensity (B), respectively, of a thin $[\text{Ru}(\text{bpy})_2(\text{PVP})_{10}]^{2+}$ film in the presence of (—) and absence of (—) 1 mM $\text{Na}_2\text{C}_2\text{O}_4$ co-reactant. Blank glassy carbon electrode without polymer, in the absence of oxalate is shown as (—). The voltammogram was carried out in 0.1 M PBS buffer (pH 7) with glassy carbon electrode as working electrode at scan rate 0.1 V s^{-1} . The surface coverage of the $[\text{Ru}(\text{bpy})_2(\text{PVP})_{10}]^{2+}$ film is $(4.39 \pm 0.06) \times 10^{-8} \text{ mol cm}^{-2}$.

From Figure 5.5 (A) it is seen that the mediated oxidation of $[\text{Ru}(\text{bpy})_2(\text{PVP})_{10}]^{2+}$ film through interaction with oxalate occurs at 1.12 V. Also this mediated oxidation is accompanied by significant emission of light as seen in Figure 5.5 (B). The onset of light coincides with the potential where the Ru^{3+} species are generated. This behaviour is expected as oxalate reduces the electrogenerated Ru^{3+} species to the excited reduced product Ru^{2+*} which relaxes to the ground state by emitting a photon as per Scheme 1.

5.4.3 Determination of optimum modulation parameters

In order to apply the above technique, an optimum D.C. potential and amplitude of the sine wave had to be determined. Figure 5.6 shows a plot of D.C. potential dependence of ECL intensity for $[\text{Ru}(\text{bpy})_2(\text{PVP})_{10}]^{2+}$ film (solid blue line) and $[\text{Ru}(\text{bpy})_3]^{2+}$ (dotted blue line) in solution. The term D.C. potential here refers to the base applied potential. Examination of this plot reveals that emission of light for both cases begins only after 1.0 V and there are regions *i.e.*, < 1 V where application of potential does not produce any light.

The maximum ECL intensity is observed at 1.12 V and 1.16 V for $[\text{Ru}(\text{bpy})_2(\text{PVP})_{10}]^{2+}$ film and $[\text{Ru}(\text{bpy})_3]^{2+}$ in solution, respectively. Hence the maximal and minimal intensity regions can be treated as fully “on” and fully “off” regions of light. Jirka *et.al.*,²¹ conducted similar studies with luminol/ H_2O_2 system and $[\text{Ru}(\text{bpy})_3]^{2+}$ /Oxalate system and found that for $[\text{Ru}(\text{bpy})_3]^{2+}$ /Oxalate system the optimum center potential was potential at half maximum emission in the D.C. ECL voltammogram. Significantly, similar results were observed in $[\text{Ru}(\text{bpy})_2(\text{PVP})_{10}]^{2+}$ film and hence the potential at which half maximum emission in the D.C. ECL was observed was chosen as the optimum center potential for both the film and solution. As smaller modulation amplitude provides for a more selective measurement by narrowing down the potential range over which ECL emission is observed, the smallest modulation, which gave good, stable signals, *i.e.*, 60 mV (0.042 Vrms), was chosen as the modulation amplitude.

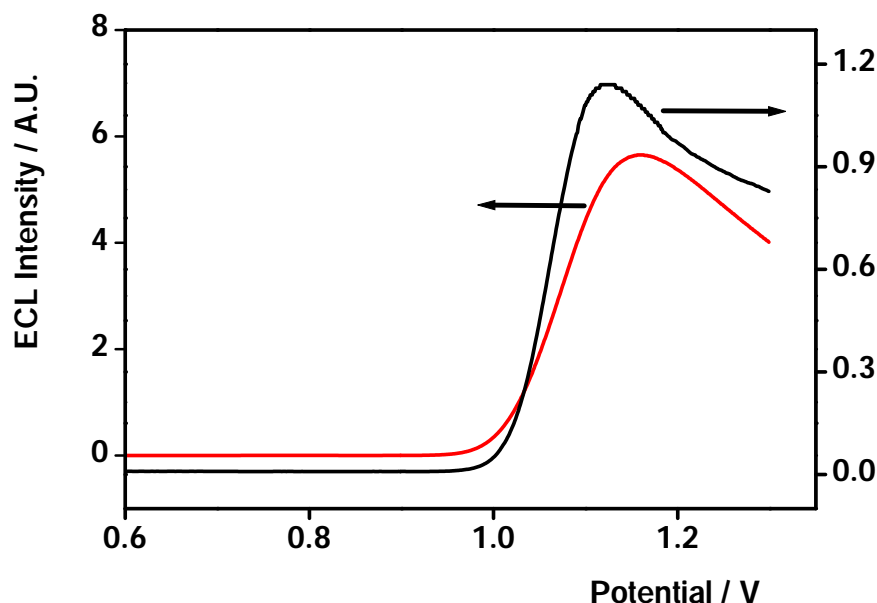


Figure 5.6: D.C. Potential dependence of ECL intensity for a thin $[\text{Ru}(\text{bpy})_2(\text{PVP})_{10}]^{2+}$ film (—) and 1.0 mM $[\text{Ru}(\text{bpy})_3]^{2+}$ in solution (—) in the presence of 1 mM $\text{Na}_2\text{C}_2\text{O}_4$ co-reactant. The voltammogram was carried out in 0.1 M PBS buffer (pH 7) with glassy carbon electrode as working electrode at scan rate 0.1 V s^{-1} . The surface coverage of the $[\text{Ru}(\text{bpy})_2(\text{PVP})_{10}]^{2+}$ film is $(4.39 \pm 0.06) \times 10^{-8} \text{ mol cm}^{-2}$.

5.4.4 Frequency dependence of modulated ECL

The dependence of the modulated ECL intensity on the modulation frequency was determined. In order to perform this measurement on the $[\text{Ru}(\text{bpy})_2(\text{PVP})_{10}]^{2+}$ film, the lock-in amplifiers' internal oscillator was set to a particular frequency with a sine wave of 60 mV amplitude (0.042Vrms). To this, a constant D.C. potential of 1.08 V was applied. Thus, the ECL was modulated between 1.14 and 1.02 V which modulated the ECL intensity at the modulation frequency.

Figure 5.7 shows the dependence of ECL emission intensity on applied frequency for frequencies ranging between 0.001-100 Hz after synchronous filtering.

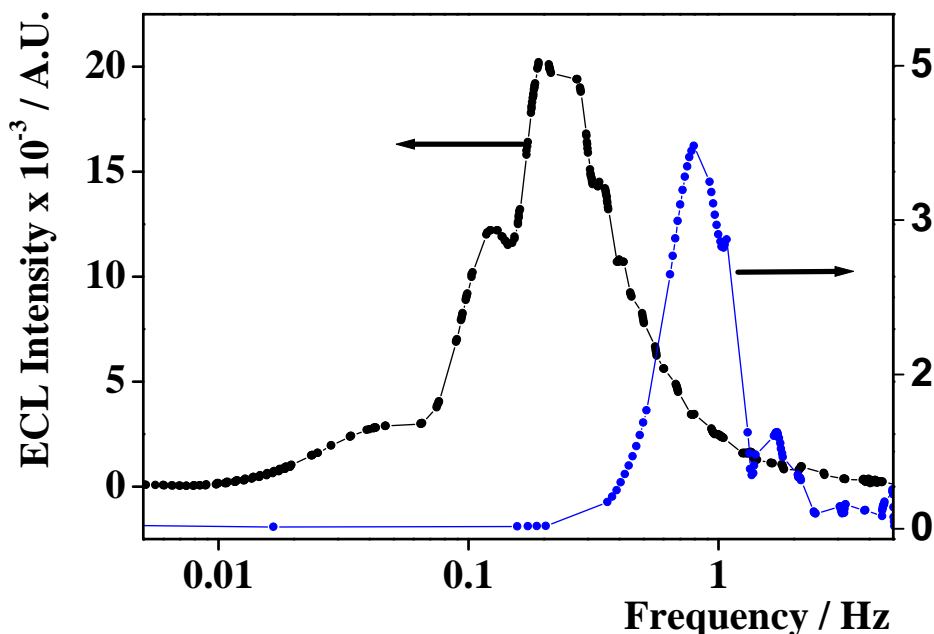


Figure 5.7: Dependence of modulated ECL intensity on modulation frequency of 1 mM $[\text{Ru}(\text{bpy})_3]^{2+}$ in solution (●) and a thin $[\text{Ru}(\text{bpy})_2(\text{PVP})_{10}]^{2+}$ film (●). A sine wave of 50 mV (0.034 Vrms), 1.06 V center potential and 60 mV (0.042 Vrms), 1.08 V center potential was applied for $[\text{Ru}(\text{bpy})_3]^{2+}$ and $[\text{Ru}(\text{bpy})_2(\text{PVP})_{10}]^{2+}$ film respectively, at a range of frequencies from 0.001-100 Hz. GCE was used with 0.1 M PBS buffer (pH 7) as supporting electrolyte in the presence of 5 mM $\text{Na}_2\text{C}_2\text{O}_4$ co-reactant. The surface coverage of the $[\text{Ru}(\text{bpy})_2(\text{PVP})_{10}]^{2+}$ film is $(4.39 \pm 0.06) \times 10^{-8} \text{ mol cm}^{-2}$.

Figure 5.7, shows marked differences between the species in solution and the one in film. Firstly, in both the cases the ECL intensity has a peak. This peak means that there is an optimum frequency at which maximum emission is observed and on either side of the maximum frequency, the intensity of emission drops. From the plot it also appears that while the optimum frequency for $[\text{Ru}(\text{bpy})_3]^{2+}$ is centered around 1 Hz, for $[\text{Ru}(\text{bpy})_2(\text{PVP})_{10}]^{2+}$ film it is around 250 mHz. Although it cannot be quantitatively ascertained, it appears that the

$[\text{Ru}(\text{bpy})_3]^{2+}/\text{Oxalate}$ ECL reaction is faster than the $[\text{Ru}(\text{bpy})_2(\text{PVP})_{10}]^{2+}/\text{Oxalate}$ system. Also, for both the systems, the intensity observed is 3 orders of magnitude lower than the constant potential signal under the same conditions and is accompanied by a phase shift. This is however expected as emission of light decays with time and this leads to a shift in the phase compared to the input signal. The output of the lock in amplifier is a product of two sine wave functions. Thus, as the two sine waves are multiplied, the ultimate amplitude of the signal will be half its initial value.⁴⁹

5.4.5 Analytical performance

5.4.5.1 Limit of detection (LOD)

Calibration curves for both D.C. and modulated potential conditions were obtained for $[\text{Ru}(\text{bpy})_2(\text{PVP})_{10}]^{2+}$ film (Γ is $4.39 \pm 0.06 \times 10^{-8} \text{ mol cm}^{-2}$). For modulated ECL, 250 mHz and 1 Hz sine were applied to the film at different oxalate concentrations. The run time of each measurement was 30 s. On application of a modulated potential a sharp increase in the signal intensity could be seen which dropped significantly when the potential input was stopped. A similar response was observed with a phase shift where application of modulated potential caused the randomly changing phase angle to be fixed to a particular value. It remained at this value until the stimulus was present and when the potential stimulus was removed, it became random again. This behaviour of the ECL intensity and phase shift is as shown in Figure 5.8 (A) and (B) respectively.

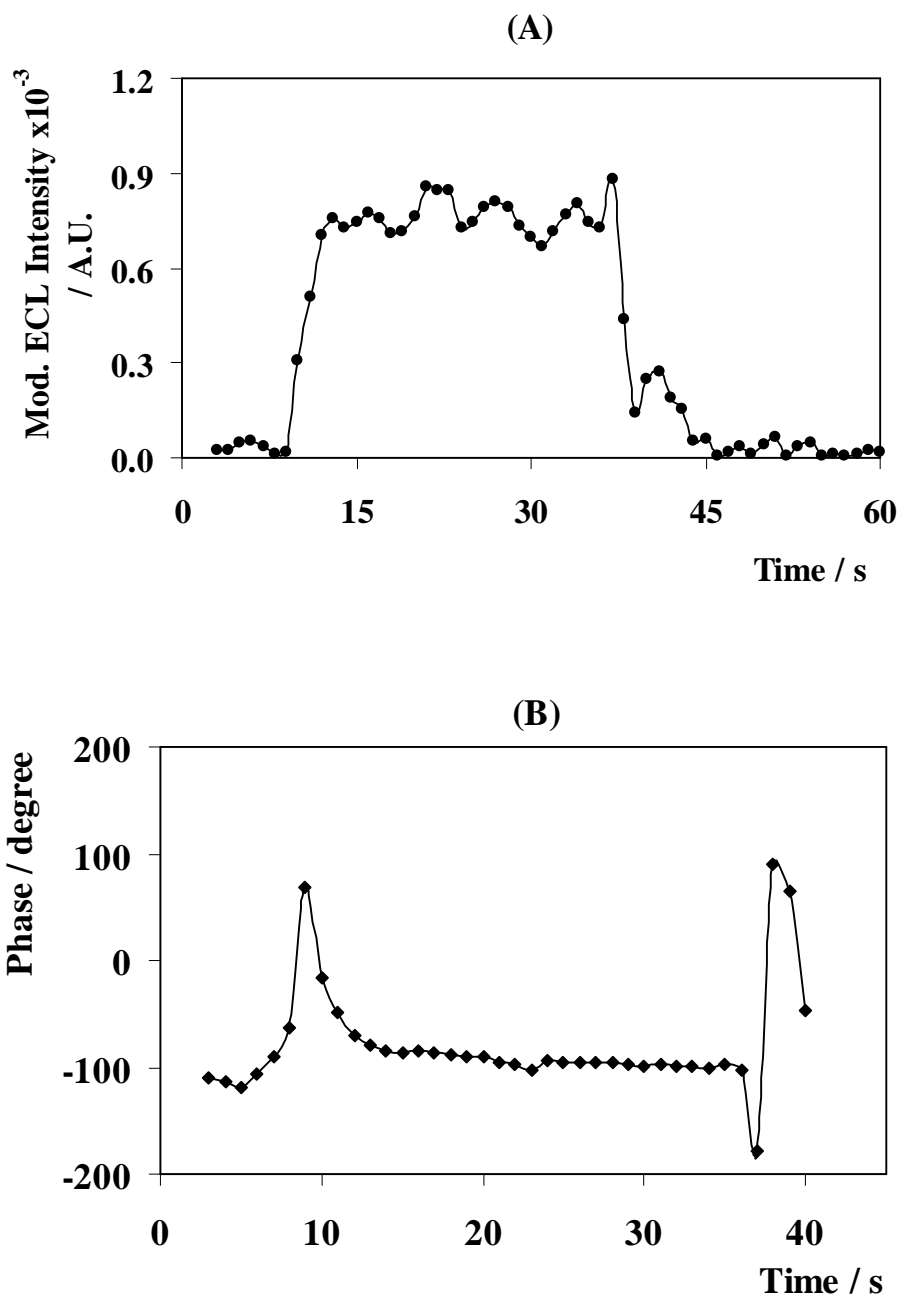


Figure 5.8: Modulated ECL intensity (A) and corresponding phase shift (B) observed when a thin $[\text{Ru}(\text{bpy})_2(\text{PVP})_{10}]^{2+}$ film is subjected to a sine wave of 60 mV (0.042 Vrms), 1.08 V center potential with 30 s run time 24 dB filter and 250 mHz frequency. The film was formed on GCE and the electrolyte was 0.1 M PBS buffer (pH 7) with 100 μM $\text{Na}_2\text{C}_2\text{O}_4$ as co-reactant. The surface coverage of the $[\text{Ru}(\text{bpy})_2(\text{PVP})_{10}]^{2+}$ film is $(4.39 \pm 0.06) \times 10^{-8} \text{ mol cm}^{-2}$.

Calibration curves showing the dependence of ECL intensity for the D.C. detection technique is shown Figure 5.9. It is seen that the calibration curve is highly linear with sensitivity being 0.9 intensity units per mM oxalate concentration. Figure 5.10 shows the dependence of ECL intensity for modulation technique and Table 5.1 gives the corresponding values for D.C., 250 mHz modulation frequency and 1 Hz modulation frequency, respectively. The dependence of phase shift on oxalate concentration is as shown in Figure 5.11 with Table 5.2 giving the corresponding values.

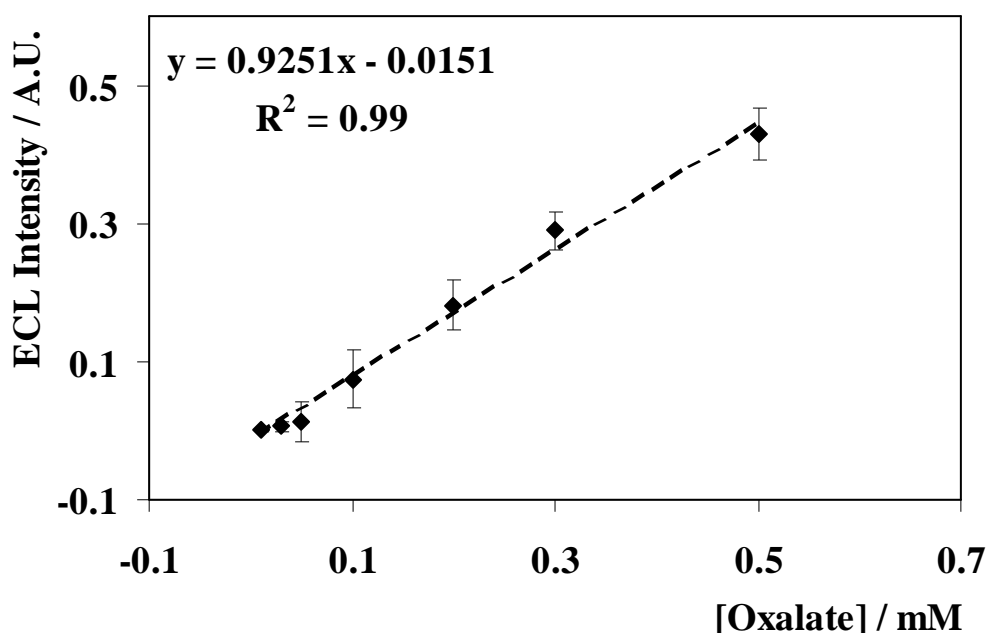


Figure 5.9: Calibration plot obtained for thin $[\text{Ru}(\text{bpy})_2(\text{PVP})_{10}]^{2+}$ film under un-modulated D.C. potential. The film was formed on GCE and the electrolyte was 0.1 M PBS buffer (pH 7) with different $\text{Na}_2\text{C}_2\text{O}_4$ concentrations. The surface coverage of the $[\text{Ru}(\text{bpy})_2(\text{PVP})_{10}]^{2+}$ film is $(4.39 \pm 0.06) \times 10^{-8} \text{ mol cm}^{-2}$ and the voltammogram was performed at 0.1 Vs^{-1} scan rate.

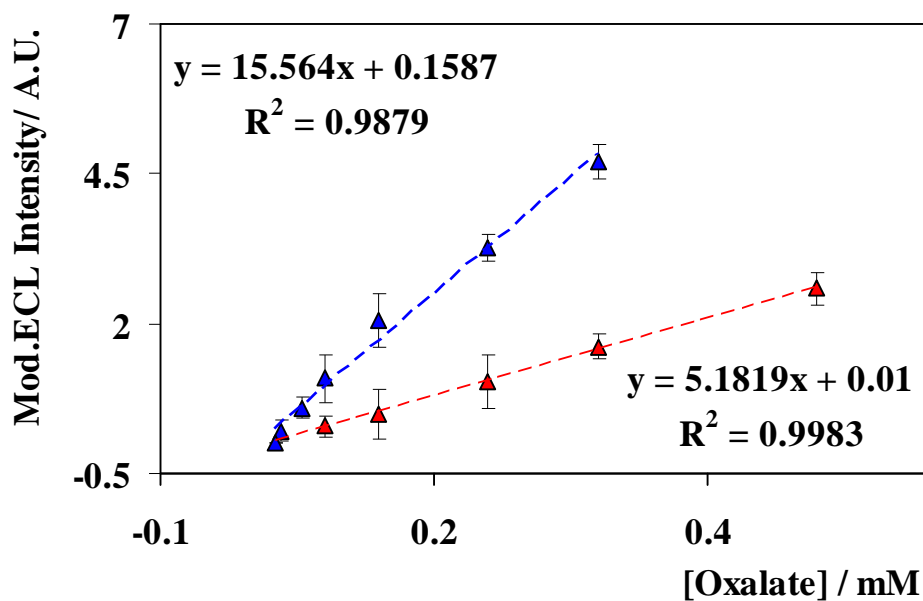


Figure 5.10: Calibration plots obtained for $[\text{Ru}(\text{bpy})_2(\text{PVP})_{10}]^{2+}$ film under modulated potential at 250 mHz (\blacktriangle) and 1 Hz (\blacktriangle). A sine wave of 60 mV (0.042 Vrms), 1.08 V center potential was applied on polymer modified GCE electrode in 0.1 M PBS (pH 7) buffer electrolyte and different $\text{Na}_2\text{C}_2\text{O}_4$ concentrations. The surface coverage of the $[\text{Ru}(\text{bpy})_2(\text{PVP})_{10}]^{2+}$ film is $(4.39 \pm 0.06) \times 10^{-8} \text{ mol cm}^{-2}$.

Table 5.1: Calibration plot values obtained for $[\text{Ru}(\text{bpy})_2(\text{PVP})_{10}]^{2+}$ film under un-modulated D.C. potential, 250 mHz modulated potential and 1 Hz modulated potential. For modulation a sine wave of 60 mV (0.042 V_{rms}), 1.08 V center potential was applied on modified GCE electrode in 0.1 M PBS (pH 7) buffer electrolyte and different $\text{Na}_2\text{C}_2\text{O}_4$ concentrations. The surface coverage of the $[\text{Ru}(\text{bpy})_2(\text{PVP})_{10}]^{2+}$ film is $(4.39 \pm 0.06) \times 10^{-8} \text{ mol cm}^{-2}$.

$[\text{Na}_2\text{C}_2\text{O}_4]$ /mM	D.C. Intensity $\times 10^{-2}$ / A.U.	250 mHz. Intensity/A.U.	1 Hz. Intensity /A.U.
1	112 \pm 4	7.4 \pm 0.3	3.4 \pm 0.3
1.1.1.1.1 0	42.8 \pm 3	5.9 \pm 0.2	2.6 \pm 0.2
1.1.1.1.2 0	29 \pm 4	4.7 \pm 0.4	1.6 \pm 0.4
0.2	18 \pm 4	3.0 \pm 0.4	1.0 \pm 0.4
1.1.1.1.3 0	7.4 \pm 3	2.1 \pm 0.2	0.5 \pm 0.2
1.1.1.1.4 0	1.3 \pm 0.7	1.1 \pm 0.2	0.3 \pm 0.1
1.1.1.1.5 0	0.60 \pm 0.2	0.6 \pm 0.002	—
1.1.1.1.6 0	0.02 \pm 0.01	0.3 \pm 0.002	—
1.1.1.1.7 0	—	0.0002 \pm 8 $\times 10^{-5}$	—

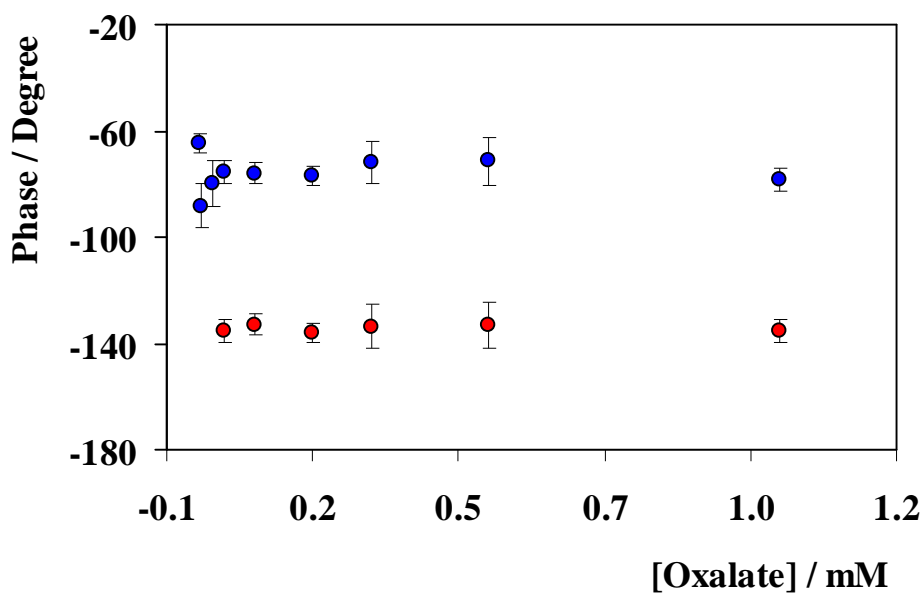


Figure 5.11: Change in phase with respect to oxalate concentration for $[\text{Ru}(\text{bpy})_2(\text{PVP})_{10}]^{2+}$ film on GCE when subjected to potential modulation at 250 mHz (●) and 1 Hz (●) using a sine wave of 60 mV (0.042 V_{rms}), 1.08 V center potential, in 0.1 M PBS (pH 7) buffer electrolyte and different $\text{Na}_2\text{C}_2\text{O}_4$ concentrations. The surface coverage of the $[\text{Ru}(\text{bpy})_2(\text{PVP})_{10}]^{2+}$ film is $(4.39 \pm 0.06) \times 10^{-8} \text{ mol cm}^{-2}$.

Table 5.2: Change in phase obtained for $[\text{Ru}(\text{bpy})_2(\text{PVP})_{10}]^{2+}$ under un-modulated D.C. potential, 250 mHz modulated potential and 1 Hz modulated potential. For modulation a sine wave of 60 mV (0.042 V_{rms}), 1.08 V center potential was applied on modified GCE electrode in 0.1 M PBS (pH 7) buffer electrolyte and different $\text{Na}_2\text{C}_2\text{O}_4$ concentrations. The surface coverage of the $[\text{Ru}(\text{bpy})_2(\text{PVP})_{10}]^{2+}$ film is $(4.39 \pm 0.06) \times 10^{-8} \text{ mol cm}^{-2}$.

$[\text{Na}_2\text{C}_2\text{O}_4] / \text{mM}$	250 mHz Phase shift /deg	1 Hz Phase shift /deg.
1	-78.7 \pm 4	-135.2 \pm 4
1 1 1 1 8 0	-71.5 \pm 9	-133.2 \pm 9
1 1 1 1 9 0	-71.9 \pm 8	-133.6 \pm 4
0.2	-77.1 \pm 4	-136.0 \pm 4
1 1 1 1 10 0	-76.0 \pm 4	-132.8 \pm 4
1 1 1 1 11 0	-75.2 \pm 4	-135.0 \pm 1
1 1 1 1 12 0	-79.9 \pm 9	—
1 1 1 1 13 0	-88.0 \pm 8	—
1 1 1 1 14 0	-65.0 \pm 3	—

Further examination of the calibration curves reveals that the modulated potential technique with 250 mHz modulation frequency has a lower detection limit of 5 μM , where as the D.C. technique can detect concentrations of 10 μM of oxalate. The modulated potential technique with 1 Hz modulation frequency has the highest detection limit of only 50 μM . However, all three techniques have similar dynamic range and are linear over a wide range of concentrations *i.e.*, 10 μM -0.5 mM. It is also significant to note that the modulation technique shows a higher sensitivity with slope equal to 15.6 (250 mHz) and 5.2 (1 Hz) intensity units mM^{-1} when compared to the un-modulated D.C. with a slope of 0.93 intensity units mM^{-1} . The results of three calibration charts are summarized in Table 5.3.

Table 5.3: Calibration curve parameters for surface confined $[\text{Ru}(\text{bpy})_2(\text{PVP})_{10}]^{2+}$ / oxalate system. The surface coverage of the $[\text{Ru}(\text{bpy})_2(\text{PVP})_{10}]^{2+}$ film is $(4.39 \pm 0.06) \times 10^{-8} \text{ mol cm}^{-2}$.

Method	Frequency/Hz	LOD/ μM	Sensitivity / $\text{ECL}_{\text{INTENSITY}} /$ $\text{mM}_{\text{OXALATE}}$
D.C.ECL	-	10	0.93
1.1.1.1.15 Mod.	0.25	5	15.6
1.1.1.1.16 Mod.	1.0	50	5.2

It is significant to note that when the logarithm to base 10 of the calibration curves is calculated for surface confined $[\text{Ru}(\text{bpy})_2(\text{PVP})_{10}]^{2+}$ /Oxalate system and compared to the solution phase $[\text{Ru}(\text{bpy})_3]^{2+}$ /Oxalate system reported by Nieman *et.al.*, under D.C. conditions, the solution phase system has lower slope of 0.813²¹ where as the surface confined system has a greater slope of 1.4. However, the solution phase system reported by Nieman *et.al.*,²¹ has a lower limit of detection (LOD) of 3 μM . Whereas the surface confined system can clearly detect up to 10 μM of oxalate. The modulation technique (250 mHz) on the other hand, under optimised conditions shows a lower LOD of 5 μM , lower than the D.C. technique. Significantly, when the sensitivity of the modulation technique is considered it exhibits a far greater sensitivity of 15.6, 14 units higher than the one reported in

literature²¹ for solution phase system at 1 Hz. Thus, the surface confined D.C. experiments are more sensitive with higher signal to noise ratios compared to solution phase D.C. experiments and modulated potential experiments are more sensitive with higher limits of detection when compared to D.C. techniques.

Analysis of Figure 5.11 could give valuable information about the kinetics of the system considered. It can be seen that for both solution and film systems the frequencies the output signals lags by an angle. This is expected as after application of the potential it takes time for the chemical system to react to the stimulus and hence the output signal lags behind the input. However, it is surprising to see that on application of 250 mHz modulation, the phase shift is just 75 ± 12 deg whereas under 1 Hz modulation the system response is much slower with lag of nearly 140 deg.

Also it is seen that at higher concentrations of oxalate the phase shift is fairly constant (± 12 deg) but at low concentrations the constancy of the phase shift is perturbed and it no longer appears to have a constant value for a particular frequency. This is more clearly seen at 250 mHz than at 1 Hz. This could reflect the two limiting regimes mentioned in Section 5.1, *i.e.*, when the concentration of oxalate is sufficiently high the half life of the analyte is very short and the catalytic Ru^{3+} centers are consumed more rapidly than they can be regenerated by homogenous charge transport through the layer. Under these conditions the ECL reaction becomes independent of the analyte concentration and thus phase change remains fairly constant. However, at low concentrations

of oxalate the cross reaction between Ru^{3+} and oxalate becomes the rate limiting reaction and it depends on the diffusion of oxalate species from the solution to the surface of the electrode.²³ This could be the reason for a non constant phase shift observed at low concentrations.

5.4.5.3 Determination of kinetic parameters

The response of the polymer layer depends on the relative size of the diffusion layer δ and the polymer film thickness ϕ . Based on the sizes, two limiting cases arise namely thin-layer behaviour ($\delta \gg \phi$) and semi-infinite diffusion behaviour ($\delta \ll \phi$). Most redox polymers exhibit behaviour, which is intermediate between these two limiting cases called finite diffusion behaviour.⁵⁰ As mentioned, the important parameter in determining the extent of diffusion effects depends on δ and ϕ . The thickness of the diffusion layer in turn depends on charge transfer diffusion coefficient, D_{CT} and experimental time scale, t . The effects of D_{CT} , δ and ϕ can be expressed by a dimensionless parameter χ given by Equation 5.10.³¹

$$\chi = \frac{tD_{CT}}{\phi^2} \quad 5.10$$

Using the calculated value of D_{CT} of the $[\text{Ru}(\text{bpy})_2(\text{PVP})_{10}]^{2+}$ film, $4.28 \times 10^{-11} \text{ cm}^2\text{s}^{-1}$, film thickness of $8 \pm 1 \text{ kÅ}$ and experimental time t being 50 s, χ is calculated to be 0.3. If $\chi > 1$ the polymer film exhibits thin-layer behaviour but if $\chi < 1$, semi-infinite diffusion behaviour can be seen. Hence, the polymer film considered above exhibits semi-infinite linear diffusion behaviour in the high frequency kinetic control regime, where $f = 3.16 \times 10^{-3} \text{ Hz}$ and therefore $\omega = 0.019 \text{ rad s}^{-1}$.

Impedance analysis of the polymer film will allow the interfacial properties of the modified electrode to be studied. Hence, in order to obtain an impedance spectra of the ECL polymer film without the co-reactant in solution, an AC sine modulation of 60 mV (peak amplitude) was applied over a range of D.C.

potentials starting from 0.8 V to 1.3 V vs. Ag/AgCl, over a frequency range of 1 mHz-100 KHz, in 0.1 M PBS buffer (pH 7), to the polymer coated glassy carbon electrodes. Depending on the center potential applied to the electrode, the concentration of the Ru^{3+} and Ru^{2+} species varies. Figure 5.12 shows the impedance plane plot obtained at different center potentials.

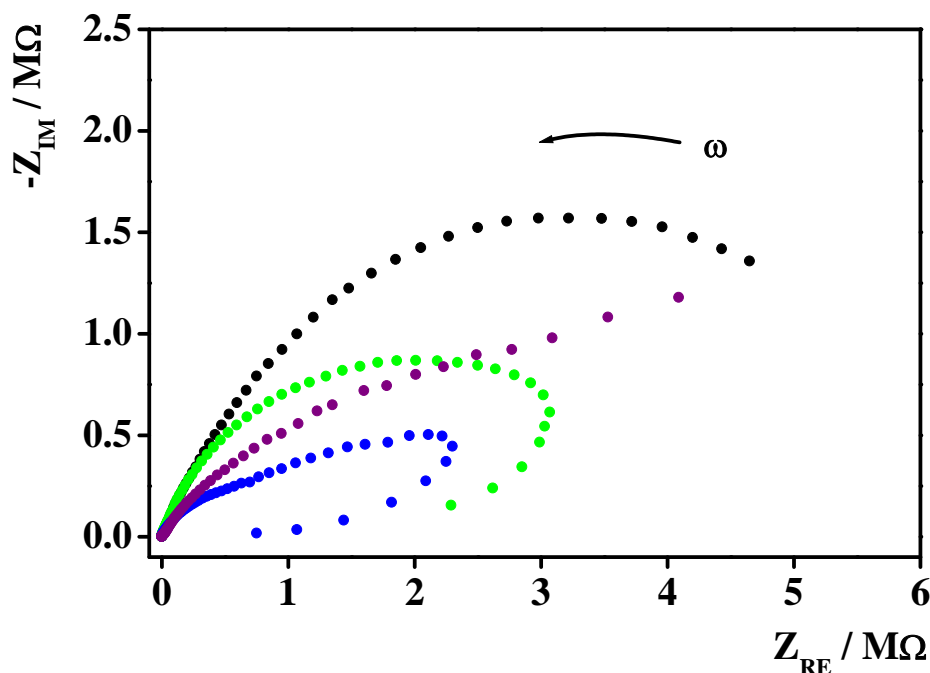


Figure 5.12: Nyquist plots recorded for $[\text{Ru}(\text{bpy})_2(\text{PVP})_{10}]^{2+}$ film on GCE with an AC sine modulation of 60 mV (peak amplitude), over a range of D.C. center potentials, 1.0 V (●), 1.08 V (●), 1.2 V (●) and 1.3 V (●) vs. Ag/AgCl, at frequency range of 1 mHz-100 KHz, in 0.1 M PBS buffer electrolyte (pH 7). The surface coverage of the $[\text{Ru}(\text{bpy})_2(\text{PVP})_{10}]^{2+}$ film is $(4.39 \pm 0.06) \times 10^{-8} \text{ mol cm}^{-2}$.

By fitting a semi-circular arc to the high frequency charge transfer regime, as shown in Figure 5.13, solution resistance (R_{SOL}), charge transfer resistance (R_{CT}) and maximum angular frequency (ω_{max}) were obtained. The double layer capacitance (C_{dl}), and τ (time constant for the Faradaic process) at different applied potentials can be obtained from Equations 1.30, 1.31 and 1.32 in Chapter 1. In the absence of oxalate in solution, Equation 1.26, and 1.28,

Chapter 1, where the terms have their usual meaning, were used to calculate the values of I_0 and k_s .^{18,50,51} These parameters are summarised in Table 5.4.

$$I_0 = nFAk_s C_O^{(1-\alpha)} C_R^\alpha \quad 1.26$$

$$R_{CT} = \frac{RT}{nFI_0} \quad 1.28$$

Comparing the impedance plot in Figure 5.14 to the ideal one, *i.e.*, Figure 3.5, Chapter 3, it can be seen that at 1.0 V center potential the impedance plot shows just the semicircular region over the entire range of applied frequencies. The absence of any linear region at low frequency is due to the absence of diffusion controlled charge transport through the bulk of the film. For thicker films charge saturation dominates only at very low frequencies and diffusional control is seen over a large frequency range. $[\text{Os}(\text{bpy})_2(\text{PVP})_x\text{Cl}]\text{Cl}$ films exhibit purely capacitive behaviour at low frequencies.⁴ This was observed in the form of a sharp rise in the Z_{IM} by Sharp *et.al.*⁴ For $[\text{Ru}(\text{bpy})_2(\text{PVP})_{10}]^{2+}$ films however it is observed that the diffusional control dominates over the charge saturation region in the frequency range applied and hence a vertical line perpendicular to the real axis is not observed.

At 1.0 V, as seen from Figure 5.3, not all ruthenium centers are oxidized and interfacial electron transfer controls impedance within the entire range of the applied frequency. The large depressed semicircle signifies very sluggish electron transfer kinetics and a possible blocking behaviour of the polymer electrode. By fitting a semi-circular arc to the experimental data as shown in Figure 5.13, the values of $R_{SOL} = 500 \Omega$ and $R_{CT} = 3.7 \text{ M}\Omega$ are obtained at this potential. At the formal potential however, there is a small diffusion tailing seen in the Warburg diffusion region but the angle of the straight line is lesser than the expected value of 45° .^{31,34,52,53} The observation of the diffusional tailing is not clearly understood but could be due to charge propagation through the polymer layer. Also a straight line at an angle less than 45° is usually observed when the surface of the modified electrode is rough or the polymer layer is inhomogeneous. These two characteristics of the interface can be accounted for

by introducing a constant phase element (CPE)^{31,52} instead of a pure capacitor while designing an equivalent electrical circuit like the one shown in Figure 5.1.

A further increase in the center potential causes the diameter of the impedance arc, which measures the charge transfer resistance across the electrode surface, to decrease as shown in Figure 5.13. The negative capacitive behaviour seen at very low frequencies and at higher potentials is due to the ingress of charge compensating counter ions into the polymer film from the electrolyte solution.^{44,54}

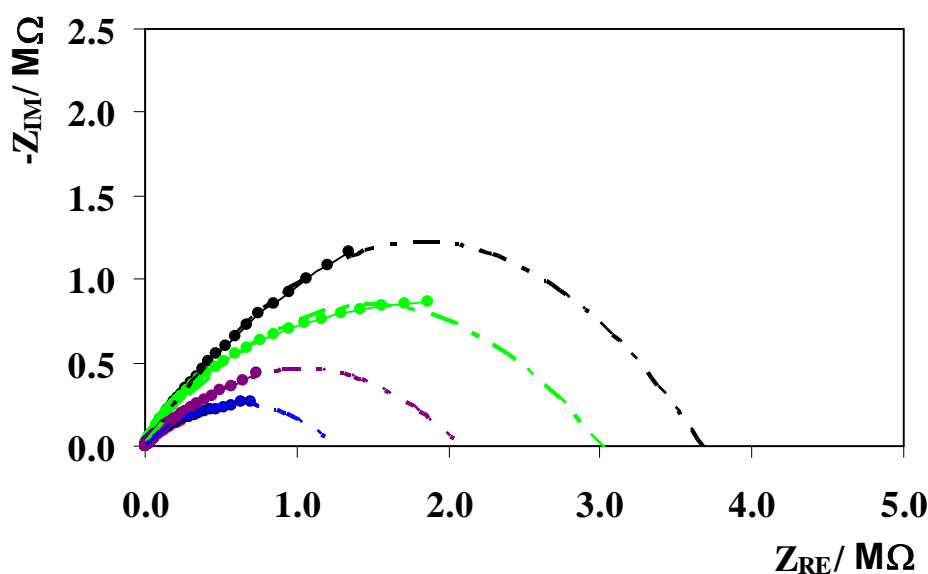


Figure 5.13: Semicircular arc fit for impedance plane plot for $[\text{Ru}(\text{bpy})_2(\text{PVP})_{10}]^{2+}$ film on GCE the absence of co-reactant at 1.0 V (●), 1.08 V (●), 1.2 V (●) and 1.3 V (●) applied potentials. An AC sine modulation of 60 mV (peak amplitude), D.C. center potentials 1.0 V vs. Ag/AgCl, at frequency range of 1 mHz-100 KHz, in 0.1 M PBS buffer electrolyte (pH 7). The surface coverage of the $[\text{Ru}(\text{bpy})_2(\text{PVP})_{10}]^{2+}$ film is $(4.39 \pm 0.06) \times 10^{-8} \text{ mol cm}^{-2}$.

Table 5.4: Kinetic parameters evaluated for $\text{Ru}(\text{bpy})_2(\text{PVP})_{10}]^{2+}$ film on GCE in the absence of co-reactant at different potentials. The surface coverage of the $[\text{Ru}(\text{bpy})_2(\text{PVP})_{10}]^{2+}$ film is $(4.39 \pm 0.06) \times 10^{-8} \text{ mol cm}^{-2}$.

E / V	$R_{CT} / \text{M}\Omega$	$\omega_{\max} / \text{Hz}$	$C_{dl} / \mu\text{F}$	τ / s	$I_0 / \text{A cm}^{-2} \times 10^{-6}$	$k_s / \text{cm s}^{-1} \times 10^{-9}$	$D_{CT} / \text{cm}^2 \text{s}^{-1} \times 10^{-11}$
1.00	3.7	0.13	2.1	7.8	0.3	0.15	4.7
1.08	2.1	0.11	4.4	9.2	1.2	0.5	12.0
1.15	0.6	0.23	7.3	4.4	2.0	1.0	16.2
1.2	3.0	0.34	0.9	2.7	0.12	0.08	7.5
1.3	1.2	0.42	1.9	2.4	2.15	3.0	10.2

Similar AC impedance measurements were done with 1 mM sodium oxalate in 0.1 M PBS buffer (pH 7). The impedance plot is as shown in Figure 5.15.

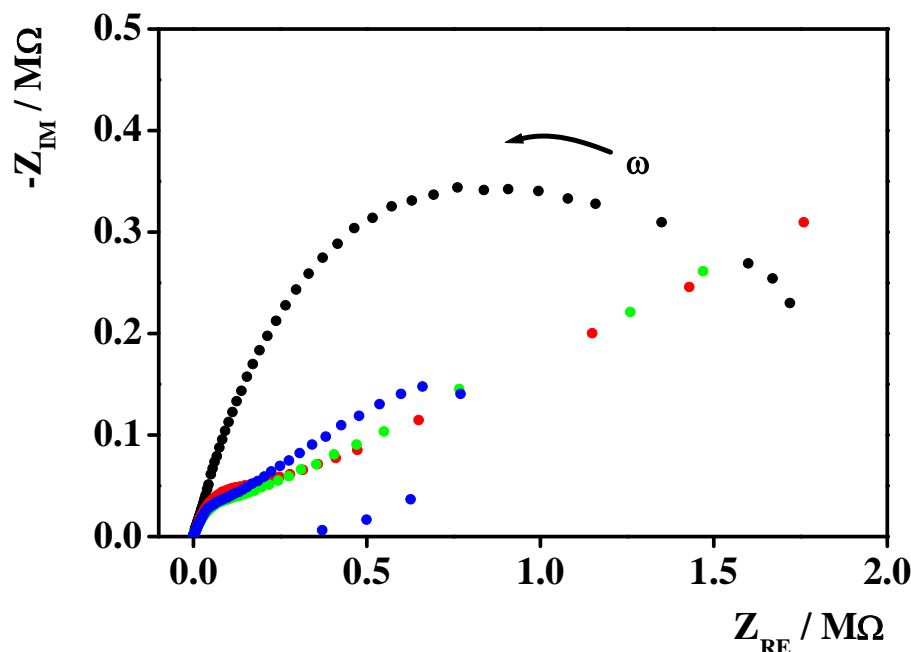


Figure 5.14: Impedance plane plots recorded for $[\text{Ru}(\text{bpy})_2(\text{PVP})_{10}]^{2+}$ film on GCE in the presence of 1 mM sodium oxalate co-reactant in solution, with an AC sine modulation of 60 mV (peak amplitude), over a range of D.C. potentials, 1.0 V (●), 1.15 V (●), 1.2 V (●) and 1.3 V (●) vs. Ag/AgCl, at frequency range of 1 mHz-100 KHz, in 0.1 M PBS buffer electrolyte (pH 7). The surface coverage of the $[\text{Ru}(\text{bpy})_2(\text{PVP})_{10}]^{2+}$ film is $(4.39 \pm 0.06) \times 10^{-8} \text{ mol cm}^{-2}$.

In presence of oxalate also it is observed that at 1.0 V, the film exhibits sluggish behaviour but the R_{CT} is roughly three times lesser than in the absence of oxalate, as shown in Figure 5.15. As the center potential is increased to potential where oxalate begins to oxidize, Warburg diffusion region at low frequency represented by a straight line at an angle less than 45° is observed. Also, a well defined but depressed semi-circular charge transfer resistance region at high frequencies is observed. As the applied potential is constantly increased, a point is reached (~ 1.3 V) where there is ingress of charge neutralising ions and the appearance of negative capacitance. In the presence of co-reactant by fitting a semi-circular arc to the high frequency charge transfer regime, as shown in Figure 5.15, solution resistance (R_{SOL}), charge transfer

resistance (R_{CT}) and maximum angular frequency (ω_{max}) were obtained. The double layer capacitance (C_{dl}), and τ (time constant for the Faradaic process) at different applied potentials can be obtained from Equations 1.30, 1.31 and 1.32 in Chapter 1. Equation 1.27, and 1.28, Chapter 1, were used to calculate the values of I_0 and k_s where the terms have their usual meaning.^{18,50,51} These parameters are summarised in Table 5.5.

$$I_0 = nFAk_s C_O \exp[-\alpha nF(E_{DC} - E^0)/RT] \quad 1.27$$

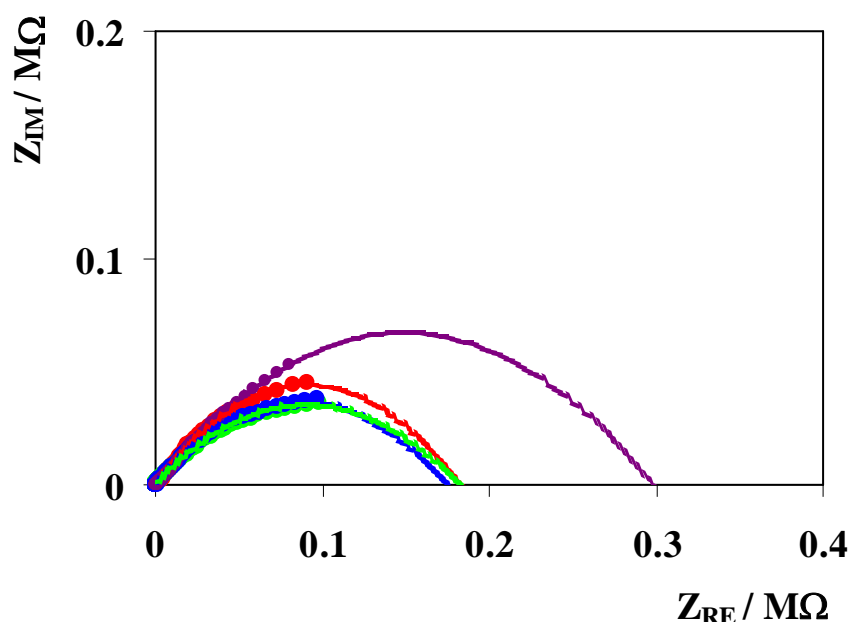


Figure 5.15: Semicircular arc fit for impedance plane plot for $[Ru(bpy)_2(PVP)_{10}]^{2+}$ film on GCE in the presence of 1 mM sodium oxalate co-reactant at 1.08 V (●), 1.15 V (●), 1.2 V (●) and 1.3 V (●) applied potentials. An AC sine modulation of 60 mV (peak amplitude), D.C. center potentials 1.0 V vs. Ag/AgCl, at frequency range of 1 mHz-100 KHz, in 0.1 M PBS buffer electrolyte (pH 7). The surface coverage of the $[Ru(bpy)_2(PVP)_{10}]^{2+}$ film is $(4.39 \pm 0.06) \times 10^{-8} \text{ mol cm}^{-2}$.

Table 5.5: Kinetic parameters evaluated for $\text{Ru}(\text{bpy})_2(\text{PVP})_{10}]^{2+}$ film on GCE in the presence of 1 mM sodium oxalate co-reactant at different potentials. The surface coverage of the $[\text{Ru}(\text{bpy})_2(\text{PVP})_{10}]^{2+}$ film is $(4.39 \pm 0.06) \times 10^{-8} \text{ mol cm}^{-2}$.

E / V	R_{CT} / MΩ	ω_{max} / Hz	C_{dl} / μF	τ / s	I₀ / A cm⁻² ×10⁻⁶	k_s / cm s⁻¹ ×10⁻⁸	D_{CT} / cm² s⁻¹ ×10⁻¹¹
1.00	1.3	0.09	8.92	11.24	0.3	0.036	4.7
1.08	0.3	0.61	5.44	1.63	1.2	0.67	12.0
1.15	0.18	0.51	10.8	1.96	2.0	4.28	16.2
1.2	0.18	0.6	8.99	1.63	2.03	11.3	7.5
1.3	0.17	1.6	3.59	0.62	2.15	82.0	10.2

When sodium oxalate (co-reactant) is present in the electrolyte solution there is diffusion of oxalate ions into the polymer matrix. This diffusion is taken into account by the introduction of the series Warburg element, Z_W , and the charge transfer resistance, R_{CT} , to the equivalent circuit shown in Figure 5.1.

In the absence of co-reactant the D_{CT} value obtained at 1.0 V is very close to the D_{CT} value obtained for $[\text{Ru}(\text{bpy})_2(\text{PVP})_{10}]^{2+}$ film from cyclic voltammetry ($4.7 \times 10^{-11} \text{ cm}^2 \text{ s}^{-1}$). This is quite expected, as the perturbation of 60 mV would bring the actual potential experienced by the film to values close to its formal potential. As this is a dynamic system, the absolute values of the D_{CT} do not give us much information. The change of D_{CT} with increasing potential enables us to predict that as the potential is increased the D_{CT} increases to some extent

and beyond a certain point it begins to drop. This is what would be expected from the kinetics of the system as beyond a certain potential, diffusion effects will be dominant and there will be a shift from charge transfer control regime to diffusion control regime. In the presence of co-reactant the values of D_{CT} observed are an order of magnitude higher than in the absence of co-reactant. The rate constant for cross-reaction however deviate by significant amounts and the values predicted by the model are too small. The expected value for the rate constant of cross reaction is $307 \text{ cm}^2 \text{ s}^{-1}$. This indicates that there may be still some circuit elements which are playing key role in the determination of the kinetics of the system which have not been considered in the above model. No change in the diffusion coefficient value is seen in the presence and absence of co-reactant. Hence, it is clear that the model has not considered oxalate co-reactant in solution and additional components need to be added to get a better fitting model. The experimental data points were fit to the modified Randle-Ershler circuit shown in Figure 5.1 using CH Instruments 760B simulation software. The values obtained are as shown in Table 5.6. Error is quoted for the fitting of the entire dataset to the electrical circuit.

Table 5.6: Kinetic parameters obtained from best fit curve using CH instruments simulation software for modified Randle-Ershler circuit for thin $[\text{Ru}(\text{bpy})_2(\text{PVP})_{10}]^{2+}$ film on GCE in the presence of 1 mM sodium oxalate co-reactant at different potentials. The surface coverage of the $[\text{Ru}(\text{bpy})_2(\text{PVP})_{10}]^{2+}$ film is $(4.39 \pm 0.06) \times 10^{-8} \text{ mol cm}^{-2}$.

E /V	R_{FILM} / Ω	R_{CT}/ MΩ	Z_w/ Ωs^{-0.5}	CPE/μ F	C_{FILM}/ F	D_{CT}/ cm²s⁻¹ ×10⁻¹¹	Error
1.08	253	0.9	0.9	12.5	0.42	2.0	0.13
1.15	229	0.7	0.9	12.2	7.1	0.13	0.25
1.2	277	0.24	2×10^{-5}	7.2	6.6	8.5	0.26

R_{sol} value was obtained to be $1 \times 10^{-20} \Omega$.

From simulations, it is observed that the modified Randle-Ershler model fits the data set. D_{CT} values lie in the predicted range but the charge transfer resistance values are somewhat lower.

5.5 CONCLUSIONS

From the equivalent circuit model the D_{ct} at 1.08 V is $2.0 \times 10^{-11} \text{ cm}^2 \text{ s}^{-1}$ and the average charge transfer diffusion coefficient from cyclic voltammetry was calculated to be $4.2 \times 10^{-11} \text{ cm}^2 \text{ s}^{-1}$. When the R_{FILM} and C_{FILM} values are compared, a very good correlation between the model and experimentally calculated values with an error of just ± 0.25 is obtained. Hence the modified Randles-Ershler circuit can sufficiently explain the $[\text{Ru}(\text{bpy})_2(\text{PVP})_{10}]^{2+}$ ECL system considered here. However, it is incapable of predicting the rate of cross reaction between the co-reactant and the Ru^{3+} . Further additions to the electrical circuit are necessary.

Therefore, in conclusion, the modulated potential technique, not only allows to detect micro molar concentrations of oxalate in the system but also gives greater sensitivity. The phase locked method allows ECL detection to be performed outside the 'black box' conditions and thus this technique has great potential in the development of flow through and non-flow through ECL sensors. A modified Randle-Ershler circuit has been successfully developed which can sufficiently explain the $[\text{Ru}(\text{bpy})_2(\text{PVP})_{10}]^{2+}/\text{Oxalate}$ ECL system.

5.6 REFERENCES

- (1) Venkatanarayanan, A.; Spehar-Deleze, A.; Dennany, L.; Pellegrin, Y.; Keyes, T. E.; Forster, R. J. *Langmuir* **2008**, *24*, 11233-11238.
- (2) Hogan, C. F.; Forster, R. J. *Anal. Chim. Acta* **1999**, *396*, 13-21.
- (3) Spehar-Deleze, A.; Pellegrin, Y.; Keyes, T. E.; Forster, R. J. *Electrochem. Commun.* **2008**, *10*, 984-986.
- (4) Larsson, H.; Sharp, M. *J Electroanal Chem* **1995**, *381*, 133-142.
- (5) Doherty, A. P.; Forster, R. J.; Smyth, M. R.; Vos, J. G. *Anal. Chim. Acta* **1991**, *255*, 45-52.
- (6) Forster, R. J.; Kelly, A. J.; Vos, J. G.; Lyons, M. E. G. *J Electroanal Chem* **1989**, *270*, 365-379.
- (7) Zhang, T.; Fang, Q.; Wang, S.; Qin, L.; Wang, P.; Wu, Z.; Fang, Z. *Talanta* **2005**, *68*, 19-24.
- (8) Carlsson, K. *Micron* **1995**, *26*, 317-322.
- (9) Feng, Z. Q.; Sagara, T.; Niki, K. *Anal. Chem.* **1995**, *67*, 3564-3570.
- (10) Pyati, R.; Mark, R. M. *Annu. Rep. Prog. Chem. , Sect C* **2007**, *103*, 12-78.
- (11) Debad, J. D.; Glezer, E. N.; Wohlstadter, J.; Sigal, G. B. In *Clinical and biological applications of ECL; Electrogenerated Chemiluminescence*; Marcel Dekker, Inc, Maryland, U.S.A, 2004; pp 19.
- (12) Andrew, W. K.; Gillian, M. G. *Analyst* **1994**, *119*, 879-890.
- (13) Bezman, R.; Faulkner, L. R. *J. Am. Chem. Soc.* **1972**, *94*, 6324-6330.
- (14) Fähnrich, K. A.; Pravda, M.; Guibault, G. G. *Talanta* **2001**, *54*, 531-559.
- (15) Wightman, R. M.; Forry, S. P.; Maus, R.; Badocco, D.; Pastore, P. J. *Phys. Chem. B* **2004**, *108*, 19119-19125.
- (16) Miao, W.; Choi, J. P.; Bard, A. J. *J. Am. Chem. Soc.* **2002**, *124*, 14478-14485.
- (17) Bard, A. J., Ed.; In *Electrogenerated Chemiluminescence*; Marcel Dekker, Inc: United states of america, 2004; , pp 540.
- (18) Bard, A. J.; Faulkner, L. R., In *Electrochemical methods: Fundamentals and applications*; John Wiley & Sons Inc: New York, 1980; , pp 718.
- (19) Rubinstein, I.; Martin, C. R.; Bard, A. J. *Anal. Chem.* **1983**, *55*, 1580-1582.
- (20) Kanoufi, F.; Bard, A. J. *J. Phys. Chem. B* **1999**, *103*, 10469-10480.
- (21) Jirka, G. P.; Nieman, T. A. *Microchim. Acta.* **1994**, *113*, 339-347.
- (22) Forster, R. J.; Hogan, C. F. *Anal. Chem.* **2000**, *72*, 5576-5582.
- (23) Hogan, C. F.; Forster, R. J. *Anal. Chim. Acta* **1999**, *396*, 13-21.
- (24) Nagatani, H.; Sagara, T. *Anal. Sci.* **2007**, *23*, 1041-1048.
- (25) Sagara, T.; Kubo, Y.; Hiraishi, K. *J. Phys. Chem. B* **2006**, *110*, 16550-16558.
- (26) Sagara, T.; Kato, N.; Toyota, A.; Nakashima, N. *Langmuir* **2002**, *18*, 6995-7001.
- (27) Ametek signal recovery Low level optical detection using lock-in amplifier techniques. www.signalrecovery.com (accessed Oct, 2009).
- (28) Knight, A. W. *Tr. Anal. Chem* **1999**, *18*, 47-62.

- (29) Miao, W. *Chem. Rev.* **2008**, *108*, 2506-2553.
- (30) Kharitonov, A. B.; Alfonta, L.; Katz, E.; Willner, I. *J Electroanal Chem* **2000**, *487*, 133-141.
- (31) Katz, E.; Willner, I. *Electroanalysis* **2003**, *15*, 913-947.
- (32) Yu-Qing, M. a.; Jian-Guo, G. a. *Anal. Lett.* **2004**, *37*, 1053-1062.
- (33) Kohma, T.; Hasegawa, H.; Oyamatsu, D.; Kuwabata, S. *Bull. Chem. Soc. Jpn.* **2007**, *80*, 158-165.
- (34) Aoki, A.; Miyashita, T. *Colloids. Surf. A: Physicochem. Eng. Aspects* **2002**, *198-200*, 671-676.
- (35) Brazill, S. A.; Singhal, P.; Kuhr, W. G. *Anal. Chem.* **2000**, *72*, 5542-5548.
- (36) Engblom, S. O.; Myland, J. C.; Oldham, K. B. *J Electroanal Chem* **2000**, *480*, 120-132.
- (37) Singhal, P.; Kuhr, W. G. *Anal. Chem.* **1997**, *69*, 3552-3557.
- (38) Singhal, P.; Kawagoe, K. T.; Christian, C. N.; Kuhr, W. G. *Anal. Chem.* **1997**, *69*, 1662-1668.
- (39) Singhal, P.; Kuhr, W. G. *Anal. Chem.* **1997**, *69*, 4828-4832.
- (40) Huang, Q.; Hui, R.; Wang, B.; Zhang, J. *Electrochim. Acta* **2007**, *52*, 8144-8164.
- (41) Lambers, J. V., *ETNA*, **2008**, *31*, 86-109.
- (42) Bosch, R. W.; Bogaerts, W. F. *Corros. Sci* **1996**, *52*, 204.
- (43) Medina, J. A.; Schwartz, D. T. *J. Electrochem. Soc.* **1997**, *144*, 155-164.
- (44) Zhu, H.; Robert, K. J. *J. Electrochem. Soc.* **2006**, *153*, 9, 1765-1772.
- (45) Forster, R. J.; Keyes, T. E.; Vos, J. G. In *Interfacial Supramolecular Assemblies*; John Wiley & Sons, Ltd: 2003; .
- (46) Randles, J. E. B. *Discuss. Faraday Soc.* **1947**, *1*, 11.
- (47) Barsoukov, E.; Macdonald, J. R.; In *Impedance spectroscopy: Theory, experiment and applications*; Macdonald, J. R., Johnson, W. B.; Fundamentals of impedance spectroscopy; John Wiley & Sons, Inc.: New Jersey, 2005.
- (48) Dennany, L.; Hogan, C. F.; Keyes, T. E.; Forster, R. J. *Anal. Chem.* **2006**, *78*, 1412-1417.
- (49) Van Munster, E. B.; Gadella, T. W. J. In *Fluorescence Lifetime Imaging Microscopy (FLIM)*; Advances in Biochemical Engineering / Biotechnology; 2005; Vol. 95, pp 143-175.
- (50) Holze, R. In *Encyclopedia of electrochemistry* (A.J. Bard and M. Stratmann eds), vol 3: instrumentation and electroanalytical chemistry (P.R. Unwin ed); 2007; Vol. 11, pp 134-135.
- (51) Brett, C. M. A.; Brett, A. M. O., In *Electrochemistry: Principles, methods and applications*; Oxford University Press Inc: NewYork, 1993; pp 427.
- (52) Fernández-Sánchez, C.; McNeil, C. J.; Rawson, K. *Tr. Anal. Chem* **2005**, *24*, 37-48.
- (53) Bott, W. A. *Curr. Separations* **2001**, *19-3*, 71-75.
- (54) Wang, X.; Hsing, I.; Leng, Y.; Yue, P. *Electrochim. Acta* **2001**, *46*, 4397-4405.

CHAPTER VI

SINGLE WALLED CARBON NANOTUBE FOREST PLATFORMS FOR IMMUNOSENSOR

6.1 INTRODUCTION

Micro arrays of biomolecules are emerging as powerful diagnostic tools for genomics and proteonomics as they allow screening of biologically important binding events in a parallel and high throughput fashion.¹ As the microarrays are fabricated on solid support, the nature of the support, coating on its surface and immobilization strategies, all play pivotal role in its success. Indium tin oxide films have been used widely due to their conductive and optically transparent characteristics.² Previous research with single walled carbon nanotube (SWCNT) forests^{3,4} showed that efficient, direct electronic communication was achieved between highly conductive nanotubes and the peroxidase enzymes conjugated at their ends. CNTs have attracted the researchers as nano scale building blocks for diagnostic devices as they possess a unique combination of excellent mechanical, electrical and electrochemical properties.^{5,6} Significantly vertically aligned carbon nanotubes are more advantageous for sensor application than non-aligned ones, since the edges of the nanotubes are exposed. This orientation of the nanotube has been shown to exhibit the highest electro catalytic activity coupled with fast electron transfer.⁶ The self assembly of single walled carbon nanotube into vertical forest like structures through coordination of the carboxylic acid groups of acid oxidized SWCNT to Fe^{3+} adsorbed on a nafion-coated pyrolytic graphite electrode, has already been reported.^{4,7,8} This fabrication technique is simple compared to other techniques like electron beam lithography⁹ or chemical vapour deposition¹⁰ which lead to the formation of vertically aligned nanotubes. These platforms have enabled researchers to achieve high sensitive detection of cancer biomarkers with a detection limit of 4 nM for prostate specific antigen.³ Also the forests are carboxyl terminated which makes them attractive for functionalization of biomolecules. In all the previous reports the SWCNT forests have been assembled on non transparent pyrolytic graphite substrates. In this chapter the patterned assembly of nanotube forests on transparent ITO substrates has been reported. Also two different methodology, drop coating and inkjet printing has been attempted along with ultrasensitive detection of proteins by a novel approach using G1.5 acid terminated PAMAM dendrimers as size selective protein linkers. Particle based assays have gained great importance as

electrochemical¹¹ and luminescence¹² signal enhancers. Particles can be easily used for multiplexing and offer a large surface area for the attachment of biomolecules or luminophores.¹³ Metal¹⁴ and silica nanoparticles¹⁵ have been extensively used for signal enhancement and detection limits of 0.5 nM for prostate specific antigen and 2.98 nM for TPA respectively, have been achieved. As ECL signal from a single ruthenium molecule will be miniscule compared to the signal from a million molecules, amine functionalized silica nanospheres have been used for signal enhancement. In order to coat the silica nanospheres, high brightness luminescent $[\text{Ru}(\text{bpy})_2\text{PICH}_2]^{2+}$ complex with a quantum yield $\phi=0.067$ *i.e.*, 30% higher than the quantum yield of $[\text{Ru}(\text{bpy})_3]^{2+}$ was used.¹⁶ Thus this chapter gives an overview of the SWCNT-ITO immunosensor's analytical performance.

6.2 EXPERIMENTAL

6.2.1 Apparatus

Electrochemical measurements were carried out with CH instruments, model 760b potentiostat. Cyclic voltammetric measurements were conducted using a typical three-electrode cell configuration. An aqueous Ag/AgCl/saturated KCl (3M) electrode was used as reference for electrochemical measurements with a platinum mesh counter electrode. All potentials are quoted *vs.* an Ag/AgCl reference electrode and all measurements were made at room temperature.

Electrochemiluminescence measurements were performed with Gene Gnome HR gel documentation system equipped with 16 bit CCD camera with a dynamic range of 4.8. Image analysis was done using Genesnap software, high sensitivity acquisition setting and 40 s acquisition time. A schematic of the ECL setup is as shown in Figure 6.1.

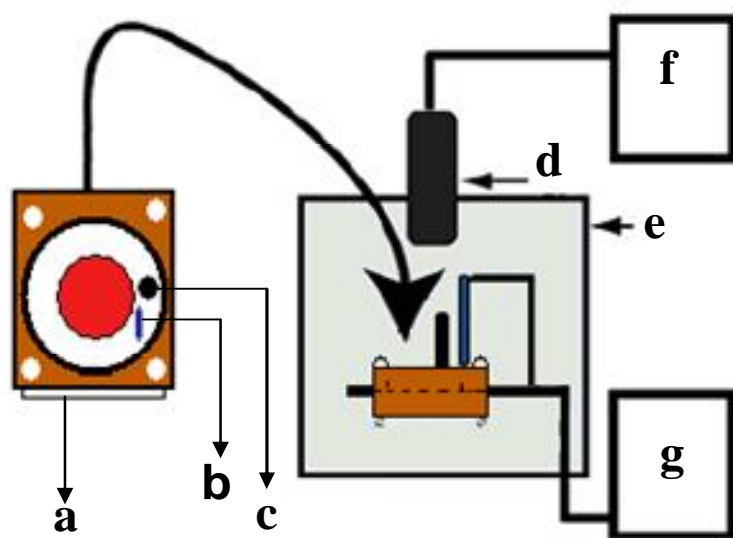


Figure 6.1: Schematic diagram of the ECL immunoassay instrumentation (a) SWCNT-ITO electrode, (b) platinum wire mesh counter, (c) Ag/AgCl/KCl (3M) reference electrode, (d) CCD camera, (e) gel-doc dark room, (f) computer and (g) potentiostat.

6.2.2 Immunoassay procedure

The immunoassay was performed using previously^{3,7,8} reported procedures on anti-IgG coated ITO electrodes. The various steps followed are as follows:

1. The anti-IgG SWCNT ITO sensors constructed as described in Chapter 3, Section 3.3.4 was slowly agitated with 2 mL of 2% casein + 0.05% Tween-20, for 20 minutes followed by washing with 0.05% Tween-20 and 0.01 M PBS buffer. This was done to block the surface and minimize nonspecific adsorption of proteins onto the SWCNT-ITO sensor surface.
2. Different concentrations of IgG-G1.5-[Ru(bpy)₂PICH₂] bio-conjugate were added to the immunosensor and the sensors were incubated for an hour at room temperature.

3. The incubation was followed by washing with 0.05% tween-20 and 0.01 M PBS buffer.
4. The immunosensor was then placed in an electrochemical cell containing 3 mL of 50 mM sodium oxalate in 0.01 M PBS buffer (pH 7). ECL was detected using the CCD of the GeneGnome gel documentation system, as shown in Figure 6.1, by applying a constant voltage of 1.6 V *vs.* Ag/AgCl reference, with a platinum mesh wire as counter electrode. Two signals were measured for each electrode; one at time = 0 s and one (after integration of collected light) at time = 40 s.

A schematic of the procedure is shown in Figure 6.2. The constant potential was applied over the entire 40 s accumulation time and the ECL was recorded using the high sensitivity setting. Control experiments using SWCNT forests sensor without anti-IgG (Ab_1) coating and ruthenium coated spheres without secondary antibody- IgG (Ab_2), were also performed and the results are reported below.

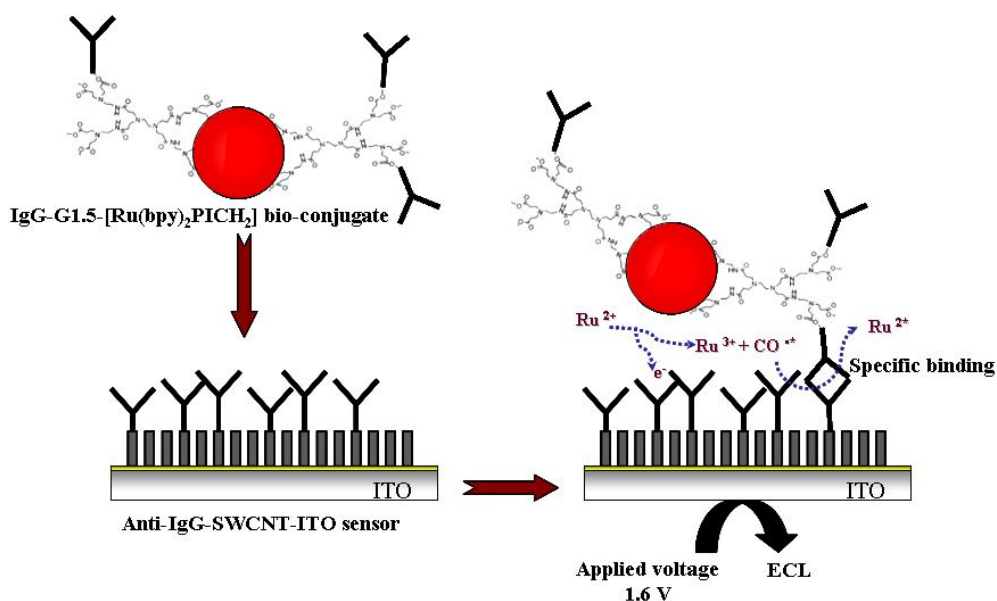


Figure 6.2: Schematic diagram of the anti-IgG-IgG immuno assay procedure.

6.3 RESULTS AND DISCUSSIONS

6.3.1 Analytical performance

Figure 6.3 shows the CCD response obtained from the Gel documentation system when the SWCNT-ITO sensor was incubated with different concentrations of IgG coated ruthenium functionalised spheres. The ECL intensity due to a particular concentration has been average over 2 trials ($n = 2$). The sensor was thoroughly washed after incubation to remove unbound spheres. Table 6.1 gives the respective number of IgG-spheres and ECL intensity corresponding to Figure 6.3. ECL is generated upon application of 1.6 V *vs.* Ag/AgCl reference electrode, which oxidizes the Ru^{2+} centers present on the silica spheres to Ru^{3+} centers. The oxidized Ru^{3+} centers interact with the 50 mM sodium oxalate (co-reactant) in electrolyte solution to produce the excited Ru^{2*} state that emits ECL upon relaxation to the original Ru^{2+} form. The ECL emission route is thought to be similar to the one suggested by Miao and co-workers for $[\text{Ru}(\text{bpy})_2[\text{bpy}(\text{COOH})_2]]^{2+}$ immobilized on ITO where they suggest an alternate route in which TPA radicals diffuse and react with the immobilized

luminophore.¹⁷ The authors show, through SECM measurements, that the long lifetime of the TPA radical (*i.e.*, 0.2 ms) and its typical diffusion coefficient of $5 \times 10^{-6} \text{ cm}^2 \text{ s}^{-1}$ are responsible for TPA intermediates formed at the surface of the electrode to quickly diffuse before deprotonation and cause excitation of the immobilized $[\text{Ru}(\text{bpy})_3]^{2+}$. Their experiments confirm the ability of form excited states at all positions of a $2.8 \text{ }\mu\text{m}$ bead on an electrode surface. Emission by catalytic route may also occur at the ruthenium coated silica bead | CNT interface.^{17,18}

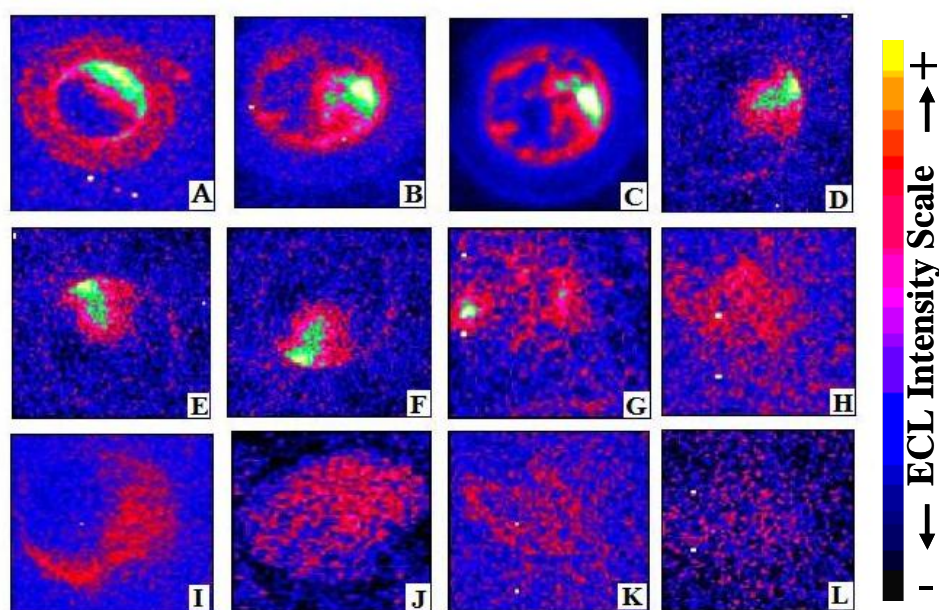


Figure 6.3: False colour CCD ECL response of 12 printed SWCNT /anti-IgG spots after incubation with different concentrations of IgG coated ruthenium spheres. The image was collected after 40 s accumulation time at constant voltage of 1.6 V in 0.01 M PBS buffer (pH 7) in the presence of 50 mM sodium oxalate co-reactant.

Table 6.1: Calibration data values showing the dependence of ECL intensity on IgG coated ruthenium sphere concentration obtained under constant potential of 1.6 V, in 0.01 M PBS (pH 7) buffer electrolyte in the presence of 50 mM Na₂C₂O₄, 40 s accumulation time.

Sample	Total no of IgG-spheres added	ECL (ECL _{t=40} - ECL _{t=0})
A	1.06x10 ¹²	45.7±10.2
B	1.1.1.1.17 5.3	26.4±7.4
C	1.1.1.1.18 2.6	12.8±4.1
D	3.64x10 ¹⁰	7.0±3.2
E	1.1.1.1.19 2.1	6.3±2.5
F	1.1.1.1.20 1.0	4.3±1.1
G	1.1.1.1.21 5.3	4.0±1.3
H	1.1.1.1.22 2.6	3.7±1
I	1.1.1.1.23 1.0	3.3±1.1
J	1.1.1.1.24 3.6	3.1±1.1
K	1.1.1.1.25 5.0	3.0±1.0
L	1.1.1.1.26 3.6	2.84±1.0

It can be seen from Figure 6.3 that the ECL signal intensity increases with the increase in the total number of IgG-spheres. Spots of intense ECL are formed up to 5.3x10⁹ spheres but as the number of IgG-spheres is gradually decreased, a more distributed luminescence is observed. The signal homogeneity is not as good as that seen for commercially available fluorescent antibody arrays.^{19,20} It is important to note that unlike the ECL array reported here, those arrays are printed onto nonconductive substrates and there is significant amount of light scattering, auto-fluorescence and interference due to luminescent impurities in

fluorescence assays.²¹ In contrast, ECL assays are more selective and the electrode potential precisely controls the generation of excited states, in this case the ruthenium coupled to the secondary antibody and oxalate in solution. With the gradual decrease in the number of added spheres, fewer IgG-anti-IgG couplings are expected to take place. Hence, not all the capture antibodies are used up. Indeed after measuring the ECL intensity from Sample H, as shown in Figure 6.4, when more nanospheres are titrated in, an increase in the signal intensity is observed. This increase in signal indicates the presence of free capture antibodies on the sensor surface. Table 6.2 gives the respective IgG-spheres numbers and ECL ratio corresponding to Figure 6.4.

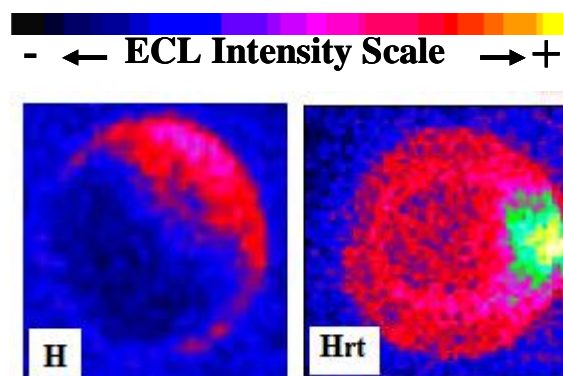


Figure 6.4: ECL response of SWCNT /anti-IgG spot after incubation with 2.65×10^8 IgG coated ruthenium spheres (H) and the same sensor after reactivation and addition of another 2.65×10^8 IgG coated ruthenium spheres (Hrt). The image was collected after 40 s accumulation time at constant voltage of 1.6 V in 0.01 M PBS buffer (pH 7) in the presence of 50 mM sodium oxalate co-reactant.

Table 6.2: Calibration data for SWCNT /anti-IgG spots after incubation with 2.65×10^8 IgG coated ruthenium spheres (H) and the same sensor after addition of another 2.65×10^8 IgG coated ruthenium spheres (Hrt). The image was collected after 40 s accumulation time at constant voltage of 1.6 V in 0.01 M PBS buffer (pH 7) in the presence of 50 mM sodium oxalate co-reactant.

Sample	Total no of spheres	ECL ($ECL_{t=40} - ECL_{t=0}$)
H	1.1.1.1.27	3.74 ± 1
Hrt	1.1.1.1.28	38.3 ± 7

The nonspecific adsorption of ruthenium coated spheres on anti-IgG surface was determined. This was done by first coupling the anti-IgG to the surface of two SWCNT-ITO sensors, blocking the surfaces with 2 mL of 2% casein + 0.05% Tween-20 and measuring the ECL after incubation with 5.30×10^9 (G1) and 1.00×10^8 (I1) ruthenium coated spheres respectively. As the ruthenium coated spheres did not contain any IgG coupled to them, the ECL signal produced, as seen in Figure 6.5, is indicative of nonspecific binding of the spheres to the surface of SWCNT-ITO sensor. Significantly, a very low average ECL intensity of 1.3 ± 0.3 was observed. The ECL intensity observed for the two different concentrations of uncoupled ruthenium spheres are given in Table 6.3.

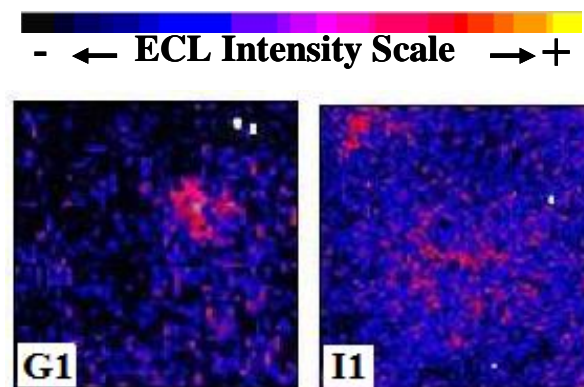


Figure 6.5: ECL response for non specific binding of anti-IgG on sensor surface and ruthenium spheres without IgG. G1 and I1 represent SWCNT spots with anti-IgG after incubation with 5.30×10^9 and 1.00×10^8 ruthenium coated spheres respectively. The nanospheres do not contain secondary antibodies (IgG) coupled to them. The image was collected after 40 s accumulation time at constant voltage of 1.6 V in 0.01 M PBS buffer (pH 7) in the presence of 50 mM sodium oxalate co-reactant.

Table 6.3: Calibration data obtained for non specific binding of anti-IgG and ruthenium spheres without IgG. G1 and I1 represent SWCNT spots with anti-IgG after incubation with 5.30×10^9 and 1.00×10^8 ruthenium coated spheres respectively. The nanospheres do not contain secondary antibodies (IgG) coupled to them. The image was collected after 40 s accumulation time at constant voltage of 1.6 V in 0.01 M PBS buffer (pH 7) in the presence of 50 mM sodium oxalate co-reactant.

Sample	Total no of spheres	ECL ($ECL_{t=40} - ECL_{t=0}$)
G1	1.1.1.1.29	1.6 ± 0.4
I1	1.1.1.1.30	0.9 ± 0.2

Also, another case of non-specific binding *i.e.*, between IgG coupled ruthenium spheres and SWCNT-ITO surface was assessed. In this case the SWCNT-ITO sensor surface was left unmodified and blocked with 2 mL of 2% casein + 0.05% Tween-20. This was followed by incubation with 5.30×10^9 (G2) and 1.00×10^8 (I2) IgG coupled ruthenium-coated spheres respectively, for an hour at room temperature. The sensor surface was washed thoroughly after incubation and the ECL signal was collected and is as shown in Figure 6.6. This signal represents nonspecific adsorption of the IgG coupled spheres to the surface of SWCNT-ITO in the absence of capture antibody (anti-IgG). Even in this case a very low average ECL intensity of 0.5 ± 0.3 was observed. The values obtained for G2 and I2 are given in Table 6.4.

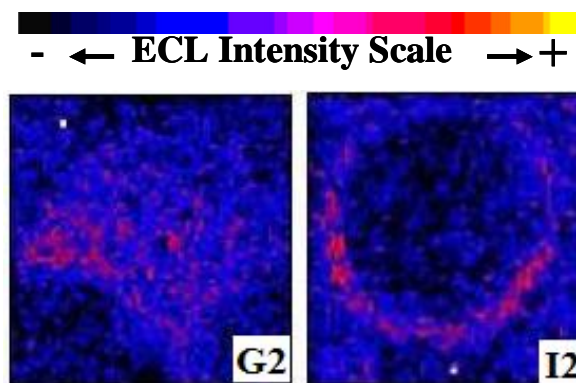


Figure 6.6: ECL response for non specific binding of IgG on spheres to printed SWCNT surface (without anti-IgG). G2 and I2 represent SWCNT spots without anti-IgG after incubation with 5.30×10^9 and 1.00×10^8 ruthenium-IgG spheres respectively. The image was collected after 40 s accumulation time at constant voltage of 1.6 V in 0.01 M PBS buffer (pH 7) in the presence of 50 mM sodium oxalate co-reactant.

Table 6.4: Calibration data obtained for NSB of IgG on printed SWCNT without anti-IgG. G2 and I2 represent SWCNT spots without anti-IgG after incubation with 5.30×10^9 and 1.00×10^8 ruthenium-IgG spheres respectively. The image was collected after 40 s accumulation time at constant voltage of 1.6 V in 0.01 M PBS buffer (pH 7) in the presence of 50 mM sodium oxalate co-reactant.

Sample	Total no of IgG-spheres	ECL ($ECL_{t=40} - ECL_{t=0}$)
G2	1.1.1.1.31	0.92 ± 0.1
I2	1.1.1.1.32	0.17 ± 0.1

The SWCNT-ITO sensor shows wide dynamic range and is able to detect 10^{12} to 10^6 IgG-spheres. However, a high array to array variability was seen, evidenced by the high error values shown in Table 6.1. This could be due to instability of the self assembled single walled nanotubes. The smooth surface of ITO results in poor stability of the self assembled films which tend to get washed away from the surface of the electrode. This problem could be overcome by use of rough electrodes like pyrolytic graphite. Also, it is observed that the NSB of the silica spheres coated with IgG to the carbon nanotube surface is high with the signal intensity being almost half of that obtained due to specific coupling (G1 and G). However, it is seen that in the absence of capture antibodies, lesser number of spheres tend to bind (non-specifically) to the surface of the sensor. Protein – protein interaction may be the cause for such behaviour.¹ Antibodies are known to strongly bind to the sensor surface by electrostatic interaction and display high cross-reactivity to proteins with and without sequence homology.²¹ Due to this the dendrimer coated ruthenium spheres tend to bind more to the surface containing capture antibodies when compared to a surface without capture antibodies. Figure 6.7 shows an ECL intensity plot generated from the above experiment where the ECL intensity is given by the difference between the ECL

intensity at $t = 40$ s and ECL intensity at $t = 0$ s. ECL intensity decreases linearly with the decrease in IgG-sphere concentration up to 1×10^8 spheres with the lowest detection limit being 3.64×10^6 spheres. Thomas *et.al.*,²² have used interdigitated array electrodes (IDA) to electrochemically detect 1000, 2.8 μm dia spheres corresponding to 177 pM mouse IgG. The SWCNT-ITO arrays reported here allows much smaller beads to be detected with increased sensitivity and decreased detection limits.

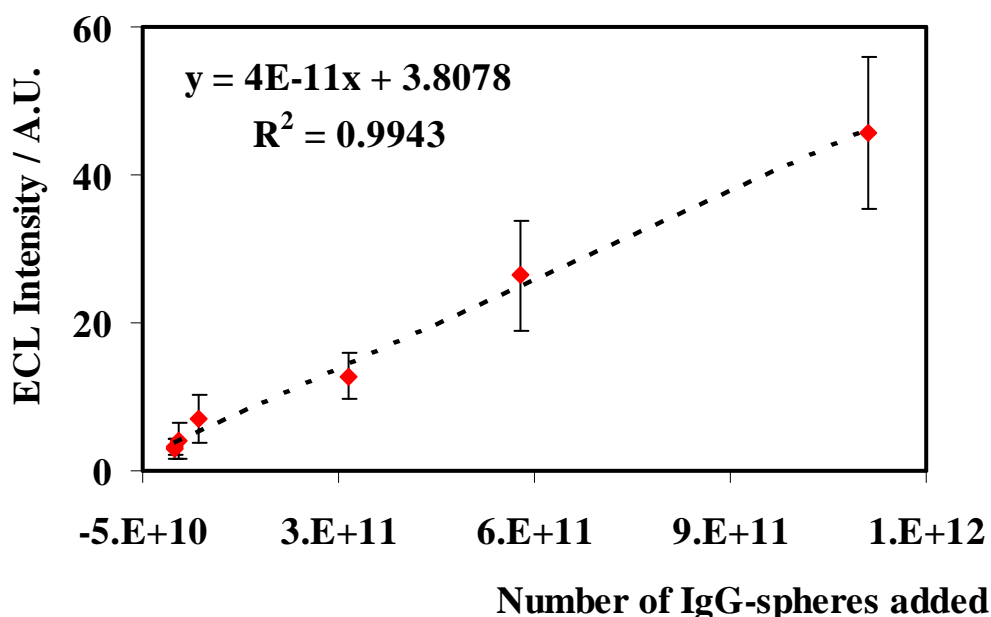


Figure 6.7: Calibration plot obtained for IgG-G1.5- $[\text{Ru}(\text{bpy})_2\text{PICH}_2]^{2+}$ bio conjugate under constant voltage of 1.6 V, 40 s accumulation time in 0.01 M PBS buffer (pH 7) in the presence of 50 mM sodium oxalate co-reactant.

The majority of the antibody arrays that have been reported are based on ELISA^{1,21,23} (enzyme linked immuno sorbent assay) format in micro titre plates or fluorescence format in the form of printed proteins or DNA spots on glass slides.^{11,24,25} An alternative format to microarrays is the xMAP technology of Luminex Corporation^{26,27} which does not rely on the spatial separation of capture molecules on glass slides (protein arrays), but instead uses beads for immobilization that are colour-coded by different ratios of two fluorescent dyes. This allows multiplex analysis of up to 100 different species in a liquid environment without any washing steps. But these assays mainly use indirect

labelling protocols²¹ which normally involves generic binders, such as species-specific labelled secondary antibodies for the detection of primary antibodies or labelled protein for the detection of recombinant antibody. However, due to high non specific binding seen in this format, sandwich assays using indirect labelling are becoming more and more popular.²⁸ Cross reactivity is a huge issue with sandwich assays. Deiss and co-workers¹⁸ have tried to combat this issue using an electrochemiluminescence pathway. A multiplex assay using large polystyrene particles (3 μm) loaded into wells of an electrode prepared from etched fiber optic bundles coated with gold was conducted. They used biotinylated detection antibody which binds to the streptavidin modified $[\text{Ru}(\text{bpy})_3]^{2+}$ complex to generate ECL with TPA co-reactant. Though they report negligible cross reactivity, very high levels of antigen (1 mM of VEGF antigen) concentrations were used to show proof of principle. Commercial ECL sandwich assays are available from Meso scale diagnostics (MSD),²⁹ where they make use of specially made microtiter plates containing carbon electrodes in each well. Each electrode is coated with capture molecules to immobilize different analytes in the sample. Following attachment of a $[\text{Ru}(\text{bpy})_3]^{2+}$ labelled bead,³⁰ ECL intensity is measured from each well. Magnetic bead based assays are also commercially available from BioVeris³⁰ whose working principle is as shown in Figure 1.11, Chapter 1. The MSD assays report a linear dynamic range of 3-4 logs for IgG-anti-IgG coupling with 0.5-5 nM limits of detection.²⁹ The sensitivity of the MSD has been found to be 100 fold better than the ELISA and 10 fold better than BioVeris assays. However the ECL signal still originates from a macroscopic surface.¹⁸

Significantly, the above SWCNT-ITO sensor has very little signal due to nonspecific binding and can easily detect a few million nanoparticles (3.6×10^6 IgG-coupled ruthenium spheres).

Using the concentration of IgG on 3.64×10^{12} spheres (Section 3.3.5, Chapter 3), the concentration of IgG at various sphere concentrations (Table 6.1) can be calculated. Figure 6.8 shows a plot of IgG concentration vs. ECL ratio and Table 6.5 gives the respective values.

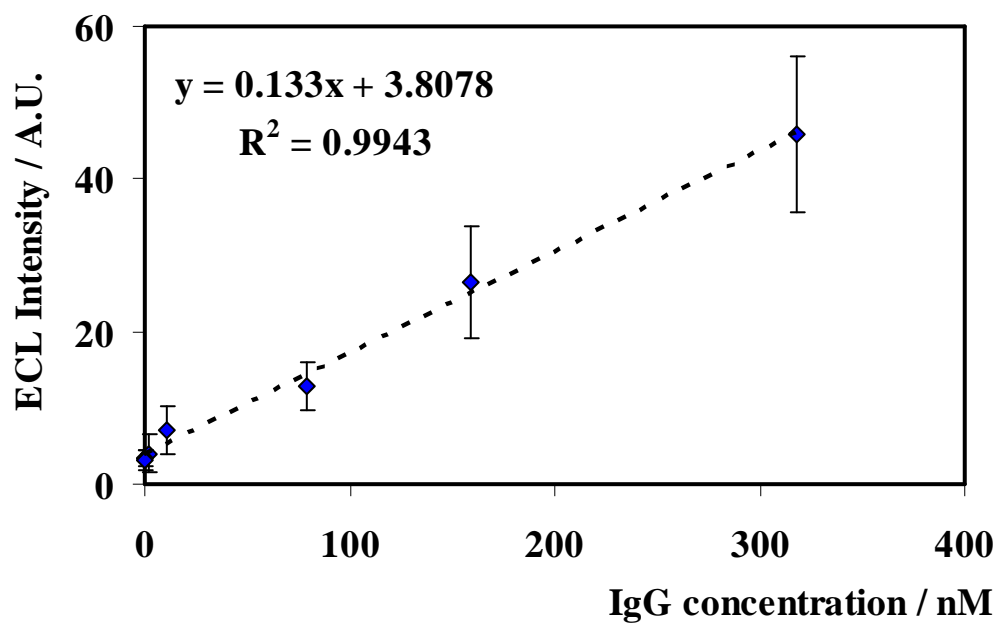


Figure 6.8: Dependence of ECL ratio on IgG concentration of IgG-G1.5- $[\text{Ru}(\text{bpy})_2\text{PICH}_2]^{2+}$ bio conjugate under constant voltage of 1.6 V, 40 s accumulation time in 0.01 M PBS buffer (pH 7) in the presence of 50 mM sodium oxalate co-reactant.

Table 6.5: Calibration data values showing the dependence of ECL ratio on calculated IgG concentration obtained under constant potential of 1.6 V, in 0.01 M PBS (pH 7) buffer electrolyte in the presence of 50 mM Na₂C₂O₄, 40 s accumulation time.

Sample	IgG Conc. / nM	ECL (ECL _{t=40} - ECL _{t=0})
A	318	45.7±10.2
B	1.1.1.1.33 159	26.4±7.4
C	1.1.1.1.34 79.	12.8±4.1
D	10.9	7.0±3.2
E	1.1.1.1.35 6.3	6.3±2.5
F	1.1.1.1.36 3.2	4.3±1.1
G	1.1.1.1.37 1.5	4.0±1.3
H	1.1.1.1.38 0.0	3.7±1
I	1.1.1.1.39 0.0	3.3±1.1
J	1.1.1.1.40 0.0	3.1±1.1
K	1.1.1.1.41 0.0	3.0±1.0
L	1.1.1.1.42 0.0	2.84±1.0

Thus, a linear plot of IgG concentration vs. ECL intensity is obtained with a dynamic range 318 nM-0.019 nM with a lowest detection at 1.1 picoM. This is slightly lower than the value reported by Sanchez and co workers³¹ who detected 2.3 picoM IgG on carbon paste electrode by enzyme amplification strategy.

6.4 CONCLUSIONS

In conclusion, a rapid, sensitive vertically aligned SWCNT-ITO ECL sensor has been successfully developed. This chapter describes a new approach to antibody arrays using bead based electrochemiluminescence detection. The array emits ECL upon application of suitable positive voltage and the CCD placed above the arrays captures the emitted light from all the spots simultaneously. The SWCNT surface allows easy attachment of primary antibodies and increases the sensitivity of the sensor as a whole. The surfaces of the nanotubes were effectively blocked with 2 % casein to result in very low nonspecific binding of IgG-ruthenium spheres. Precise control over the pattern of SWCNT forest was achieved by inkjet printing. G1.5 acid terminated PAMAM dendrimers were used which acted as size selective protein linkers and $[\text{Ru}(\text{bpy})_2\text{PICH}_2]^{2+}$ coated silica nanospheres, signal enhancement was achieved. However, a high array to array variability is seen evidenced by the high error values. The stability of the self assembled single walled nanotubes on the smooth ITO surface could be the reason for this high variability. However, this issue can be overcome by use of rough electrodes like pyrolytic graphite. Significantly, when compared to a similar technology reported in literature by Sanchez and co workers³¹ who detected 2.3 pM IgG on carbon paste electrodes, this transparent ITO sensor shows a wide linear dynamic range and a remarkably low detection limit of 1.1 pM for IgG.

6.5 REFERENCES

- (1) Schena, M.; Heller, R. A.; Theriault, T. P.; Konrad, K.; Lachenmeier, E.; Davis, R. W. *Tr. Biotechnol.* **1998**, *16*, 301-306.
- (2) Penza, M.; Cozzi, S.; Tagliente, M. A.; Mirengi, L.; Martucci, C.; Quirini, A. *Thin Solid Films* **1999**, *349*, 71-77.
- (3) Yu, X.; Munge, B.; Patel, V.; Jensen, G.; Bhirde, A.; Gong, J. D.; Kim, S. N.; Gillespie, J.; Gutkind, J. S.; Papadimitrakopoulos, F.; Rusling, J. F. *J. Am. Chem. Soc.* **2006**, *128*, 11199-11205.
- (4) O'Connor, M.; Kim, S. N.; Killard, A. J.; Forster, R. J.; Smyth, M. R.; Papadimitrakopoulos, F.; Rusling, J. F. *Analyst* **2004**, *129*, 1176-1180.
- (5) Wang, J. *Electroanalysis* **2005**, *17*, 7-14.
- (6) Balasubramanian, K.; Burghard, M. *Anal Bioanal Chem* **2006**, *385*, 452-468.
- (7) Yu, X.; Kim, S. N.; Papadimitrakopoulos, F.; Rusling, J. F. *Mol. Biosyst.* **2005**, *1*, 70-78.
- (8) Yu, X.; Chattopadhyay, D.; Galeska, I.; Papadimitrakopoulos, F.; Rusling, J. F. *Electrochem. Commun.* **2003**, *5*, 408-411.
- (9) Yu, Z.; McKnight, T. E.; Ericson, M. N.; Melechko, A. V.; Simpson, M. L.; Morrison, B. *Nano. Lett.* **2007**, *7*, 2188-2195.
- (10) Ghavanini, F. A.; Le Poche, H.; Berg, J.; Saleem, A. M.; Kabir, M. S.; Lundgren, P.; Enoksson, P. *Nano Letters* **2008**, *8*, 2437-2441.
- (11) Wang, J. *Electroanalysis* **2007**, *19*, 769-776.
- (12) Massay, R. J.; Blackburn, G. F.; Wilkins, E. W.; Leland, J. K. U.S. Patent 5,746,974, 1995.
- (13) Forster, R. J.; Bertonecello, P.; Keyes, T. E. *Annu. Rev. Anal. Chem* **2009**, *2*, 359-385.
- (14) Mani, V.; Chikkaveeraiah, B. V.; Patel, V.; Gutkind, J. S.; Rusling, J. F. *ACS Nano* **2009**, *3*, 585-594.
- (15) Zhang, L.; Dong, S. *Anal. Chem.* **2006**, *78*, 5119-5123.
- (16) Pellegrin, Y.; Forster, R. J.; Keyes, T. E. *Inorg. Chim. Acta* **2009**, *362*, 1715-1722.
- (17) Miao, W.; Choi, J. P.; Bard, A. J. *J. Am. Chem. Soc.* **2002**, *124*, 14478-14485.
- (18) Deiss, F.; LaFratta, C. N.; Symer, M.; Blicharz, T. M.; Sojic, N.; Walt, D. R. *J. Am. Chem. Soc.* **2009**, *131*, 6088-6089.
- (19) Zhou, J.; Belov, L.; Huang, P. Y.; Shin, J.; Solomon, M. J.; Chapuis, P. H.; Bokey, L.; Chan, C.; Clarke, C.; Clarke, S. J.; Christopherson, R. I. *J. Immunol. Methods* **2010**, *355*, 40-51.
- (20) Wolf, M.; Juncker, D.; Michel, B.; Hunziker, P.; Delamarche, E. *Biosensors and Bioelectronics* **2004**, *19*, 1193-1202.
- (21) Angenendt, P., *Drug Discov. Today* **2005**, *10*, 503-511.
- (22) Thomas, J. H.; Kim, S. K.; Hesketh, P. J.; Halsall, H. B.; Heineman, W. R., *Anal. Biochem.* **2004**, *328*, 113-122.
- (23) Cretich, M.; Damin, F.; Pirri, G.; Chiari, M. *Biomol. Eng.* **2006**, *23*, 77-88.
- (24) Wang, C.; Zhang, Y. *Sensors Actuators B: Chem.* **2006**, *120*, 125-129.

- (25) Deregt, D.; Furukawa-Stoffer, T. L.; Tokaryk, K. L.; Pasick, J.; Hughes, K. M. B.; Hooper-McGrevy, K.; Baxi, S.; Baxi, M. K. *J. Virol. Methods* **2006**, *137*, 88-94.
- (26) Sewter, C. Multianalyte profiling using xMAP technology. <http://www1.imperial.ac.uk/resources/E6F0A63F-C0DE-49D9-A6BF-ECBCEDBD9643/2010>).
- (27) Elshal, M. F.; McCoy, J. P. *Methods* **2006**, *38*, 317-323.
- (28) Kingsmore, S. F. *Nat Rev Drug Discov* **2006**, *5*, 310-321.
- (29) Meso scale discovery Immunogenicity assays using MSD's multiarray technology. http://www.mesoscale.com/CatalogSystemWeb/WebRoot/literature/notes/pdf/Immunogenicity_Applications.pdf2010).
- (30) Debad, J. D.; Glezer, E. N.; Wohlstadter, J.; Sigal, G. B. In *Clinical and biological applications of ECL*; Electrogenerated Chemiluminescence; Marcel Dekker.Inc: Maryland, U.S.A., 2004; pp 19.
- (31) Fernández-Sánchez, C.; McNeil, C. J.; Rawson, K. *Tr. Anal. Chem* **2005**, *24*, 37-48.

CHAPTER VII

SUMMARY AND FUTURE WORK

7.1 CONCLUSIONS AND FUTURE WORK

In conclusion, this thesis reports on the development of application of novel nanomaterials in solid state ECL biosensors. The majority of the ECL applications make use of solution phase systems where the ruthenium complex is in liquid phase and is continuously pumped to the reaction zone.¹ Though this method is rapid and simple, it is associated with several disadvantages, such as signal loss due to diffusion of the ECL reagent out of the detection zone, limited ability to repeatedly electrochemically cycle an individual luminophore and high reagent consumption.¹ Immobilization of the ECL luminophore on an electrode surface helps to eliminate these problems. Ultimately, the development of sensitive and selective ECL biosensors depends on understanding the underlying charge transport kinetics and biomolecular interactions between the ECL reactants. Thus, this work focused on studying the underlying mechanisms of charge transport through modified electrode surfaces with particular emphasis on the effect of nature of the luminophore, electrolyte, potential waveform and pH on ECL emission with a view to their application as a biosensor platform.

Quantification of biological or biochemical processes are of utmost importance for medical, biological and biotechnological applications. However, converting the biological information to an easily processed electronic signal is challenging due to the complexity of connecting an electronic device directly to a biological entity. Redox polymer films are very attractive for this purpose. In many of solid state ECL systems available it has been observed that it is difficult to control the thickness and morphology of the polymer film and to confirm if the emission arises from the bound material or from the electrolyte solution containing the leached surface material. These key issues were addressed in Chapter 4 through electropolymerization of $[\text{Ru}(\text{aphen})_2\text{bpy}]^{2+}$ and $[\text{Ru}(\text{aphen})_3]^{2+}$. Though electropolymerisation of similar compounds has been done in the past, to the best of the authors' knowledge, their ECL properties have not been reported. It was found that though electropolymerisation gave control over the thickness of the electrochemically synthesised polymers, the morphology of the films were significantly influenced by the pH of the

deposition medium. For $[\text{Ru}(\text{aphen})_3]^{2+}$ films, acidic deposition medium not only increased the surface coverage of the electrochemically synthesised polymers formed but also increased the charge transfer coefficients and ECL intensity by one order of magnitude (from 4.8×10^5 A.U. in CH_3CN to 2.1×10^6 A.U. in H_2SO_4) when compared to a basic deposition medium. But on the other hand, $[\text{Ru}(\text{aphen})_2\text{bpy}]^{2+}$ films needed higher pH. This clearly indicates that even though there are subtle differences in the structure of the polymers, their behaviour could be very different depending on the surrounding environment. This finding is crucial as depending on the type of biological sample measured, biosensors need to operate in a range of pH values. Future work will require a comprehensive investigation into the effect of solvent on the swelling properties of the electropolymerised films and its effect on the kinetics of ECL reaction. This could give valuable insights into the ECL kinetics of electropolymerised films.

Recently, biosensor research is driven by the need to miniaturize the devices. Nano scale measurements are extremely challenging and device characterization and optimization becomes more and more difficult. Novel tools that combine different sensing methods provide complementary information that is needed to understand the limitations of the sensor and to optimize its performance. Chapter 5 describes the successful application of $[\text{Ru}(\text{bpy})_2\text{PVP}_{10}]^{2+}$ within a surface confined layer coupled with sensitive lock-in detection. The phase locked detection technique provided by the lock-in amplifier and the immobilized redox polymer layer enabled the achievement of significantly low limits of detection for oxalate ($5 \mu\text{M}$). Reduced signal to noise and better sensitivities were also obtained when compared to the solution phase study reported in literature.² AC impedance spectroscopy and modified Randle-Ershler model were also used to model the polymer/electrode ECL system. Encouraging results from the equivalent circuit was obtained with regards to predicting charge transfer rates however, it does not predict kinetic parameters accurately. There was a significant deviation from the expected values and hence, further investigations addressing the addition of new circuit elements to the model or changing the initial assumptions is necessary.

Early, low-cost point-of-care detection of biomarkers for diseases is crucial to diagnose and to manage health problems world wide. An excellent example is the widespread use of the glucose biosensor for monitoring diabetes mellitus. Many biomarkers are present in the nano molar range (cardiac troponin I ~0.35 ng/mL) in blood. Hence, there is a fundamental requirement for biosensors which can detect pico or femto molar concentrations of biomarkers. This was achieved in Chapter 6, by signal amplification and superior biomolecule immobilization strategy. The patterned assembly of nanotube forests on transparent ITO substrates is described. Though reports of self assembled carbon nanotube forests on non transparent substrates are available, for the first time, a transparent substrate has been used in this work. A novel approach was used to develop an ECL sensor using G1.5 acid terminated PAMAM dendrimers and $[\text{Ru}(\text{bpy})_2\text{PICH}_2]^{2+}$ coated silica nanospheres. The dendrimers acted as size selective protein linkers and the ruthenium coated spheres lead to significant signal amplification. Remarkably, the ITO sensor showed a wide linear dynamic range and was capable of detecting as few as a million IgG-spheres (800 nm dia) with a lowest detection limit being 1.1 picoM IgG. Future direction towards testing clinical samples and developing multiplex arrays is clearly envisaged.

7.2 REFERENCES

- (1) Forster, R. J.; Hogan, C. F. *Anal. Chem.* **2000**, 72, 5576-5582.
- (2) Jirka, G. P.; Nieman, T. A. *Microchim. Acta.* **1994**, 113, 339-347.